

ÉCOLE DOCTORALE de Physique et Chimie Physique
Institut de Physique et Chimie des Matériaux de Strasbourg

THÈSE présentée par :

Tindara VERDUCI

soutenue le : **13 décembre 2016**

pour obtenir le grade de : **Docteur de l'université de Strasbourg**

Discipline/ Spécialité : Physique de la matière condensée

**Optimizing OFETs properties for
spintronics applications**

THÈSE dirigée par :

M. B. DOUDIN

M. P. Samori

Professeur, Université de Strasbourg

Professeur, Université de Strasbourg

RAPPORTEURS :

M. M. COEY

M. M. CALAME

Professeur, Trinity College Dublin

Professeur, University of Basel

AUTRES MEMBRES DU JURY :

M. D. VUILLAUME

M. E. ORGIU

Directeur de recherche, CNRS (IEMN)

Maître de conférences, Université de Strasbourg

Résumé de thèse

Cette thèse a conduit à l'étude du transport des porteurs de charge de plusieurs dispositifs afin d'identifier les propriétés spécifiques permettant la réalisation de vanes à spin organique de géométrie latérale. En effet, cette thèse a porté sur deux domaines de recherche principaux: l'électronique organique et la spintronique organique. Le premier construit des dispositifs électroniques utilisant des matériaux semi-conducteurs organiques, exploitants ainsi leurs uniques propriétés, telles que leur facile et faible coût de fabrication, la possibilité d'ajuster chimiquement ces propriétés (en modifiant leur structure moléculaire), et leur production à basse température (<180 °C) à partir d'une solution sur une grande surface ou des supports souples. Ces avantages ne sont pas offerts par le silicium ou tout autre matériau inorganique.

Les applications de l'électronique organique sont énormes grâce à la possibilité de construire des dispositifs pouvant être pliés, tordus, et se moulant sur toutes surfaces ou qui peuvent interagir avec des environnements biologiques. Des exemples de ces dispositifs sont les diodes électroluminescentes organiques (OLED) [1, 2], les cellules photovoltaïques organiques (OPV) [3, 4], et les transistors organiques à effet de champ (OFET) [5, 6]. Les OLEDs sont déjà en production commerciale pour fabriquer des écrans de haute efficacité, de forte luminosité, et couleur pour les téléphones mobiles et les appareils photo numériques.

La spintronique vise à incorporer la fonctionnalité du spin au sein des technologies, déjà émergente, de l'électronique afin d'exploiter non seulement la charge de l'électron, mais aussi son spin. Elle promet ainsi une large gamme de nouveaux phénomènes et applications. La spintronique est apparue grâce à la découverte de la magnétorésistance géante (GMR) en 1988 et la magnétorésistance de tunnel (TMR) sept ans plus tard. Ces deux effets sont basés sur le flux d'un courant électrique polarisé par spin à travers de multiples couches de matériaux magnétiques et non-magnétiques. Une variation considérable de la résistance électrique de ces structures est obtenue par commutation de l'aimantation des couches magnétiques de parallèle à antiparallèle [7, 8]. Dans le cas du GMR, la couche non magnétique est un métal, tandis que pour le TMR, il s'agit de très minces isolants. La découverte des GMR et TMR a conduit à une véritable révolution dans le monde du stockage magnétiques des données informatiques, principalement parce qu'ils ont permis la fabrication de têtes de disque dur beaucoup plus efficace pour la lecture et l'écriture de petits paquet de données magnétiques. Cependant, le développement réel de la spintronique

correspond au moment où des matériaux semi-conducteurs ont été mis en œuvre en tant que canaux actifs entre les couches magnétiques.

Outre la flexibilité, le faible coût de production, et la possibilité d'être produit par ingénierie chimique, les matériaux organiques sont attrayants pour la construction de dispositifs de spintronique car leur longue durée de vie théorique, τ_s [9, 10]. τ_s est un paramètre important pour la spintronique parce qu'il représente la période pendant laquelle les porteurs maintiennent leur mémoire de spin au sein du canal actif. Dans les matériaux organiques, la durée de vie des spins dépasse de plusieurs ordres de grandeur les valeurs typiquement trouvés pour les matériaux inorganiques et devient donc avantageuse car elle permet de manipuler les spins pendant leur transport. Cependant, la longue durée de vie du spin ne se traduit pas par une grande longueur de diffusion du spin l_{sf} , qui définit la distance sur laquelle les porteurs maintiennent leur mémoire de spin.

Dans les systèmes fonctionnant en régime diffusif, la longueur de diffusion de spin est proportionnelle à la durée de vie du spin au travers de la relation:

$$l_{sf} = \sqrt{D \cdot \tau_s} \quad (1)$$

Où $D = \frac{k_B T}{e} \cdot \mu$ est le coefficient de diffusion du support et dépend de la mobilité μ du semi-conducteur organique (OSC). Ici, le problème est que le transport porteur dans les OSC n'est pas de type bande, mais implique des sauts entre les sites d'énergie voisins. Ce transport par sauts limite la mobilité μ de ces matériaux, qui est typiquement faible (entre 0,01 cm²/V·s et 3 cm²/V·s pour les OFET à base de polymère), et donc la longueur de diffusion de spin l_{sf} qui est habituellement de l'ordre de quelques nm [10]. Dans le cadre de notre discussion, on peut facilement déduire qu'une manière d'augmenter la longueur de diffusion du spin est d'utiliser des OSC à haute mobilité.

Le transport du courant polarisé par spin est généralement étudié dans des dispositifs connus sous le nom de vanes de spin qui se composent de deux électrodes ferromagnétiques (FM) séparées par un séparateur en semi-conducteur. Dans le cas des vanes à spin organique, le séparateur est constitué d'un semi-conducteur organique. Comme pour les dispositifs de GMR métalliques et les jonctions à effet tunnel magnétique, une modulation importante de la résistance du dispositif est attendue lors du changement de l'aimantation relatif des électrodes FM.

Les vanes à spin se déclinent en deux géométries: verticales et latérales. La géométrie latérale est plus adaptée à notre étude en raison de nombreux avantages. Tout d'abord, elle permet d'appliquer simultanément différents stimuli, tels que le stimulus électrique, le stimulus magnétique, le stimulus optique, pour lesquels un changement des propriétés de transport est attendu, ce qui permet des dispositifs à multiple stimuli. Il offre également la possibilité de mettre en œuvre une troisième électrode, une grille, qui permet d'ajuster la conductivité du matériau semi-conducteur de sorte qu'il soit possible de créer un dispositif de spintronique commandé par grille. De plus, la géométrie latérale est plus adaptée pour la chimie moléculaire humide et des polymères fabriqués à partir de solutions et donnant ainsi la possibilité de choisir parmi l'énorme gamme de molécules offertes par la chimie organique tandis que la géométrie verticale limite le choix aux quelques molécules qui peuvent être déposées sous vide poussé (UHV) sans se briser.

Cependant, l'un des principaux goulots d'étranglement au sein des vanes à spin latérales est la contamination massive par l'oxydation des électrodes ferromagnétiques (FM) exposées à l'air qui rend le signal polarisé spin des électrons totalement aléatoire. En fait, la couche d'oxyde (hydroxyde) joue le rôle de centre de diffusion de spin, mélangeant la polarisation du spin des électrons et rendant les propriétés magnétiques imprévisibles. On s'attend donc à ce que la polarisation du spin des charges injectées (collectées) dans l'OSC diminue fortement.

En général, le mécanisme de fonctionnement d'une vanes à spin nécessite trois ingrédients clés: l'injection d'un courant polarisé par spin de la première électrode FM, le transport (et éventuellement manipulation) le long du canal actif et la détection par la seconde électrode FM.

Le modèle d'injection de spin (et de détection) a été développé par Fert et Jaffres pour une vanes à spin inorganique en régime diffusif [12]. Les résultats de ce modèle peuvent être résumés en considérant le graphique de la figure 1 où la magnétorésistance $\Delta R/R^P$ (où $\Delta R = R^{AP} - R^P$ est le changement de résistance entre la configuration d'aimantation antiparallèle et parallèle des électrodes). En fonction du rapport entre la résistance de contact par unité de surface r_b^* et la résistance de canal dépendant du spin r_{NM} (défini comme le produit de la résistivité du canal ρ_N et la longueur de diffusion de spin l_{sf}^{NM}) pour différentes valeurs de t_N/l_{sf}^{NM} (Où t_N est la longueur du canal). D'après le graphique de la Figure 1, il s'avère que l'injection/détection de spin est obtenue lorsque les interfaces entre le semi-conducteur et les électrodes FM sont dépendantes du spin et avec des valeurs

contenues dans une fenêtre bien définie centrée à $r_b^*/r_N \sim 1$. Cette exigence est particulièrement difficile à réaliser car les OSCs sont caractérisés par des valeurs de résistivité qui sont plusieurs ordres de grandeur plus grandes que celles rapportées pour des électrodes métalliques, ce qui donne des valeurs de résistance de contact qui sont trop grandes. Ce problème est connu sous le nom de distorsion de conductance et représente l'un des principaux problèmes de la spintronique organique [12, 13, 14].

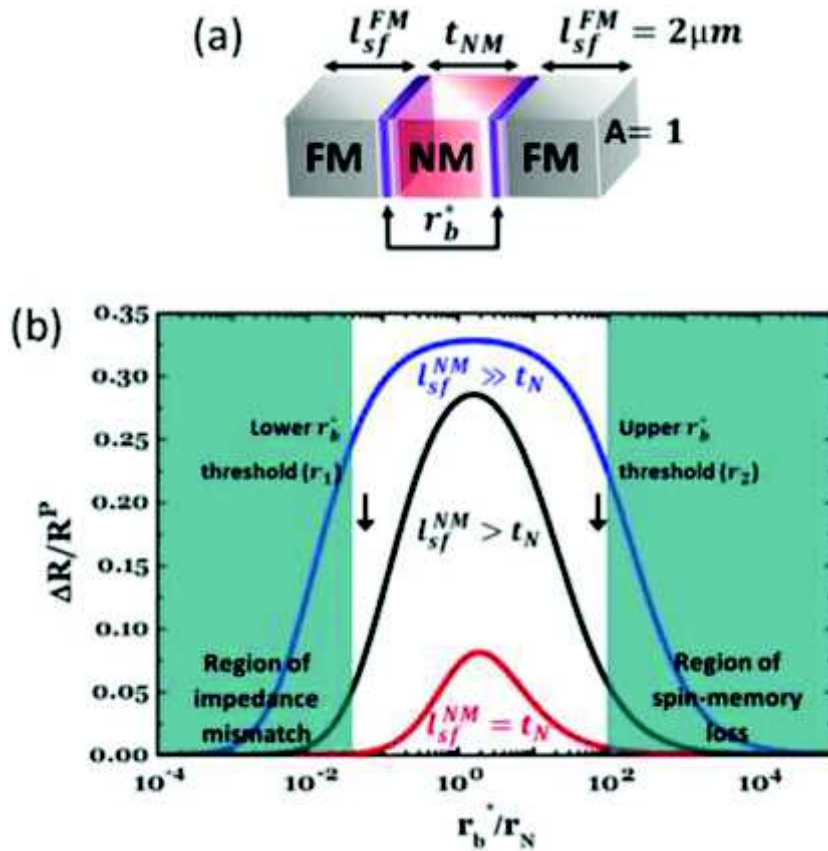


Figure 1 (a) Géométrie de la structure calculée. (b) $\Delta R/R^P$ calculé pour la structure de type (a) en fonction du ratio r_b^*/r_N pour trois différents séparateurs d'électrode t_N (20 nm, 200 nm, and 2 μm) et pour une longueur de diffusion du spin fixe $l_{sf}^{NM} = 2 \mu\text{m}$. Les calculations ont été réalisées pour $F_1 = F_2 = \text{Co}$ ($r_F = 4.5 \times 10^{-15} \Omega\text{m}^2$, $\beta = 0.46$, $l_{sf}^{FM} = 60 \text{ nm}$); $\text{NM} = \text{SC}$ ($r_N = 4 \times 10^{-9} \Omega \cdot \text{cm}^2$, $l_{sf}^{NM} = 2 \mu\text{m}$) et $\gamma = 0.5$ pour le coefficient d'asymétrie de spin de la résistance d'interphase. La fenêtre optimale pour le signal MR est entre une résistance inférieure r_1 et une résistance supérieure r_2 . Adopté de [12].

Une autre condition importante issue du modèle de Fert et Jaffres est que le courant injecté sera maintenu en polarisation de spin au travers le canal si sa longueur t_N est inférieure à la longueur de diffusion de spin l_{sf}^{NM} ($t_N < l_{sf}^{NM}$). Autrement, la mémoire du spin

sera perdue avant d'atteindre la seconde électrode FM de détection. En conséquence, en raison des courtes longueurs de diffusion de spin des matériaux organiques, la réduction de la longueur du canal à des dimensions nanoscopiques est impérative pour la réalisation de vanes à spin.

De ces considérations, nous déduisons qu'il y a trois conditions importantes à satisfaire pour la spintronique organique:

1. **avoir des électrodes FM sans oxyde à leur surface** afin d'avoir des injecteurs / détecteurs polarisés;

2. une importante longueur de diffusion du spin du canal actif, pour la conservation du signal de spin pendant le transport tout au long du canal, et donc **des OSC à mobilité élevée**;

3. **de faibles valeurs de résistance de contact** à l'interface entre le canal organique et l'électrode métallique afin d'assurer l'injection/détection des spins.

Pour résoudre le problème de l'oxydation de la surface de l'électrode FM, nous avons utilisé une approche basée sur la passivation de la surface de ces électrodes par des couches de carbone ultra-minces. En particulier, en tant que matériau FM nous avons utilisé du nickel, car il s'est avéré être un excellent catalyseur de la croissance directe du Graphène et de films de carbone à sa surface [15, 16]. Les films de Ni/Graphène ont déjà été utilisés comme électrodes inférieures dans des dispositifs de spin inorganiques verticaux [17, 18, 19] et ainsi on a déjà prouvé qu'ils agissaient comme de bons injecteurs de spin.

Des couches de carbone ultra-minces ont été cultivées directement sur des électrodes de Ni de 100 nm d'épaisseur en utilisant deux approches [20]. Le premier utilise des températures élevées (750-850 °C) de croissance et un dépôt chimique en phase gazeuse (CVD) exploitant un composé de carbone gazeux et sa décomposition pour créer le film mince de carbone. La deuxième approche repose sur un revêtement de carbone solide (tel que le PMMA) sur le métal catalytique et est basée sur le chauffage de l'échantillon en utilisant une technique de cuisson thermique rapide (RTA) à des températures plus basses (ne dépassant pas 550 °C).

Au travers d'une analyse chimique et morphologique complète (impliquant la spectroscopie Raman, la microscopie à force atomique, la spectroscopie de photoélectrons aux rayons X et la spectroscopie de masse des ions secondaires de temps de vol), nous avons observé que la couche de carbone, produite par CVD ou RTA, réduit fortement l'oxydation du Ni. Les résultats montrent également que le traitement du Ni à des températures inférieures à 550 °C permet de conserver la qualité morphologique du film et une

composition optimale de Ni, exempte d'oxydes et de diverses formes de carbure. Lorsqu'on utilise des températures supérieures à 600 ° C, on obtient une couverture de Graphène cristallin (multicouche), mais aussi une détérioration de la rugosité des échantillons.

Les films de Ni/carbone traités passivés par CVD et RTA (et appelés Ni/CVD et Ni/RTA, respectivement) ont été mis en œuvre dans des transistors organiques à effet de champ (OFET) en tant qu'électrodes de source et de drain pour étudier leurs capacités d'injection au sein d'un polymère de type p, le poly[1,1'-bis(4-decyltetradecyl)-6-méthyl-6'-(5'-méthyl-[2,2'-bithiophen]-5-yl)-[3,3' biindolinylidene]-2,2'-dione] (IIDDT-C3) et de les comparer à des électrodes de nickel ou d'or pures. IIDDT-C3 a été choisi pour ses propriétés telles que sa mobilité élevée ($> 3 \text{ cm}^2/\text{V} \cdot \text{s}$ dans les dispositifs de fond bas) et son haut degré de cristallinité.

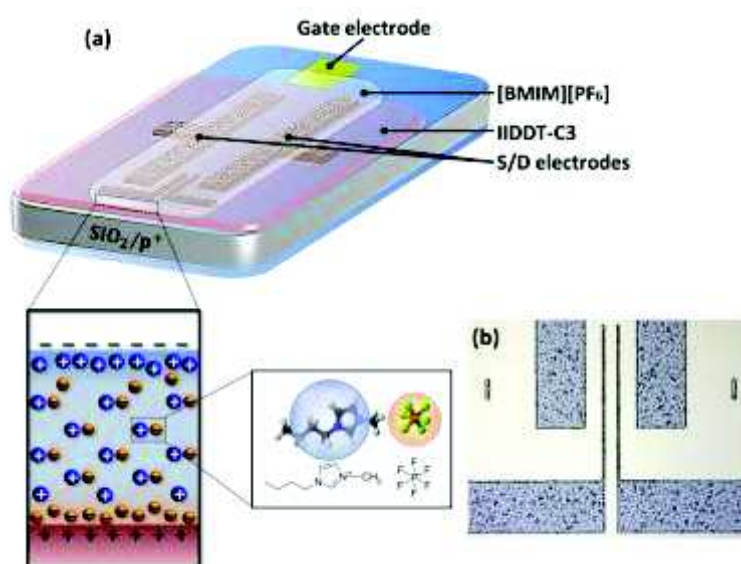


Figure 2 (a) Schéma de la géométrie du dispositif utilisé pour les mesures de résistance de contact à quatre sondes, ainsi que la section transversale du gel ionique illustrant la distribution et la structure chimique des ions utilisés. (b) Image optique du Graphène traité par CVD au-dessus des électrodes de nickel. La texture des couches de Graphène placées sur la surface du catalyseur et de même forme est clairement distinguée.

Le transport du support de charge en fonction du dopage a été étudié dans des dispositifs de longueur de canal $L = 50 \mu\text{m}$ en utilisant un gel d'ions électrolyte (gel contenant des ions mobiles) comme diélectrique de grille. La raison principale pour laquelle nous avons utilisé un porte électrolyte est la possibilité d'effectuer un dopage électrochimique sur le canal

conducteur afin d'accéder à des états de conductivité supérieur de l'OSC afin de satisfaire la deuxième condition (spin conservation) de la spintronique organique. La géométrie du dispositif, représentée sur le schéma de la figure 2, permet de réaliser des mesures à quatre sondes lors de l'estimation de la résistance de contact [21, 22] nécessaires pour vérifier si les valeurs de résistance de contact résultantes sont suffisamment basses pour être compatibles avec la troisième condition (injection / détection de spin).

La figure 3 montre une comparaison de la résistance de contact $R_C \cdot W$ (avec R_C la résistance de contact exprimée en Ω et W la largeur des électrodes) pour quatre types d'électrodes métalliques différentes (Ni, Ni/CVD, Ni/RTA et Au) en fonction de la tension de grille appliquée V_G . Pour tous les dispositifs, on observe une chute typique de la résistance de contact avec une tension de grille croissante. Dans la plage de valeurs V_G (supérieures à -3V) appliquées, les valeurs de résistance de contact des dispositifs Ni/CVD et Ni/RTA sont respectivement de un à deux ordres de grandeur inférieures à celles liées au dispositif de Ni pure. Ces faibles valeurs de résistance de contact, ainsi que les résultats de la caractérisation des propriétés physico-chimiques, démontrent clairement que notre couche de carbone ultra-mince agit efficacement comme barrière imperméable contre l'oxydation de la surface de Ni, améliorant la capacité d'injection dans les polymères conjugués. En outre, les électrodes traitées par RTA présentent la plus faible résistance d'interface pour l'injection de trous dans des dispositifs à transistors organiques, à égalité avec les électrodes d'or qui sont la référence [20]. Ces valeurs sont trois ordres de grandeur plus petites que les meilleures mesurées au sein d'OFETs avec un diélectrique de grille standard ($\sim 10 \text{ K}\Omega \cdot \text{cm}$) montrant que le passage d'électrolyte représente une approche appropriée pour satisfaire la condition d'injection/détection de spin.

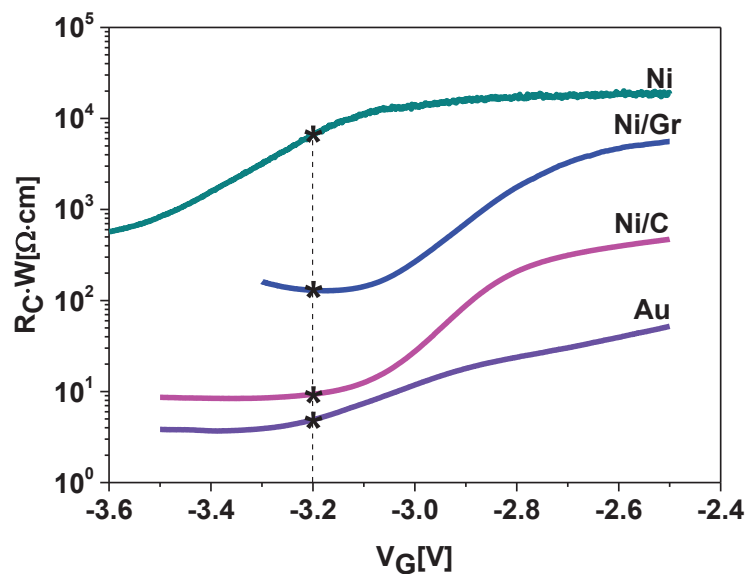


Figure 3 Résistance de contact totale normalisée en fonction de la tension de la grille pour des électrodes d'or, de Ni/RTA, de Ni/CVD, ou de pure Ni de 100 nm d'épaisseur.

Ces faibles valeurs de résistance de contact ont également été validées pour un autre polymère conjugué de type p, le PBTTT, caractérisé également par une mobilité élevée ($\sim 0.1 \text{ cm}^2/\text{V} \cdot \text{s}$), une bonne cristallinité et une longue longueur de diffusion de spins avec une valeur record de 200 nm. La figure 4 montre le graphique de la résistance de contact en fonction de la température pour des dispositifs à base de PBTTT avec des électrodes Au et Ni/RTA. À des températures élevées, la résistance de contact des deux appareils est à nouveau similaire avec des valeurs autour de $10 \text{ } \Omega \cdot \text{cm}$. Cependant, à basse température, Ni/RTA se comporte mieux que l'or avec des valeurs de résistance de contact d'un ordre de grandeur inférieur à 1,5 K. L'étude du transport de porteurs de charge dans ces dispositifs en fonction du niveau de dopage (V_G) et la température montre que les électrodes Ni/RTA sont bien adaptées pour remplacer l'or pour les appareils électroniques, offrant une alternative de faible coût. En outre, ils sont censés être de bons candidats pour la fabrication d'injecteurs de spin et de détecteurs pour les dispositifs de spintronique organique.

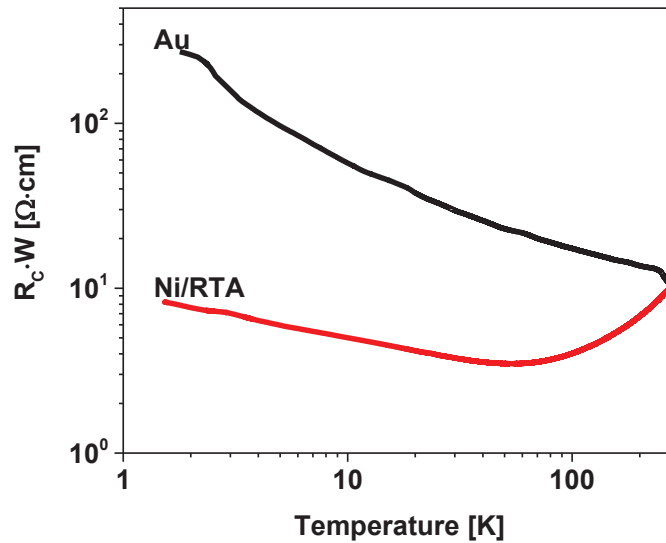


Figure 4 Résistance de contact spécifique des dispositifs à grande échelle ($L = 50 \mu\text{m}$) à base de PBTBT avec des électrodes d'or ou de Ni/RTA en fonction de la température.

La condition pour la conservation de spin déduite du modèle de Fert et de Jaffres, nécessite également la réduction d'échelle des dispositifs à des longueurs de canal t_N plus petites que la longueur de diffusion de spin l_{sf}^{NM} ($t_N < l_{sf}^{NM}$), c'est-à-dire équivalente à plusieurs dizaines de nm.

Jusqu'à présent, la réduction de la longueur du canal au sein des OFET ont entraîné une variété d'effets défavorables de canal court [23] du fait de deux problèmes principaux. Tout d'abord, le raccourcissement du canal actif augmente la force de champ électrique longitudinale induite entre source et drain par la tension de drain appliquée V_D . Cela signifie que l'approximation mathématique du canal n'est graduellement plus valide, ce qui donne des courbes de sortie super-linéaires, sans saturation au-dessus de la tension de pincement et de faibles valeurs $I_{ON/OFF}$ typiquement autour de 10. Deuxièmement, elle devient dominée par la résistance de contact des interfaces électrode/OSC plutôt que par la masse du polymère organique.

L'électrolyte représente une approche intéressante pour supprimer les effets de canaux courts, car il augmente le champ électrique transversal du fait de la haute capacité électrique de la double couche mince (quelque angströms) formée à l'interface électrolyte-semi-conducteur [24]. Ce mécanisme permet de conserver valide l'approximation progressive des canaux.

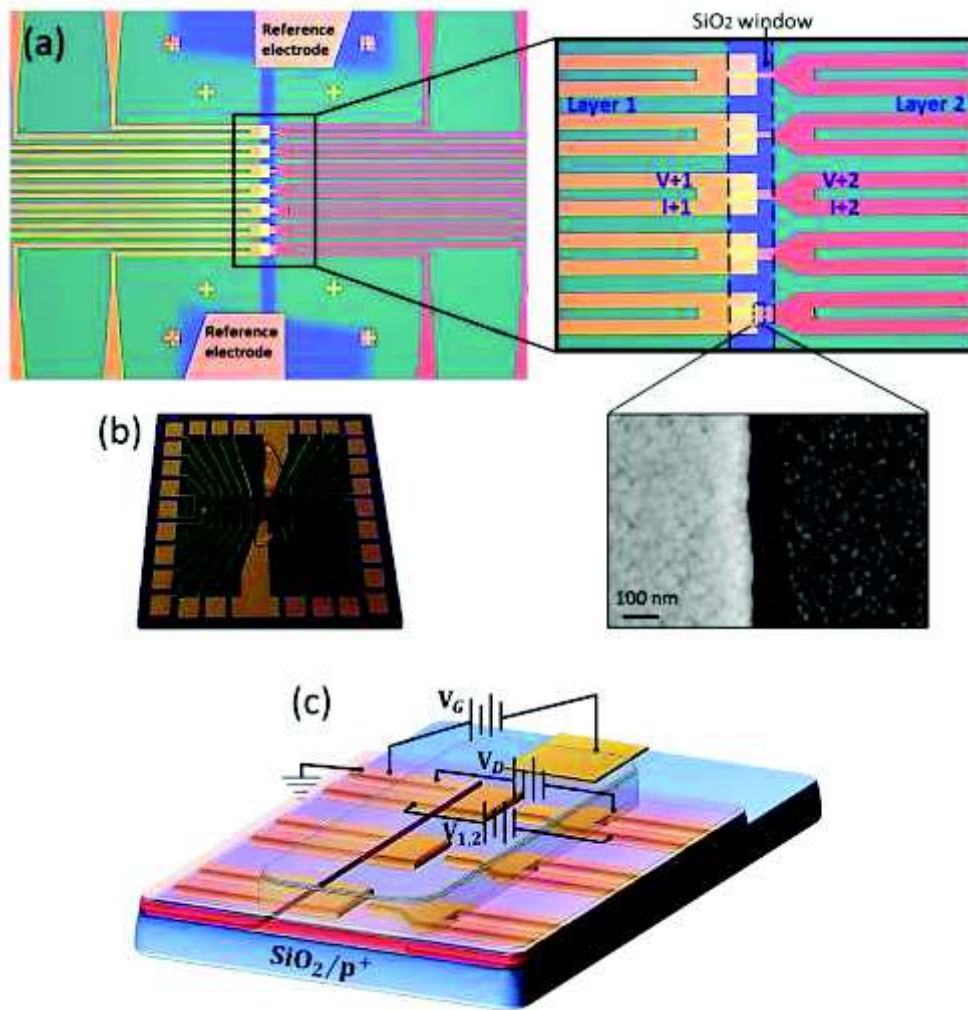


Figure 5 (a) Image microscopique optique de l'échantillon contenant sept nano-gaps en parallèle. Un zoom du canal montre une image SEM d'un des intervalles. (b) Photographie du substrat complet après application du revêtement de PBTTC par centrifugation et la déposition du gel ionique. (c) Schéma de circuit utilisé pour l'extraction de la résistance de l'échantillon. L'électrode source est mise à la masse et $V_D = -0,2$ V est maintenue constante tout en augmentant V_G .

Nous avons utilisé cette approche pour étudier le transport de porteurs de charge au sein de dispositifs à canaux courts utilisant encore les polymères IIDDT-C3 et PBTTC comme canal actif de manière similaire aux dispositifs à grande échelle. Nos échantillons sont constitués d'intervalles nanoscopiques d'or à haut rapport d'aspect, appelés nanotranchés, fabriqués par lithographie optique utilisant la méthode dite d'évaporation de bord d'ombre. La figure 5 montre la géométrie de l'échantillon, comprenant sept intervalles différents sur chaque puce. Des images de microscopie électronique à balayage (SEM) révèlent que la distance entre les électrodes métalliques est typiquement autour de 80 nm.

La figure 6 montre les courbes de sortie et de transfert mesurées à température ambiante pour les dispositifs à base de PBTTT. Nous avons observé une tendance typique des courbes de sortie à comportement linéaire et à faible polarisation source-drain, une bonne saturation à de hautes tensions source-drain et une très bonne modulation pour différentes tensions de grille.

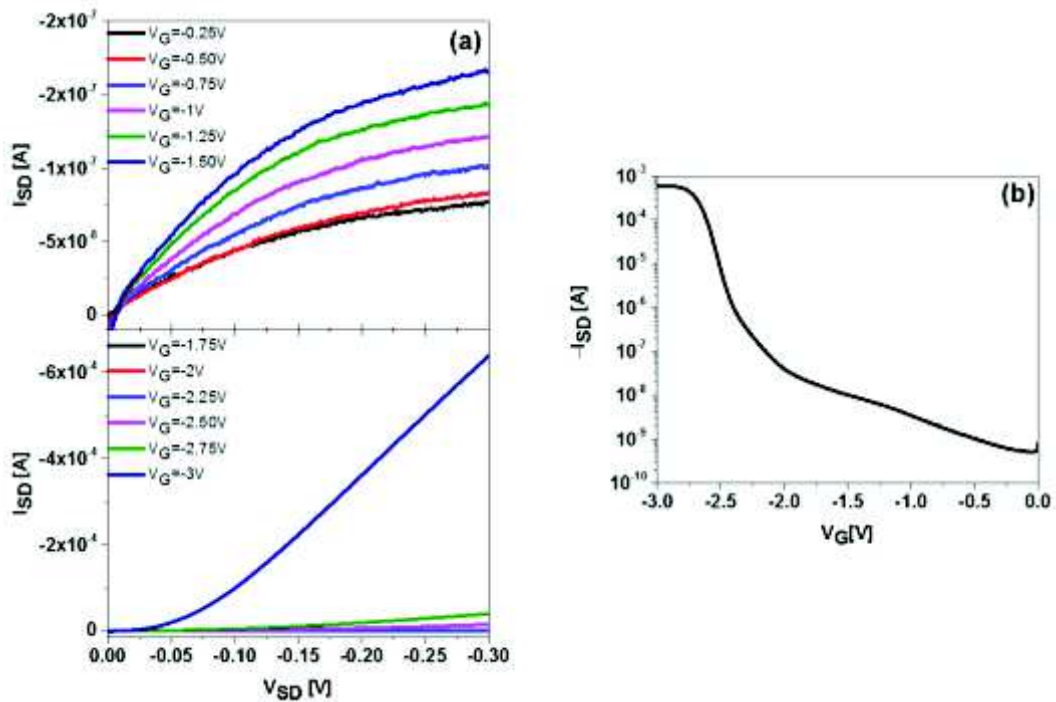


Figure 6 Caractéristiques de la sortie (a) et du transfert (b) du nanotransistor d'or ($L = 80$ nm) à base de PBTTT à température ambiante. A des tensions de drain élevées, les courbes de sortie se courbent lorsque le point de pincement est approché en accord avec le comportement OFET à canaux longs. $I_{ON/OFF}$ jusqu'à 10^6 est observé dans la courbe de transfert. Seule la trace directe est tracée.

Une modulation claire du courant dans le canal de semi-conducteur est également observée dans les courbes de transfert conjointement avec un rapport $I_{ON/OFF}$ étonnamment élevé de l'ordre de 10^6 . Des résultats similaires ont été obtenus pour IIDDT-C3 avec $I_{ON/OFF}$ de 10^{10} . Les résultats de la Figure 6 montrent une suppression claire du premier problème déterminant les effets de canal court.

En ce qui concerne la résistance de contact, à partir de la géométrie du dispositif de la Figure 5, nous avons réalisé que nous ne pouvons pas mesurer indépendamment la résistance du canal $R_{channel}$ et la résistance de contact R_c car nous sommes limités à une

géométrie à deux points. Nous avons donc déterminé la résistance de canal et de contact des nanodispositifs en utilisant les valeurs de conductivité extraites de dispositifs à grande échelle, de géométrie montrée à la Figure ,2 en assumant que les propriétés intrinsèques du canal semi-conducteur sont maintenues d'un échantillon à l'autre.

Le graphique de la résistance totale mesurée en fonction de la température de la Figure 7 pour trois nanotransistors de même longueur de canal L et de largeur W différente (entre 30 μm et 50 μm) présente des valeurs remarquablement faibles pour tous les échantillons. Les valeurs de résistance de contact R_c (comprises entre 0,035 $\Omega\cdot\text{cm}^2$ et 0.1 $\Omega\cdot\text{cm}^2$) sont comprises entre deux et trois ordres de grandeur inférieures à celles mesurées pour les dispositifs à grande échelle. Des valeurs similaires ont été trouvées également pour les dispositifs de longueur de canal $L = 30 \text{ nm}$ et 300 nm et avec le polymère IIDDT-C3 comme canal semi-conducteur et montrent clairement la suppression du second problème déterminant les effets de canal court. Ces résultats sont remarquables étant donné que jusqu'à présent, tous les dispositifs à canaux courts publiés présentent toujours des valeurs de résistance de contact qui sont plusieurs ordres de grandeur supérieures à celles mesurées pour les dispositifs à grande échelle.

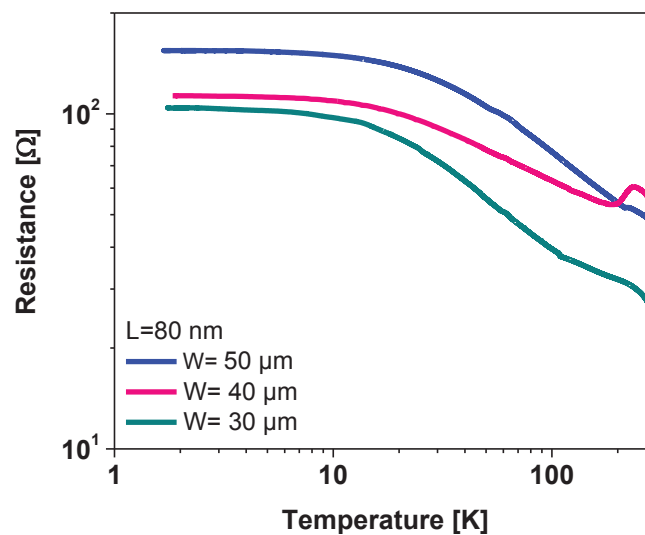


Figure 7 Résistance d'échantillon en fonction de la température pour trois dispositifs différents (avec la même longueur de canal L et la largeur W différente) fermée au niveau maximum de dopage. Des valeurs remarquables sont observées jusqu'à 1.5 K.

Un aspect principal que nous devons considérer à ce stade est que tous les dispositifs étudiés dans cette thèse sont en configuration décalée et sont donc caractérisés par une grande zone de contact entre les électrodes source/drain et grille en raison de leur géométrie. Dans ce cas, les supports sont injectés/collectés non seulement à partir du bord de contact, mais également à partir des zones de l'électrode qui chevauchent la grille. Par conséquent, comme représenté sur la Figure 8, il existe une répartition non uniforme du courant source-drain qui est significative au niveau des bords des contacts et décroît exponentiellement avec la distance des bords de l'électrode, avec une distance caractéristique L_T , appelée longueur de transfert et donné par:

$$L_T = \sqrt{\frac{r_b [\Omega \cdot \text{cm}^2]}{R_{\text{Sheet}} [\Omega]}} \quad (2)$$

Où $r_b = R_c \cdot W \cdot L_T$ est la résistivité de contact spécifique, c'est-à-dire la résistance de contact par unité de surface [exprimée en $\Omega \cdot \text{cm}^2$] et $A = W \cdot L_T$ est la zone d'injection effective. Cet effet est connu comme courant d'encombrement du courant [25].

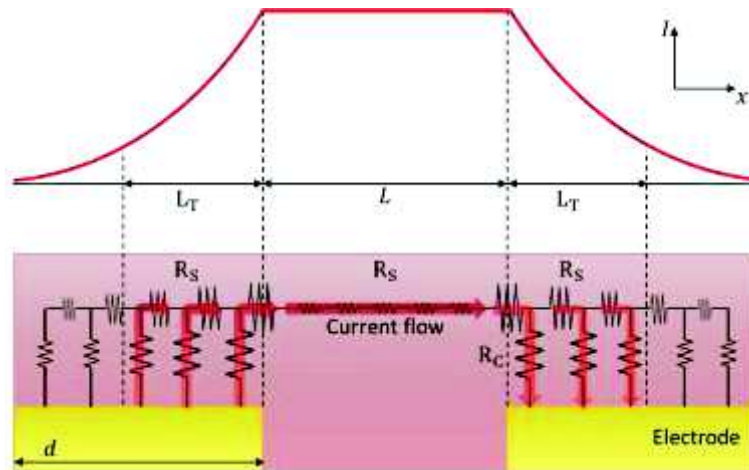


Figure 8 Schéma de l'effet d'encombrement de courant montrant le courant non uniforme circulant dans un film mince plus résistif que les électrodes de source et de drain. Ceci fait que le canal actif de longueur $2L_T + L$, où L est la distance entre les électrodes, et L_T est la longueur de mise à l'échelle du courant, augmente de façon exponentielle à l'écart de l'intervalle entre les électrodes. L'écoulement du courant source-drain est indiqué par des flèches. Sous le contact source (drain), la composante verticale du courant augmente (décroît) en se rapprochant (vers l'extérieur) du bord. Dans la zone active du canal, le courant ne circule qu'à l'horizontale. Ce modèle a été appliqué à la structure de transistor décalée (grille supérieure non représentée ici) ou à des couches uniformément conductrices.

L'effet d'encombrement du courant conduit à une diminution de la résistance de contact en fonction de la tension de grille. Par conséquent, il devient de plus en plus important lorsque la résistance d'interface domine ce qui est le cas lorsque l'on miniaturise des appareils. Il est notre opinion que l'effet d'encombrement du courant est la raison principale des faibles valeurs de résistance de contact que nous observons dans nos dispositifs à canaux courts.

Les valeurs de longueur de transfert L_T , extraites expérimentalement pour nos nanodispositifs, vont de 520 nm à 160 nm pour 300°K et sont donc plus grandes que l'espacement entre les électrodes ($L_T \gg L$). Sous cette assumption on obtient:

$$2R_c \sim R_{channel} \sim \frac{1}{2} R_{sample} \quad (3)$$

Ce qui signifie que l'encombrement du courant est le fait de l'injection de charge produit sur une zone plus grande, jusqu'à une résistance de contact équilibrant la résistance du canal.

Étant donné que les longueurs de diffusion de spin indiquées dans les composés organiques se comparent aux valeurs les plus petites de longueur d'encombrement du courant trouvées, il existe un grand besoin de soulever la question de l'encombrement du courant pour les applications de spintronique organique.

Tout d'abord, nous devons vérifier que la prise en compte de L_T , et donc de l'effet de crowding actuel, dans le calcul de r_b , n'affecte pas la validation de l'état de l'injection/détection spin ($r_b / r_N \sim 1$). Nous avons observé que les valeurs obtenues de r_b , lorsqu'elles sont ajoutées à la courbe de la magnétorésistance MR calculée par Fert et Jaffres pour une vanne de spin latérale en fonction du rapport r_b / r_N , correspondent à l'état d'injection / détection de spin. En particulier, nous avons observé que nos valeurs de r_b / r_N (rectangle bleu sur la Figure 9) sont centrées autour de 1.

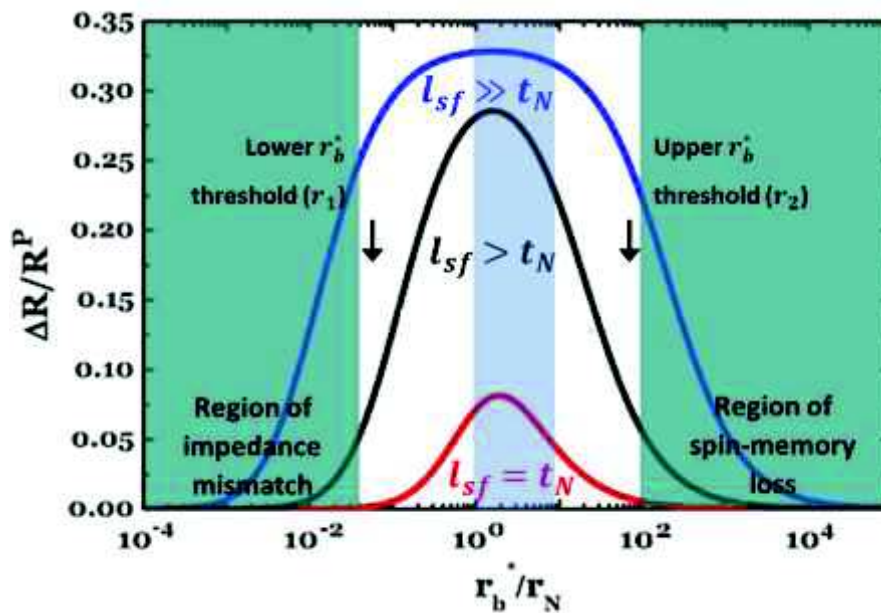


Figure 9 La magnétorésistance ($\Delta R/R_p$) en fonction du rapport r_b/r_N calculé pour une vanne de spin avec des électrodes de cobalt pour trois longueurs de canal différentes t_N (20 nm, 200 nm et 2 μm) pour une longueur de diffusion de spins fixe $L_{sf}^{NM} = 2 \mu\text{m}$. Le rectangle bleu représente la plage des valeurs r_b/r_N extraites des dispositifs nanoscopiques à base d'or et de PBTBT à température ambiante. Les valeurs sont centrées autour de la fenêtre optimale pour le signal de magnétorésistance entre les valeurs de seuil de résistance basse r_1 et résistance haute r_2 . Adopté de [12].

Un autre aspect important que nous devrions prendre en considération pour les applications de spintronique est que la longueur de canal efficace d'un dispositif planaire (d'écarté) devrait être considérée comme étant de l'ordre de $2L_T + L$, dépassant la plus grande estimation publiée de la longueur de mémoire de spin des matériaux [25]. Cependant, en construisant des vannes latérales de spin avec une longueur de canal aussi petite que 20-30 nm, il serait possible, en principe, que le courant polarisé de spin, lié aux porteurs de charge injectés au bord des contacts, soit détecté même s'il est réduit de manière significative Par la contribution des porteurs de charges injectés loin des bords de contact.

Nous avons également étudié le transport des porteurs de charge et la résistance de contact sur des dispositifs fabriqués avec des électrodes FM pour une future recherche dans le domaine de la spintronique organique. En effet, nous avons fabriqué des dispositifs nanoscopique de Ni et des électrodes de Ni couverte de carbone (Ni/RTA) destinées à tester des films fins de PBTBT, à conductivité élevée, au sein de dispositifs de vannes à spin latéral. PBTBT a été choisi comme canal actif étant donné la longue distance de diffusion du spin prédite (200 nm).

Comme le montre la Figure 10 à 300°K, la résistance pour l'échantillon de Ni/RTA est environ deux ordres de grandeur plus petite que dans l'échantillon de Ni pure. Cette différence augmente quand les échantillons sont refroidis. Cependant, alors que les dispositifs Ni/RTA à grande échelle présentent un comportement similaire à l'or, la Figure 10 montre des preuves évidentes que Ni/RTA ne peut pas atteindre les faibles valeurs de résistance d'interface trouvées pour l'or. Cela pourrait être dû à l'action du procédé RTA dans les nanotranchés, qui a pour résultat des couches de carbone amorphe très épaisses lorsque l'épaisseur du catalyseur Ni est inférieure à 100 nm. Par conséquent, nous en déduisons que la fabrication de nanotranchés Ni/RTA de 100 nm d'épaisseur est nécessaire afin de diminuer la résistance de l'échantillon et donc la LT .

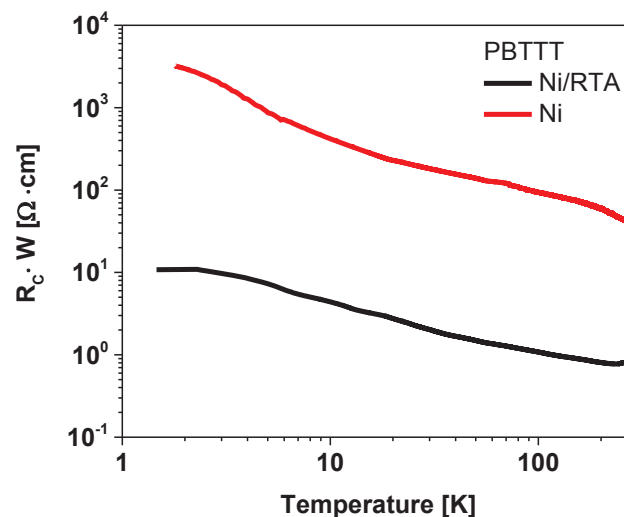


Figure 10 Résistance de contact spécifique en fonction de la température des dispositifs nanoscopique à base de PBTTT avec des électrodes Ni ou Ni/RTA.

Si on superpose les valeurs r_b/r_N à température ambiante sur le graphique de la magnétorésistance de Fert et Jaffres comme pour les dispositifs d'or, on observe que les valeurs r_b/r_N pour Ni/RTA sont toujours à l'intérieur de la fenêtre définie par la valeur seuil de la désynchronisation de l'impédance et de la perte de mémoire du spin. Ces résultats montrent le potentiel des dispositifs nanoscopique Ni/RTA comme matrice pour construire des vannes de spin latérales, même si une fabrication mieux contrôlée et optimisée des électrodes de métal de transition passivées demeure nécessaire.

En résumé, l'étude développée dans cette thèse a permis d'établir les propriétés requises pour qu'un dispositif soit un candidat légitime pour être un dispositif électronique organique de géométrie latérale. A travers l'étude d'un dispositif planaire, nous avons proposé une solution possible pour satisfaire les critères nécessaires à la réalisation d'un transport de courant polarisé par spin de type diffusif dans un matériau semi-conducteur organique. Enfin, la possibilité d'injecter/détecter le spin dans nos dispositifs à canaux courts a été identifiée grâce à d'impressionnantes valeurs mesurées de résistance de contact.

Références

1. Friend, R. H. *et al.* Electroluminescence in conjugated polymers. *Nature* **397**, 121–128 (1999).
2. Forrest, S. R. The path to ubiquitous and low-cost organic electronic appliances on plastic. *Nature* **428**, 911–918 (2004).
3. Brabec, C. J., Sariciftci, N. S. & Hummelen, J. C. Plastic Solar Cells. *Adv. Funct. Mater.* **11**, 15–26 (2001).
4. Peumans, P., Uchida, S. & Forrest, S. R. Efficient bulk heterojunction photovoltaic cells using small-molecular-weight organic thin films. *Nature* **425**, 158–162 (2003).
5. Dimitrakopoulos, C. d. & Malenfant, P. r. l. Organic Thin Film Transistors for Large Area Electronics. *Adv. Mater.* **14**, 99–117 (2002).
6. Gundlach, D. J., Lin, Y. Y., Jackson, T. N., Nelson, S. F. & Schlom, D. G. Pentacene organic thin-film transistors-molecular ordering and mobility. *IEEE Electron Device Lett.* **18**, 87–89 (1997).
7. Baibich, M. N. *et al.* Giant Magnetoresistance of (001)Fe/(001)Cr Magnetic Superlattices. *Phys. Rev. Lett.* **61**, 2472–2475 (1988).
8. Binasch, G., Grünberg, P., Saurenbach, F. & Zinn, W. Enhanced magnetoresistance in layered magnetic structures with antiferromagnetic interlayer exchange. *Phys. Rev. B* **39**, 4828–4830 (1989).
9. Dediu, V. A., Hueso, L. E., Bergenti, I. & Taliani, C. Spin routes in organic semiconductors. *Nat. Mater.* **8**, 707–716 (2009).
10. Szulczewski, G., Sanvito, S. & Coey, M. A spin of their own. *Nat. Mater.* **8**, 693–695 (2009).
11. Fert, A. & Jaffrès, H. Conditions for efficient spin injection from a ferromagnetic metal into a semiconductor. *Phys. Rev. B* **64**, 184420 (2001).
12. Schmidt, G., Ferrand, D., Molenkamp, L. W., Filip, A. T. & van Wees, B. J. Fundamental obstacle for electrical spin injection from a ferromagnetic metal into a diffusive semiconductor. *Phys. Rev. B* **62**, R4790–R4793 (2000).
13. Rashba, E. I. Theory of electrical spin injection: Tunnel contacts as a solution of the conductivity mismatch problem. *Phys. Rev. B* **62**, R16267–R16270 (2000).
14. Weatherup, R. S. *et al.* On the Mechanisms of Ni-Catalysed Graphene Chemical Vapour Deposition. *ChemPhysChem* **13**, 2544–2549 (2012).
15. Li, X., Cai, W., Colombo, L. & Ruoff, R. S. Evolution of Graphene Growth on Ni and Cu by Carbon Isotope Labeling. *Nano Lett.* **9**, 4268–4272 (2009).
16. Dlubak, B. *et al.* Graphene-Passivated Nickel as an Oxidation-Resistant Electrode for Spintronics. *ACS Nano* **6**, 10930–10934 (2012).
17. Martin, M.-B. *et al.* Sub-nanometer Atomic Layer Deposition for Spintronics in Magnetic Tunnel Junctions Based on Graphene Spin-Filtering Membranes. *ACS Nano* **8**, 7890–7895 (2014).
18. Godel, F. *et al.* Voltage-controlled inversion of tunnel magnetoresistance in epitaxial Nickel/Graphene/MgO/Cobalt junctions. *Appl. Phys. Lett.* **105**, 152407 (2014).

19. Verduci, T. *et al.* Carbon-Passivated Ni Electrodes for Charge Injection in Organic Semiconductors. *Adv. Mater. Interfaces* **3**, n/a-n/a (2016).
20. Natali, D. & Caironi, M. Charge Injection in Solution-Processed Organic Field-Effect Transistors: Physics, Models and Characterization Methods. *Adv. Mater.* **24**, 1357–1387 (2012).
21. Pesavento, P. V., Chesterfield, R. J., Newman, C. R. & Frisbie, C. D. Gated four-probe measurements on pentacene thin-film transistors: Contact resistance as a function of gate voltage and temperature. *J. Appl. Phys.* **96**, 7312–7324 (2004).
22. Haddock, J. N. *et al.* A comprehensive study of short channel effects in organic field-effect transistors. *Org. Electron.* **7**, 45–54 (2006).
23. Panzer, M. J. & Frisbie, C. D. Exploiting Ionic Coupling in Electronic Devices: Electrolyte-Gated Organic Field-Effect Transistors. *Adv. Mater.* **20**, 3177–3180 (2008).
24. Richards, T. J. & Sirringhaus, H. Analysis of the contact resistance in staggered, top-gate organic field-effect transistors. *J. Appl. Phys.* **102**, 094510 (2007).
25. Watanabe, S. *et al.* Polaron spin current transport in organic semiconductors. *Nat. Phys.* **10**, 308–313 (2014).

Table of Contents

Introduction.....	1
PART I FUNDAMENTALS AND BACKGROUND.....	7
1 A few organic electronics concepts.....	8
1.1 Organic electronic: an introduction.....	9
1.2 The long and winding road of organic semiconductors.....	10
1.2.1 Conjugated polymers.....	11
1.2.2 Charge carriers in conducting polymers.....	13
1.2.3 The role of disorder.....	14
1.3 Charge Transport and injection.....	15
1.3.1 Miller-Abrahams and Marcus hopping rates.....	15
1.3.2 Gaussian disorder model.....	17
1.3.3 The mobility edge and the Metal-Insulator transition.....	20
1.3.4 Nearest neighbor and variable range hopping.....	22
1.3.5 Doping in conducting polymers.....	24
1.3.6 Electron spin resonance signature of electronic states in conjugated polymers.....	26
1.3.7 Charge injection.....	27
1.4 Devices.....	33
1.4.1 Organic field-effect transistor.....	33
1.4.2 OFETs geometry.....	38
1.4.3 EGOFETs.....	38
1.4.4 Parasitic Contact resistance.....	41
1.4.5 Contact resistance measurements.....	42
1.4.6 Downscaling of OFETs: the short channel effects.....	45
2 Organic spintronics.....	56
2.1 Spintronics.....	57
2.2 Organics for spintronics.....	58
2.2.1 Spin valves: vertical vs. lateral geometry.....	60
2.2.2 Ferromagnetic surface oxidation.....	65
2.2.3 Graphene- and graphite- passivated Ni electrodes: a source of spin-polarized electrons.....	66
2.3 Basics of spin transport in diffusive systems.....	69
2.3.1 Spin injection: conductance mismatch problem.....	70
2.3.2 Spin detection: spin memory loss.....	74

PART II EXPERIMENTAL WORK.....	82
3 Carbon/Nickel interface characterization	83
3.1 Introduction.....	84
3.2 Routes towards graphene	84
3.3 Graphene growth methods: CVD vs. RTA.....	86
3.4 X-ray Photoelectron Spectroscopy (XPS) as a preliminary screening tool	90
3.5 Characterization	92
3.5.1 XPS characterization.....	92
3.5.2 Raman spectroscopy of the carbon adlayer.....	94
3.5.3 Surface topography	97
3.5.4 ToF-SIMS thickness and composition analysis	98
3.5.5 Magnetic properties: SQUID and MOKE measurements	101
3.6 Conclusions.....	103
4 Carbon-passivated Ni electrodes for charge injection in organic semiconductors	107
4.1 Introduction.....	108
4.2 Selecting the active channel material: work function measurements	108
4.3 Device fabrication	110
4.4 Gated-four probes measurements.....	114
4.4.1 Transport characteristics.....	115
4.4.2 Contact resistance extrapolation	120
4.5 Conclusions.....	124
5 Study of the contact resistance in short channel EGOFETs	127
5.1 Introduction.....	128
5.2 PBTTT thin films.....	129
5.3 Contact resistance study on large scale EGOFETs.....	131
5.3.1 Charge carriers transport at low temperature.....	134
5.3.2 AFM imaging of PBTTT and IIDDT-C3 thin films	137
5.4 Fabrication of short channel devices	137
5.4.1 Nanotrenches fabrication.....	138
5.4.2 Device preparation.....	140
5.4.3 Top-gate electrolyte	140
5.5 Room temperature electrical characterization of nanotransistors	141
5.6 Low temperature measurements	143

5.7 Measurements as a function of doping	145
5.8 Magnetoresistance	147
5.9 Comparative study with thin film IIDDT-C3 nanodevices	149
5.10 Estimation of the contact resistance in short channel devices.....	152
5.11 Conclusions	154
6 Current crowding for spintronics devices	156
6.1 Introduction: Current crowding effect.....	157
6.2 Experimental extrapolation of L_T and r_b from the current crowding model.....	160
6.3 Outcomes for organic spintronics	162
6.4 Nanodevices with FM electrodes.....	167
6.4.1 Large scale devices measurements.....	168
6.5 Nanotrenches fabrication with FM electrodes	169
6.5.1 Study on short channel devices with FM electrodes	171
6.6 Conclusions	174
7 Conclusions and perspectives	178

Introduction

In the past several decades organic electronics has attracted considerable interest because of unique advantages of organic semiconductors (OSCs), such as low cost fabrication, lightweight and mechanical flexibility. Moreover, richness in the chemical engineering of molecular properties makes OSCs perfectly tunable by design. Remarkable progress has been made in electronic and optical performances of devices based on organic semiconductor materials, such as organic light emitting diodes (OLEDs), organic field-effect transistor (OFET) and organic photovoltaic cell. OLEDs are already in commercial production as high efficient, bright and colorful displays in mobile phones and digital cameras.

Another important and promising application of organic electronics which exploits also the spin degree freedom of the electron is organic spintronics [1]. OSCs are very attractive for spin transport because of their weak spin-orbit coupling and hyperfine interaction, which lead to very long spin relaxation times for this class of materials [2, 3]. Spin transport phenomena are usually studied in organic spin valve (SV) devices in which the spacer is an organic semiconductor. Substantial modulation of the device resistance is expected upon changing the relative orientation of the ferromagnetic (FM) electrodes magnetization.

SVs can be fabricated in two geometries: lateral and vertical. This thesis is aimed at the investigation of organic devices in lateral geometry. This configuration has several advantages such as a better control of the channel length, the possibility to implement a third electrode for the gating control of the device, and the ability to respond to several independent stimuli (electric field, magnetic field, light) resulting in multi-functional devices. Lateral geometry is also useful for the characterization of spin-dependent transport in OSCs, using non-local measurements for detecting carrier spin polarization with ferromagnetic electrodes.

The observation of spin-dependent phenomena in lateral and vertical organic SVs by Dediu *et al.* [4] and Xiong *et al.* [5] in 2002 and 2004, respectively, can be considered as the starting point of organic spintronics research activity. Although large magnetoresistance (MR) effects in organic spintronic devices (mostly in vertical geometry) have been reported in the last decade [6, 7, 8, 9, 10, 11], there are still a number of important unsolved issues to be faced. In this thesis, we will focus on devices where the active channel length exceeds several tens of nm, therefore prohibiting direct tunneling between the two FM electrodes. We then

consider that a spin-dependent current is injected in the OSC, transported, and finally collected at the other magnetic electrode.

Efficient spin-polarized current injection from the first electrode, spin conservation through the organic spacer, and spin-sensitive detection in the second electrode need to be optimized for the realization of an organic spin valve. Although several experiments can be used as evidence for the first two components (injection and transport) in organic spin devices [12, 13, 14], the coexistence of the three processes remains an open question, and the necessary material criterions need to be established. As an example, (non-local) Hanle effect, related to precession and dephasing of a spin current in a transverse applied magnetic field, can be considered a good indicator that a spin current can propagate and be extracted from an OSC. Such effect [15], observed in metallic and inorganic semiconductors, has not been so far detected in organic materials [16, 17]. The reason for this is still unclear.

Our approach aims at taking most advantage of solvent-based chemistry, using therefore a wet chemistry approach to integrate OSCs in devices. A key bottleneck in this case is the expected oxidation of the ferromagnetic electrodes surface when they are exposed to ambient/wet atmosphere. This oxidation leads to the formation of a variety of antiferromagnetic transition metal oxides, which alter the spin polarization properties at the FM surfaces. This is expected to diminish the efficiency of spin injection/detection and, more importantly, will make this property very difficult to probe, reproduce and control from a device fabrication point of view.

In the picture of injection-transferring-extracting a spin current in a diffusive-like transport model, two main conditions are mandatory for a SV device to work properly [18]:

- the length over which the memory of the spin of carriers is preserved, or spin diffusion length of the spacer $l_{spin-flip}$ must be larger than the distance $l_{channel}$ between injector and detector ($l_{spin-flip} \gg l_{channel}$);
- the interface resistance r_b^* between electrode and spacer must be spin dependent, neither too large no too small, namely be approximately equal to the spin impedance of the OSC r_N ($r_b^* \approx r_N$).

The first condition (spin conservation) is related to the properties of the active channel. For an efficient SV it is essential that the injected spin current can be transferred over a length L with the minimum spin relaxation. Until now, the reported spin flip lengths of OSC are disappointingly small [19]. The main explanation is that OSCs are essentially 'bad' conductors, with hopping transport limiting mobility and conductivity of materials. Whereas the long spin

relaxation time is a clear advantage of organic materials, the relatively low conductivity of most OSCs is a serious drawback.

From the second condition (spin injection/detection) it results that the main obstacle to spin injection/detection is the resistance mismatch between the FM/OSC interface contact resistance and the OSC active channel resistance. It is by now established that solving the problem of resistance mismatch requires low and spin-dependent contact resistances [18]. Therefore, the control and the understanding of the FM/organic interface is another fundamental issue in organic SV devices.

This thesis mostly focuses on organic electronics, aiming at findings wet chemistry based approaches to make devices of relevance for future organic spintronics applications. From the above discussion it results evident that the major ingredients for lateral SV realization are **oxide-free ferromagnetic electrodes** surface, **low interface contact resistance**, and **high mobility OSCs**. The aim of this thesis is to identify the technical and fundamental issues related to these key elements and to propose a possible strategy for the realization of suitable devices for organic spintronic applications. Tentative solutions are validated in OFET geometry.

Another important aspect covered in this thesis, which is common to organic electronics and organic spintronics, is the device miniaturization issue. Since the switching speed (cut-off frequency) of an ideal transistor is inversely proportional to the channel length (L), commercialization of organic electronics requests OFETs dimensions as small as possible to improve the maximal operation frequency. Moreover, reducing OFETs channel length can improve the “on” conductance and increase the $I_{ON/OFF}$ ratio. In the case of organic spintronic devices, the downscaling to the nanoscopic dimensions is imperative since spin diffusion lengths in organic materials are relatively short (between 10 and 100 nm). However, as the OFETs are downscaled, device physics becomes increasingly critical, particularly because the large resistance between the contacts and the OSC layer is expected to largely dominate the channel resistance. Therefore one must be careful to avoid contact resistance-limited devices when shrinking L , and this is a very challenging issue for organic electronics applications.

The manuscript is divided as follows. **Chapter 1** and **chapter 2** review the basic background in organic electronics and spintronics, respectively. The current pertinent issues in both fields are also identified and discussed.

Chapter 3 is devoted to solve the problem of the oxidation of the FM contacts surface, proposing Ni electrodes passivated by ultra-thin carbon layers. The details of Ni/carbon electrodes fabrication and the relative morphological and chemical characterization are presented. We identify the best candidates for integration in devices, mostly emphasizing the necessary trade-off between morphological quality of the electrodes and crystallinity of the carbon adlayers.

In **chapter 4** Ni/carbon electrodes are implemented as source/drain contacts in OFET structures in order to test the electrical capabilities of the resulting devices. We propose to use electrolyte gating in order to reduce the contact resistance at the metal/OSC interface and discuss how Ni/carbon electrodes perform for the best OSCs conductors, comparing them to the best-suited benchmark gold electrodes. The main outcome is the identification of the best candidates for charge injection/collection for spintronics applications.

Chapter 5 focuses on the downscaling of OFETs in the sub-100 nm scale. Suppression of short channel effects results from a proper saturation of the output curves together with measured high values of $I_{ON/OFF}$ ratio and very low contact resistance found for electrochemically gated highly conducting OSC channels. These original spectacular results show that this type of device does not suffer from usual organic short channels drawbacks in performance.

Chapter 6 extends the downscaling to devices with ferromagnetic electrodes, which are crucial for spintronics applications. Results are discussed in terms of current crowding effect, which is shown to have important implications in the conditions for spin Injection/detection in lateral spin valve devices.

Finally, a summary of the main findings of this thesis and an outlook of possible research directions are given in **Chapter 7**.

References

1. Sun, D., Ehrenfreund, E. & Vardeny, Z. V. The first decade of organic spintronics research. *Chem. Commun.* **50**, 1781–1793 (2014).
2. Naber, W. J. M., Faez, S. & van der Wiel, W. G. Organic Spintronics. *J. Phys. D: Appl. Phys.* **40**, R205-R228 (2007).
3. Dediu, V. A., Hueso, L. E., Bergenti, I. & Taliani, C. Spin routes in organic semiconductors. *Nat. Mater.* **8**, 707–716 (2009).
4. Dediu, V., Murgia, M., Maticotta, F. C., Taliani, C. & Barbanera, S. Room temperature spin polarized injection in organic semiconductor. *Solid State Commun.* **122**, 181–184 (2002).
5. Xiong, Z. H., Wu, D., Vally Vardeny, Z. & Shi, J. Giant magnetoresistance in organic spin-valves. *Nature* **427**, 821–824 (2004).
6. Pramanik, S., Bandyopadhyay, S., Garre, K. & Cahay, M. Normal and inverse spin-valve effect in organic semiconductor nanowires and the background monotonic magnetoresistance. *Phys. Rev. B* **74**, 235329 (2006).
7. Pramanik, S. *et al.* Observation of extremely long spin relaxation times in an organic nanowire spin valve. *Nat. Nanotechnol.* **2**, 216–219 (2007).
8. Santos, T. S. *et al.* Room-Temperature Tunnel Magnetoresistance and Spin-Polarized Tunneling through an Organic Semiconductor Barrier. *Phys. Rev. Lett.* **98**, 016601 (2007).
9. Wang, F. J., Yang, C. G., Vardeny, Z. V. & Li, X. G. Spin response in organic spin valves based on $\text{La}_{2/3}\text{Sr}_{1/3}\text{MnO}_3$ electrodes. *Phys. Rev. B* **75**, 245324 (2007).
10. Lin, L. *et al.* Large room-temperature magnetoresistance and temperature-dependent magnetoresistance inversion in $\text{La}_{0.67}\text{Sr}_{0.33}\text{MnO}_3/\text{Alq}_3$ - Co nanocomposites/Co devices. *Solid State Commun.* **151**, 734–737 (2011).
11. Morley, N. A. *et al.* Room temperature organic spintronics. *J. Appl. Phys.* **103**, 07F306 (2008).
12. Cinchetti, M. *et al.* Determination of spin injection and transport in a ferromagnet/organic semiconductor heterojunction by two-photon photoemission. *Nat. Mater.* **8**, 115–119 (2009).
13. Drew, A. J. *et al.* Direct measurement of the electronic spin diffusion length in a fully functional organic spin valve by low-energy muon spin rotation. *Nat. Mater.* **8**, 109–114 (2009).
14. Nguyen, T. D., Ehrenfreund, E. & Vardeny, Z. V. Spin-Polarized Light-Emitting Diode Based on an Organic Bipolar Spin Valve. *Science* **337**, 204–209 (2012).
15. Johnson, M. & Silsbee, R. H. Interfacial charge-spin coupling: Injection and detection of spin magnetization in metals. *Phys. Rev. Lett.* **55**, 1790–1793 (1985).
16. Grünewald, M. *et al.* Vertical organic spin valves in perpendicular magnetic fields. *Phys. Rev. B* **88**, 085319 (2013).
17. Riminucci, A. *et al.* Hanle effect missing in a prototypical organic spintronic device. *Appl. Phys. Lett.* **102**, 092407 (2013).
18. Fert, A. & Jaffrès, H. Conditions for efficient spin injection from a ferromagnetic metal into a semiconductor. *Phys. Rev. B* **64**, 184420 (2001).

19. Szulczewski, G., Sanvito, S. & Coey, M. A spin of their own. *Nat. Mater.* **8**, 693–695 (2009).

PART I
FUNDAMENTALS AND BACKGROUND

1

A few organic electronics concepts

This chapter gives a general overview of organic electronics with emphasis on charge transport and injection mechanisms taking place in organic materials and field-effect transistors for both pristine and highly doped organic semiconductors. The aim is to provide the required background to understand the scientific results and findings presented in the second part of the thesis.

1.1 Organic electronic: an introduction

In 1996 Intel co-founder Gordon Moore made the observation that the number of transistors per square inch on integrated circuits doubled with a rate of 18 months approximately since their invention, and that this trend would have continued in the future. This prediction, now famous as Moore's law, deeply impacted the silicon chip industry driving it to increase devices performances by continuous downscaling of their sizes. However, already in 2000s, it was clear that the simple geometric device downscaling was close at its end. Anyway, over the past years new techniques allowed to follow the Moore's law trend: strained silicon was introduced at 90 nm; new materials layered on silicon were able to reach 45 nm; and tri-gate transistors maintained the scaling down to 22 nm. Each of these improvements took a decade to be put in production. A 10 nm Cannonlake processor, a shrunk version of the 14 nm Skylakes shipping today, expected to be released by Intel this year, will be postponed to the second half of 2017 due to defects in the microprocessor. All these factors are a clear indication that the continuous shrinking of devices, dictated by the Moore's law, is quickly approaching a limit and new materials and technologies are needed to go beyond silicon electronics [1]. Among them is organic electronics.

The interest in organic electronics can be attributed to the discovery in 1976 by Heeger, MacDiarmid and Shirakawa [2] of the possibility to range the electrical conductivity of trans-polyacetylene from insulator to metal upon electrochemical doping. This discovery, recognized by the 2000 Nobel Prize in Chemistry, initiated an extensive research on the chemistry and physics of conjugated polymers. Organic semiconductors (OSCs) offer many fundamental advantages with respect to traditional electronic materials including easy and low-cost fabrication methods (such as spin-coating, screen or ink-jet printing, self-assembly, drop casting etc.), low temperatures (<180 °C) processing from solution, lightweight, large area coverage, relatively easy engineering and tunability of molecular properties and mechanical flexibility compatible with plastic substrates. With the synthesis of new organic materials, chemists have improved charge-carrier mobility values for small-molecule organic field-effect transistors (OFETs) from < 1 cm²/V·s in 2000 to 8-11 cm²/V·s nowadays and for polymer OFETs from about 0.01 cm²/V·s in 2000 to more than 1-3 cm²/V·s in 2010.

Many devices based on these materials are already commercial realities. For example, both small molecules and polymers are being used in the manufacture of organic light emitting diode (OLED) displays (e.g., TV and cell phone displays), solar cells, and transistors.

1.2 The long and winding road of organic semiconductors

OSCs, as any other organic material, are mostly constituted of carbon and hydrogen. An isolated carbon atom has six electrons in its ground state (C: $1s^2 2s^2 2p$). Four of them are located in the valence shell – two 2s, and two 2p orbitals. However, in order to achieve a more stable configuration when covalently bonded to other atoms, the wavefunctions of the 2s, $2p_x$ and $2p_y$ orbitals hybridize to form the so-called sp^2 -hybridizations where sp^2 -orbitals form a triangle within the plane with one p_z -orbital pointing out perpendicular to the plane. By the overlap of two sp^2 -orbitals, a strong σ bond between two neighboring carbons can be formed. The remaining p_z orbitals overlap with the neighboring p_z -orbitals resulting in the formation of π -bonds. This electronic delocalization of the π -electrons situated above and below the plane of the molecule allows charge carriers to move along the backbone of the polymer chain giving to the molecule conducting properties.

The delocalized electrons occupy the bonding π -orbitals, while the anti-bonding π^* -orbitals remain empty. The bonding π -orbital with the highest energy is called the highest occupied molecular orbital (HOMO), while the anti-bonding π^* -orbital with the lowest energy is called the lowest unoccupied molecular orbital (LUMO). As the number of interconnected carbon atoms increases, the energy rises, resulting in a narrower bandgap between HOMO and LUMO which eventually becomes zero for an infinitely long chain. However, in order to lower the total energy, symmetry is broken by forming single and double bonds: the LUMO goes up in energy and the HOMO goes down. This so-called Peierls distortion leads to the presence of an energy difference, a band gap, of several eV (between 1.5 and 3 eV) between the HOMO and LUMO. As a result, these organic materials are insulating or semiconducting.

Organic semiconductors can be classified in two groups depending on the molecular weight of the molecule:

- small molecules, including low-generation dendrimers (repeated branch of small molecules) and other oligomers (limited number of repeating monomer units) with molecular weight smaller than 1000 D;
- conjugated polymers, with a molecular weight exceeding 1000 D.

These two classes differ in their physical and chemical properties, morphology, and also in the way they are processed. The OSCs used in this thesis are two high conducting conjugated polymers belonging to the families of polythiophene and isoindigo.

1.2.1 Conjugated polymers

Conjugated polymers are long chains (reaching several hundreds of nanometers) formed from a given monomer with an indeterminate number of repeating units, and usually feature connections of oligo-segments of various lengths, leading to a random distribution of conjugation lengths. In the chain direction, the monomers are bound by covalent bonds that lead to strong electronic coupling. In the perpendicular direction to the chain direction (π - π stacking direction) the chains interact through weaker Van der Waals forces, however still sufficient to make delocalization of the electronic wave functions possible.

The main advantage with π -conjugated polymers is that they can be processed from solution, e.g., by spin coating, printing or other very inexpensive techniques. This easy low-temperature processability derives from the weak Van der Waals bonding which allows the polymer chains in solid form to be separated in solution and then assembled in (for example) films on the device substrate. The solubility is obtained by substitution of side groups to the monomers units, typically alkyl chains, which lower the melting temperature and separate the conjugated backbones. This process reduces the rigidity of the backbone but also the intermolecular overlap so that the charges hopping between molecules becomes more difficult.

The morphological structure of conjugated polymers is complex and inhomogeneous, made of crystalline (ordered) regions (also called grains or lamellae), which can be considered as “metallic” islands, and amorphous (disordered) regions [3]. In the amorphous regions the chains are twisted and bent forming a spaghetti-like structure. Inside the grains the electronic wave functions are delocalized while in the amorphous regions the electronic wave functions are localized. Consequently, electrical transport through the whole structure is largely influenced by the presence of the amorphous regions.

In this simple picture, charge transport occurs by carriers both moving along the chain (intra-molecular conduction) and hopping between different chains (inter-molecular conduction) as shown in Figure 1.1. Intra-chain transport depends on the intrinsic properties of the macromolecules and the doping level, while inter-chain transport is a function of the polymer morphology and the packing density.

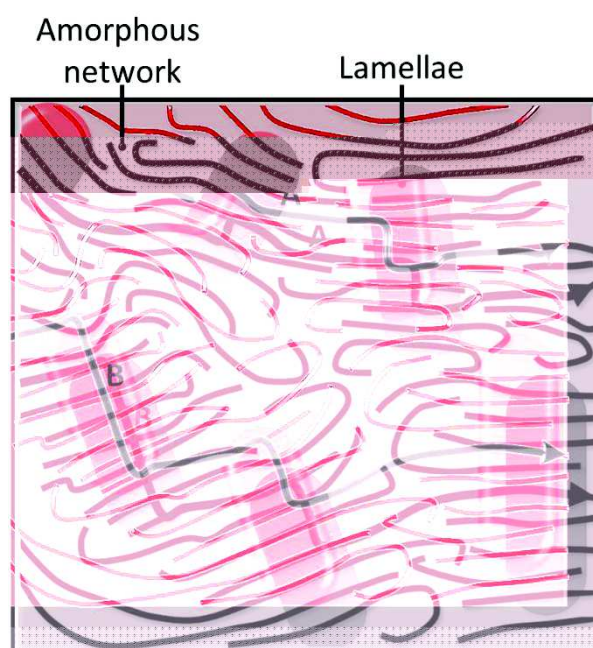


Figure 1.1 Schematic top-view of semi-crystalline conjugated polymer showing ordered regions, lamellae, embedded in an amorphous matrix. Lamellae (highlighted in red blocks), are nicely structured compared to the amorphous regions. A and B indicates the intra-chain and inter-chain transport, respectively. The charge motion path is represented with the red arrows.

Mobility is the measure of the capability an electric field has to put charges in motion and it is the critical parameter from a device performance point of view. Mobility of charge carriers in OSCs is several orders of magnitude lower than in inorganic semiconductors. In amorphous films, at room temperature, electron and hole mobility is in the range of 10^{-6} to 10^{-2} $\text{cm}^2 \cdot \text{V}^{-1} \text{s}^{-1}$. High-purity single crystals of rubrene and pentacene reach mobility higher than 10 $\text{cm}^2 \cdot \text{V}^{-1} \text{s}^{-1}$ [4, 5]. For comparison, mobility in high-purity Si crystals and amorphous silicon has values $\sim 10^3$ $\text{cm}^2 \cdot \text{V}^{-1} \text{s}^{-1}$ and $0.5 - 1$ $\text{cm}^2 \cdot \text{V}^{-1} \text{s}^{-1}$, respectively. However, there has been rapid progress in developing conjugated polymers with higher transport mobility required for high-performance field-effect transistors (FETs). Currently, mobility values of 1 $\text{cm}^2 \cdot \text{V}^{-1} \text{s}^{-1}$ in thin films OFETs electrostatically doped are commonly reported, in particular for solution-processed poly(2,5-bis(3-tetradecylthiophen-2-yl)thieno[3,2-b]thiophene) (PBTTT) [6]. Semicrystalline polymers can exhibit high mobility as long as their molecular weight is large enough that the long polymer chains can connect ordered regions providing a percolating network between neighboring grains [7, 8].

1.2.2 Charge carriers in conducting polymers

Depending on the backbone of the polymer chain, conjugated polymers have either degenerate or non-degenerate ground state geometry which corresponds to the different nature of the charge carriers involved in the electronic transport [9]. Most of the conjugated polymers are of non-degenerate ground state type. In this case the charge carriers are known as polarons. In degenerate ground state polymers, the charge carriers are known as solitons.

For charge transport to take place in OSCs, charge carriers must be introduced into the polymer. This can be done via chemical or electrochemical doping, or via charge-injection. It is well established that, when an electron is removed (added) from a π -orbital (to a π^* -orbital), there is a rearrangement of the spatial distribution of the electrons located in the remaining binding orbitals of the polymer. This redistribution results in a different local molecular geometry and, more specifically, in a readjustment of the bond length of the molecules. Therefore, there is not only a change in the geometry of the charged molecule but also in the mean distance to the neighboring molecules. The molecule is then no longer in the ground state but in a charged excited state. This variation of the equilibrium geometry of the molecule is called electron-phonon coupling.

The induced charge and the associated geometric distortion of the molecule is referred to as a polaron, which is localized over a small segment of the chain with a stabilization energy known as “geometric reorganization energy” or polaron binding energy E_p . Moreover, moving the charge from one molecule to another also requires changing the electronic configuration of the initial and final molecules. Austin and Mott demonstrated that the energy required to reorganize the molecule, the reorganization energy λ , is twice E_p [10]. A polaron can be positively or negatively charged and carries a spin $\frac{1}{2}$.

If a second electron is removed from the polymer chain, we have bipolaron formation. The formation of bipolarons implies that the energy gained by the interaction with the lattice is larger than the Coulomb repulsion between the two like charges confined in the same location. Only a pair of charges in the singlet state (total spin 0) can form a bipolaron, which is then spinless.

Calculations for polyacetylene, polypyrrole and polythiophene (among the most conductive organic materials) indicate that while the energy required for polaron pairs and bipolarons creation (distorsion energy) is nearly identical, the decrease in ionization energy is much more important in the case of bipolarons. Consequently, bipolarons formation is more thermodynamically favorable than polaron pairs for these compounds [11, 12].

This raises a question for organic spintronics applications: can the formation of spinless bipolarons be disadvantageous for spin-based devices? Ren *et al.* [13] studied the influence of bipolarons concentration on spin polarization of OSCs in spin valve-like devices. Their calculations reveal that when the fraction of polarons is only 20 %, the spin polarization is 90 % of the value attainable with only polarons and no bipolarons. Therefore, the spinless bipolarons are not detrimental and a large spin polarization can be realized even if spin polarons are the minority of carriers in the OSCs.

1.2.3 The role of disorder

Another important parameter to consider in OSCs and charge transport is the disorder. The presence of disorder perturbs the overlap of neighboring p-orbitals and thus breaks the π -conjugation. This results in strong diminishing of the length over which a carrier can move coherently.

When discussing the role of disorder, we have to distinguish between dynamic disorder and static disorder. Dynamic disorder is caused by thermal fluctuations in the intermolecular distances and thus is related to electron-phonon interactions. It results in a time-dependent variation of the microscopic transport parameters, i.e., of the site energies and transfer integrals (electronic couplings).

Static disorder, also called structural disorder, is mainly caused by variations of the polymer backbone conformation such as twists or chemical impurities, and by electrostatic/polarization effects coming from the surrounding, such as dipolar disorder due to random orientation of polar groups of the OSC, or the gate dielectric. It competes with Van der Waals interactions that favor a particular orientation of the polymer chains with respect to each other. Static disorder leads to time independent, spatial variations of the energy and hopping distances from site to site.

In 1958 Philip Anderson pointed out that in amorphous solids, as well as conjugated polymers, in presence of disorder the wave function of the electrons may become localized [14], or Anderson localization. When the disorder is weak, only the states at the band edge are truly localized. Increasing the amount of disorder more and more localized states appear in the band, until the point in which, for strong disorder, all the states become localized, and an insulating state prevails.

Both dynamic and static disorders affect the charge-transport properties but in rather different ways. While static disorder is always detrimental for charge transport, dynamic disorder can lead to an enhancement of the charge transport via a phonon-assisted contribution to the charge carrier mobility. As already said, moving the charge from one molecule to the neighboring one means that first the reorganization energy has to be overcome. This is possible by thermal activation, where the energy is provided by phonons.

1.3 Charge Transport and injection

Charge transport is a fundamental phenomenon that governs the functionality of all organic devices including OFETs. Therefore, understanding this phenomenon has a significant importance not only from a scientific but also from a technological and applicative point of view. It is widely accepted that charge transport in OSCs occurs by hopping, i.e., thermal assisted tunneling, of charge carriers between localized states.

Apart from the conduction mechanism, charge injection into the organic material is also a key point for the performance of the device, not only in organic electronics but, as we will see in the next chapter, also in organic spintronics. Charge injection mechanism strongly depends on the interface between contact and organic material. Therefore, the quality and the understanding of the charge/spin injection and transport at this interface is of crucial importance.

In the following sections we will introduce the main theoretical models used to explain the charge transport and injection in disordered OSCs.

1.3.1 Miller-Abrahams and Marcus hopping rates

The rate of hopping of a charge carrier between two sites depends on the overlap of their electronic wave functions, which allows tunneling from one site to another. In charge carrier transport theories, the rate for a carrier transition from an occupied site i to an empty site j , separated by a distance r_{ij} , is described by two hopping rate expressions: Miller-Abrahams and Marcus rates.

Miller–Abrahams (M-A) expression [¹⁵] is given as

$$v_{ij} = v_0 \exp(-2\gamma r_{ij}) \begin{cases} \exp\left(\frac{\varepsilon_i - \varepsilon_j}{kT}\right), \varepsilon_j > \varepsilon_i \\ 1, \varepsilon_j < \varepsilon_i \end{cases} \quad (1)$$

here, γ is the inverse of the localization length of charge carriers in the localized states, usually of the order of 10^8 cm^{-1} [16, 17], ε_i and ε_j are the carrier energies on sites i and j , respectively, k is the Boltzman constant and T is the temperature. The prefactor v_0 , often called the attempt-to-escape frequency, depends on the interaction mechanism that causes the transition. In the case of interaction with phonons, its value is usually assumed close to the phonon frequency [18], $v_0 \approx 10^{12} \text{ s}^{-1}$. Whenever a charge carrier hops to a site with higher (lower) site energy the difference in energy is compensated by absorption (emission) of a phonon. This is why hopping charge transport is said to be phonon-assisted. The first exponential term in equation 1 is the tunneling probability between sites with equal energy. The second exponential term is a Boltzmann factor for a jump upward in energy and is equal to 1 for a jump downward in energy. Therefore charge carriers preferably hop to sites with lower energy because a phonon taking away the energy in excess can easily be emitted.

The probability to absorb a phonon of the correct energy depends on the availability of phonons present in the system. This assumption introduces a temperature dependence in the model for upwards hops and makes a difference between hopping transport and classical band transport theory. In a crystalline material, decreasing the temperature reduces the disorder and hence the electron scattering in the system. So the conductivity increases as the temperature decreases and remains finite to zero temperature. For hopping transport, decreasing the temperature reduces the number of available phonons and, hence, the conductivity, which vanishes as $T \rightarrow 0$. By increasing the temperature the Boltzmann penalty for hops upwards in energy becomes less strong. Downwards hops are instead temperature independent.

In the presence of an electric field, an additional term, expressed as $-e\vec{r}\vec{E}$, is introduced in the energetic balance for upwards jumps, with \vec{r} the vector connecting the centers of the two sites and \vec{E} the electric field vector. Thus, in the Miller-Abrahams formalism, downward jumps are not accelerated by the electric field and are assumed to always occur whatever the extent of the site energy difference.

In the presence of a charge-induced lattice deformation (polaron formation) the hopping rate of a charge carrier can be described by the Marcus rate. Marcus noted that electron transfer requires a reorganization of the system reflected in the reorganization

energy λ closely related to the thermal activation energy E_a . In the absence of entropy changes upon electron transfer, this thermal activation energy can be written as

$$E_a = \frac{(\lambda + \Delta E)^2}{4\lambda} \quad (2)$$

here $\Delta E = \varepsilon_j - \varepsilon_i$ is the difference in equilibrium energies of the initial and final sites (E_a is equal to ΔE in the M-A expression). It follows that in this case the electron-transfer rate is given by

$$v_{ij} = \frac{J_{ij}^2}{\hbar} \sqrt{\frac{\pi}{4E_a kT}} \exp\left[-\frac{(\lambda + \Delta E)^2}{4\lambda kT}\right] \quad (3)$$

where J_{ij} is the effective charge transfer integral (electronic coupling), i.e., the wave function overlap between i and j sites. It decays exponentially with the distance as $J_{ij} = J_0 e^{-\gamma r_{ij}}$.

Marcus rate is more realistic, but introduce an additional parameter to the simulations. For this reason M-A rate is more often used. In both M-A and Marcus approaches, the transition rates are thermally activated and vanish when the temperature approaches absolute zero.

1.3.2 Gaussian disorder model

In 1993 Heinz Bässler published an article on transport in photoconductors used for electrophotolithography [19] which has become a decisive milestone for the theory of charge transport in disordered OSCs. The Bässler model, also known as Gaussian disorder model (GDM) describes charge transport in disordered materials that occurs via incoherent tunneling (hopping). The charge carrier motion is numerically solved using Monte Carlo simulations assuming that the polaronic effect (thus the reorganization energy) can be neglected but at the same time the electron-phonon coupling is strong enough to ensure charge carrier thermalization. Therefore, the hopping rate used is the M-A rate. Both positional disorder and energetic disorder are introduced.

The model consists of a cubic lattice of N lattice points, representing the conjugated segments of the polymer chains, with localized electronic states. Each lattice point is characterized by a Gaussian energy distribution [19, 20, 21]

$$g(\varepsilon) = \frac{N}{\sigma\sqrt{2\pi}} \exp\left(-\frac{\varepsilon^2}{2\sigma^2}\right) \quad (4)$$

where σ is the standard deviation of the density of states (DOS), usually estimated around 0.1 eV [19], and N is the total density of randomly distributed localized states (sites).

There is no direct experimental proof for using a Gaussian distribution; the only justification comes from the shape of the absorption bands in disordered organic materials [22]. The energy ε in equation 4 is measured relative to the center of the DOS.

In Bässler model, Fermi-Dirac statistics are not important because only one charge can travel in an otherwise empty DOS. This represents the condition of low charge carrier density, where Coulomb interactions between two closely placed carriers are negligible and the occupancy of a single site by more than one carrier is prohibited.

One of the main features of the GDM is the energy relaxation of charge carriers performing a random walk. This relaxation is shown in Figure 1.2. The charge carriers will relax into a tail state with again a Gaussian distribution of the occupied DOS (ODOS) having a mean energy

$$\langle \varepsilon_{\infty} \rangle = -\frac{\sigma^2}{kT} \quad (5)$$

After relaxation, hopping downwards in energy becomes slower because the number of nearby states that are lower in energy decreases dramatically. At this point, the charges will have to hop from the ODOS to closer sites that are higher in energy. Therefore, their transport will require a thermal activation, known as activation energy E_a , to higher states. The energy of these higher states is called transport energy E_t with a position between $\langle \varepsilon_{\infty} \rangle$ and the center of the DOS.

As charges move up on energy, the hopping down process starts competing since the number of available states lower in energy increases. Therefore the transport occurs around the transport energy: above this level, carriers hop downwards and below carriers hop upwards.

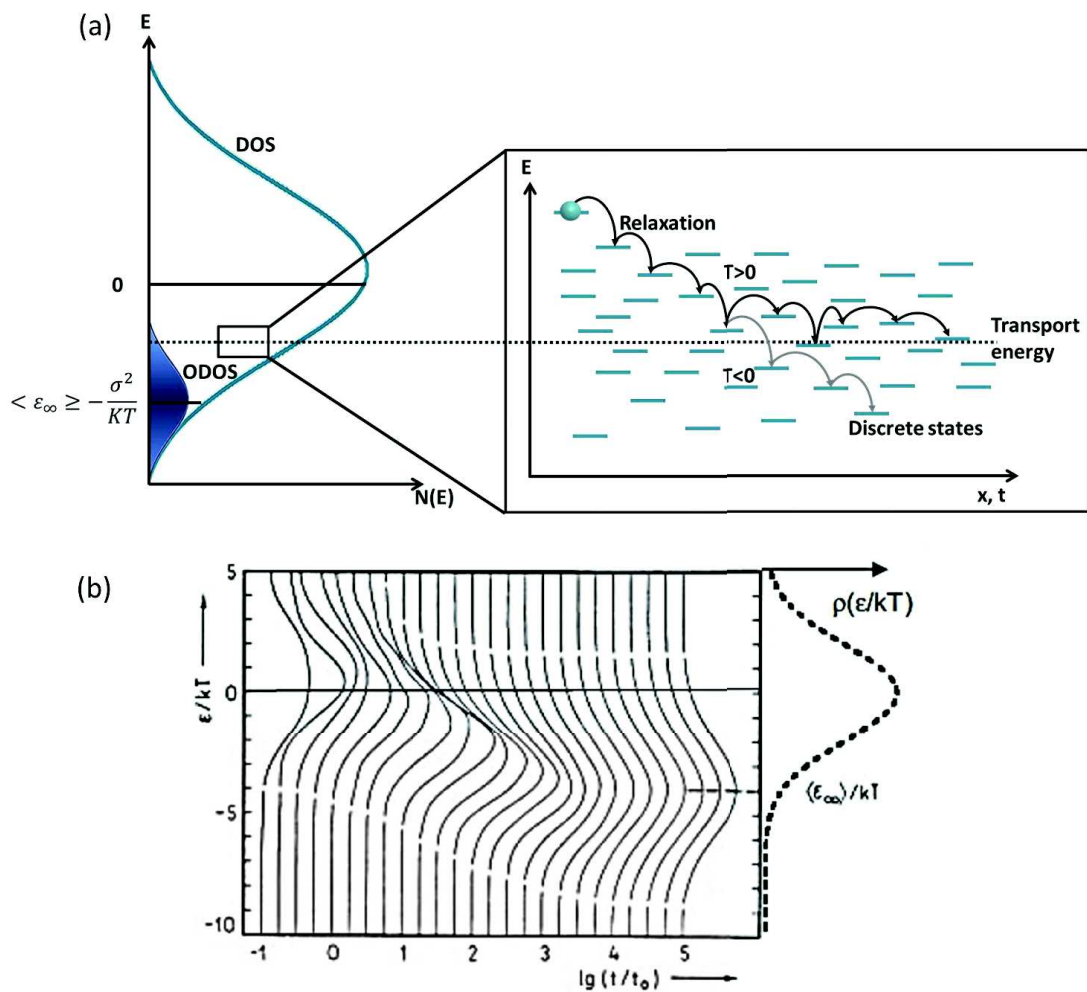


Figure 1.2 (a) Schematic illustration of charge transport process in disordered materials. The charge transport takes place around the transport energy which is at $-\sigma^2/kT$ with respect to the center of the DOS. After photoexcitation into upper states the charge relaxes to sites of lower energy in the tail of the DOS. (b) Relaxation of energy distribution of an injected charge-carrier hopping in a Gaussian DOS as a function of time from the center of the DOS to its tail. The dashed line on the right represents the DOS. A gaussian distribution of DOS is assumed. Reprinted from [20]

The time at which the energy of the charge carrier reaches $\langle \varepsilon_\infty \rangle$ increases very rapidly with decreasing temperature [19]. Nevertheless, the decrease in $\langle \varepsilon_\infty \rangle$ with decreasing temperature does not continue all the way down to zero temperature. Instead, below some temperature T_C , $\langle \varepsilon_\infty \rangle$ will show an upward curvature even with decreasing temperature. This happens because at very low temperature an activated jump to a higher energy state (which is necessary to achieve an equilibrium between thermally activated upward jumps and relaxing downward jumps) becomes extremely difficult once the charge carrier reaches a sufficiently low state. This frustration effect of the relaxation process results in a freezing of

the charge carrier energy at some value higher than $\langle \varepsilon_{\infty} \rangle$ [23, 24, 25]. In this case the charge carriers transport mode is called multiple trapping (MT) model.

1.3.3 The mobility edge and the Metal-Insulator transition

In the model introduced by Arnold Sommerfeld for a metal, the electron states in a crystalline metal are occupied up to the Fermi energy E_F . The density of states at E_F determines the electronic specific heat and Pauli paramagnetism. This is still true if the material is non-crystalline with the difference that, in this case, the states at the bottom of the band are localized. This means that electrons wave functions are localized in a limited area and decay exponentially as:

$$\Psi = f(r)e^{-r/\xi} \tag{6}$$

where ξ is the localization radius or localization length. (For ideal band structure without level disorder, the wave function will extend over the entire system and the intensity of a wave function initiated on one site will be zero after infinite time.) Due to the presence of the exponential part in equation (6), the neighboring sites can only feel some "tails" of the wave function with exponentially small amplitude, so that the intensity of the wave function remains finite at all time [26]. In this case the system is called a Fermi glass. Although the specific heat and Pauli magnetism behave as in a metal, the conductivity has a different trend, tending to zero as temperature decreases. Therefore, even if there is no energy gap in a Fermi glass, its behavior is the one of an insulator. Anyway, if the electronic wave functions overlap, an electron can move from one of these local states to another by exchanging energy with lattice vibration. Therefore there is a finite probability for electrons to tunnel (hop) from one site to another.

As already discussed, according to Anderson, in presence of disorder some of the electronic states, particularly those close to the band edge, are no longer delocalized, but become localized. A sharp energy called the "mobility edge" (E_C) is used to separate the localized states from the delocalized states. The position of E_F with respect to E_C determines in which regime of conduction (metallic, critical or insulating) the system lies.

If E_F is above E_C ($E_F > E_C$) the system is metallic with the conductivity tending to a finite value as temperature tends to zero. On the other hand if E_F is below E_C ($E_F < E_C$), the

material is an insulator, electrons can only move by thermally activated hopping with a conductivity vanishing at zero temperature. Therefore the mobility edge marks the transition between a metal and an insulator material.

If E_F and E_C can be varied, then a metal-insulator transition, known as Anderson transition, would occur [27]. The relative position of E_F and E_C can be changed in several ways such as: changing the composition, the number of electrons in the conduction band or the degree of disorder, applying uniaxial strain, changing the magnetic field in magnetic semiconductors, changing the gate voltage on two dimensional conduction at the gate interface in the field effect transistors.

For a system in which one can vary the number of charges, the plot of resistivity ρ as a function of $1/T$ will be as in Figure 1.3. If there is a high density of charges, so that E_F lies above E_C the conductivity is nearly independent of temperature. In this case the carrier statistics to be used is the Fermi-Dirac.

As the density of charges is lowered, the Fermi energy falls until it reaches E_C and the conductivity σ tends to the “minimum metallic conductivity” σ_{min} [28, 29]. If the density falls still further, states are localized and the transport is given by two mechanisms:

- i. the excitation of the charges to the extended states at the mobility edge, at high temperatures, with a temperature dependence of the conduction given by

$$\sigma = \sigma_0 \exp\left(-\frac{E_a}{kT}\right) \quad (7)$$

where $E_a = E_F - E_C$ is the activation energy and the pre-exponential factor is closer to the value σ_{min} ;

- ii. the hopping of the charges at E_F , which can be nearest neighbor hopping (NNH) and Variable range hopping (VRH), at lower temperatures.

Metallic behavior with $\sigma(T)$ remaining constant as T approaches zero has been reported for electrolyte-gated PBTTT thin films through studies of the temperature dependence of the resistivity signature [30, 31, 32] and electron spin resonance [33].

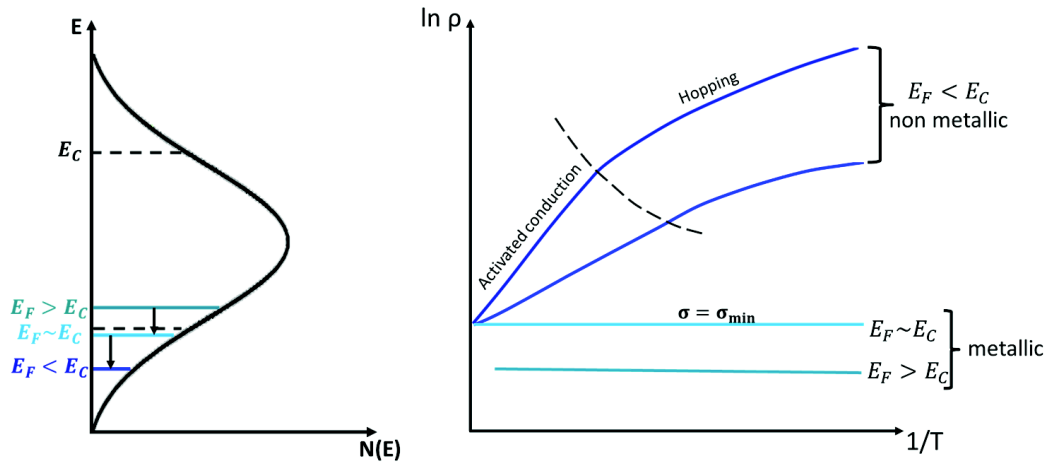


Figure 1.3 Schematic representation of the relative position of the Fermi energy E_F and mobility edge E_C in a Gaussian DOS at different level of charges filling. (b) Corresponding plot of $\ln \rho$ versus $1/T$ for a system in which the density of charges can be modified so that $E_F - E_C$ changes sign, giving Anderson metal-insulator transition. The dotted line separates the regimes where the conduction is given by excitation to E_C and by hopping. Adapted from [27]

1.3.4 Nearest neighbor and variable range hopping

For Nearest neighbor hopping (NNH) and Variable range hopping (VRH) models the used hopping rate between sites is again the Miller-Abrahams rate. Therefore, NNH and VRH conductivity takes place when the Coulomb interactions between the localized electrons are negligible.

Nearest-Neighbor Hopping (NNH) [15] is a thermally activated hopping. At finite temperatures an electron in an occupied state with energy below E_F can move to a nearby state above E_F by receiving energy from a phonon. The excited electrons move to the nearest empty site [16] and the expression for conductivity is as follows:

$$\sigma = \sigma_0 \exp\left(-\frac{W}{kT}\right) \quad (8)$$

The activation energy W is determined by percolation method and the relative calculation is explained in [15].

The nearest neighbor hopping happens when the tunneling part of the equation 1 (first exp term) is so much slower than the energy contribution, that only the nearest neighbors are addressed in hops. As long as a carrier can find shallow and unoccupied sites

with energies below its current state, it will perform a nearest neighbor hopping to energetically lower sites, since in this case the rates are only limited by the spatial tunneling distances. This is the case for very high temperatures or very small localization radii.

However, at some point the next unoccupied site with deeper energy might be so far away that it is faster for the carrier to perform an activated hop upward in energy. In this situation it could be more energetically convenient for the carrier to choose a site far in the space over the nearest neighbor instead of jumping upwards in energy in the nearest states. This transport mechanism, formulated in 1968 by Neville Mott [34], is known as Variable range hopping (VRH) and is the most common low temperature charge carrier transport mechanism used in literature (usually around and below 80K [35]) describing conduction between localized states in strongly disordered systems with a constant DOS with energy around E_F . In this situation, all transport happens within an energy range $\Delta\varepsilon$ around E_F . In this case, the temperature dependence of conductivity is given by [36]:

$$\sigma(T) = \sigma_0 \exp\left(-\left(\frac{T_0}{T}\right)^{\frac{1}{d+1}}\right) \quad (9)$$

where the parameter σ_0 can be considered the limiting value of conductivity at infinite temperature, d is the system dimensionality and T_0 is the characteristic temperature above which the transport is not anymore determined by thermally activated hopping among localized states at different energies (VRH) and is considered a measure of disorder.

When the system approaches the transition to the metallic state, the temperature dependence of the conductivity becomes weaker and is described by a power law T-dependence:

$$\sigma(T) = T^\beta \quad (10)$$

with β normally ranging between 0.3 and 1 [36, 37].

1.3.5 Doping in conducting polymers

As already said in Section 1.3.3, at sufficiently high carrier densities OSCs can reach the metal-insulator boundary with room temperature conductivities around $10^4 \text{ S}\cdot\text{cm}^{-1}$ and weak temperature dependence [³⁰, ³⁸, ³¹, ³⁹]. For this reason they are also called synthetic metals.

The increase of charge carrier concentration can be achieved by doping which is essentially a charge transfer reaction resulting in the partial oxidation (p-doping) or reduction (n-doping) of the polymer with consequent change in the conductivity. Doping in conjugated polymers has led to extensive scientific and technological interest since its first demonstration in 1977 [⁴⁰] when an intrinsically insulating organic polymer, polyacetylene, was exposed to iodine dopant. The result was an increase in the conductivity by several orders (from the intrinsic value lower than $10^{-5} \text{ S}\cdot\text{cm}^{-1}$ to values around $10^3 \text{ S}\cdot\text{cm}^{-1}$).

Two commonly used doping methods are chemical doping [⁴⁰, ⁴¹, ⁴²] and electrochemical doping [⁴², ⁴³, ⁴⁴]. Other methods include photoexcitation (based on photo-absorption and charge separation), as in photovoltaic devices, charge injection without counterions involved, as in diodes and OFETs, and doping by acid-base treatment.

Chemical doping takes place via a redox reaction where electrons are transferred between the conjugated polymer and the added dopants. More specifically, in the case of n-doping, an electron is transferred from the HOMO of the dopant (donor) to the LUMO of the polymer; while for p-doping, an electron is transferred from the HOMO of the polymer to the LUMO of the dopant (acceptor). The mechanism of chemical doping is shown in Figure 1.4. Since the HOMO of most of the OSCs is around -5 to -6 eV below the vacuum level, it follows that a p-type dopant should be a very strong electron acceptor. Even more strict conditions are applied to n-type dopants, which should have HOMO level near to -2.5 to -3.5 eV. This clearly limits the choice of chemical dopants to be used.

It is also important to point out that chemical doping not only increases the density of carriers, but also the disorder, leading to localization of the carrier wave functions. This additional source of disorder is eliminated in field-effect transistors (FETs) by using the capacitance and gate voltage to induce sufficient carrier densities to reach the metallic regime [⁴⁵]. However, the observation of metallic conduction in the two-dimensional regime within the channel of FETs has been generally limited by the low values of both capacitance and electric breakdown field of commonly used gate dielectric materials, such as SiO_2 [⁴⁶].

Another drawback of chemical doping is the time instability. During the doping process, the dopants can penetrate into or diffuse out of the polymer leading to change in its morphology. Moreover chemical doping is homogeneous only in heavily doped polymers, but not at intermediate doping levels. This problem is expected to be less critical with electrochemical doping.

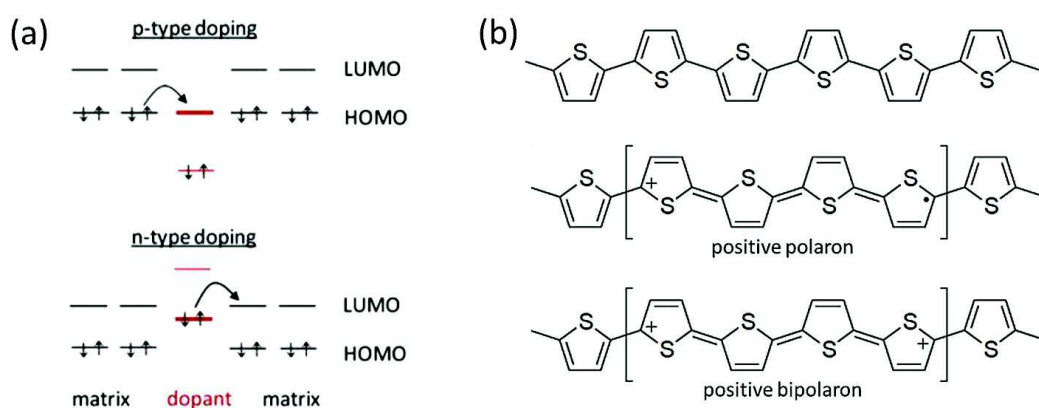


Figure 1.4 (a) Schematic of the molecular doping mechanism for p-type doping (top) and n-type doping (down). (b) Schematic structure of undoped (top) and doped (middle and bottom) polythiophenes. Upon p-doping, a positive charge and an unpaired electron with a change in the bond alternation pattern between them (positive polaron) is generated on the chain by removing an electron from the polymer chain. If two polarons get close to each other they combine and form a bipolaron.

Electrochemical doping requires the organic semiconductor to be in contact with an electrochemically conducting working electrode, which supplies the charge, and an ionically conducting electrolyte in contact with a counter electrode. Applying a potential difference between the two electrodes will cause an injection of charges from the working electrode. The injected charges are then neutralized by the counterions from the electrolyte solution. Upon p-doping, the polymer is oxidized (an electron is removed from the polymer to the working electrode) and simultaneously the anions move from the electrolyte and penetrate into the interchain sites of the polymer as charge balancing ions. In case of n-doping the polymer is reduced (an electron is added to the polymer) and the electrolyte cations are introduced into the polymers as counterions. Electrons of π character can be relatively easily removed or added to form a polymeric ion without much disruption of the σ bonds, which are primarily responsible for holding the polymer together.

One of the main advantages of the electrochemical doping is that in this case the doping level can be easily controlled by the applied voltage between the polymer and the counterelectrode. Another advantage is that it is a reversible process. During the doping interchain chemical bonds are not disrupted and therefore, upon de-doping the original polymer is recovered with almost no degradation of the polymer backbone.

Based on the electrochemical doping process, the electrolyte-gated OFETs (EGOFETs) represent a reliable technique to control the doping level reversibly in devices and offer the possibility to study conduction properties as a function of the carrier density up to high values compared with conventional dielectrics. The working principle of these devices is described in detail in Section 1.4.3.

The onset of metallicity in PBTTT- and P3HT-based EGOFETs have been reported by few authors [⁴⁷, ³¹, ³⁸] while a true metallic behavior, with related decreasing of the resistivity under cooling, it has been only observed in PEO-LiClO₄-gated PBTTT by Dhoot *et al* [³⁰].

1.3.6 Electron spin resonance signature of electronic states in conjugated polymers

Macroscopic transport measurements do not provide complete information about the intrinsic electronic state of charge carriers in OSCs. To this purpose, it is necessary to use microscopic methods such as electron spin resonance (ESR). In this case the electronic state of the charge carriers in the polymer can be determined simply by direct comparison of the spin concentration with the charge concentration.

Using this technique the microscopic signature of a metallic state in electrochemically-gated PBTTT transistors has been reported from the observation of Pauli susceptibility (expected for metals) [³²]. In particular it has been observed that in the insulating state, at low gate voltage (low doping level), spin and charge concentrations agree well with each other, indicating the presence of positive polarons, which have both spin and charge. In the metallic state, at high gate voltage (high doping level), the spin-charge relation is characterized by a spin concentration saturation, contrasting to the monotonic increase in the charge concentration. As a result, a large difference between spin and charge concentrations is observed, indicating that pairs of spin 1/2 polarons merge into spinless bipolarons as the doping level increases.

Similar results have been obtained by optical absorption measurements as a function of the gate voltage for PEO-LiClO₄-gated P3HT [48] and PBTTT [49]. In all the cases, a decrease in the intensity of the π - π^* absorption peak, centered at 560 nm (visible), is observed when increasing the negative gate voltage together with the appearance of a new absorption band which is ascribed to the polaron absorption of PBTTT [50]. At high doping levels the polaron absorption peak turns to a broad band and shifts to longer wavelengths absorption around the near infrared (~800nm). This can be related to the formation of bipolarons which are known to induce a single absorption band in the infrared region [51, 52].

Moreover, ESR measurements on electrolyte-gated PBTTT thin films also indicate that the edge-on orientation of PBTTT is maintained even after the electrochemical doping. Therefore the penetration of the ions coming from the electrolyte gate do not disturb the morphology of the polymer and are expected to be located either between the side chains of the PBTTT backbone or at the grain boundaries [32].

1.3.7 Charge injection

The charge injection process at the metal and organic material interface has a large impact on the electrical properties of OSC devices. When a metal and an OSC are put in contact, a potential barrier is created at the interface due to the energy difference between the Fermi level of the metal and the frontier orbitals of the organic material. This energy barrier limits the efficient charge injection at the contacts [53].

To better understand the charge carrier injection process let's first consider the most simple case, that is the interface between a metal and an inorganic semiconductor. When two materials with different Fermi levels (E_F) are brought into contact, they reach thermal equilibrium and establish a common E_F by exchanging carriers. In this condition, electrons diffuse from the material with the highest E_F (for example the metal) towards the material with the lowest E_F (for example the semiconductor). This gives rise to a contact potential across the interface, equal to the difference of the Fermi levels of the isolated materials. The diffusion of electrons from the metal to the semiconductor gives rise to a space charge in the latter, and the resulting electric field tends to drive electrons back in the metal until diffusion current is cancelled out by drift current.

Moreover, an electron leaving a metal will induce a positive charge density at the metal surface to screen its electrostatic field. This screening effect is represented by an image

charge of the electron at the same distance in the metal. Therefore, at an arbitrary distance x away from the metal/semiconductor interface, located at $x = 0$, the electrostatic potential of a carrier relative to the Fermi level of the metal is described as the superposition of the Coulomb field binding the carrier with its image twin on the electrode, an external electric field F (V_{SD}), and the site energy E :

$$U(x, E) = \Phi_b - \frac{e^2}{16\pi\epsilon_0\epsilon x} - eFx + E \quad (11)$$

where Φ_b is the barrier height in absence of both the external field and the image charge effect, e is the elementary charge, ϵ is the dielectric constant, and ϵ_0 is the dielectric permittivity.

The interplay between electrostatic potential and image potential results in a local maximum of the electrostatic potential given by

$$\frac{U_{max}}{e} = \Phi_b - \Delta\Phi = \Phi_b - \sqrt{\frac{eF}{4\pi\epsilon}} \quad (12)$$

Under an applied external field F , the energy maximum of the barrier gets lower by $-eFx$ than the original Φ_b and closer to the interface, and a net carrier injection occurs by partial suppression of the drift component in favor of the diffusive one thus favoring injection with respect to backflow [54, 53, 55]. This effect is known as Schottky effect. It must be noted that a significant electric field is needed (10^6 V/cm) to produce a relevant drop of the barrier (see Figure 1.5).

Once the carrier is injected into the SC, it can either go back to the metal due to the attractive image potential, or escape with a finite probability to diffuse into the bulk. For low mobility SCs, backflow will occur due to the large concentration of charge carriers accumulated at the interface. In fact, in this case the velocity of the charge carriers in the bulk of the semiconductor is smaller than that in the interfacial area. This results in a stack of carriers at the interface. Therefore low mobilities of the OSCs are also related to poor injection and in this case the injection is space charge limited (SCL).

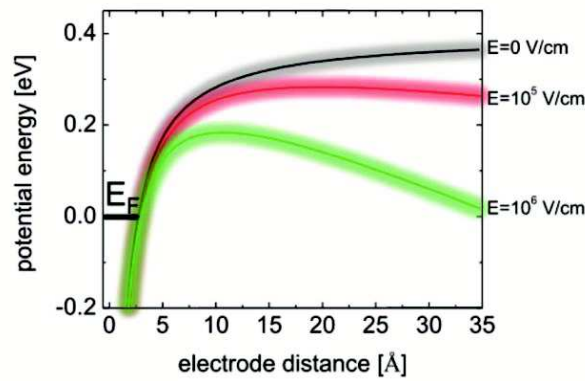


Figure 1.5 Representation of Schottky effect: lowering of the of the potential energy distribution at the metal-semiconductor interface for three values of the external applied electric field (nominal barrier $\Phi_b = 0.4$ eV). The larger the external electric field, the lower the maximum of the potential energy becomes. Reprinted from [53], based on simulation from [55]

Depending on the magnitude of the energy barrier the measured current can either be injection limited (IL) or diffusion limited, i.e., space charge limited (SCL). The latter case requires one of the electrodes to be Ohmic, thus able to supply enormous number of charge carriers. This will form a space charge cloud near the injecting electrode. At low bias SCL current results in linear current-voltage characteristics in log-log scale, while at high bias current-voltage characteristics becomes quadratic. In this case the device performance is limited by the transport properties of the organic material. Since most of the OSCs have bandgaps >2 eV (while in inorganic SCs the bandgaps are typically 1-2 eV), the formation of low-resistance, ohmic contacts with common metals is often challenging and in many case the injection process in OFETs reported in literature can be regarded as IL.

IL conduction is commonly described either by the Richardson-Schottky model of thermionic emission or by the Fowler-Nordheim model for tunneling injection [56].

The Richardson-Schottky (RS) model assumes that an electron from the contact can be injected once it has acquired a thermal energy sufficient to cross the maximum of the electrostatic potential without being scattered. The current density J is given by

$$J = A^*T^2 \exp\left(-\frac{\Phi_b - \Delta\Phi}{kT}\right) \quad (13)$$

where A^* is the effective Richardson constant. The RS model gives rise to an injection current with an Arrhenius-type dependence on the temperature ($\ln j \propto T$) and Φ_b , which is due to the decreasing of the number of metal electrons with enough energy to be injected for higher barrier height or lower temperatures, and a Poole-Frenkel-type dependence on the field ($\ln j \propto \sqrt{F}$). Tunneling through the barrier is ignored. The thermionic emission model is not applicable to low mobility SCs, because backflow will occur due to the large concentration of the charge carriers at the interface [57].

At high electric fields the tunneling of the charge carriers through a triangular barrier occurs, described by the Fowler-Nordheim (FN) model. The FN model ignores the image-charge effects and considers the tunneling of the electrons from the contact through a triangular barrier into unbound continuum states. It predicts a current density

$$J = BF^2 \exp\left(-\frac{C}{F}\right) \quad (14)$$

independent on the temperature, with $B = \frac{e^3}{4\pi^2\hbar m^* \Phi_b}$ and $C = \frac{4\sqrt{2}m^*}{3e\hbar} \Phi_b^{3/2}$ where m^* is the effective mass of electrons and \hbar is the reduced Planck constant.

Both RS and FN models were developed for band type materials under the main assumption of a strong electronic coupling between the constituting lattice elements that leads to wide valence and conduction bands. This means that the scattering length of charge carriers is much larger than the interatomic separation. In OSCs the electronic coupling between molecules is of Van der Waals type and thus weak. Accordingly the transport is an incoherent process (hopping) and the mean-free path is comparable or even lower than the intermolecular distance (~ 1 nm). As shown in Figure 1.5 at an electrical field ranging from 10^5 to 10^6 V/cm, the maximum of the potential distribution is located between 3.2 and 0.8 nm away from the interface. Since in OSCs the typical jump distance is around 0.6 nm, a carrier cannot cross the potential barrier by a single thermally or tunneling jump. Therefore the classical injection models fail in the description of metal/organic interfaces.

An experimental signature of this failure is that the temperature dependence of the injection current is weaker than the one expected considering the estimated energy barriers and it is sub-linear on an Arrhenius scale [58]. This is in total disagreement with the classical thermionic injection models in which the temperature dependence of the injection process is dominated by the injection barrier (equation (13)).

As an alternative to the above mentioned classical injection mechanisms, a more suited model to describe charge injection from metal to organics has been formulated by Bässler and coworkers using both an analytic approximation to the calculation and a Monte Carlo simulation [59, 55, 60]. The model describes thermal injection of charge carriers into a conjugated polymer as a two-step process represented in Figure 1.6.

On the first step, carriers make initial thermally activated jumps from the Fermi level of the metal contact into a tail (localized) state of the Gaussian density of states distribution. This site needs to have at least one hopping neighbor at equal or even lower energy to ensure that the primarily injected carrier can continue its motion away from the interface, rather than recombine with its image charge in the electrode. On the second step, the carrier random walk within the system of hopping sites is described as a continuous diffusive motion in the combined Coulomb potential of the image charge and the externally applied potential treated in terms of a one-dimensional Onsager-like process [61, 62].

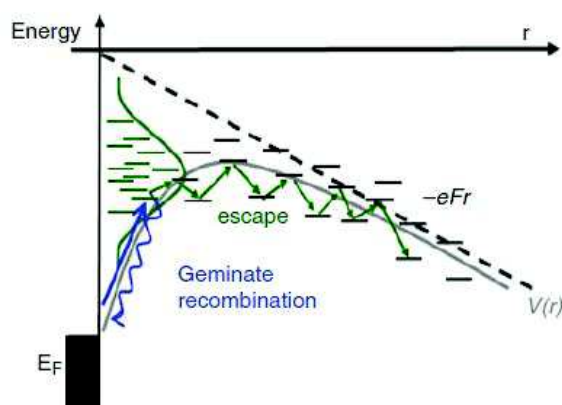


Figure 1.6 Charge injection mechanism into a metal/OSC interface.

It has been observed that energetic disorder, present in all OSCs, enhances the injection by populating interface tail states, which can act as a carrier reservoir. In fact, as explained in Section 1.3.2 at thermal equilibrium, low carrier density and relatively high temperature (so that the Fermi-Dirac distribution can be approximated with the Boltzmann one), the occupied density of states (ODOS) has a Gaussian distribution centered at $-\sigma^2/kT$ with respect to the center of the DOS. The lower the temperature is, the farther this distribution lies from the nominal LUMO (Figure 1.7). As a result, the injection barrier

decreases with decreasing temperature, making easier for a metal electron to jump into an unoccupied semiconductor state. Therefore, the injection process is easier at low temperatures leading to a weaker temperature dependence of the current.

In conclusion, the knowledge of the mechanisms of charge injection into conjugated polymers is not as comprehensive as for inorganic semiconductors. Ohmic injection in metal/organic interface is difficult to achieve because of finite Schottky barrier formation. Optimization of charge injection and extraction at the electrode/semiconductor interface is therefore required to realize low contact resistance devices and thus improve their performances. Such an optimization can be achieved by properly choosing the metal work function which needs to be matched with the semiconductor charge transport levels to minimize the energetic mismatch between the molecular orbitals of the OSC and the E_F of the electrode and to reduce the resulting series (contact) resistance.

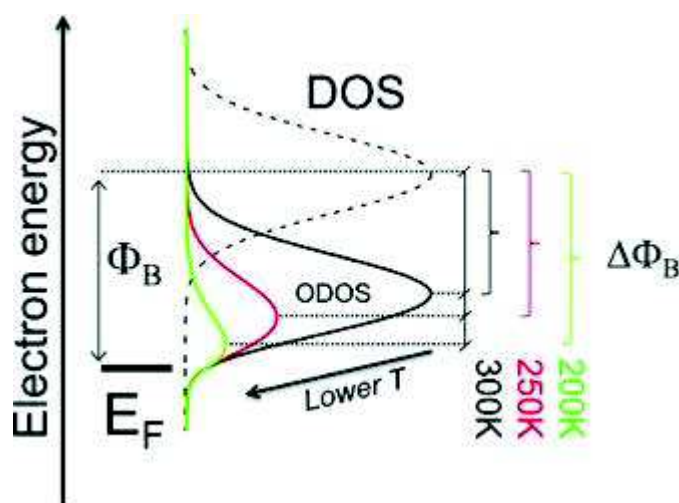


Figure 1.7 Effect of the disorder on energetic barrier at the metal/OSC interface. At room temperature, the center of the occupied DOS (ODOS, black solid curve) lies close to the Fermi level of the metal. Upon lowering the temperature, the effective energetic barrier is lower than the nominal one by $\Delta\Phi = -\sigma^2/kT$. Reprinted from [53]

Another approach for the control of metal/organic semiconductor interface is the use of polar, thiol-based self-assembled monolayers (SAMs), such as hexamethyldisilazane (HMDS) or octadecyltrichlorosilane (OTS), which induce a shift in the metal work function [63]. Moreover the variation in the wettability of the electrode induced by the SAM can also have an effect on the film morphology at the interface with the electrode favoring the

organization of the polymer chains into lamellar structures with consequent improvements of the mobility [64, 65, 66].

Interface modification can be also reached with other methods, such as interfacial dipole formation [67] and bulk doping of the OSC [68, 69]. Also high doping of the OSC may accelerate the hopping process of the injected charges by filling the trap states.

Finally, the metal/OSC interface properties are especially important for spin injection/detection, as it will be discussed in more detail in the next chapter.

1.4 Devices

Organic electronics gave rise to the realization of different devices such as organic photovoltaic cells, light emitting diodes, and field-effect transistors. This thesis deals with the latter ones.

1.4.1 Organic field-effect transistor

The basic building block for organic electronics is the organic field-effect transistor (OFET). The first organic transistor was demonstrated in 1984 and it included an electrolyte as the gating medium [70]. It was not a field-effect transistor but instead an electrolyte transistor based on solid-state electrochemical reduction and oxidation (redox) of poly(pyrrole). The first OFET that demonstrated electrostatic field effect transistor behavior was reported by Tsumura *et al.* in 1986 by using poly(thiophene) as polymeric semiconductor [71].

In Figure 1.8 (a) a schematic of the structure of an OFET is shown. OFET is a three-terminal device that consists of source (S), drain (D) and gate (G) electrodes, respectively.

The conducting channel between source and drain electrodes is made of an organic semiconducting material which has width W and length L defined by the extensions and separation of source and drain electrodes, respectively. The semiconductor layer is separated from the gate electrode by a layer of an insulating material referred to as the gate dielectric or gate insulator. This stack of materials can be seen as a capacitor, with a capacitance per unit area C_i :

$$C_i = \frac{\epsilon_0 k}{d} \tag{15}$$

where ϵ_0 is the vacuum permittivity, k is the relative permittivity, and d is the gate insulator thickness.

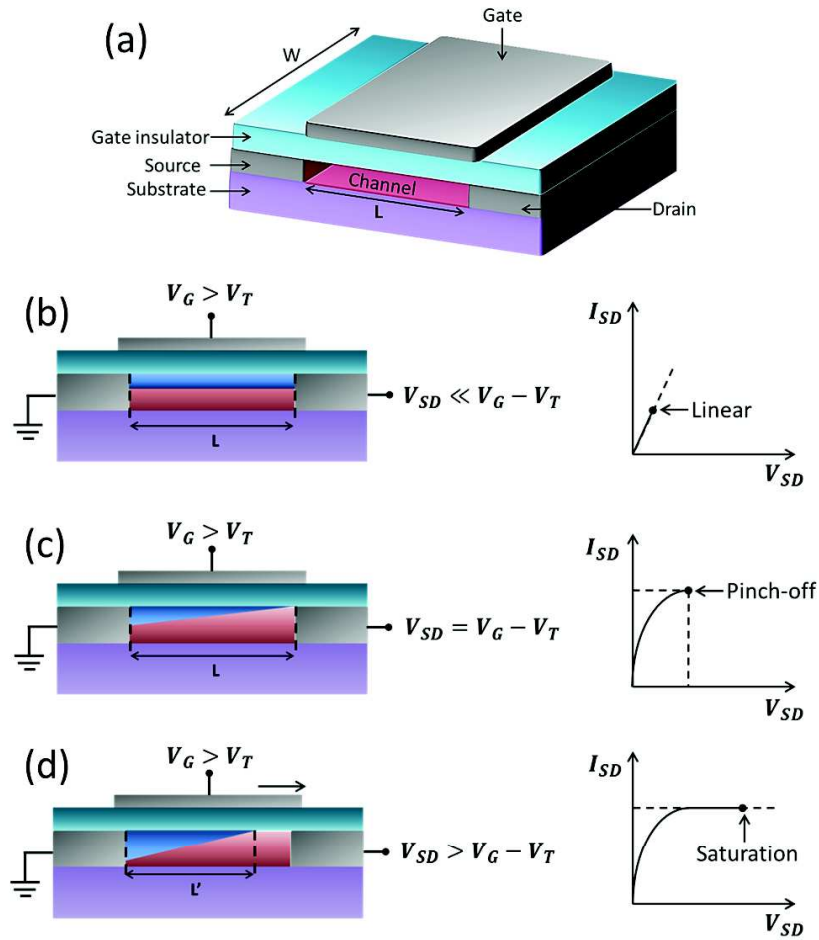


Figure 1.8 (a) Schematic illustration of an OFET. Representation of the charge distributions in the channel and the relative current-voltage characteristics in the different operating regimes: linear (b), pinch-off (c), and saturation regime (d).

Applying a potential to the gate electrode induces a uniform distribution of charge carriers at the insulator/SC interface. A positive gate voltage induces negative charges (electrons), while a negative gate voltage induces positive charges (holes). The applied gate voltage has to exceed a threshold voltage V_T before the channel becomes conducting and the transistor is turned ON. Therefore, the effective gate voltage is $V_G - V_T$.

The mobile charges per unit area, Q , at a specific gate voltage ($V_G > V_T$) in the absence of drain voltage is

$$Q = C_i(V_G - V_T) \quad (16)$$

From this equation it is easy to see the importance of C_i parameter. Since the charge density is proportional to the capacitance of the gate dielectric, it is important to use gate materials with high specific capacitance. In standard SiO_2 dielectrics the maximum induced carrier density is $<10^3 \text{ cm}^{-2}$ due to the low capacitance. According to equation (16), there are two ways to increase C_i : by decreasing the insulator thickness d or by increasing the dielectric constant k adopting high- k insulators [72, 73, 74], ultra-thin cross-linked polymers [75, 76, 77, 78, 79], and self-assembled monolayers [80, 81, 82]. Another limit of SiO_2 gate is the low dielectric breakdown field ($<10 \text{ MV/cm}$).

When a small drain voltage is applied ($V_{SD} \ll V_G - V_T$), a linear gradient of charge density is formed between source and drain electrodes (see Figure 1.8 (b)). In this condition, the potential in the semiconductor is a function of the position x in the channel as well as the induced channel charge density which is given by

$$Q(x) = C_i(V_G - V_T - V(x)) \quad (17)$$

This results in a linear increase of the drain current with increasing V_{SD} . The drain current can be expressed as

$$I_{SD,lin} = \frac{W}{L} \mu_{lin} C_i (V_G - V_T) V_{SD} \quad (18)$$

where μ_{lin} is the charge mobility. This operation regime is called linear regime. The field-effect mobility in the linear regime can be obtained by the derivative of equation (18) with respect to the gate voltage at a constant drain voltage

$$\mu_{lin} = \frac{L}{WC_i V_{SD}} \frac{\partial I_{SD}}{\partial V_G} \quad (19)$$

As the drain voltage is increased, the number of accumulated charge carriers in the channel close to the drain electrode decreases. When $V_{SD} = V_G - V_T$, the channel is pinched-off (Figure 1.8 (c)). Therefore a depletion region is formed next to the drain electrode where a space-charge limited saturation current flows. The charge concentration at the pinch-off point (P) will be zero. This point denotes the start of the saturation regime. Increasing the drain voltage even further ($V_{SD} > V_G - V_T$) will move P away from the drain electrode leading to the reduction of the channel length to an effective value L' given by the distance between the source electrode and P (Figure 1.8 (d)). This operation regime is called saturation regime. The saturation drain current is

$$I_{SD,sat} = \frac{W}{2L} \mu_{sat} C_i (V_G - V_T)^2 \quad (20)$$

from which the field-effect mobility in the saturation regime can be extracted as follows:

$$\mu_{sat} = \frac{2L}{WC_i} \left(\frac{\partial \sqrt{I_{SD,sat}}}{\partial V_G} \right)^2 \quad (21)$$

The current-voltage (IV) characteristics of OFETs are the output (I_{SD}, V_{SD}) curves and the transfer (I_{SD}, V_G) curves as shown in Figure 1.9 (a) and (b), respectively.

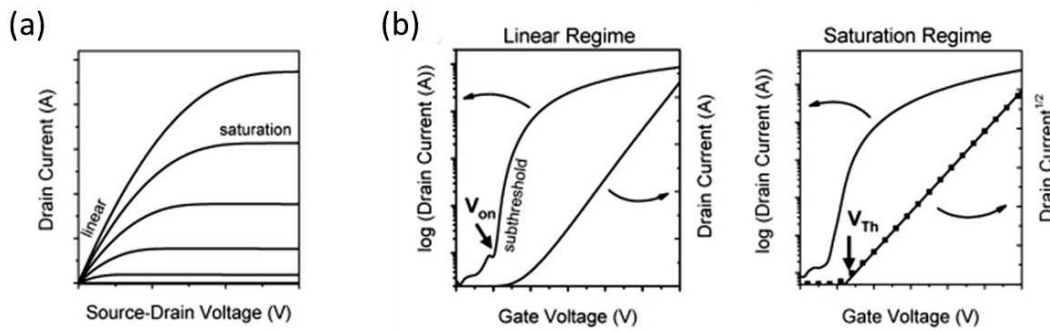


Figure 1.9 Typical current-voltage characteristics OFETs: (a) output characteristics indicating the linear and saturation regimes; transfer characteristics in (b) the linear regime ($V_{SD} \ll V_G$); and (c) the saturation regime ($V_{SD} > V_G - V_T$). Reprinted from [83]

The output curves show how the source-drain current evolves for different gate voltage control values. The transfer curve shows the source-drain current as a function of the gate voltage V_G , while the drain voltage V_{SD} is kept constant either in the linear or in the saturation regime. The transfer characteristics illustrates how the gate voltage can switch the transistor “ON” and “OFF”.

Several important parameters can be extracted from the transfer characteristics such as the on/off current ratio, the subthreshold slope, the threshold voltage, and the field effect mobility in the linear and saturation regimes. The on/off current ratio is the ration of the drain current in the on-state at a given gate voltage to the drain current in the off-state. A high on/off ratio exceeding 10^6 is usually desirable in order to have a distinctive on- and off-state. Related to the on-off ratio is the subthreshold slope (S), which is the slope of the transfer curve, after V_T , and determines how susceptible is the transition from off- to on-state to the control gate voltage. A low S indicates a faster switch. The turn-on voltage (V_0), which is defined as the voltage at which the transistor turns from the off-state to the subthreshold region (the region where the gate voltage is lower than the threshold voltage), can be also extracted from the transfer curve.

According to equation (19), the field effect mobility in the linear regime, μ_{lin} , is proportional to the gradient of the drain current increase in the linear regime. The field effect mobility in the saturation regime, μ_{sat} , can be estimated from the plot of the square root of the drain current versus the gate voltage, following the equation (21).

From the same plot it is possible to extract the threshold voltage V_T by extrapolating the linear fit of the square root of the drain current in the saturation region to the gate voltage axis. In an ideal OFET, V_T is zero. However, due to the mismatch between the work-functions of the metal electrodes and the OSC, the presence of localized states (traps) at the insulator-OSC interface, V_T has generally a finite value.

In the output characteristics, for a given gate voltage, the drain current initially increases linearly with the drain voltage and then levels-off as V_{SD} becomes larger than the effective gate voltage ($V_G - V_T$). In this plot it is possible to clearly distinguish the linear and the saturation regimes.

1.4.2 OFETs geometry

From a geometrical point of view, OFETs can be divided in two main configurations depending on the sequence of deposition of the different components (source, drain and gate electrodes, and SC): coplanar, with the accumulated channel and the S/D contacts laying at the SC/dielectric interface; and staggered, with the SC in between the dielectric and the plane containing S and D.

Coplanar devices can be bottom-gate, bottom-contact (BGBC), where the SC is deposited as last step; or top-gate, top-contact (TGTB), where and S/D contacts are deposited on top of the OSC and the gate electrode is deposited as last step.

Staggered devices can be top-gate, bottom-contact (TGBC), where S/D are deposited as first step and the gate electrode as last one (as in Figure 1.8); or bottom-gate, top-contact (BGTC), where the gate electrode is deposited as first step and S/D as last one.

Charge injection and thus device performances depend on the adopted OFET configuration. For example, in the coplanar configuration the contact area between source electrode and OSC is determined by the contact thickness and the channel width W and the charge carriers are injected directly into the channel from the edge of the source electrode through a very thin (~ 3 nm) accumulation layer along the width of the channel. In the staggered geometry the contact area is much larger because source/drain electrodes overlap with the gate electrode. In this case, the injected carriers travel through the bulk of the OSC before reaching the active channel so that charge carriers can be also injected from a large area of the source contact, further away from the channel. This phenomenon is called current crowding effect [82] and will be better investigated in Chapter 6.

1.4.3 EGOFETs

As said in Section 1.4.1, in order to have good carrier levels in OFETs channel, it is necessary to maximize the capacitance of the gate insulator (see equation (16)). A possibility is to replace the dielectric insulator with electrolytes, including polymer electrolytes, ionic liquids/gels, and mesoporous materials. These materials can reach capacitances exceeding $10 \mu\text{F}/\text{cm}^2$, a value much larger than what is typically achieved with SiO_2 or polymer dielectrics ($\sim 10 \text{ nF}/\text{cm}^2$). In this way it is possible to induce in the channel a very large carrier concentration (10^{15} cm^{-2}) at relatively low applied gate voltages ($< 3\text{V}$) [38, 84].

These high values of capacitance are reached thanks to a redistribution of ions with opposite polarity upon application of a (gate) voltage, resulting in nanometer-thick (~ 1 nm) [85] electric double layers (EDLs) at the gate/electrolyte and at the electrolyte/OSC interfaces with a neutral charge region in between. In this case nearly all the applied gate voltage will be dropped across the EDLs. The electric field will therefore be very high at the interfaces ($\sim 10^9$ V/m) and negligible inside the electrolyte bulk. Based on this principle a new kind of transistor, called electrolyte-gated organic field-effect transistor (EGOFET), with much larger doping values and improved carrier mobility can be realized. The high carrier mobility values observed in these devices can be reached thanks to the doping-tuned filling of the localized tail states up to the mobility edge giving access to some of the delocalized states present above the mobility edge.

The operation principle of EGOFETs is shown in Figure 1.10 for a hole-conducting (p -type) organic semiconductor. The application of a negative gate voltage to the gate electrode causes the mobile cations of the ion gel to be attracted by the negative surface charge on the gate so that an EDL will be established at the gate/electrolyte interface. At the same time negative ions (anions) will be pushed on the opposite side of the dielectric and a layer of anionic charge will be formed at the opposite electrolyte/SC interface which determines the formation of a second EDL [84]. The electrostatic capacitive coupling of the gate bias across the dielectric layer to the semiconductor induces charges carriers in the semiconductor channel (holes) to be swept from the source and drain contacts to balance the negative ionic charges.

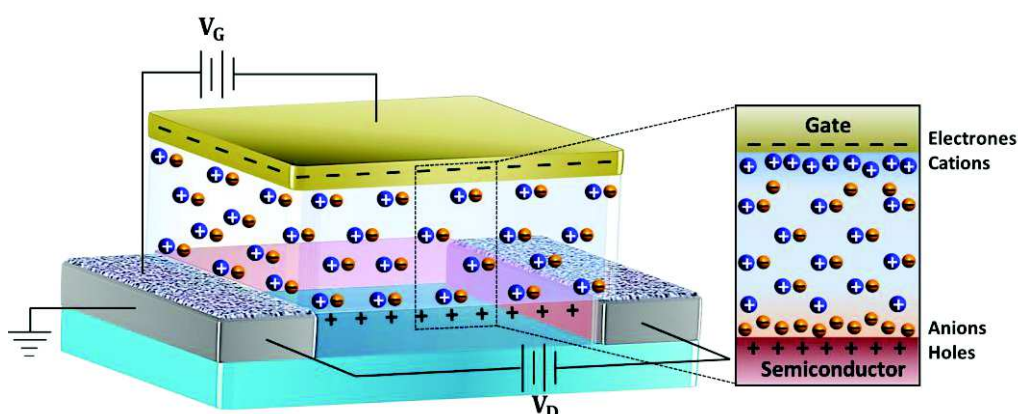


Figure 1.10 Schematization of the operation of EGOFETs together with the cross-section of the EDLs showing the charges distribution at the gate/electrolyte and electrolyte/OSC interfaces for a hole conducting OSC upon application of a negative V_G .

In this case the capacitance is independent of the thickness of the insulator [86] and is simply given by the sum of the capacitances of the two electric double layers formed at the interface of the electrolyte/SC and electrolyte/gate due to the ions migrations upon application of a gate potential:

$$C_{electrolyte} = \frac{C_{EDL1} \cdot C_{EDL2}}{C_{EDL1} + C_{EDL2}} \quad (22)$$

It has been lively debated whether the operating mechanism in electrolyte-gated transistors is field-effect (electrostatic charging) or electrochemical doping. In an ideal EGOFET, the ionic and electronic charges are separated at the interface and compose oppositely charged layers exactly as explained above.

Alternatively if the OSC is permeable, ions will penetrate the semiconductor, therefore the EDL model is not valid anymore and the electrochemical doping regime is observed. In this case there is a significant increase of the drain current since the channel becomes three-dimensional. EGOFETs in electrochemical doping regime rely on reversible doping and de-doping of the polymer.

Nowadays it is well-established that the two operating regimes, field-effect and electrochemical doping, can be controlled with the gate voltage [87]. One of the indicative features of electrochemical doping is the presence of hysteresis in the I_D - V_G curves. When a low gate voltage is applied, no evident hysteresis is observed, suggesting that EDLs are formed rapidly. A high degree of hysteresis is observed at higher gate voltages, indicating electrochemical doping, with the related redox reactions that require time for being fully reversed.

EGOFETs show as promising alternative to traditional OFETs. One example is represented by the applications in bioelectronics and bio-sensing thanks to the facile integration of electrolytes with biological media (salty water is an electrolyte) [88]. Some interesting electrical properties, such as superconductivity [89, 90], metal-insulator transition [30], and tunable thermoelectric behavior [91] have been already observed in electrolyte-gated devices. Motivated by these first encouraging results, in this thesis we have intensively studied EGOFETs using ion-gels as electrolyte in the electrochemical doping regime, which allows to access high conductivity states of OSCs.

1.4.4 Parasitic Contact resistance

In OFETs the total resistance (R_{TOT}) is the sum over the channel resistance (R_{Ch}), which is the resistance associated with the active channel, and the contact resistance (R_C), related to the metal/OSC interface:

$$R_{TOT} = R_{Ch} + R_C \quad (23)$$

where $R_{Ch} = R_{Sheet} \cdot \frac{L}{W}$ (in unit Ω/\square and with R_{Sheet} the sheet resistance) and R_C is the sum of the resistances associated with carrier injection from the source contact (R_S) and collection to the drain contact (R_D): $R_C = R_S + R_D$.

R_C is a very important parameter of OFETs because it reflects all the other factors that limit the injection, such as injection barriers, geometrical factors, trapping sites. For OFETs in lateral geometry, the charge injection occurs through a very thin area along the width W of the channel. Therefore the conductive channel is only a few nanometers thick and the charge injection interface is essentially independent of the OSC thickness. This is why usually in organic electronics contact resistance values are reported in terms of specific contact resistance $R'_C = R_C \cdot W$ and expressed in $\Omega \cdot cm$ (or $\Omega \cdot m$) [92, 53].

Keeping the contact resistance small compared to the channel resistance is crucial to the realization of “ohmic contacts” in OFETs (in particular $R_C \ll R_{Ch}$). In term of sheet resistance R_{Sheet} and specific contact resistance R'_C , the total resistance can be rewritten as:

$$R_{TOT} = R_{Sheet} \frac{L}{W} + \frac{R'_C}{W} \quad (24)$$

This equation highlights the influence of the channel dimensions (L and W) on the relative magnitudes of the channel resistance and contact resistance. As a matter of fact, from equation (24) it is evident that R_{Ch} scales down proportionally with L while the R_C does not. This means that making smaller OFETs by reducing L , results in smaller channel resistances. Consequently, the contact resistance becomes quickly much more important in the shorter channel devices because it contributes a larger fraction of the total resistance. This represents one of the main problems of device downscaling in planar OFETs, essentially limited to several microns minimum size.

1.4.5 Contact resistance measurements

There are different ways to measure R_C (see Figure 1.11). The most used method is the transmission line method (TLM), which consists of making multiple OFETs with various channel lengths L (but constant W) and measuring the total resistance versus channel length for each of them. Since the channel resistance increases with increasing the channel length, but the contact resistance remains the same between samples (equation (24)), linear extrapolation of the plot of the total resistance versus channel length to $L = 0$ effectively eliminates the channel resistance and yields the contact resistance value, for each applied gate voltage V_G , as the y-intercept [93, 94, 95]. The linear extrapolation lines at different V_G often converge at a common point, called the convergence point, which can be used to qualify the charge injection and charge transport [96].

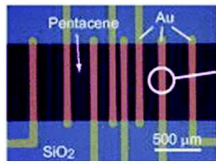
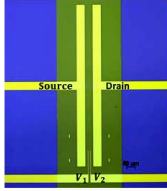
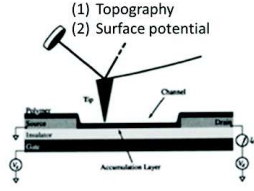
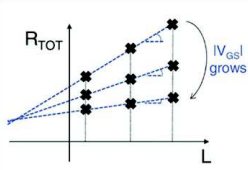
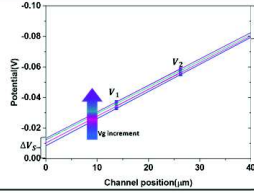
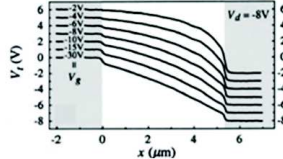
Method	TLM	gFP	KPM
Structure			
Measure			
Extraction	$R_{TOT} = \frac{\partial V_d}{\partial I_d}$ $R_C = \text{intercept}(R_{TOT}, L)$	$\Delta V_S = V_1 - \left(\frac{V_2 - V_1}{L_2 - L_1} \right) \times L_1 - V_S$ $\Delta V_D = V_d - \left[V_2 + \left(\frac{V_2 - V_1}{L_2 - L_1} \right) \times L - L_2 \right]$	Direct measurement
Pros & Cons	<ul style="list-style-type: none"> ✓ V_G dependence; ✓ any device structure; ✗ fabrication and test of multiple devices; ✗ Cannot discriminate R_S and R_D 	<ul style="list-style-type: none"> ✓ determination of R_S and R_D; ✓ accurate values; ✗ more complicate pattern; ✗ unsuitable for small L 	<ul style="list-style-type: none"> ✓ direct measurement of R_S and R_D (no extraction method); ✓ accurate values; ✗ unsuitable for top gated devices

Figure 1.11 Contacts resistance extraction methods.

TLM can be used regardless of the device structure and size. However, this technique has two main disadvantages. First, it requires the fabrication and measurements of several devices in order to obtain the resistance versus channel length plot. Moreover, this plot provides only an average R_c value for the set of devices. Second, it cannot separate the source and drain contributions (R_S and R_D) to the contact resistance.

In order to separate the individual contributions of the source and drain contacts to the contact resistance, the gated four-probe (gFP) technique is used [97, 98, 53, 99]. In this case two thin voltage-sensing probes are patterned between the source and drain electrodes and slightly protruding the channel to measure the channel potentials V_1 and V_2 at the two probes positions (L_1 and L_2) without passing any current. This method is valid only for strict linear regime OFET operation ($V_G \gg V_D$) where the charge carriers density in the channel is expected to be uniform with a linear drop in the electrostatic potential along L from source to drain. Therefore, the potential profile along the channel, obtained by linear extrapolation between V_1 and V_2 , will reveal the electrostatic potential drops (due to the contact resistance) occurring at the source (ΔV_S) and drain (ΔV_D) contacts given as the difference between the extrapolated values and the applied voltage at each contact. Then knowing the total current flowing through the device (I_D), the resistance at source (R_S) and drain (R_D) contacts can then be simply calculated from Ohm's law as $\Delta V_S / I_D$ and $\Delta V_D / I_D$, respectively. The gFP method is clearly not valid in the saturation regime where the nonuniform channel electric field (pinch-off) complicates the voltage profile. By isolating the source and drain contact contributions to the total contact resistance, gFP technique provides more information than TLM and permits to determine the contact resistance values testing a single device. However, it requires the careful fabrication of probes integrated in the device and a patterned gated area.

While TLM and gFP techniques require extrapolation of the measured data for the determination of the contact resistance, Kelvin probe microscopy (KPM) determines the source and drain contributions to the contact resistance directly by measuring the electrostatic potential along the channel [100, 101] with a conductive atomic force microscopy tip scanning the device channel. The electrostatic potential data are then converted into the channel potential profile by subtracting an appropriate background trace. The main drawback of KPM is that it requires accessibility to the top channel surface, thus precluding analysis of top-gated devices.

Semiconductor	Structure	Contacts	μ [cm ² V ⁻¹ s ⁻¹]	RC [Ω ·cm]	Method
TES-ADT	BGTC	Au	0.07	1×10^6	KPM
TES-ADT	BGBC	Au	0.11	5.9×10^4	KPM
P3HT	BGBC	Au/ naphthalene	0.001	1×10^6	TLM
P3HT	BGBC	Au	0.01	1×10^4	KPM
P3HT	BGBC	Pt	0.16	1.5×10^4	TLM
P3HT	BGBC	Au	0.11	1.5×10^4	TLM
P3HT	BGBC	Recessed Au	0.15	1×10^4	TLM
P3HT	BGBC	Au	0.15	8×10^4	TLM
PTVPhI-Eh	TGBC	Au	0.54	1×10^5	TLM
F8T2	TGBC	PEDOT:PSS	0.015	1.2×10^6	TLM
TIPS-p	BGBC	MWCNT:PSS blend	0.13	9×10^4	TLM
TIPS-p	BGBC	Au	0.20	2.2×10^4	KPM
TIPS-p: PS blend	BGBC	Au	1.01	8.7×10^4	KPM
TIPS-p	TGBC	Ag printed	0.06	6×10^5	TLM
TIPS-p	TGBC	Ag printed/ F4TCNQ	0.9	2×10^4	TLM
TIPS-p	TGBC	Au/ PFDT	0.64	6.5×10^5	TLM
TIPS-p	TGBC	Au	0.16	1×10^6	TLM
Au/ PFDT	TGBC	Au	0.06	2.1×10^4	TLM
PBTTT	TGBC	Au/ PFDT	0.4	4.5×10^4	gFP
F8BT	TGBC	Au/ PFDT	0.0018	3×10^8	gFP
PBTTT	BGBC	Au	0.56	4.4×10^4	TLM
PBTTT	BGTC	Au	0.84	6.5×10^3	TLM
TIPS-Pentacene	TGBC	NOTP/Au	0.103	291×10^3	TLM
TIPS-Pentacene	TGBC	Au	0.047	998×10^3	TLM
P3HT	TGBC	BTFMBT/Au	0.26	180×10^3	TLM
P3HI	TGBC	Au	0.16	610×10^3	TLM
C8-BTBT	BGTC	MoO3/Au	2.3	10×10^3	TLM
C8-BTBT	BGTC	Au	0.87	5×10^6	TLM
C8-BTBT	BGTC	FeCl3/Au	7.0	8.8×10^3	TLM
C8-BTBT	BGTC	Au	3.4	2×10^5	TLM
P3HT	BGBC	Au	-	1×10^4	TLM
P3HT	BGBC	Cu	-	3×10^6	TLM
P3HT	BGBC	Cr	-	1×10^5	TLM
P3HT	BGBC	Au	-	$< 5 \times 10^3$	KPM
P3HT	BGBC	Ag	-	2×10^4	KPM
P3HT	BGBC	Cu	-	3×10^5	KPM
P3HT	BGBC	Cr	-	5×10^6	KPM
F8T2	BGBC	Au	-	1×10^7	KPM
F8T2	BGBC	Cr/Au	-	$> 7 \times 10^7$	KPM
P3HT	TGBC	Au	0.5	4	gFP/TLM
F8T2	TGBC	Au	0.04	14	gFP/TLM
PBTTT	TGBC	Au	-	4	gFP

Table 1.1 Survey of contact resistance values together with mobility and measurement methods in OFETs with different solution-processed organic semiconductors, device architecture, contact materials and treatments, from [53, 92, 97, 103, 104]

Table 1.1 shows a collection of contact resistance values measured in OFETs using different solution-deposited polymeric semiconductors, device structures, metal contacts (with and without treatments with SAMs) and methods. From this survey it results that for OFETs operating with standard gate dielectric, typical values of R_C are always on the order of some $\text{k}\Omega\cdot\text{cm}$. The lowest R_C value of $6.5 \text{ k}\Omega\cdot\text{cm}$ has been so far obtained for PBTTT devices with Au contacts deposited after OTS treatment of SiO_2 surface [102].

The record values for contact resistance have been measured in TGBC electrolyte-gated transistors, with ion gel as dielectric. In these devices R_C values as low as $4 \Omega\cdot\text{cm}$ have been reported for Au/P3HT [103] and Au/PBTTT interfaces [104].

These values are at least three orders of magnitude lower than those reported for devices with standard dielectric layers. Such low R_C can be achieved by the electrochemical doping that assists charge injection by reducing the carriers crowding at the interface through the compensation of the ions. Therefore, electrolyte-gated OFETs represent an optimal template to lower the contact resistance at the metal/OSC interface which is a prerequisite for OFETs downscaling and, as it will be explained in the next chapter, for organic spintronics devices.

1.4.6 Downscaling of OFETs: the short channel effects

One of the main aspects for improving the OFETs performances, that still needs to be fully explored, is the miniaturization of the device dimensions and, in particular, the downscaling of the channel length L , which is currently into the submicrometer scale. However, with the progress of fabrication processes, devices with channel lengths smaller than 100 nm have been achieved using techniques such as photolithography [105, 106], electron-beam lithography [107, 108, 109, 80, 110], nanoimprint lithography [111], inject printing [112, 113, 114] and mask-free photolithography [115].

In principle, since both packing density and linear regime cut-off frequency (f) scale as $1/L^2$ [116]

$$\text{Packing Density} \propto \frac{1}{L^2} \quad (25)$$

$$f = \frac{\mu V_{SD}}{2\pi L^2} \quad (26)$$

where μ is the field-effect mobility and V_{SD} is the drain–source voltage, the decreasing of the channel length should improve the device performances by increasing the operational frequency and the number of devices integrated in the circuits.

However, many of the reported OFETs with sub–micrometer channels have shown deteriorated, instead of improved, current-voltage characteristics that deviate from the ideal, long-channel behavior, and are referred to as short-channel effects [116, 117, 118, 119]. Short channel effects have been reported in polymers [111, 120, 121, 122] and small molecules processed from solution [123] as well from ultra-high vacuum deposition [124, 125].

The equations introduced in Section 1.4.1 describing long channel OFETs behavior in the linear and saturation regime, are only valid under the gradual-channel approximation which says that the transverse electric field E_{ox} , generated by the applied gate voltage, needs to be much larger than the longitudinal electric field E_{SD} , induced between the source and drain electrodes by the applied drain voltage [117]:

$$E_{ox} = \frac{V_G}{t} \gg \frac{V_{SD}}{L} = E_{SD} \quad (27)$$

where V_G is the gate voltage and t is the dielectric layer thickness. This condition is valid for long channel transistors where the channel length is much larger than the dielectric layer thickness ($L > 10t$) [75, 76, 77].

For short channel OFETs the horizontal electric field dominates and the gradual-channel approximation is no longer valid. As a consequence, the depletion region associated with the source and drain junctions can now occupy a large fraction of the channel and eventually becomes comparable to the channel length as the drain voltage is increased. This leads to a reduction and drain voltage-dependence of the effective channel length. Since the drain current is inversely proportional to the channel length, the drain current will increase with the drain voltage resulting in channel-length modulation, that is, superlinear output curves without saturation above the pinch-off voltage and thus with a poor gate controllability [80]. The channel length modulation is defined by a non-zero channel conductance, g_d , where

$$g_d = \frac{\partial I_{SD}}{\partial V_{SD}} \neq 0 \quad (28)$$

The increase of the depletion region also reduces the required applied gate voltage to reach inversion and hence lowers the device threshold voltage, V_T (threshold voltage roll-off) [126]. Moreover the increased and drain-voltage dependent sub-threshold current will reduce the on/off current ratio leading to a degradation of the switching performance [127, 119, 128, 80, 129]. A space charge limited current (SCLC) will flow in the depletion region through the bulk of the OSC layer and not just in a limited region near the gate insulator [111, 130, 119, 128] which will give the transistor diode-like output characteristics. Finally, below a critical channel length, the contact resistance can dominate the resistance of the organic channel, so that the device is contact-limited [131, 93, 58]. Therefore, the gradual-channel approximation implies that for an adequate downscaling of the channel length it is essential to properly scale other device parameters, such as the gate-insulator thickness and the substrate doping concentration [117].

One way to suppress short channel effects is to decrease the longitudinal electric field by inserting an insulating mesa-like structure between source and drain electrodes [110, 108] or by using ultrathin gate dielectrics [132, 123]. Another possibility is to enhance the transverse electric field by reducing the film thickness using self-assembled monolayers (SAMs) [107].

Finally, as alternative to increase the transversal electric field, electrolytes as gate insulator are promising candidates. As a matter of fact, the small separation of the charges in the EDL (only a few angstroms) at the electrolyte/SC interface, provides a very high transverse electric field in the channel that suppresses short-channel effects. To our knowledge, only one report in short channel effects in electrolyte-gated transistors exists in the literature [133]. In chapter 5 we will present a complete study on short channel EGOFETs.

References

1. Waldrop, M. M. The chips are down for Moore's law. *Nature* **530**, 144–147 (2016).
2. Shirakawa, H., Louis, E. J., MacDiarmid, A. G., Chiang, C. K. & Heeger, A. J. Synthesis of electrically conducting organic polymers: halogen derivatives of polyacetylene, (CH)_x. *J. Chem. Soc. Chem. Commun.* 578 (1977). doi:10.1039/c39770000578
3. Street, R. A., Northrup, J. E. & Salleo, A. Transport in polycrystalline polymer thin-film transistors. *Phys. Rev. B* **71**, 165202 (2005).
4. Menard, E. *et al.* High-Performance n- and p-Type Single-Crystal Organic Transistors with Free-Space Gate Dielectrics. *Adv. Mater.* **16**, 2097–2101 (2004).
5. Jurchescu, O. D., Popinciuc, M., van Wees, B. J. & Palstra, T. T. M. Interface-Controlled, High-Mobility Organic Transistors. *Adv. Mater.* **19**, 688–692 (2007).
6. Hamadani, B. H., Gundlach, D. J., McCulloch, I. & Heeney, M. Undoped polythiophene field-effect transistors with mobility of 1cm²V⁻¹s⁻¹. *Appl. Phys. Lett.* **91**, 243512 (2007).
7. Noriega, R. *et al.* A general relationship between disorder, aggregation and charge transport in conjugated polymers. *Nat. Mater.* **12**, 1038–1044 (2013).
8. Kline, R. j., McGehee, M. d., Kadnikova, E. n., Liu, J. & Fréchet, J. m. j. Controlling the Field-Effect Mobility of Regioregular Polythiophene by Changing the Molecular Weight. *Adv. Mater.* **15**, 1519–1522 (2003).
9. Heeger, A. J. & Pethig, R. Charge Storage and Charge Transport in Conducting Polymers: Solitons, Polarons and Bipolarons [and Discussion]. *Philos. Trans. R. Soc. Lond. Math. Phys. Eng. Sci.* **314**, 17–35 (1985).
10. Austin, I. G. & Mott, N. F. Polarons in crystalline and non-crystalline materials. *Adv. Phys.* **18**, 41–102 (1969).
11. Bredas, J. L. & Street, G. B. Polarons, bipolarons, and solitons in conducting polymers. *Acc. Chem. Res.* **18**, 309–315 (1985).
12. Brédas, J. L., Wudl, F. & Heeger, A. J. Polarons and bipolarons in doped polythiophene: A theoretical investigation. *Solid State Commun.* **63**, 577–580 (1987).
13. Ren, J. F., Fu, J. Y., Liu, D. S., Mei, L. M. & Xie, S. J. Spin-polarized current in a ferromagnetic/organic system. *J. Appl. Phys.* **98**, 074503 (2005).
14. Anderson, P. W. Absence of Diffusion in Certain Random Lattices. *Phys. Rev.* **109**, 1492–1505 (1958).
15. Miller, A. & Abrahams, E. Impurity Conduction at Low Concentrations. *Phys. Rev.* **120**, 745–755 (1960).
16. Gill, W. D. Drift mobilities in amorphous charge-transfer complexes of trinitrofluorenone and poly-n-vinylcarbazole. *J. Appl. Phys.* **43**, 5033–5040 (1972).
17. Rubel, O., Baranovskii, S. D., Thomas, P. & Yamasaki, S. Concentration dependence of the hopping mobility in disordered organic solids. *Phys. Rev. B* **69**, 014206 (2004).
18. BäSSLer, H. Localized states and electronic transport in single component organic solids with diagonal disorder. *Phys. Status Solidi B* **107**, 9–54 (1981).
19. BäSSLer, H. Charge Transport in Disordered Organic Photoconductors a Monte Carlo Simulation Study. *Phys. Status Solidi B* **175**, 15–56 (1993).

20. Oelerich, J. O., Huemmer, D. & Baranovskii, S. D. How to Find Out the Density of States in Disordered Organic Semiconductors. *Phys. Rev. Lett.* **108**, 226403 (2012).
21. Baranovskii, S. D. Theoretical description of charge transport in disordered organic semiconductors. *Phys. Status Solidi B* **251**, 487–525 (2014).
22. Kador, L. Stochastic theory of inhomogeneous spectroscopic line shapes reinvestigated. *J. Chem. Phys.* **95**, 5574–5581 (1991).
23. Hoffmann, S. T. *et al.* Spectral diffusion in poly(p-phenylene)-type polymers with different energetic disorder. *Phys. Rev. B* **81**, 115103 (2010).
24. Movaghar, B., Grünewald, M., Ries, B., Bassler, H. & Würtz, D. Diffusion and relaxation of energy in disordered organic and inorganic materials. *Phys. Rev. B* **33**, 5545–5554 (1986).
25. Movaghar, B., Ries, B. & Grünewald, M. Diffusion and relaxation of energy in disordered systems: Departure from mean-field theories. *Phys. Rev. B* **34**, 5574–5582 (1986).
26. Shklovskii, B. I. & Efros, A. L. *Electronic Properties of Doped Semiconductors*. **45**, (Springer Berlin Heidelberg, 1984).
27. Mott, N., Pepper, M., Pollitt, S., Wallis, R. H. & Adkins, C. J. The Anderson Transition. *Proc. R. Soc. Lond. Math. Phys. Eng. Sci.* **345**, 169–205 (1975).
28. Mott, N. F. Conduction in non-crystalline systems IX. the minimum metallic conductivity. *Philos. Mag.* **26**, 1015–1026 (1972).
29. Wich, H. N. F. Mott. Metal-insulator transitions. Taylor & Francis Ltd., London 1974 XVI, 278 Seiten, 158 Figuren. Preis geb. \$ 6.50. *Krist. Tech.* **10**, K57–K58 (1975).
30. Dhoot, A. S. *et al.* Beyond the metal-insulator transition in polymer electrolyte gated polymer field-effect transistors. *Proc. Natl. Acad. Sci.* **103**, 11834–11837 (2006).
31. Ito, H., Harada, T., Tanaka, H. & Kuroda, S. Critical regime for the insulator–metal transition in highly ordered conjugated polymers gated with ionic liquid. *Jpn. J. Appl. Phys.* **55**, 03DC08 (2016).
32. Tanaka, H., Nishio, S., Ito, H. & Kuroda, S. Microscopic signature of insulator-to-metal transition in highly doped semicrystalline conducting polymers in ionic-liquid-gated transistors. *Appl. Phys. Lett.* **107**, 243302 (2015).
33. Tanaka, H., Hirate, M., Watanabe, S. & Kuroda, S. Microscopic Signature of Metallic State in Semicrystalline Conjugated Polymers Doped with Fluoroalkylsilane Molecules. *Adv. Mater.* **26**, 2376–2383 (2014).
34. Mott, N. F. Conduction in glasses containing transition metal ions. *J. Non-Cryst. Solids* **1**, 1–17 (1968).
35. Lien, C.-C., Wu, C.-Y., Li, Z.-Q. & Lin, J.-J. Electrical conduction processes in ZnO in a wide temperature range 20–500 K. *J. Appl. Phys.* **110**, 063706 (2011).
36. Menon, R., Yoon, C. O., Moses, D., Heeger, A. J. & Cao, Y. Transport in polyaniline near the critical regime of the metal-insulator transition. *Phys. Rev. B* **48**, 17685–17694 (1993).
37. Ahlskog, M., Menon, R., Heeger, A. J., Noguchi, T. & Ohnishi, T. Metal-insulator transition in oriented poly(p-phenylenevinylene). *Phys. Rev. B* **55**, 6777–6787 (1997).

38. Panzer, M. J. & Frisbie, C. D. High Carrier Density and Metallic Conductivity in Poly(3-hexylthiophene) Achieved by Electrostatic Charge Injection. *Adv. Funct. Mater.* **16**, 1051–1056 (2006).
39. Lee, K. *et al.* Metallic transport in polyaniline. *Nature* **441**, 65–68 (2006).
40. Chiang, C. K. *et al.* Electrical Conductivity in Doped Polyacetylene. *Phys. Rev. Lett.* **39**, 1098–1101 (1977).
41. Reghu, M., Cao, Y., Moses, D. & Heeger, A. J. Counterion-induced processibility of polyaniline: Transport at the metal-insulator boundary. *Phys. Rev. B* **47**, 1758–1764 (1993).
42. Kohlman, R. S. *et al.* Limits for Metallic Conductivity in Conducting Polymers. *Phys. Rev. Lett.* **78**, 3915–3918 (1997).
43. Lee, K. *et al.* Nature of the Metallic State in Conducting Polypyrrole. *Adv. Mater.* **10**, 456–459 (1998).
44. Hulea, I. N. *et al.* Wide Energy-Window View on the Density of States and Hole Mobility in Poly(β -Phenylene Vinylene). *Phys. Rev. Lett.* **93**, 166601 (2004).
45. Dhoot, A. S., Wang, G. M., Moses, D. & Heeger, A. J. Voltage-Induced Metal-Insulator Transition in Polythiophene Field-Effect Transistors. *Phys. Rev. Lett.* **96**, 246403 (2006).
46. Ueno, K. *et al.* Field-Induced Superconductivity in Electric Double Layer Transistors. *J. Phys. Soc. Jpn.* **83**, 032001 (2014).
47. Zanettini, S. *et al.* Magnetoconductance anisotropy of a polymer thin film at the onset of metallicity. *Appl. Phys. Lett.* **106**, 063303 (2015).
48. Mills, T., Kaake, L. G. & Zhu, X.-Y. Polaron and ion diffusion in a poly(3-hexylthiophene) thin-film transistor gated with polymer electrolyte dielectric. *Appl. Phys. A* **95**, 291–296 (2008).
49. Yuen, J. D. *et al.* Electrochemical Doping in Electrolyte-Gated Polymer Transistors. *J. Am. Chem. Soc.* **129**, 14367–14371 (2007).
50. Zhao, N. *et al.* Polaron Localization at Interfaces in High-Mobility Microcrystalline Conjugated Polymers. *Adv. Mater.* **21**, 3759–3763 (2009).
51. Cornil, J. & Brédas, J.-L. Nature of the optical transitions in charged oligothiophenes. *Adv. Mater.* **7**, 295–297 (1995).
52. Furukawa, Y. Electronic Absorption and Vibrational Spectroscopies of Conjugated Conducting Polymers. *J. Phys. Chem.* **100**, 15644–15653 (1996).
53. Natali, D. & Caironi, M. Charge Injection in Solution-Processed Organic Field-Effect Transistors: Physics, Models and Characterization Methods. *Adv. Mater.* **24**, 1357–1387 (2012).
54. Concepts in Photoconductivity and Allied Problems (Interscience Tracts on Physics and Astronomy, Number 19) by Rose, Albert: Interscience Publishers - Zubal-Books.
55. Arkhipov, V. I., Wolf, U. & Bäessler, H. Current injection from a metal to a disordered hopping system. II. Comparison between analytic theory and simulation. *Phys. Rev. B* **59**, 7514–7520 (1999).
56. Sze, S. M. & Ng, K. K. *Physics of Semiconductor Devices*. (John Wiley & Sons, 2006).
57. Simmons, J. G. Richardson-Schottky Effect in Solids. *Phys. Rev. Lett.* **15**, 967–968 (1965).

58. Hamadani, B. H. & Natelson, D. Temperature-dependent contact resistances in high-quality polymer field-effect transistors. *Appl. Phys. Lett.* **84**, 443–445 (2004).
59. Wolf, U., Arkhipov, V. I. & Bässler, H. Current injection from a metal to a disordered hopping system. I. Monte Carlo simulation. *Phys. Rev. B* **59**, 7507–7513 (1999).
60. Barth, S. *et al.* Current injection from a metal to a disordered hopping system. III. Comparison between experiment and Monte Carlo simulation. *Phys. Rev. B* **60**, 8791–8797 (1999).
61. Blossey, D. F. One-dimensional Onsager theory for carrier injection in metal-insulator systems. *Phys. Rev. B* **9**, 5183–5187 (1974).
62. Arkhipov, V. I., Emelianova, E. V., Tak, Y. H. & Bässler, H. Charge injection into light-emitting diodes: Theory and experiment. *J. Appl. Phys.* **84**, 848–856 (1998).
63. Cheng, X. *et al.* Controlling Electron and Hole Charge Injection in Ambipolar Organic Field-Effect Transistors by Self-Assembled Monolayers. *Adv. Funct. Mater.* **19**, 2407–2415 (2009).
64. Sirringhaus, H., Tessler, N. & Friend, R. H. Integrated Optoelectronic Devices Based on Conjugated Polymers. *Science* **280**, 1741–1744 (1998).
65. Sirringhaus, H. *et al.* Two-dimensional charge transport in self-organized, high-mobility conjugated polymers. *Nature* **401**, 685–688 (1999).
66. Salleo, A., Chabinyc, M. L., Yang, M. S. & Street, R. A. Polymer thin-film transistors with chemically modified dielectric interfaces. *Appl. Phys. Lett.* **81**, 4383–4385 (2002).
67. Ishii, H., Sugiyama, K., Ito, E. & Seki, K. Energy Level Alignment and Interfacial Electronic Structures at Organic/Metal and Organic/Organic Interfaces. *Adv. Mater.* **11**, 605–625 (1999).
68. Rep, D. B. A., Morpurgo, A. F. & Klapwijk, T. M. Doping-dependent charge injection into regioregular poly(3-hexylthiophene). *Org. Electron.* **4**, 201–207 (2003).
69. Hamadani, B. H., Ding, H., Gao, Y. & Natelson, D. Doping-dependent charge injection and band alignment in organic field-effect transistors. *Phys. Rev. B* **72**, 235302 (2005).
70. White, H. S., Kittleson, G. P. & Wrighton, M. S. Chemical derivatization of an array of three gold microelectrodes with polypyrrole: fabrication of a molecule-based transistor. *J. Am. Chem. Soc.* **106**, 5375–5377 (1984).
71. Tsumura, A., Koezuka, H. & Ando, T. Macromolecular electronic device: Field-effect transistor with a polythiophene thin film. *Appl. Phys. Lett.* **49**, 1210–1212 (1986).
72. Dimitrakopoulos, C. D., Purushothaman, S., Kymissis, J., Callegari, A. & Shaw, J. M. Low-Voltage Organic Transistors on Plastic Comprising High-Dielectric Constant Gate Insulators. *Science* **283**, 822–824 (1999).
73. Bartic, C., Jansen, H., Campitelli, A. & Borghs, S. Ta₂O₅ as gate dielectric material for low-voltage organic thin-film transistors. *Org. Electron.* **3**, 65–72 (2002).
74. Wang, G. *et al.* Poly(3-hexylthiophene) field-effect transistors with high dielectric constant gate insulator. *J. Appl. Phys.* **95**, 316–322 (2004).
75. Chua, L.-L., Ho, P. K. H., Sirringhaus, H. & Friend, R. H. High-stability ultrathin spin-on benzocyclobutene gate dielectric for polymer field-effect transistors. *Appl. Phys. Lett.* **84**, 3400–3402 (2004).

76. Noh, Y.-Y., Zhao, N., Caironi, M. & Sirringhaus, H. Downscaling of self-aligned, all-printed polymer thin-film transistors. *Nat. Nanotechnol.* **2**, 784–789 (2007).
77. Bürgi, L., Pfeiffer, R. & Winnewisser, C. Submicrometer polymer transistors fabricated by a mask-free photolithographic self-alignment process. *Appl. Phys. Lett.* **92**, 153302 (2008).
78. Halik, M. *et al.* Polymer Gate Dielectrics and Conducting-Polymer Contacts for High-Performance Organic Thin-Film Transistors. *Adv. Mater.* **14**, 1717–1722 (2002).
79. Noh, Y.-Y. & Sirringhaus, H. Ultra-thin polymer gate dielectrics for top-gate polymer field-effect transistors. *Org. Electron.* **10**, 174–180 (2009).
80. Collet, J., Tharaud, O., Chapoton, A. & Vuillaume, D. Low-voltage, 30 nm channel length, organic transistors with a self-assembled monolayer as gate insulating films. *Appl. Phys. Lett.* **76**, 1941–1943 (2000).
81. Majewski, L. A., Schroeder, R. & Grell, M. Low-Voltage, High-Performance Organic Field-Effect Transistors with an Ultra-Thin TiO₂ Layer as Gate Insulator. *Adv. Funct. Mater.* **15**, 1017–1022 (2005).
82. Klauk, H., Zschieschang, U., Pflaum, J. & Halik, M. Ultralow-power organic complementary circuits. *Nature* **445**, 745–748 (2007).
83. Zaumseil, J. & Sirringhaus, H. Electron and Ambipolar Transport in Organic Field-Effect Transistors. *Chem. Rev.* **107**, 1296–1323 (2007).
84. Panzer, M. J. & Frisbie, C. D. Exploiting Ionic Coupling in Electronic Devices: Electrolyte-Gated Organic Field-Effect Transistors. *Adv. Mater.* **20**, 3177–3180 (2008).
85. Ono, S., Seki, S., Hirahara, R., Tominari, Y. & Takeya, J. High-mobility, low-power, and fast-switching organic field-effect transistors with ionic liquids. *Appl. Phys. Lett.* **92**, 103313 (2008).
86. Bäcklund, T. G., Österbacka, R., Stubb, H., Bobacka, J. & Ivaska, A. Operating principle of polymer insulator organic thin-film transistors exposed to moisture. *J. Appl. Phys.* **98**, 074504 (2005).
87. Laiho, A., Herlogsson, L., Forchheimer, R., Crispin, X. & Berggren, M. Controlling the dimensionality of charge transport in organic thin-film transistors. *Proc. Natl. Acad. Sci.* **108**, 15069–15073 (2011).
88. *Iontronics: Ionic Carriers in Organic Electronic Materials and Devices.* CRC Press (2010).
89. Ye, J. T. *et al.* Superconducting Dome in a Gate-Tuned Band Insulator. *Science* **338**, 1193–1196 (2012).
90. Ye, J. T. *et al.* Liquid-gated interface superconductivity on an atomically flat film. *Nat. Mater.* **9**, 125–128 (2010).
91. Bubnova, O., Berggren, M. & Crispin, X. Tuning the Thermoelectric Properties of Conducting Polymers in an Electrochemical Transistor. *J. Am. Chem. Soc.* **134**, 16456–16459 (2012).
92. Liu C., Xu Y., Noh Y.-Y. Contact engineering in organic field-effect transistors. *Materials Today* **18**, 79-96 (2015).
93. Necliudov, P. V., Shur, M. S., Gundlach, D. J. & Jackson, T. N. Contact resistance extraction in pentacene thin film transistors. *Solid-State Electron.* **47**, 259–262 (2003).

94. Meijer, E. J. *et al.* Scaling behavior and parasitic series resistance in disordered organic field-effect transistors. *Appl. Phys. Lett.* **82**, 4576–4578 (2003).
95. Minari, T., Miyadera, T., Tsukagoshi, K., Aoyagi, Y. & Ito, H. Charge injection process in organic field-effect transistors. *Appl. Phys. Lett.* **91**, 053508 (2007).
96. Liu, C. *et al.* Evaluating injection and transport properties of organic field-effect transistors by the convergence point in transfer-length method. *Appl. Phys. Lett.* **104**, 013301 (2014).
97. Organic Field-Effect Transistors. *CRC Press* (2007).
98. Chesterfield, R. J. *et al.* Variable temperature film and contact resistance measurements on operating n-channel organic thin film transistors. *J. Appl. Phys.* **95**, 6396–6405 (2004).
99. Pesavento, P. V., Chesterfield, R. J., Newman, C. R. & Frisbie, C. D. Gated four-probe measurements on pentacene thin-film transistors: Contact resistance as a function of gate voltage and temperature. *J. Appl. Phys.* **96**, 7312–7324 (2004).
100. Puntambekar, K. P., Pesavento, P. V. & Frisbie, C. D. Surface potential profiling and contact resistance measurements on operating pentacene thin-film transistors by Kelvin probe force microscopy. *Appl. Phys. Lett.* **83**, 5539–5541 (2003).
101. Bürgi, L., Richards, T. J., Friend, R. H. & Sirringhaus, H. Close look at charge carrier injection in polymer field-effect transistors. *J. Appl. Phys.* **94**, 6129–6137 (2003).
102. Umeda, T., Kumaki, D. & Tokito, S. Surface-energy-dependent field-effect mobilities up to 1 cm²/V s for polymer thin-film transistor. *J. Appl. Phys.* **105**, 024516 (2009).
103. Braga, D., Ha, M., Xie, W. & Frisbie, C. D. Ultralow contact resistance in electrolyte-gated organic thin film transistors. *Appl. Phys. Lett.* **97**, 193311 (2010).
104. Zanettini, S. *et al.* High conductivity organic thin films for spintronics: the interface resistance bottleneck. *J. Phys. Condens. Matter* **27**, 462001 (2015).
105. Prevot, P.-H., Alvares, D., Micolich, A., Lovell, N. & Ladouceur, F. An all-organic active pixel photosensor featuring ion-gel transistors. *J. Org. Semicond.* **3**, 8–13 (2015).
106. Di, C. *et al.* Noncoplanar organic field-effect transistor based on copper phthalocyanine. *Appl. Phys. Lett.* **88**, 121907 (2006).
107. Xu, Y., Liu, C., Khim, D. & Noh, Y.-Y. Development of high-performance printed organic field-effect transistors and integrated circuits. *Phys. Chem. Chem. Phys.* **17**, 26553–26574 (2015).
108. Du, H., Lin, X., Xu, Z. & Chu, D. Electric double-layer transistors: a review of recent progress. *J. Mater. Sci.* **50**, 5641–5673 (2015).
109. Handa, N. V., Serrano, A. V., Robb, M. J. & Hawker, C. J. Exploring the synthesis and impact of end-functional poly(3-hexylthiophene). *J. Polym. Sci. Part Polym. Chem.* **53**, 831–841 (2015).
110. Wang, J. Z., Zheng, Z. H. & Sirringhaus, H. Suppression of short-channel effects in organic thin-film transistors. *Appl. Phys. Lett.* **89**, 083513 (2006).
111. Austin, M. D. & Chou, S. Y. Fabrication of 70 nm channel length polymer organic thin-film transistors using nanoimprint lithography. *Appl. Phys. Lett.* **81**, 4431–4433 (2002).
112. Wu, G. & Xiao, H. Paste-type thin-film transistors based on self-supported chitosan membranes. *RSC Adv.* **5**, 105084–105089 (2015).

113. Senanayak, S. P. *et al.* Self-Assembled Nanodielectrics for High-Speed, Low-Voltage Solution-Processed Polymer Logic Circuits. *Adv. Electron. Mater.* **1**, n/a–n/a (2015).
114. Choi, J.-H., Xie, W., Gu, Y., Frisbie, C. D. & Lodge, T. P. Single Ion Conducting, Polymerized Ionic Liquid Triblock Copolymer Films: High Capacitance Electrolyte Gates for n-type Transistors. *ACS Appl. Mater. Interfaces* **7**, 7294–7302 (2015).
115. Liu, J. *et al.* Vertical polyelectrolyte-gated organic field-effect transistors. *Appl. Phys. Lett.* **97**, 103303 (2010).
116. Wiley: Physics of Semiconductor Devices, 3rd Edition - Simon M. Sze, Kwok K. Ng.
117. Operation and Modeling of the MOS Transistor - Hardcover - Yannis Tsididis; Colin McAndrew - Oxford University Press.
118. Pierret, R. F. *Semiconductor Device Fundamentals*. (Prentice Hall College Div, 1995).
119. Wang, H. *et al.* Solvent Effects on Polymer Sorting of Carbon Nanotubes with Applications in Printed Electronics. *Small* **11**, 126–133 (2015).
120. Chabinyk, M. L. *et al.* Short channel effects in regioregular poly(thiophene) thin film transistors. *J. Appl. Phys.* **96**, 2063–2070 (2004).
121. Xu, Y. & Berger, P. R. High electric-field effects on short-channel polythiophene polymer field-effect transistors. *J. Appl. Phys.* **95**, 1497–1501 (2004).
122. Chen, Y., Zhu, W. W., Xiao, S. & Shih, I. Fabrication of short channel organic thin film transistors by Si-etching method. *J. Vac. Sci. Technol. A* **22**, 768–770 (2004).
123. Kam, A. P. *et al.* Nanoimprinted organic field-effect transistors: fabrication, transfer mechanism and solvent effects on device characteristics. *Microelectron. Eng.* **73–74**, 809–813 (2004).
124. Leufgen, M. *et al.* Optimized sub-micron organic thin-film transistors: the influence of contacts and oxide thickness. *Synth. Met.* **146**, 341–345 (2004).
125. Torsi, L., Dodabalapur, A. & Katz, H. E. An analytical model for short-channel organic thin-film transistors. *J. Appl. Phys.* **78**, 1088–1093 (1995).
126. Yau, L. D. A simple theory to predict the threshold voltage of short-channel IGFET's. *Solid-State Electron.* **17**, 1059–1063 (1974).
127. Barron, M. B. Low level currents in insulated gate field effect transistors. *Solid-State Electron.* **15**, 293–302 (1972).
128. Chen, S.-H. *et al.* High performance electric-double-layer amorphous IGZO thin-film transistors gated with hydrated bovine serum albumin protein. *Org. Electron.* **24**, 200–204 (2015).
129. Fujimori, F. *et al.* Current transport in short channel top-contact pentacene field-effect transistors investigated with the selective molecular doping technique. *Appl. Phys. Lett.* **90**, 193507 (2007).
130. Haddock, J. N. *et al.* A comprehensive study of short channel effects in organic field-effect transistors. *Org. Electron.* **7**, 45–54 (2006).
131. Klauk, H. *et al.* Contact resistance in organic thin film transistors. *Solid-State Electron.* **47**, 297–301 (2003).
132. Tukagoshi, K. *et al.* Suppression of short channel effect in organic thin film transistors. *Appl. Phys. Lett.* **91**, 113508 (2007).

133. Herlogsson, L. *et al.* Downscaling of Organic Field-Effect Transistors with a Polyelectrolyte Gate Insulator. *Adv. Mater.* **20**, 4708–4713 (2008).

2

Organic spintronics

This chapter focuses on the fundamentals of spin injection, transport and detection in organic semiconductors. Issues related to device architecture, spin injection and detection with finite interface resistance and their implication to organic spintronics are also discussed.

2.1 Spintronics

Spin-based electronics, or more simply spintronics, is a research field aimed to exploit both electron charge and spin degree of freedom in solid state electronics.

The correlation between spin electron and charge transport has been observed for the first time in 1856 by William Thomson with the discovery of anisotropic magnetoresistance (AMR). He demonstrated that the electrical resistivity of a ferromagnet (FM) changes depending on the orientation and strength of an external applied magnetic field. In 1991 IBM commercialized magnetoresistive read head based on this effect [1].

The potential of using the electron's spin degree of freedom in electronic devices was first conceived in 1975 by Jullière through the discovery of the tunneling magnetoresistance (TMR) in the ferromagnet (FM)/insulator/superconductor magnetic tunnel junction (MTJ) [2]. In TMR devices, electrons tunnel from one electrode to another through the thin (1-3 nm) insulating oxide layer and the magnetoresistance (MR) effect is proportional to the interfacial density of states at the Fermi level of the two FM electrodes.

A couple of years after Tedrow et al. showed spin polarization in the ferromagnetic/insulator tunnel barrier [3]. The practical observation of TMR effect with high MR response (up to 30% at 4.2 K) was reported in 1995 using Al₂O₃ as insulating layer [4, 5]. Later in 2004, the discovery of spin filtering using magnesium oxide (MgO) as insulating layer, allowed to measure MR around 200% at room temperature [6, 7] and more recently MR up to 600% has been observed in the same devices [8].

In the late eighties, Fert [9] and Grünberg [10] independently proved the diffusion of spin polarized carriers through a non-magnetic (NM) metal spacer in contact with FM layers for an in-plane current and called this effect the giant magnetoresistance (GMR). GMR effect consists in a significant change in the electrical resistance of multilayered structures of magnetic and non-magnetic metallic thin films (initially Fe/Cr, then Co/Cu), depending on whether the magnetization of adjacent ferromagnetic layers is in a parallel or antiparallel alignment. The resistance is lowest when the magnetic moments of the FM layers are aligned and highest when they are anti-aligned. The alignment can be controlled, for example, by applying an external magnetic field. The current can flow either perpendicular to the interfaces between layers (Current Perpendicular to Plane, CPP), or parallel (Current In Plane, CIP). The relative MR can reach very high values and it was already 80% in the Fe/Cr multilayer used in the original work [9]. GMR effect is based on the dependence of electron scattering events on their spin orientation and it is strictly related to the multilayer structure.

This discovery was awarded with the Nobel Prize in 2007 and can be considered the beginning of the spin-based electronic.

The discovery of TMR and GMR in metallic spin valves devices has led to a revolution in magnetic memory and paved the way for future spin-logic devices. After the introduction of spin valve sensor in 1997 by IBM to replace the AMR sensor in magnetoresistive read heads, the growth rate for storage areal density immediately increased up to 100% per year. Nowadays, the most promising spintronic devices are the magnetoresistive random-access-memories (MRAM) based on spin torque transfer phenomena (STT-MRAM) which relies on spin-polarized electrons switching the resistance state of a memory cell without external magnetic field.

In order to continue the development in spintronics technology a deeper understanding of the mechanisms involved together with the investigation of new materials and techniques are needed. A promising alternative is represented by organic materials.

2.2 Organics for spintronics

As discussed in the previous chapter, OSCs offer many advantages for organic electronics such as low cost production, chemical engineering, and mechanical flexibility. Beyond these properties, organic materials have attracted much attention also for spintronics mainly because of their long spin-relaxation times, τ_s , which allow conservation and manipulation of the spin polarization of the carriers for very long times, typically ranging from 10^{-6} and 10^{-3} s and exceeding by several orders of magnitude the spin-relaxation times of inorganic materials. The long spin relaxation time in OSCs is a direct consequence of the weakness of the two major spin relaxation processes, namely the spin-orbit coupling (SOC) and the hyperfine interaction [11].

SOC describes the interaction between the electron spin and its orbital motion around an atomic nucleus. As SOC generally scales as the fourth power of the atomic number (Z^4) and organic materials consist mainly of low-Z materials (carbon, hydrogen, nitrogen, sulfur), spin-orbit coupling is usually small in most OSCs [12].

Hyperfine interaction results from the interaction of the spin of the injected carrier with the nuclear magnetic moments of the surrounding molecules. Due to the absence of magnetic moment in the ^{12}C nuclei (spin singlet), hyperfine interaction in OSCs mainly originates from H atoms (nuclear spin 1/2) bound to the carbon rings and is described by a

magnetic field of the order of 10 mT which causes the electron spin to precess [13]. Because the hyperfine field is random at every site, this precession will change in a random direction between hops, causing a loss of spin polarization. Hyperfine interaction can be overcome with a small external field, and this could be the origin of the organic magnetoresistance (OMAR) effect [14]. Because of the relatively large effects (up to 10-20%) at room temperature and small magnetic field (10 mT) OMAR is very interesting for applications.

Though OSCs are very promising for spintronics applications, the understanding of spin polarized carrier injection and transport properties in organic materials is still missing due to fundamental issues.

First, as already discussed in the previous chapter, carrier transport in organic materials is not band-type but involves hopping between neighboring energy sites. This hopping transport leads to low mobility and interaction with phonons, which limits the distance at which carriers can travel without losing their spin memory. This distance is quantified by the related spin diffusion length $l_{sf} = \sqrt{D \cdot \tau_s}$ which represents the distance that an electron can travel without losing its spin polarization. Since the carrier diffusion coefficient D is proportional to the carrier mobility μ ($D = \mu kT/e$), low mobility of OSCs can strongly limit their spin diffusion length which typically does not exceed 20 nm [11]. Therefore, even in the case where efficient spin injection into the organic layer is achieved there is still the problem of maintaining a spin-polarized current during the transport throughout the channel due to the short spin diffusion length.

Secondly, the gap between the Fermi level of the typical FM electrodes and the HOMO/LUMO levels of the organic materials in combination with a multi-step hopping process (see discussion in Chapter 1, Section 1.3.7) impedes the carrier injection (collection) and makes its spin dependent properties unknown.

Finally, there is the conductivity mismatch problem as a consequence of using high resistive OSC materials as spin transporting materials, in analogy to the same problem identified for inorganic semiconductors [15].

From this discussion it becomes clear that a big attention must be paid in the choice of the OSC material for the realization of organic spin valves in order to solve the key issues related to spin injection/detection and transport. In this perspective, high conducting (high mobility) OSCs represent an attractive approach since they are expected to exhibit long spin diffusion length and low contact resistance at the interface with ferromagnetic electrodes.

2.2.1 Spin valves: vertical vs. lateral geometry

The prototypical device in spintronics is the spin valve (SV) which consists of two ferromagnetic electrodes with different coercive fields (H_c) separated by a non-magnetic spacer. The role of the spacer is to decouple the two FM electrodes without hindering the spin transport through it. The resistance of such a device can be switched between two different states corresponding to parallel and anti-parallel magnetization of the FM electrodes. For organic spintronics the spacer is an organic semiconductor.

If the thickness of the OSC layer is thin enough so that electrons can tunnel through it (generally comparable with coherence length of the hopping process), then the device works in the tunneling regime (TMJ) [16, 17]. The typical thickness of such an organic tunneling barrier is around 2–3 nm or even less. In this case the conductance is only weakly temperature dependent, proportional to the device area, and it decays exponentially with the barrier thickness.

If the spacer is thicker we deal with injection devices in which there is a net flow of spin-polarized carriers directly into the electronic levels of the OSC [18]. Then the conductance is still proportional to the device area, but it scales as a power law with both the temperature and the spacer thickness.

SVs come in two different geometries: vertical one, where the FM electrodes and the OSC are vertically stacked, and lateral one, in which the FM electrodes and the OSC are laid out coplanarly. Both geometries have advantages and disadvantages.

Vertical SVs are well suited to study tunneling transport. However, although widely used [19, 20, 21, 22, 18, 23], this geometry suffers from many artifacts caused by the direct evaporation of the top metal electrode on top of the soft organic layer (see Figure 2.1). In this step, the hot atoms involved in the evaporation process diffuse through the OSC forming unwanted effects such as, diffusion and penetration of the metal atoms into the OSC [18, 19, 20], possible reaction with the organic molecules, radiation damage in the organic layer [24] and magnetic inclusions [25], which make the interface between the FM and OSC poorly defined and the measured sample thickness and area uncertain.

As an example, the so-called “ill-defined” layers up to distances of about 50-100 nm are routinely mentioned in the literature [18, 23]. Under these conditions, the hot atoms of the top electrode can reach the bottom electrode providing short circuit regime, or can reduce the gap between the two FM electrodes to the point that spin-polarized tunneling

between the FM electrodes may take place, resulting in tunneling magnetoresistance (TMR) as an alternative to the GMR effect in organic SVs.

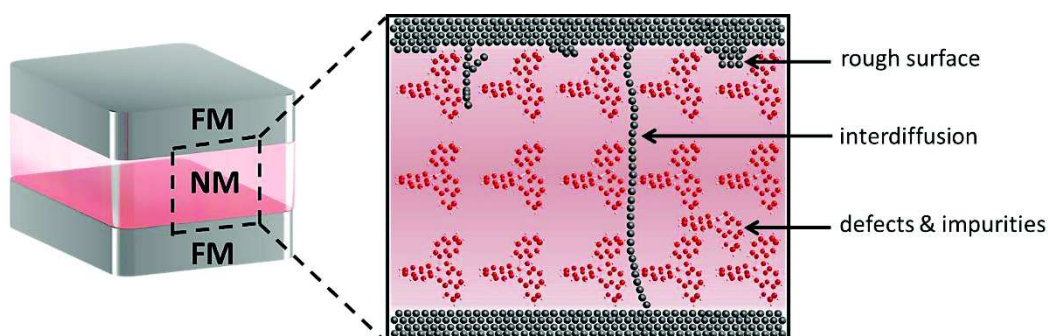


Figure 2.1 Schematic illustration of a conventional OSV in vertical geometry. The deposition of a FM layer onto the OSC is associated with interdiffusion of the metal atoms, rough surface, defects and impurities.

Recently, the difficulty in distinguishing between the magnetoresistance signature from a short-cut and the one due to transport through the organic channel has been demonstrated by Galbiati *et al.* [26] combining magnetoresistance and Inelastic Electron Tunneling Spectroscopy (IETS) measurements. They did a comparative study of two Co/Al₂O₃/tris[8-hydroxyquinoline]aluminium (Alq₃)/Co vertical devices, one well-defined (Sample 1 in Figure 2.2) and one short-cut (Sample 2), with a reference Co/Al₂O₃/Co inorganic device. Sample 1 and Sample 2 have been grown on the same wafer under the same conditions. As shown in Figure 2.2 (a) a MR of 20% is measured in the reference sample at T=2K and V=20mV. MR of ~8% and ~12% is also observed under the same conditions in Sample 1 and Sample 2, respectively. At the same time, from the IETS analysis of the three samples in Figure 2.2 (b), it results that the characteristic peaks related to molecular vibrational modes of Alq₃ are only present in the spectrum of Sample 1 (red curve), while the spectra of Sample 2 (blue curve) and the reference sample (black curve) are almost flat, indicating that the transport is occurring through the organic channel only in the Sample 1. This study reveals that the sole MR measurements of a device are not enough to discriminate between short-circuited and working devices, and that extreme attention has to be paid in the interpretation of the MR results observed for vertical devices with a tunnel barrier at the FM/OSC interface.

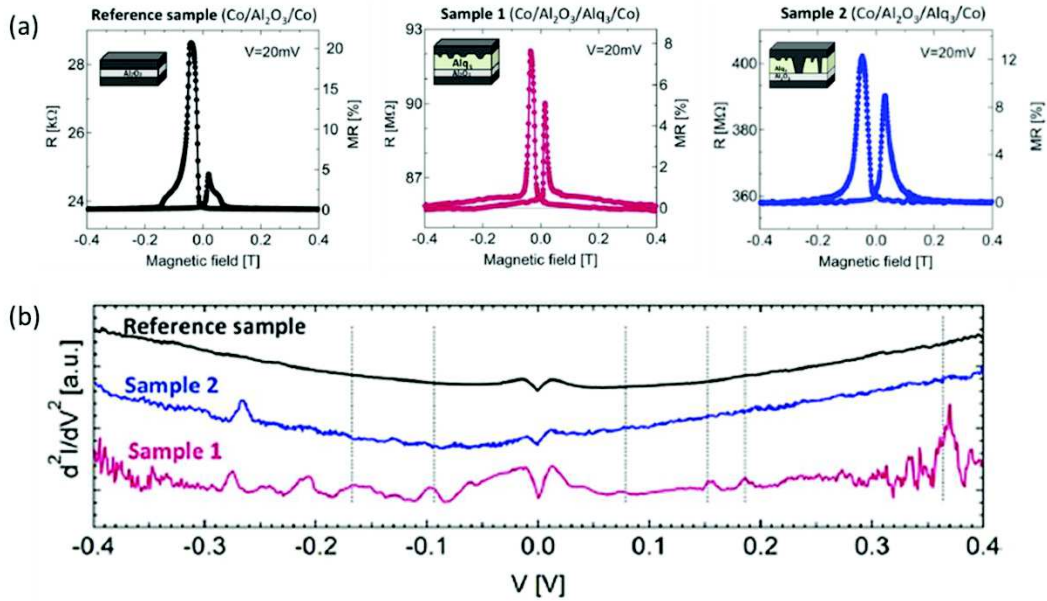


Figure 2.2 (a) Magnetoresistance curves of Co/Al₂O₃/Co (reference sample) and Co/Al₂O₃/Alq₃/Co (Sample 1 and Sample 2) junctions together with the schematic representation of the expected morphology of the top interface (inset); (b) Comparison of the IETS spectra for the reference sample (black curve), Sample 1 (red curve), and Sample 2 (blue curve). Reprinted from [26]

The ultra-high vacuum (UHV) physical deposition used to deposit the OSC films in vertical SVs also strongly limits the choice of molecules to the few that can be evaporated without breaking up.

Moreover, due to its high molecular weight, OSCs generally have rough surfaces. Therefore the OSC/top electrode interface is characterized by high roughness which determines stochastic magnetic properties of the FM electrodes [25].

All these artifacts in vertical SVs impact the reliability and reproducibility of the spin transport results and their interpretations, such as whether the measured MR signal originates from spin tunneling or injection into the OSC layer [27] or from magnetic inclusions coming from the electrode deposition [28, 23], are still intensely debated [18, 29, 30, 31, 28, 17, 32, 23, 19, 33, 34, 35, 36, 37, 38].

The logical step to overcome these limits is to use a lateral geometry, with spin injector/detector electrodes laying flat on a substrate at a distance t_N dictated by the spin diffusion length of the OSC, l_{sf}^{NM} , typically of the order of 100 nm or less [22, 20, 18, 39, 40]. As a matter of fact, the minimal requirement for a sizeable spin valve effect is that the gap separating the two FM electrodes should be in the limit $t_N \leq l_{sf}^{NM}$.

The fabrication of lateral SVs with gap down the 30 nm length scale is nowadays managed by nanolithography, e.g. e-beam lithography. The coercive fields of the contacts can be tuned in the same process step by making contacts with different widths [41, 42].

One of the main advantages of the lateral geometry over the vertical one is a better control over device parameters (e.g. geometry, channel length, interfacial roughness, channel length), which provides more choice in the materials and properties that can be studied. Thanks to its open architecture, the lateral geometry is also suited for external control or stimuli to the active organic channel properties using, for example, light (for optoelectronic investigations), electric and (electro)magnetic fields, pressure, chemical doping, resulting in devices that are capable of responding to multiple independent stimuli.

Another advantage of the planar structures is the possibility of tuning the transverse electrical field by implementing a third electrode (gate) to modulate the conductivity of the organic layer which may increase the mobility and thus, potentially impact the MR signal.

Moreover, it is possible to pattern more than two electrodes in order to access to the diffusive nature of spin signal by means of non-local measurements.

Finally, lateral structures are also well suited for wet processing of molecules and polymers in solutions and therefore allow to fully exploit the unending range of molecules offered by the chemical programmability of the physico-chemical properties of molecules undergoing hierarchical self-assembly in solutions and at surfaces.

However, so far only a limited number of experiments have been reported following this approach with results rare and inconclusive [43, 44, 45, 46, 47], difficult to interpret [48], or requiring specific FM electrodes, such as the half-metal ($\text{La}_{1-x}\text{Sr}_x\text{MnO}_3$) LSMO [49, 50, 51]. Moreover, the clearer experiment proving spin injection and spin transport in non-local SVs, namely the Hanle effect, has still not been observed in organic SVs [52, 53].

The first experiment on spin-based electronic devices with OSCs as spin-transporting material was carried out by Dediu and colleagues in 2002 in a lateral organic SV [54] (see Figure 2.3 (a)). The selected FM material was made of LSMO well known for its colossal magnetoresistive behavior and half-metallic properties (expected 100% spin polarization at 0 K), while sexithiophene (6T), a rigid conjugated oligomer rod, was chosen as channel. A strong magnetoresistance signal was recorded up to room temperature across 100 nm and 200 nm channels (Fig. 1b), while no MR was found for longer channels. The results were explained as an evidence of the conservation of the spin polarization of the injected carriers. Using the time-of-flight approach, a spin-relaxation time of the order of 1 μs was found.

However, since the coercivity of the two LSMO electrodes was almost the same, so that the device structure could not have parallel (on) and antiparallel (off) alignment of the magnetic layer, the observation of MR in this device was ambiguous and the measured signal could be likely attributed to AMR of the LSMO electrodes.

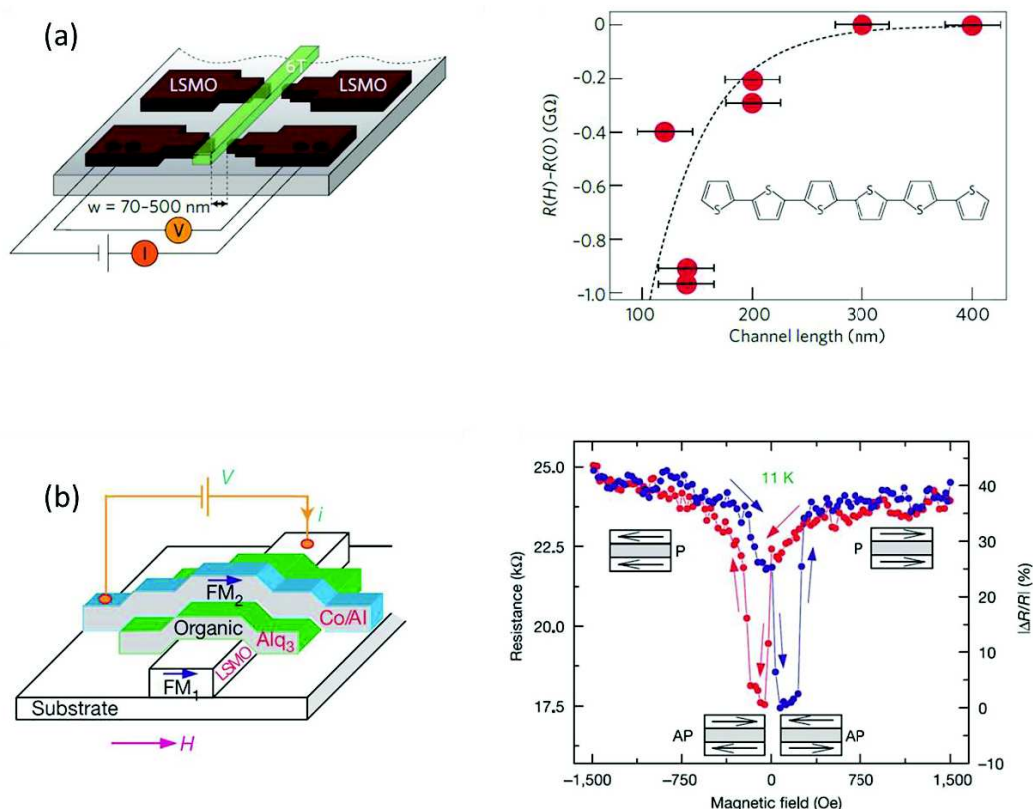


Figure 2.3 (a) Schematic structure of a lateral LSMO/T6/LSMO junction as published by Dediu *et al* [54] and the relative MR calculated as the difference between the device resistance subjected to a strong magnetic field and at zero magnetic field. The molecule of sexithiophene is also represented in the inset. Figure reprinted from [29]; (b) Schematic structure of a vertical LSMO/Alq₃/Co OSV together with the MR curve measured at 11 K. Figure reprinted from [18].

Two years later, Xiong *et al.* demonstrated GMR effects as high as 40% at low temperature and vanishing above 210–240 K in vertical SVs consisting of a thick (100–200 nm) layer of Alq₃ sandwiched between LSMO and cobalt electrodes [18] (Figure 2.3 (b)). In this case the uncertainty of the measured signal is due to the fact that Co can easily penetrate into Alq₃ layer up to about 100 nm leading to poor Co/Alq₃ interfaces.

After this report, most of the studies have been focused on Alq₃ [^{55, 56, 23, 57, 19, 39}]. An improvement in device operation was obtained by careful control of the ferromagnet/organic interface through the insertion of an insulating tunnel barrier between the Alq₃ and the top Co electrode, allowing room-temperature operation [²²].

All these pioneering experiments were performed using small molecules deposited in UHV conditions for the OSC growth. Spin-coated polymers such as region-random and region-regular poly(3-hexylthiophene) (RRaP3HT and RRP3HT, respectively) have also been employed in vertical spin valves showing (small values of) MR even at room temperature (OMAR) [^{55, 58}]. However, even in this case the possibility of short-cut from the top electrode makes these results unreliable specially when considering that all the attempts reported until now in lateral geometry using solution-processed polymers, have revealed unsuccessful results [^{43, 44, 47}].

2.2.2 Ferromagnetic surface oxidation

In the previous section we discussed the main disadvantages of vertical spin valve geometry over the lateral one. Actually, the lateral geometry also presents its own drawbacks.

A key limitation in lateral SV patterning process, still not discussed, is the chemical reactivity of the high Curie temperature transition metals such as Co, Ni, Fe (and their alloys) which are exposed to air before the OSC deposition. This chemical reactivity determines the formation of an oxide surface layer growing in environments containing more than 10⁻⁹ mbar partial pressure of oxygen or moisture. The possibly antiferromagnetic, ferromagnetic, or canted surface oxide (hydroxide) layer (e.g. CoO, NiO, Fe₂O₃) acts as strong spin scattering centers, mixing the spin polarization of the electrons and thus making the magnetic properties unpredictable. The resulting spin polarization of injected (collected) charges in (from) the OSC is therefore expected to strongly decrease, with related lack of reproducibility of the experimental results.

A solution to overcome this problem relies on using the half-metal magnetic oxide LSMO as electrode which is air stable. However, in this case the problem is the rapid decrease of the surface polarization when approaching room temperatures [^{59, 60}].

Another possibility is to passivate FM metal surfaces just before the organic layer deposition. To this purpose many different approaches, including coating with organic layers

[⁶¹, ⁶², ⁶³], polymers [⁶⁴, ⁶⁵], inert metals [⁶⁶] and even thiol-based monolayers [⁶⁷] have been employed. However, all these protective coatings modify the physical properties of the underlying metal, such as optical properties, electrical and thermal conductivity, and dimensions (due to the finite thickness of the coating). Moreover, thiolated self-assembly monolayers (SAMs) can only be assembled onto specific metals such as gold and copper, while are weakly stable on Ni and do not withstand temperatures higher than ~ 100 °C [⁶⁸].

At the same time, some experiments have demonstrated that graphene can act as a barrier against the metal surface oxidation without altering the interfacial properties. This has been proved first by Bunch *et al.* showing that single layer graphene films are impermeable to gas molecules, even to He [⁶⁹], and then by Chen *et al.* using graphene on top of copper and nickel/copper alloys surfaces to inhibit the oxidation [⁷⁰].

Actually, graphene seems to be a good candidate to passivate metal surface due to its unique characteristics. It is optically transparent in the visible wavelengths ($\sim 2.3\%$ of absorption per layer [⁷¹]), so it does not change the optical properties of the coated metal. It has exceptional thermal and chemical stability. Under an inert environment graphene is stable at temperatures as high as 1500 °C. It is electrically and thermally conductive, and it adds only 0.34 nm per layer [⁷²] to the total thickness of the underlying metal.

Recently, Dlubak *et al.* applied the graphene-passivation approach to Ni electrodes surface presenting it as a solution to the oxidation problem for spintronic applications [⁷³]. The process uses Ni electrodes as catalyst for the direct chemical vapor deposition (CVD) of graphene layers. In this way it is possible to pattern graphene directly on the electrodes. They show that the resulting graphene coating acts as an impermeable barrier against surface oxidation and as spin filter for spin transport in vertical devices. As it will be shown in the experimental part of this thesis, we used this approach to fabricate oxygen-free Ni electrodes.

2.2.3 Graphene- and graphite- passivated Ni electrodes: a source of spin-polarized electrons

Graphene-passivated FM electrodes may become useful in spintronics applications not only because graphene-coating inhibits the oxidation of FM electrodes but also because carbon coating, reaching several nm in thickness are considered as good candidates for spin

polarization currents injection or detection with graphite layers acting as almost perfect spin filter. This is due to two main properties.

First, the in-plane lattice constants of graphene and graphite match the surface lattice constants of fcc (111) and hcp (0001) Ni and Co almost perfectly, so that they share a common two-dimensional reciprocal space (Ni is particularly suitable with a lattice mismatch of only 1.3%). This matching reduces the number of defects due to the strain that otherwise limits the thickness of the tunnel barrier in vertical devices and degrades the efficiency of spin injection.

Second, the only electronic states at or close to the Fermi energy in graphene or graphite are to be found near to the high symmetry K point in reciprocal space where Co and Ni have only states with minority spin character. Therefore only the minority-spin channel can contribute to transmission from the FM surface into graphite, while majority spins have no direct conduction path and are filtered out. This is shown in Figure 2.4 where the Fermi-surface (FS) projection of graphite is compared with the projections of the FS of fcc and hcp Ni and Co onto close-packed planes (assuming perfect lattice matching at the interface). The Fermi surface of graphene is a point at the high-symmetry K point in the reciprocal space. The Fermi surfaces of graphite and doped graphene are centered on this point and close to it.

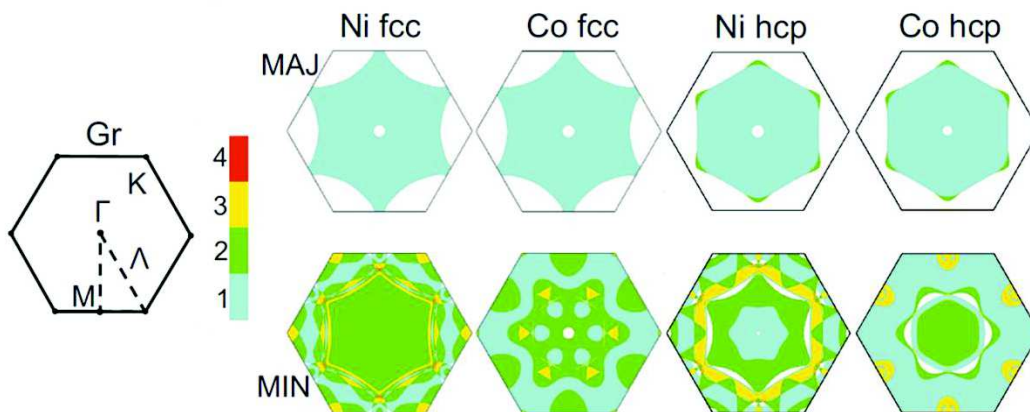


Figure 2.4 Fermi surface projections onto close-packed planes for majority and minority-spin states in fcc and hcp Ni and Co. For graphene and graphite, surface of constant energy are centered on the K point of the two-dimensional interface Brillouin zone. The number of FS sheets is shown by color bar. Reprinted from [74]

Based on these considerations, Karpan *et al.* [⁷⁵, ⁷⁴] predicted a large spin filtering at the interface between graphite and fcc or hcp Ni and Co. In their graphene spin-filter model, graphene (and/or graphite) is used as a channel for spin current transport between two FM electrodes.

In the current-perpendicular-to-plane (CPP) FM/Gr/FM (111) junctions studied by Karpan *et al.*, the electrons of the left electrode which are in regions of the reciprocal space far from the K point can reach the right electrode only by tunneling through the graphite. If the graphite film is thick enough to suppress the tunneling, majority-spin conductance will be quenched and only minority-spin conductance through the graphite will survive. In this case a perfect spin filtering will occur when the magnetizations of the FM electrodes are aligned in parallel (P), while the conductance will vanish for antiparallel (AP) alignment.

The spin filtering model proposed by Karpan *et al.* is quite insensitive to roughness and disorder. The spin polarization approaches to 100% for an ideal junction with number of layers >3, and it is only reduced to 70% for junction with large interface roughness or disorder.

Relying on the spin-filtering model of Karpan *et al.*, graphene has been integrated in Ni electrodes to realize a novel hybrid spin-based device as reported in several works. The pioneer of these series of experiments is the work of Dublak *et al.* [⁷⁶] where it is shown that the presence of graphene passivation layers is actually able to introduce a spin filtering effect together with a reversal of the spin polarization. Magneto-transport measurements performed on Ni(100nm)/graphene/Al₂O₃(1nm)/Co(15nm)/Au vertical stack at T= 1.4 K reveal a negative magneto-resistance MR= -10.8% explained in terms of filtering of majority spins by graphene coatings (Figure 2.5 (a)). They derive a large negative spin polarization for Ni/graphene P=-16%.

Martin *et al.* [⁷⁷] report on the same structure but using a thinner Al₂O₃ barrier (only 0.6 nm thick), deposited by atomic layer deposition (ALD). This stack enhances the spin-filtering effect of graphene leading to an almost fully inversed spin polarization for Ni electrode of -42% compared to the maximum reported value (P=+46% for the highest quality Ni/Al₂O₃ interfaces) [⁷⁸]. The relative MR, measured again at T= 1.4 K, is up to -31% (Figure 2.5 (b)).

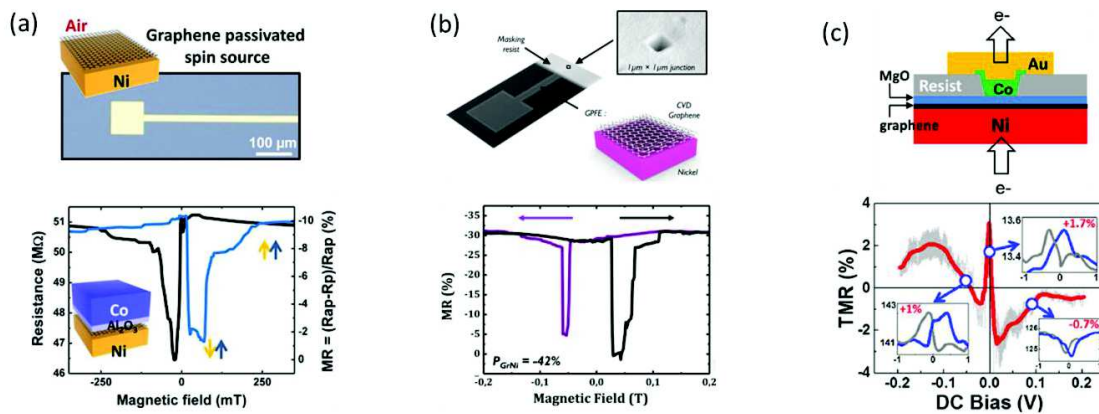


Figure 2.5 Schematic of the device and magneto-resistance signal for (a) Ni/graphene/Al₂O₃/Co and (b) Ni/graphene/MgO/Co vertical junctions. Reprinted from [76, 77, 79]

Godel *et al.* [79] studied the bias voltage dependence of the tunnel magnetoresistance (TMR) of an epitaxial (111)-oriented Ni(200nm)/graphene/MgO(3nm)/Co(50nm) tunnel junction at $T=1.5$ K. Differently from the previous works, where a negative MR was systematically observed, in this case the variation of the bias voltage leads to a reversal of the TMR sign (Figure 2.5(c)). The change in sign is explained in terms of opening/closing of spin-polarized conduction channels. Although these results are encouraging, the investigated samples are so far limited to tunneling inorganic devices made in UHV conditions.

2.3 Basics of spin transport in diffusive systems

The consequence of the exchange interaction in itinerant ferromagnetism is the splitting of the d orbitals in two spin sub-bands at the Fermi level causing an imbalance between the spin-dependent density of states (DOS). As a result the spin-up and spin-down electrons have different Fermi velocities and mean-free paths, and thus different conductivities ($\sigma_{\uparrow} \neq \sigma_{\downarrow}$) [80].

Therefore, the conduction in a FM metal can be figured out as consisted of spin-up and spin-down currents independently carried by two parallel channels as proposed by Mott in his two current model [81] and experimentally verified several decades later [82]. The basic assumption of this model is that the electron spin mean free path is much larger than the electronic mean free path so that electron can undergo several momentum scattering events before losing its spin information. As a result spin-up and spin-down in FM metals can be treated independently.

The spin polarization \mathbf{P} can be defined as the ratio of the spin current density $j_S = j_\uparrow - j_\downarrow$ and the charge current density $j = j_\uparrow + j_\downarrow$:

$$\mathbf{P} \stackrel{\text{def}}{=} \frac{j_\uparrow - j_\downarrow}{j_\uparrow + j_\downarrow} = \frac{\sigma_\uparrow - \sigma_\downarrow}{\sigma_\uparrow + \sigma_\downarrow} \quad (1)$$

Typical values for \mathbf{P} in conventional transition ferromagnetic metals are between 0.2 and 0.6 [83, 84, 85], while the bulk of a non-magnetic (NM) material ($\sigma_\uparrow = \sigma_\downarrow$) has $\mathbf{P} = 0$. This is shown in Figure 2.6(a) where the spin population in a FM/NM junction is presented. On the left side we have a sketch of the DOS of the FM in equilibrium with a shift of DOS for spin parallel and spin antiparallel to the magnetization quantization axis (“majority spin” and “minority spin” in the usual notation) and an imbalance of DOS at the Fermi energy level E_F .

2.3.1 Spin injection: conductance mismatch problem

When a FM/NM interface is formed the spin imbalance of the FM is transported into the NM and the system goes out of thermodynamical equilibrium. If electrons are sent from the FM into the NM, they feel a sudden change in spin-dependent electrical conductivity. Consequently, a spin accumulation zone is formed due to the pile-up of imbalance of electron spins (Figure 2.6 (b)). Nevertheless, away from the interface, and more precisely in the bulk of the NM material, the current densities j_\uparrow and j_\downarrow must be equal.

The necessary condition to adjust the incoming and outgoing spin fluxes requires that, in the area near the interface, more electrons from the spin-up channel flip their spin to get to the spin-down channel. This occurs through an “accumulation” of spin-up electrons, that is, a splitting of the E_F -up and E_F -down Fermi energies. This splitting of the Fermi levels is represented by the variation of the electrochemical potential for both spin species μ_\uparrow and μ_\downarrow , so that the spin accumulation is defined as $\Delta\mu = \mu_\uparrow - \mu_\downarrow$. The spin accumulation $\Delta\mu$ is maximal at the FM/NM interface, due to the Fermi level splitting, and decays exponentially on each side of the interface on the scale of the respective spin diffusion lengths l_{sf}^{FM} and l_{sf}^{NM} . Therefore, the progressive depolarization of the current is related to the spin flips events.

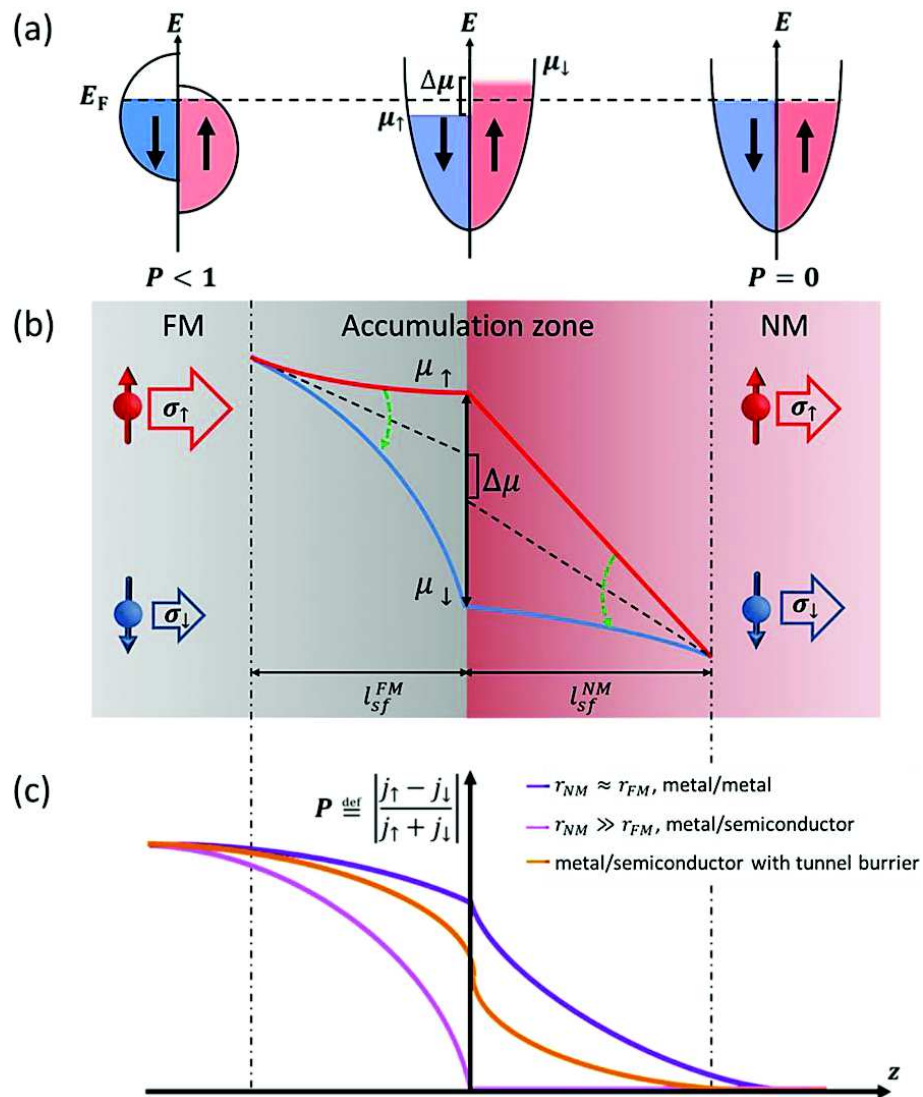


Figure 2.6 (a) Schematic representation of the DOS of the 3d sub-bands band structure in a FM metal showing the energy band spin splitting due to the exchange energy (left); of the s sub-bands in a NM material in equilibrium (right) and in a NM material close to the interface when an electron current is flowing from the FM into the NM (center). The difference in DOS can be maintained in the SC within a distance l_{sf}^{NM} from the interface (center). At bigger distances spins randomize and the DOS for spin up and spin down are equals (right). (b) Schematic representation of the splitting of the electrochemical potentials μ_{\uparrow} and μ_{\downarrow} at the FM/NM interface without contact resistance (transparent interface). The black dashed lines are the asymptotes of the electrochemical potentials to which they would collapse at large distances. The green dashed arrows symbolize the spin flips caused by the spin-split out of equilibrium. These spin flips control the progressive depolarization of the electron current between the left and the right sides. l_{sf}^{FM} and l_{sf}^{NM} are the spin diffusion length of the FM and the NM, respectively. (c) Variation of the spin polarized current as a function of the length-dimension z for three different situations: when there is an approximate balance between the spin flips on both sides, that is FM/metal (violet), when the spin flips on the left side are predominant, that is FM/SC without spin-dependent interface resistance (pink), and FM/SC with a tunnel barrier (orange). Adapted from [86]

Regarding the spin polarization of the current \mathbf{P} , in the accumulation zone, it decreases progressively going from the FM layer to the NM one, so that a spin-polarized current is “injected” into a NM material. This is shown in Figure 2.6 (c) in the case of an approximate balance between the spin-flips on both sides (metal/metal) and when the spin flips on the left side are predominant (metal/SC without spin-dependent interface resistance, for example). Actually, even with an ideal polarization, $\mathbf{P} = 1$, and no scattering at the interface, the polarization of the current at the point of injection in the NM material, can vanish simply for the particular resistances involved in the device. As a matter of fact, the spin-flip (spin relaxation) rate at the interface is inversely proportional to the spin impedances of the FM and NM materials r_F and r_N , respectively

$$|Spin\ flip\ rate|_{FM} \sim \frac{\Delta\mu}{r_F} \left(= \frac{\Delta\mu}{\rho_{FM} \cdot l_{sf}^{FM}} \right) \quad (2)$$

and

$$|Spin\ flip\ rate|_{NM} \sim \frac{\Delta\mu}{r_N} \left(= \frac{\Delta\mu}{\rho_{NM} \cdot l_{sf}^{NM}} \right) \quad (3)$$

with ρ_{FM} and ρ_{NM} the resistivity of the FM and NM materials, respectively. Thus it is clear now to understand that if $r_{NM} \approx r_{FM}$ (like in the case of metal/metal), we will observe the same number of spin flips on both side of the interface. Therefore a part of the spin polarization is retained in the NM material. By contrast, if $r_N \gg r_F$ (like in the case of metal/SC), then there are much more spin-flips, that is, a stronger depolarization of the current in the FM than in that NM and the current is already completely depolarized when it crosses the interface.

Quantitatively, it can be shown that the polarization of the current at the interface is [15]:

$$P = \frac{J_{\uparrow} - J_{\downarrow}}{J_{\uparrow} + J_{\downarrow}} = \frac{\beta}{1 + \frac{r_N}{r_F}} \quad (4)$$

where β is the bulk asymmetry coefficient of the FM electrodes. When both FM and NM are metals ($r_N \approx r_F$), the spin polarization of the current entering the SC is only moderately

reduced from its value β inside the FM. In contrast, when r_N is much larger than r_F , the spin polarization at the interface is reduced of about $\beta r_F/r_N$ so that there will be a negligible polarization in the SC. This basic obstacle for the spin polarized current injection from a FM metal emitter into a semiconductor is called the conductivity mismatch problem and, at first glance, it seems insurmountable.

Schmidt *et al.* [87] were the first to raise this issue. They showed that the problem can be circumvented using a ferromagnetic SC. This solution is anyway limited to low temperatures due to the Curie temperatures of these materials much lower than room temperatures. Later, Rashba [88] and Fert and Jaffrès [15] suggested to implement a spin dependent interface resistance r_b^* (resistance in only one of the two channels or a high resistance in both spin channels, however, with a strong spin asymmetry) between the FM and SC materials. r_b^* is defined as $r_b^* = r_b/(1 - \gamma^2)$, where γ is the spin asymmetry coefficient and r_b is the interface resistance. Interface resistance, together with a significant spin asymmetry coefficient γ can be introduced both intentionally (e.g. tunnel barrier) or unintentionally (e.g. air oxidation).

3 for both, spin injection and detection, are well described in reference [15]. Spin dependent interface resistance introduces a spin dependent discontinuity on the spin accumulation at the interface, increasing the proportion of spin flips on the semiconductor side and shifting the depolarization from the metallic to the semiconductor side. This is possible if the interface resistance r_b^* exceeds a threshold value, r_1 , related to the resistivity and spin diffusion length of the semiconductor:

$$r_b^* \geq r_1 = r_N = \rho_{NM} \cdot l_{sf}^{NM} \quad (5)$$

With such a spin dependent interface resistance, the spin polarization of the current at the interface becomes:

$$P = \frac{J_{\uparrow} - J_{\downarrow}}{J_{\uparrow} + J_{\downarrow}} = \frac{\beta r_F + \gamma r_b^*}{r_F + r_N + r_b^*} \quad (6)$$

and then decreases exponentially as $\exp(-z/l_{sf}^{NM})$ on the NM side.

In the limit where $r_b^* \gg r_N$, spin polarization can be fully recovered and reach values as high as the spin asymmetry coefficient of the interface resistance γ . When $r_b^* \approx r_N$, the recovered spin polarization at the interface amounts to $\gamma/2$.

In conclusion, a very transparent interface is not beneficial for spin injection. A minimum value of interface resistance r_1 helps to enhance the proportion of spin flips on the semiconductor side and prevents spin escape and relaxation into the electrodes (also called backflow) in order to promote spin injection.

2.3.2 Spin detection: spin memory loss

The introduction of a spin dependent interface resistance between the FM contact and the semiconducting channel solves the problem of the spin polarized current injection through a single interface. Actually, real spin valve devices are made of two interfaces, as it is shown in the schematic of the Figure 2.7 (a), and successful injection of spin-polarized current into a NM material does not entail the spin detection by the second FM electrode.

In this case the problem is not only injecting a spin polarized current but also conserving a significant output signal, that is, a significant difference between the spin polarizations in the parallel (P) and antiparallel (AP) configurations of the FM electrodes to finally detect a significant difference between the resistances of the two configurations.

The magnetoresistance of the spin valve $\Delta R/R_P$, where $\Delta R = R_{AP} - R_P$ is the resistance change between AP and P magnetization configuration of the electrodes for the structure in Figure 2.7 (a), derived by Fert and Jaffres [15], can be summarized by considering the plot in Figure 2.7(b). The magnetoresistance is showed as a function of the r_b^* -to- r_{NM} ratio for different values of t_N/l_{sf}^{NM} (respectively 10^{-2} , 10, and 1, for the blue, black and red curves) where t_N is the length of the NM channel. It turns out that, although the current is polarized throughout the channel if its length t_N is smaller than the spin diffusion length l_{sf}^{NM} , this is not a sufficient condition to get the optimum output signal; which occurs only if, in addition, the interface resistance is smaller than a second threshold value, r_2 .

In other words, a spin diffusion length longer than the channel length is a necessary but not sufficient condition and spin injection/detection is obtained when the interfaces between the SC and the FM electrodes are spin dependent and chosen in a well-defined window centered at $r_b^*/r_N = 1$:

$$\rho_{NM} t_N = r_N \frac{t_N}{l_{sf}^{NM}} = r_1 \ll r_b^* \ll r_2 = r_N \frac{l_{sf}^{NM}}{t_N} = \rho_N \frac{(l_{sf}^{NM})^2}{t_N} \quad (7)$$

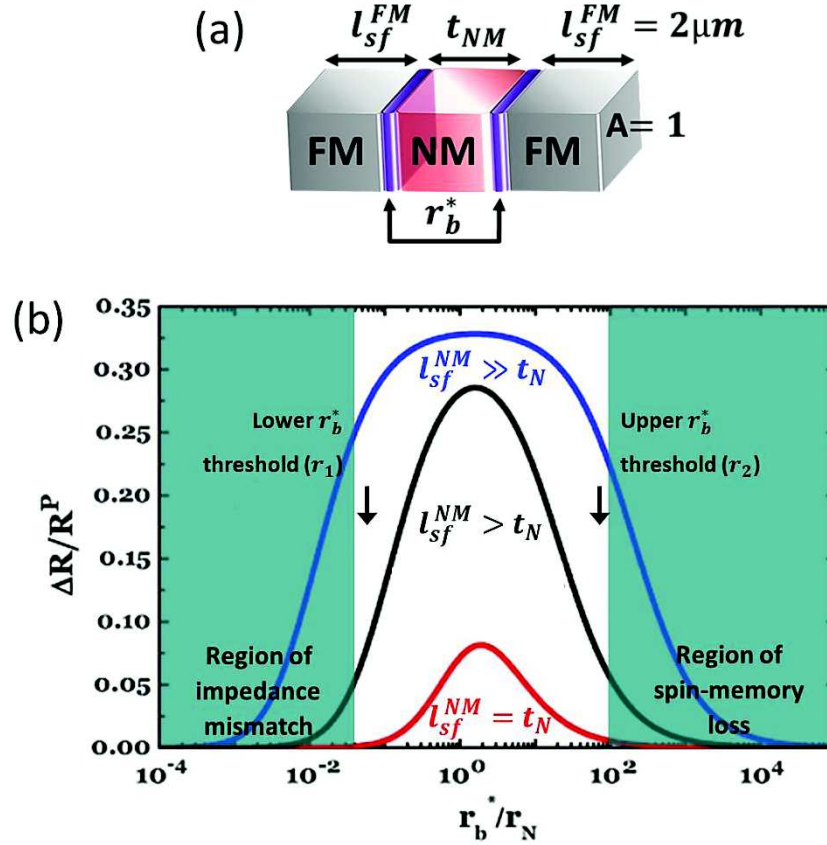


Figure 2.7 (a) Geometry of the calculated structure. (b) $\Delta R/R_P$ calculated for a structure of the type in (a) as a function of the ratio r_b^*/r_N for three different electrode spacing t_N (20 nm, 200 nm, and 2 μm) and for a fixed spin diffusion length $l_{sf}^{NM} = 2 \mu\text{m}$. The calculations have been performed for $F_1 = F_2 = \text{Co}$ ($r_F = 4.5 \times 10^{-15} \Omega\text{m}^2$, $\beta = 0.46$, $l_{sf}^{FM} = 60 \text{ nm}$); $\text{NM} = \text{SC}$ ($r_N = 4 \times 10^{-9} \Omega \cdot \text{cm}^2$, $l_{sf}^{NM} = 2 \mu\text{m}$) with $\gamma = 0.5$ for the spin asymmetry coefficient of the interface resistance. The optimal window for the MR signal is between a lower resistance r_1 and an upper resistance r_2 . Adapted from [15].

The ratio between t_N and l_{sf}^N defines the breadth of the window. The maximum of the magnetoresistance

$$\frac{\Delta R}{R_P} = \frac{\gamma^2}{1 - \gamma^2} \quad (8)$$

is only obtained for $l_{sf}^N \gg t_N$. When t_N increases and comes closer to l_{sf}^N , the maximum decreases as $\exp(-\frac{t_N}{l_{sf}^N})$. The window shrinks and disappears when l_{sf}^N becomes shorter than the length of the SC channel, t_N .

The condition corresponding to the lower edge of the window ($r_N \frac{t_N}{l_{sf}^N}$) is equivalent to the condition for spin injection through a single interface (see equation (5)) but less drastic with l_{sf}^N being replaced by the length t_N of the SC channel. The required value of r_b^* is smaller than in the case of injection through a single interface because, in P configuration, both FM electrodes, separated by only t_N , contribute to polarize the current. In the AP configuration, for a symmetric structure with also $l_{sf}^{NM} \gg t_N$, the current is non-polarized by symmetry and becomes polarized only when the structure is asymmetric.

The upper threshold r_2 is necessary because if the interface resistance is too high (exceeding r_2), the spin carriers will be reflected at the contacts and travel many times back and forth residing in the channel for a time longer than their spin flip time (dwell time bigger than the spin flip lifetime). In this way they lose their spin information before reaching the detector and the MR goes progressively to zero.

In conclusion, when the spin dependent interface resistance r_b^* is too low, the conductance mismatch prevents spin injection depolarizing the electron current before it reaches the interface; when it is too high, the dwell time of the carriers exceeds the spin lifetime so that the spin flips reduce the resistance of the AP state and thus the difference between the resistance of the on state (P) and off state (AP) is greatly reduced.

From this analysis and from what discussed in the previous chapter, it is clear how important is the role of the interface resistance in both organic electronics and organic spintronics devices. These discussions are the reason of the extensive study of contact resistance at the interface between metal/FM and OSC presented in the experimental part which constitutes most of this thesis work.

References

1. Moser, A. *et al.* Magnetic recording: advancing into the future. *J. Phys. Appl. Phys.* **35**, R157 (2002).
2. Julliere, M. Tunneling between ferromagnetic films. *Phys. Lett. A* **54**, 225–226 (1975).
3. Tedrow, P. M. & Meservey, R. Spin Polarization of Electrons Tunneling from Films of Fe, Co, Ni, and Gd. *Phys. Rev. B* **7**, 318–326 (1973).
4. Moodera, J. S., Kinder, L. R., Wong, T. M. & Meservey, R. Large Magnetoresistance at Room Temperature in Ferromagnetic Thin Film Tunnel Junctions. *Phys. Rev. Lett.* **74**, 3273–3276 (1995).
5. Miyazaki, T. & Tezuka, N. Giant magnetic tunneling effect in Fe/Al₂O₃/Fe junction. *J. Magn. Magn. Mater.* **139**, L231–L234 (1995).
6. Yuasa, S., Nagahama, T., Fukushima, A., Suzuki, Y. & Ando, K. Giant room-temperature magnetoresistance in single-crystal Fe/MgO/Fe magnetic tunnel junctions. *Nat. Mater.* **3**, 868–871 (2004).
7. Parkin, S. S. P. *et al.* Giant tunnelling magnetoresistance at room temperature with MgO (100) tunnel barriers. *Nat. Mater.* **3**, 862–867 (2004).
8. Ikeda, S. *et al.* Tunnel magnetoresistance of 604% at 300K by suppression of Ta diffusion in CoFeB/MgO/CoFeB pseudo-spin-valves annealed at high temperature. *Appl. Phys. Lett.* **93**, 082508 (2008).
9. Baibich, M. N. *et al.* Giant Magnetoresistance of (001)Fe/(001)Cr Magnetic Superlattices. *Phys. Rev. Lett.* **61**, 2472–2475 (1988).
10. Binasch, G., Grünberg, P., Saurenbach, F. & Zinn, W. Enhanced magnetoresistance in layered magnetic structures with antiferromagnetic interlayer exchange. *Phys. Rev. B* **39**, 4828–4830 (1989).
11. Szulczewski, G., Sanvito, S. & Coey, M. A spin of their own. *Nat. Mater.* **8**, 693–695 (2009).
12. McClure, D. S. Spin-Orbit Interaction in Aromatic Molecules. *J. Chem. Phys.* **20**, 682–686 (1952).
13. Wiley: NMR Spectroscopy: Basic Principles, Concepts and Applications in Chemistry, 3rd Edition - Harald Gunther.
14. Wagemans, W., Bloom, F. L., Bobbert, P. A., Wohlgenannt, M. & Koopmans, B. A two-site bipolaron model for organic magnetoresistance. *J. Appl. Phys.* **103**, 07F303 (2008).
15. Fert, A. & Jaffrès, H. Conditions for efficient spin injection from a ferromagnetic metal into a semiconductor. *Phys. Rev. B* **64**, 184420 (2001).
16. Shim, J. H. *et al.* Large Spin Diffusion Length in an Amorphous Organic Semiconductor. *Phys. Rev. Lett.* **100**, 226603 (2008).
17. Petta, J. R., Slater, S. K. & Ralph, D. C. Spin-Dependent Transport in Molecular Tunnel Junctions. *Phys. Rev. Lett.* **93**, 136601 (2004).
18. Xiong, Z. H., Wu, D., Vally Vardeny, Z. & Shi, J. Giant magnetoresistance in organic spin-valves. *Nature* **427**, 821–824 (2004).
19. Vinzelberg, H. *et al.* Low temperature tunneling magnetoresistance on (La,Sr)MnO₃/Co junctions with organic spacer layers. *J. Appl. Phys.* **103**, 093720 (2008).

20. Sun, D. *et al.* Giant Magnetoresistance in Organic Spin Valves. *Phys. Rev. Lett.* **104**, 236602 (2010).
21. Liu, C.-Y. *et al.* Interfacial studies of polymeric spin-valve structures. *Synth. Met.* **173**, 51–56 (2013).
22. Dediu, V. *et al.* Room-temperature spintronic effects in Alq_3 -based hybrid devices. *Phys. Rev. B* **78**, 115203 (2008).
23. Xu, W. *et al.* Tunneling magnetoresistance observed in $\text{La}_{0.67}\text{Sr}_{0.33}\text{MnO}_3$ /organic molecule/Co junctions. *Appl. Phys. Lett.* **90**, 072506 (2007).
24. Rybicki, J. *et al.* Tuning the Performance of Organic Spintronic Devices Using X-Ray Generated Traps. *Phys. Rev. Lett.* **109**, 076603 (2012).
25. Chan, Y.-L. *et al.* Magnetic Response of an Ultrathin Cobalt Film in Contact with an Organic Pentacene Layer. *Phys. Rev. Lett.* **104**, 177204 (2010).
26. Galbiati, M. *et al.* Is spin transport through molecules really occurring in organic spin valves? A combined magnetoresistance and inelastic electron tunnelling spectroscopy study. *Appl. Phys. Lett.* **106**, 082408 (2015).
27. Lin, R., Wang, F., Rybicki, J., Wohlgenannt, M. & Hutchinson, K. A. Distinguishing between tunneling and injection regimes of ferromagnet/organic semiconductor/ferromagnet junctions. *Phys. Rev. B* **81**, 195214 (2010).
28. Wang, F. J., Xiong, Z. H., Wu, D., Shi, J. & Vardeny, Z. V. Organic spintronics: The case of $\text{Fe}/\text{Alq}_3/\text{Co}$ spin-valve devices. *Synth. Met.* **155**, 172–175 (2005).
29. Dediu, V. A., Hueso, L. E., Bergenti, I. & Taliani, C. Spin routes in organic semiconductors. *Nat. Mater.* **8**, 707–716 (2009).
30. Vardeny, V. Spintronics: Organics strike back. *Nat. Mater.* **8**, 91–93 (2009).
31. Wang, F. & Vardeny, Z. V. Recent advances in organic spin-valve devices. *Synth. Met.* **160**, 210–215 (2010).
32. Wang, F. J., Yang, C. G., Vardeny, Z. V. & Li, X. G. Spin response in organic spin valves based on $\text{La}_{2/3}\text{Sr}_{1/3}\text{MnO}_3$ electrodes. *Phys. Rev. B* **75**, 245324 (2007).
33. Jiang, J. S., Pearson, J. E. & Bader, S. D. Absence of spin transport in the organic semiconductor Alq_3 . *Phys. Rev. B* **77**, 035303 (2008).
34. Yoo, J.-W. *et al.* Tunneling vs. giant magnetoresistance in organic spin valve. *Synth. Met.* **160**, 216–222 (2010).
35. Yoo, J.-W. *et al.* Giant magnetoresistance in ferromagnet/organic semiconductor/ferromagnet heterojunctions. *Phys. Rev. B* **80**, 205207 (2009).
36. Schoonus, J. J. H. M. *et al.* Magnetoresistance in Hybrid Organic Spin Valves at the Onset of Multiple-Step Tunneling. *Phys. Rev. Lett.* **103**, 146601 (2009).
37. Harmon, N. J. & Flatté, M. E. Spin-Flip Induced Magnetoresistance in Positionally Disordered Organic Solids. *Phys. Rev. Lett.* **108**, 186602 (2012).
38. Tran, T. L. A., Le, T. Q., Sanderink, J. G. M., van der Wiel, W. G. & de Jong, M. P. The Multistep Tunneling Analogue of Conductivity Mismatch in Organic Spin Valves. *Adv. Funct. Mater.* **22**, 1180–1189 (2012).
39. Santos, T. S. *et al.* Room-Temperature Tunnel Magnetoresistance and Spin-Polarized Tunneling through an Organic Semiconductor Barrier. *Phys. Rev. Lett.* **98**, 016601 (2007).

40. Nguyen, T. D. *et al.* Isotope effect in spin response of π -conjugated polymer films and devices. *Nat. Mater.* **9**, 345–352 (2010).
41. Michelfeit, M., Schmidt, G., Geurts, J. & Molenkamp, L. W. Organic field-effect transistors for spin-polarized transport. *Phys. Status Solidi A* **205**, 656–663 (2008).
42. Jedema, F. J., Filip, A. T. & van Wees, B. J. Electrical spin injection and accumulation at room temperature in an all-metal mesoscopic spin valve. *Nature* **410**, 345–348 (2001).
43. Kawasugi, Y., Ara, M., Ushirokita, H., Kamiya, T. & Tada, H. Preparation of lateral spin-valve structure using doped conducting polymer poly(3,4-ethylenedioxythiophene) poly(styrenesulfonate). *Org. Electron.* **14**, 1869–1873 (2013).
44. Alborghetti, S., Coey, J. M. D. & Stamenov, P. Electron and spin transport studies of gated lateral organic devices. *J. Appl. Phys.* **112**, 124510 (2012).
45. Naber, W. J. M. *et al.* Controlled tunnel-coupled ferromagnetic electrodes for spin injection in organic single-crystal transistors. *Org. Electron.* **11**, 743–747 (2010).
46. Michelfeit, M., Schmidt, G., Geurts, J. & Molenkamp, L. W. Organic field-effect transistors for spin-polarized transport. *Phys. Status Solidi A* **205**, 656–663 (2008).
47. Oliveira, T. V. A. G. de, Gobbi, M., Porro, J. M., Hueso, L. E. & Bittner, A. M. Charge and spin transport in PEDOT:PSS nanoscale lateral devices. *Nanotechnology* **24**, 475201 (2013).
48. Grünewald, M. *et al.* Large room-temperature magnetoresistance in lateral organic spin valves fabricated by in situ shadow evaporation. *Org. Electron.* **14**, 2082–2086 (2013).
49. Ikegami, T. *et al.* Planar-type spin valves based on low-molecular-weight organic materials with $\text{La}_{0.67}\text{Sr}_{0.33}\text{MnO}_3$ electrodes. *Appl. Phys. Lett.* **92**, 153304 (2008).
50. Ozbay, A. *et al.* Large magnetoresistance of thick polymer devices having $\text{La}_{0.67}\text{Sr}_{0.33}\text{MnO}_3$ electrodes. *Appl. Phys. Lett.* **95**, 232507 (2009).
51. Dediu, V., Murgia, M., Maticotta, F. C., Taliani, C. & Barbanera, S. Room temperature spin polarized injection in organic semiconductor. *Solid State Commun.* **122**, 181–184 (2002).
52. Riminucci, A. *et al.* Hanle effect missing in a prototypical organic spintronic device. *Appl. Phys. Lett.* **102**, 092407 (2013).
53. Grünewald, M. *et al.* Vertical organic spin valves in perpendicular magnetic fields. *Phys. Rev. B* **88**, 085319 (2013).
54. Dediu, V., Murgia, M., Maticotta, F. C., Taliani, C. & Barbanera, S. Room temperature spin polarized injection in organic semiconductor. *Solid State Commun.* **122**, 181–184 (2002).
55. Majumdar, S., Majumdar, H. S., Laiho, R. & Österbacka, R. Comparing small molecules and polymer for future organic spin-valves. *J. Alloys Compd.* **423**, 169–171 (2006).
56. Wang, F. J., Yang, C. G., Vardeny, Z. V. & Li, X. G. Spin response in organic spin valves based on $\text{La}_{2/3}\text{Sr}_{1/3}\text{MnO}_3$ electrodes. *Phys. Rev. B* **75**, 245324 (2007).
57. Hueso, L. E., Bergenti, I., Riminucci, A., Zhan, Y. Q. & Dediu, V. Multipurpose Magnetic Organic Hybrid Devices. *Adv. Mater.* **19**, 2639–2642 (2007).
58. Morley, N. A. *et al.* Room temperature organic spintronics. *J. Appl. Phys.* **103**, 07F306 (2008).

59. Park, J.-H. *et al.* Magnetic Properties at Surface Boundary of a Half-Metallic Ferromagnet $\text{La}_{0.7}\text{Sr}_{0.3}\text{MnO}_3$. *Phys. Rev. Lett.* **81**, 1953–1956 (1998).
60. Garcia, V. *et al.* Temperature dependence of the interfacial spin polarization of $\text{La}_{2/3}\text{Sr}_{1/3}\text{MnO}_3$. *Phys. Rev. B* **69**, 052403 (2004).
61. Gray, J. E. & Luan, B. Protective coatings on magnesium and its alloys — a critical review. *J. Alloys Compd.* **336**, 88–113 (2002).
62. Appa Rao, B. V., Yakub Iqbal, M. & Sreedhar, B. Self-assembled monolayer of 2-(octadecylthio)benzothiazole for corrosion protection of copper. *Corros. Sci.* **51**, 1441–1452 (2009).
63. Stratmann, M., Feser, R. & Leng, A. Corrosion protection by organic films. *Electrochimica Acta* **39**, 1207–1214 (1994).
64. Redondo, M. I. & Breslin, C. B. Polypyrrole electrodeposited on copper from an aqueous phosphate solution: Corrosion protection properties. *Corros. Sci.* **49**, 1765–1776 (2007).
65. Tallman, D. E., Spinks, G., Dominis, A. & Wallace, G. G. Electroactive conducting polymers for corrosion control. *J. Solid State Electrochem.* **6**, 73–84 (2001).
66. Pushpavanam, M., Raman, V. & Shenoi, B. A. Rhodium — Electrodeposition and applications. *Surf. Technol.* **12**, 351–360 (1981).
67. Lusk, A. T. & Jennings, G. K. Characterization of Self-Assembled Monolayers Formed from Sodium S-Alkyl Thiosulfates on Copper. *Langmuir* **17**, 7830–7836 (2001).
68. Sung, M. M., Sung, K., Kim, C. G., Lee, S. S. & Kim, Y. Self-Assembled Monolayers of Alkanethiols on Oxidized Copper Surfaces. *J. Phys. Chem. B* **104**, 2273–2277 (2000).
69. Bunch, J. S. *et al.* Impermeable Atomic Membranes from Graphene Sheets. *Nano Lett.* **8**, 2458–2462 (2008).
70. Chen, S. *et al.* Oxidation Resistance of Graphene-Coated Cu and Cu/Ni Alloy. *ACS Nano* **5**, 1321–1327 (2011).
71. Nair, R. R. *et al.* Fine Structure Constant Defines Visual Transparency of Graphene. *Science* **320**, 1308–1308 (2008).
72. Ni, Z. H. *et al.* Graphene Thickness Determination Using Reflection and Contrast Spectroscopy. *Nano Lett.* **7**, 2758–2763 (2007).
73. Dlubak, B. *et al.* Graphene-Passivated Nickel as an Oxidation-Resistant Electrode for Spintronics. *ACS Nano* **6**, 10930–10934 (2012).
74. Karpan, V. M. *et al.* Theoretical prediction of perfect spin filtering at interfaces between close-packed surfaces of Ni or Co and graphite or graphene. *Phys. Rev. B* **78**, (2008).
75. Karpan, V. M. *et al.* Graphite and Graphene as Perfect Spin Filters. *Phys. Rev. Lett.* **99**, 176602 (2007).
76. Dlubak, B. *et al.* Graphene-Passivated Nickel as an Oxidation-Resistant Electrode for Spintronics. *ACS Nano* **6**, 10930–10934 (2012).
77. Martin, M.-B. *et al.* Sub-nanometer Atomic Layer Deposition for Spintronics in Magnetic Tunnel Junctions Based on Graphene Spin-Filtering Membranes. *ACS Nano* **8**, 7890–7895 (2014).

-
78. Kim, T. H. & Moodera, J. S. Large spin polarization in epitaxial and polycrystalline Ni films. *Phys. Rev. B* **69**, 020403 (2004).
 79. Godel, F. *et al.* Voltage-controlled inversion of tunnel magnetoresistance in epitaxial Nickel/Graphene/MgO/Cobalt junctions. *Appl. Phys. Lett.* **105**, 152407 (2014).
 80. Blundell, S. *Magnetism in Condensed Matter*. (Oxford University Press, 2001).
 81. Mott, N. F. The Electrical Conductivity of Transition Metals. *Proc. R. Soc. Lond. Math. Phys. Eng. Sci.* **153**, 699–717 (1936).
 82. Fert, A. & Campbell, I. A. Two-Current Conduction in Nickel. *Phys. Rev. Lett.* **21**, 1190–1192 (1968).
 83. Tedrow, P. M. & Meservey, R. Spin Polarization of Electrons Tunneling from Films of Fe, Co, Ni, and Gd. *Phys. Rev. B* **7**, 318–326 (1973).
 84. Meservey, R. & Tedrow, P. M. Spin-polarized electron tunneling. *Phys. Rep.* **238**, 173–243 (1994).
 85. Moodera, J. S. & Mathon, G. Spin polarized tunneling in ferromagnetic junctions. *J. Magn. Magn. Mater.* **200**, 248–273 (1999).
 86. Fert, A., George, J.-M., Jaffres, H. & Mattana, R. Semiconductors Between Spin-Polarized Sources and Drains. *IEEE Trans. Electron Devices* **54**, 921–932 (2007).
 87. Schmidt, G., Ferrand, D., Molenkamp, L. W., Filip, A. T. & van Wees, B. J. Fundamental obstacle for electrical spin injection from a ferromagnetic metal into a diffusive semiconductor. *Phys. Rev. B* **62**, R4790–R4793 (2000).
 88. Rashba, E. I. Theory of electrical spin injection: Tunnel contacts as a solution of the conductivity mismatch problem. *Phys. Rev. B* **62**, R16267–R16270 (2000).

PART II

EXPERIMENTAL WORK

3

Carbon/Nickel interface characterization

This chapter is focused on the fabrication and characterization of carbon-passivated Nickel electrodes. Ultra-thin carbon films are grown on Ni electrodes by Chemical Vapor Deposition (CVD) and Rapid Thermal Annealing (RTA) as protective layer from the surface oxidation. Passivation is a prerogative when targeting spin-based devices where the oxide layers, spontaneously formed at the surface of the ferromagnetic electrodes, quench the spin signals at the interface with consequent reduction of the spin polarization of the injected (collected) charges. Chemical and composition analysis confirm that the carbon film strongly reduces the surface oxidation of the Ni.

3.1 Introduction

Ferromagnetic electrodes such as Fe, Ni and Co are of interest for extending organic electronics to spintronics applications. For such applications, magnetic electrodes are mandatory in order to inject (detect) spin polarized currents, and the use of transition magnetic metals is required for room temperature applications. One of the main drawbacks of these materials is their surface oxidation that randomizes their surface spin state. This is particularly critical for tunneling, highly sensitive to the material surface.

We rely on the literature on graphene synthesis over Ni, using this metal as a catalyst reporting that the resulting underlying Ni is oxidized when properly encapsulated by the carbon-based overlayer¹[²]. We take advantage of these recent findings motivated by the growing interest in graphene materials, in order to fabricate Ni electrodes passivated by ultra-thin amorphous carbon films, keeping in mind that we are looking for electrodes candidates for spin polarizing the charge currents.

3.2 Routes towards graphene

There are several methods to grow graphene (Figure 3.1) including: mechanical [³, ⁴] and chemical [⁵, ⁶] exfoliation; graphitization of SiC surfaces [⁷]; chemical vapor deposition (CVD)⁸, [¹⁰, ¹¹] and rapid thermal annealing (RTA)¹² [¹³, ¹⁴].

Exfoliation methods produce freestanding graphene isolated from any substrate which can be easily integrated with other materials. Mechanical exfoliation has been the first method used to prepare graphene and represents a easy and cheap process based on using adhesive tape that allows the fabrication of high quality graphene samples with very high electron mobility. However, it is very time consuming, generates only samples mostly only in the range of tens of micrometers and can be detected only on Si/SiO₂ substrates.

Chemical exfoliation is based on the separation of bulk graphite planes into individual graphene flakes. This can be done in solution either by pure ultrasonic cleavage or chemically assisted to make the separation more efficient. This leads to a stable suspension of graphene crystallites with submicrometer size.

Epitaxial growth from SiC is based on heating the SiC substrate at temperatures >1100 °C in ultrahigh vacuum so that Si sublimates and graphitization occurs on both the Si and C terminated surface. This method produces graphene with good mobility but it is limited to devices on SiC only.

Chemical vapor deposition (CVD) has emerged as one of the most promising and versatile methods for large area or patterned graphene growth directly on electronic devices without using any transfer process. The generic principle of CVD is to expose a catalyst substrate to a gaseous precursor at specific conditions (temperature, pressure, precursor species, etc.) for which the precursor dissociates on the catalyst. Therefore, during the process special care has to be taken to precisely control the resulting graphene layers due to its sensitivity to the various process parameters.

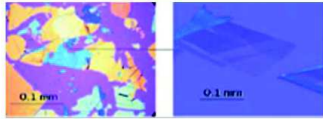
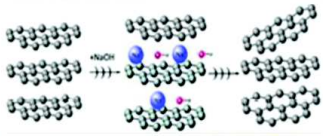
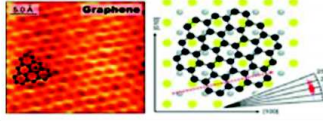
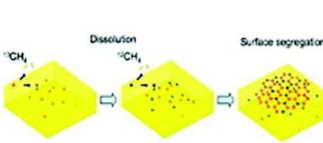
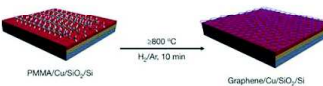
Methods		Schematic	Pros. & Cons.
Top Down	Mechanical Exfoliation (Scotch Tape)		<ul style="list-style-type: none"> High quality graphene Only lab. scale
	Chemical Exfoliation (Graphite → Go → RGO) (Graphite → Graphene)		<ul style="list-style-type: none"> Good dispersion in various solvents Large area processing Good adhesion for composite High defects density
Bottom Up	Epitaxial Growth (SiC wafer)		<ul style="list-style-type: none"> High quality graphene Only lab. scale
	CVD (Chemical Vapor Deposition)		<ul style="list-style-type: none"> Excellent electrical proprieties Large area processing Additional steps for composites Loss of quality during the transfer
	RTA (Rapid Thermal Annealing)		<ul style="list-style-type: none"> One step-process Complementary to CVD permitting lower temperature growth

Figure 3.1 Schematic of the principal methods used for graphene production.

Graphene can be grown by CVD on different metal substrates such as Ni, Co, Ru, Ir, Cu, etc. Among them, Ni and Cu have received most attention because of their cost, and wide use in the semiconductor industry. However, while large area of single layer graphene can be grown on Cu substrates [9], graphene growth on polycrystalline Ni substrates results in a wide variation in thickness from a monolayer to many layers [9, 10, 11, 16]. So far the formation of graphene monolayer has been reported only on epitaxially grown transition-metal

This process however will be difficult to be developed for industrial applications due to the high cost and limited scalability of single-crystal metal substrates [7, 18].

RTA stands as a method with strong similarities to CVD, which makes possible graphene growth at lower temperature using solid carbon precursors, such as polymer films and small molecules, deposited on the metal catalyst substrate.

Among all the methods described above, we chose CVD and RTA processes to grow graphene on top of Ni electrodes. The reason is that both processes allow the direct growth of graphene layers on the pre-patterned Ni electrodes integrated in our OFETs and both include a 'cleaning' step that removes the surface oxide of Ni prior to the carbon film growth.

In the next section a detailed description of CVD and RTA processes used in this thesis is provided.

3.3 Graphene growth methods: CVD vs. RTA

Direct graphene growth (i.e., not using any mechanical transfer procedure) on pre-patterned Ni electrodes was performed at the Korean Research Institute of Chemical Technology (KRICT) in Daejeon, South Korea, using two approaches. The first one uses high temperatures between 750 and 850 °C growth by CVD technique [19, 20, 21] exploiting a carbon-rich forming gas and its decomposition to create the carbon thin film. The second approach relies on a solid precursor made of a carbon-rich coating of the catalytic metal and is based on the sample heating using a RTA procedure [14] at lower temperatures, i.e. not exceeding 550 °C.

For the CVD graphene growth shown in Figure 3.2, the 100 nm thick UHV-grown Ni films were transferred through air in the CVD tube furnace and the pressure was reduced to 800 mTorr. Here the samples were heated to 750 °C to increase the grains size and cleaned by annealing under a 100 sccm flow for 20 minutes. During the annealing, NiO_x and Ni(OH)_y compounds, present on the Ni surface as a consequence of the natural process of oxidation of Ni, were reduced and possibly desorbed from the Ni surface: the sample was outgassed by annealing.

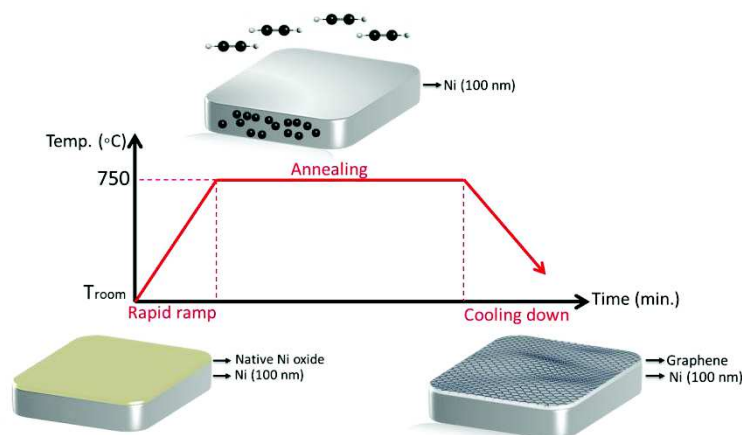
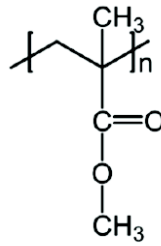


Figure 3.2 Schematic illustration for graphene growth by CVD process.

After heating, the samples were exposed to with a gas flow rate of 30 sccm for 2 minutes. Then, a gaseous mixture of H_2 30sccm and CH_4 30sccm, used as carbon precursor, was flowed into the chamber for 30 minutes for graphene synthesis process. Here the hydrocarbons molecules catalytically decomposed at the Ni surface^[21, 23] and then carbon atoms dissolved into the catalyst (due to the high solubility of carbon on Ni) to form a solid solution. The sample was finally allowed to cool to room temperature under 100 sccm Ar atmosphere for several hours while residual carbon precipitates from Ni surface layer to form graphene layers^[24, 25].

RTA process is similar to CVD with the main difference that here a solid carbon precursor is used. Many experimental works on graphene synthesis using solid precursors have been published. Among these precursors, there are polymer films, small molecules, evaporated solids etc... Food, insects, and waste have been used as well as solid carbon source to generate high quality monolayer graphene^[26].

Precursors composed of aliphatic C-C single bonds are preferable because they have lower bond dissociation energies (284-368 kJ/mol) than C=C (615 kJ/mol), C≡C (812 kJ/mol), and aromatic/heterocyclic C-C (410 kJ/mol) [7]. We chose the vinyl polymer poly(methyl methacrylate) (PMMA) as graphene precursor because its planar zigzag configuration may facilitate cyclization of C-C bonds (see Figure 3.3).



PMMA

Figure 3.3 Chemical structure of the polymer PMMA used as graphene precursor in the RTA process.

Following the RTA graphene growth (Figure 3.4), the solid carbon source PMMA2 resist, was first spincoated on 100 nm thick Ni surface (used as catalyst) resulting in a 300 nm thick film. The sample was loaded inside a quartz tube chamber of the RTA system. The chamber was then heated to 550°C for 15 min for the annealing process (outgassing of oxygen and hydrocarbon compounds presents at top of Ni surface under a flux of H₂(4%)/N₂ mixture at a pressure of 1 Torr. Once the polymer was heated above its thermal decomposition temperature (T_d ~ 310°C), its chemical bonds tend to dissociate. The low weight gaseous compounds, such as H₂O and CO₂, thermally decomposed from PMMA2 and evaporated. The solid source of PMMA2 was therefore converted into a thin layer trace amounts of amorphous carbon on top of Ni surface.

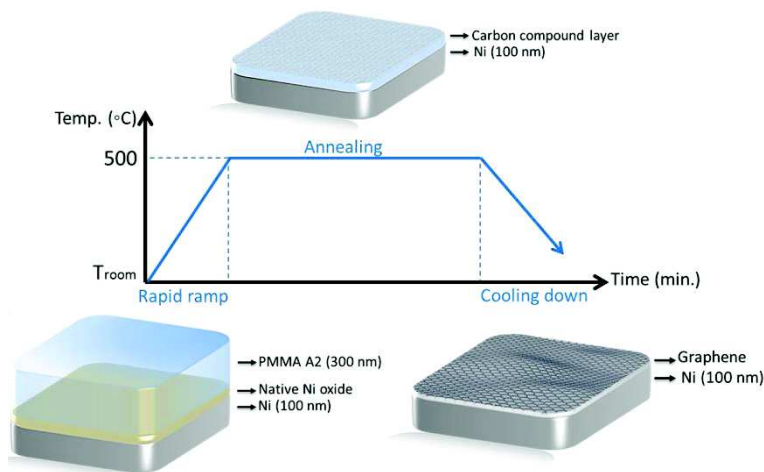


Figure 3.4 Schematic drawing of our RTA process. (Look in internet if you find the 3D molecule of PMMA and put it instead of the block in the first cartoon).

The carbon atoms of PMMA-A2 molecular backbone become the main source of sp² hybridized carbon bonds in the graphene sheets. Subsequently, the samples were held for 120 min in only H₂ for the graphene growth. PMMA-A2 first decomposed, then dissolved, and finally diffused into the whole Ni film. The sample was finally allowed to cool to room temperature and the formation of graphene occurred as a result of Ni-catalyzed crystallization of amorphous carbon compounds. RTA has a few advantages over CVD. It is short in duration, inexpensive and safe to handle unlike explosive gaseous carbon sources used in CVD process.

We grew several Ni/graphene interfaces using CVD and RTA processes at various temperatures, under different atmospheric conditions, with or without carbon precursors. The latter under the assumption that the instability of Ni, passed through atmosphere for a few days, facilitated the spontaneous formation of ultrathin (<2 nm) carbon and oxygen containing compounds on its surface. Then the formation of graphene layers resulted from annealing of the Ni films without the introduction of any intentional carbon precursor.

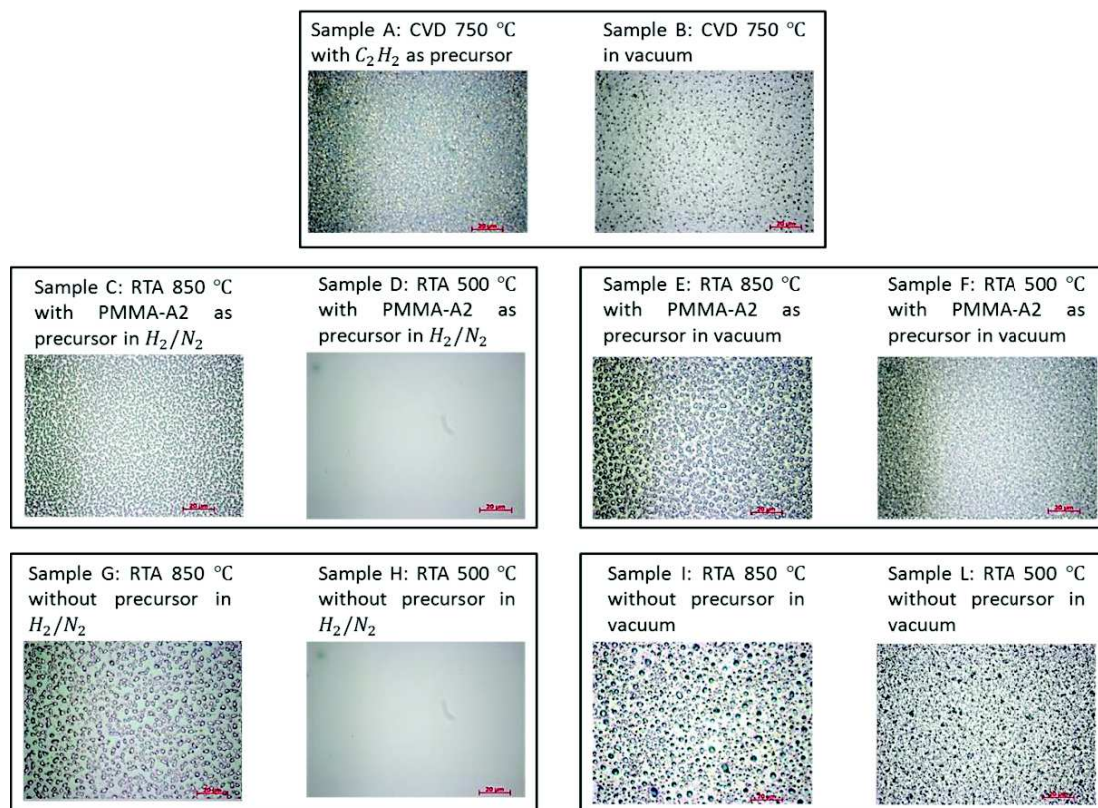


Figure 3.5 Optical images of the different Ni/graphene interfaces

Some of the processes are entirely performed in vacuum. This choice follows from the consideration that at a given temperature, the presence of a high pressure gas such as N_2 or Ar leads to much reduced oxygen evaporation rate from the Ni surface because the dense cloud of inert gas molecules hinders the transport of oxygen away from the Ni surface. As pointed out by Langmuir and Fonda^[28], the oxygen atoms desorbing from the surface have a finite probability of being reflected back to the Ni surface by collision with or Ar.

Figure 3.5 shows the optical images of all the processed Ni/graphene samples where the different textures of the surfaces after the graphene synthesis are clearly visible.

3.4 X-ray Photoelectron Spectroscopy (XPS) as a preliminary screening tool

Graphene/Ni interfaces in Figure 3.5 have been first analyzed by X-ray Photon Spectroscopy (XPS) in order to determine the oxidation state of Ni surface under graphene layers, which is the main prerequisite for the realization of our devices. XPS on bare Ni surface is also shown and used as a reference. XPS spectra were obtained at a photon energy of 1486.6 eV (Al K α) operating at a vacuum pressure of $\sim 10^{-7}$ mbar. For each sample XPS measurements were performed in two different areas of the surface and the resulting spectra were acquired after 10 scans. The spot size of the X-ray was 400 μ m and the energy step size was 0.1 eV. Spectra analysis was carried out using "XPSPEAK 41" software with a Gaussian-Lorentzian peak shape after a Shirley background correction. The results of the Ni spectra are summarized in Figure 3.6.

As shown in Figure 3.6, among all the processes used to grow graphene on Ni, only "Sample A", "Sample B", and "Sample D" provide a free-oxygen Ni surface. In particular, for our study we chose "Sample A" for CVD and "Sample D" for RTA that for the sake of clarity, from now on we will call Ni/CVD and Ni/RTA, respectively.

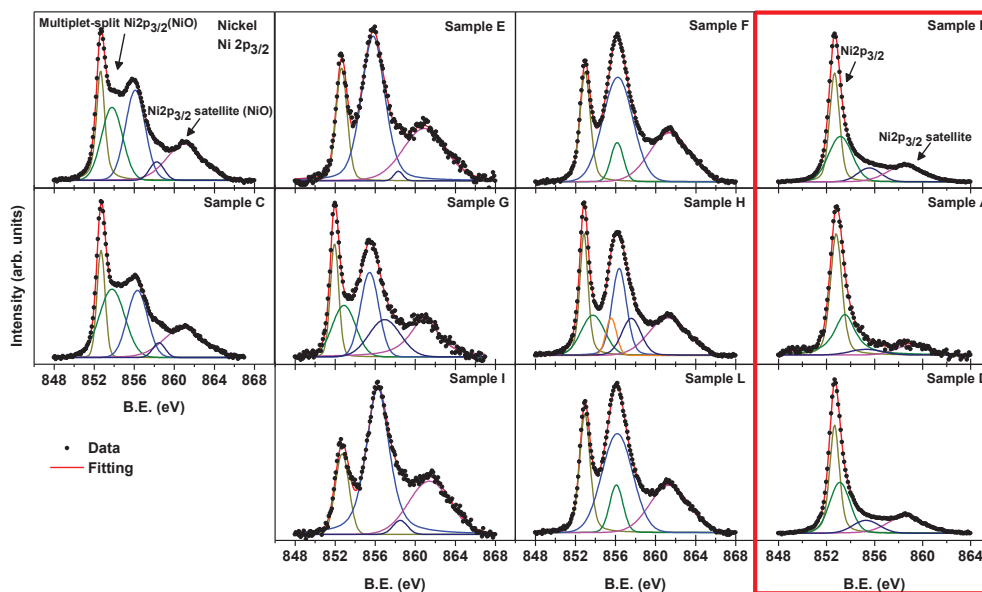


Figure 3.6 Ni $2p_{3/2}$ spectra of all Ni/ graphene processed interfaces.

Table 3.1 summarizes the quantity, expressed in percentage, of Ni, NiO and Ni_2O_3 . The total amount of the single components has been obtained by calculating the area of the corresponding peaks in the fitting.

Sample	Oxidation state	Ni%	NiO%	$\text{Ni}_2\text{O}_3\%$
Nickel bare	Oxidized	23.2	47.4	29.4
Sample A	NO Oxidized	100		
Sample B	NO Oxidized	100		
Sample C	Oxidized	19.9	55.2	24.9
Sample D	NO Oxidized	100		
Sample E	Oxidized	18.9	81.1	
Sample F	Oxidized	19.4	80.6	
Sample G	Oxidized	15.7	84.3	
Sample H	Oxidized	19.8	80.2	
Sample I	Oxidized	16.9	83.1	
Sample L	Oxidized	21.2	78.8	

Table 3.1 Percentage amount of Ni, NiO and Ni_2O_3 for each processed Ni/graphene interface, obtained by calculating the area of the corresponding XPS peaks.

3.5 Characterization

Before to measure the charge carrier injection capabilities of graphene-coated Ni electrodes, we performed a complete characterization of their physicochemical properties

3.5.1 XPS characterization

XPS spectra for Ni/CVD and Ni/RTA are here shown and discussed in detail using bare Ni film as reference. The Ni $2p_{3/2}$ spectra are displayed in figure 3.7 (a), (b) and (c). As expected, the Ni $2p_{3/2}$ spectrum for as deposited Ni surface (Figure 3.7(a)) is characteristic of oxidized Ni due to air exposure during specimen transfer before the OSC deposition. Ni $2p_{3/2}$ lines show contributions of Ni (Ni_2O_3) and Ni²⁺ (NiO) oxidation states, with intensities at binding energies (B.E.) of 856.4 eV (3) and 853.8 eV (2), which are associated to the formation of Ni³⁺ ions in the Ni surface and Ni²⁺ ions in NiO, respectively. The main peak at 852.6 eV (1) is attributed to clean Ni metal. Peaks (4) and (5) are accompanying peaks [30]. The Ni $2p_{3/2}$ spectrum for Ni/CVD (Figure 3.7 (b)) corresponds to oxidized metallic Ni. As it is clearly shown, the XPS oxide peaks, appearing in Figure 3.7 (a), are completely absent and the dominant peaks at 852.8 eV (1) and 853.5 eV (2) correspond to Ni metallic and Ni solid solution, respectively [31] and [32]. Peaks (3) and (4) with B.E. near 3.7 eV (minor) and 6.0 eV (major) above the main line (at 852.8 eV) represent the satellites corresponding to surface and bulk plasmons, respectively [30], [32]. Similar considerations can be done for Ni $2p_{3/2}$ spectrum related to Ni/RTA (Figure 3.7 (c)). For Ni/CVD sample Ni $2p_{3/2}$ signal was accessible only after etching the surface with Argon beam at energy of 1000 or 80 sec suggesting a significant multilayer thickness of the carbon layers grown by CVD.

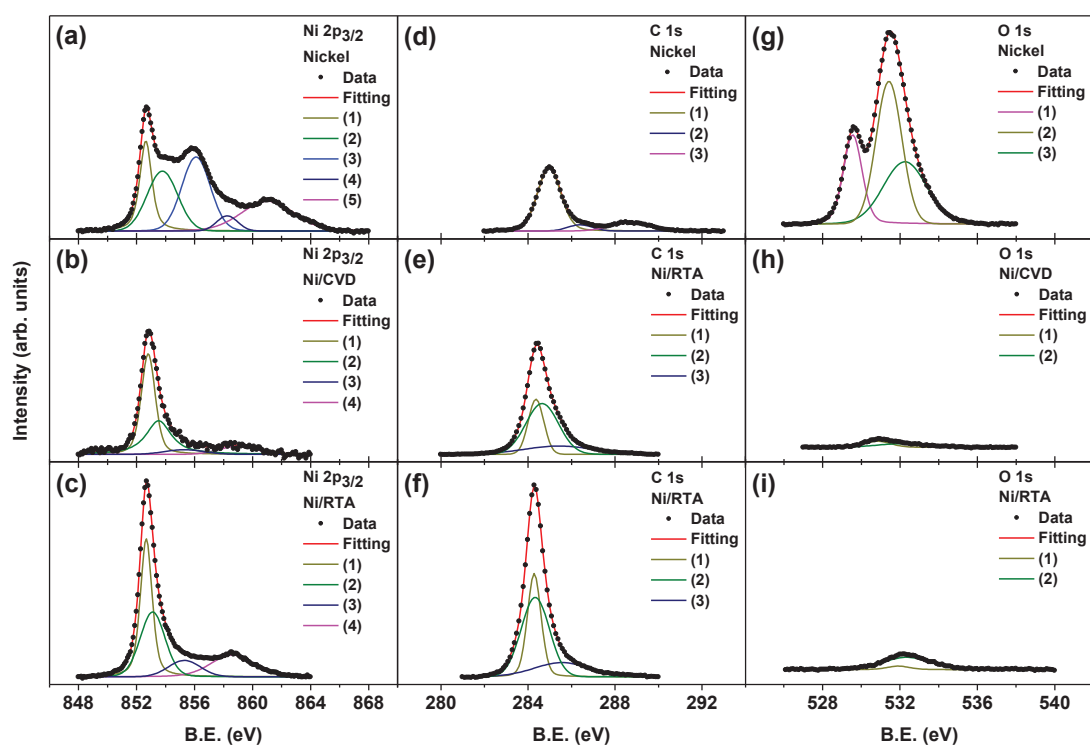


Figure 3.7 Ni $2p_{3/2}$ Spectra of (a) Ni exposed to air (b) Ni/ CVD (c) Ni/RTA. (d) C 1s core level spectra of Ni film, (e) Ni/ CVD film and (f) Ni/RTA. (g) O 1s core level spectra of bare Ni, (h) Ni/ CVD film and (i) Ni/RTA. See text for peaks numbering details.

Figure 3.7 (d), (e) and (f) show the C 1s spectra for Ni, Ni/CVD and Ni/RTA films, respectively. For Ni film (Figure 3.7 (d)) a main peak is observed, which can be deconvoluted in two components at 284.9 eV (1) and 286.4 eV (2). These peaks are correlated to carbon atoms in sp^2 (and sp^3 hydrocarbon) and sp^3 (and sp^2) configurations respectively. The peak at 288.7 eV (3), corresponds to $C=O$ bonds [2]. The C 1s high resolution XPS scan for Ni/CVD and Ni/RTA samples (Figure 3.7 (e) and (f)) samples is analyzed into three components. The first two set around 284.3 eV (1) and 284.6 eV (2) are the most intensive and they are related to sp^2 C-C bonds in aromatic networks such as graphene. The third component at 285.4 eV (3) represents C=C bonds with sp^2 hybridization [2, 32]. Another important information that can be deduced by C 1s spectra is related to the presence of detectable Ni carbide (Ni_3C). The fingerprint of Ni_3C in the photoemission spectra of C 1s should appear at binding energies lower than 284 eV, [34, 35]. The spectra in Figure 3.7 (e) and (f) do not contain any feature at this position precluding the formation of a bulk, crystalline Ni carbide during the graphene growth. The absence of Ni_3C is important to define

the magnetic properties of Ni/Graphene interfaces since it is expected to be non-ferromagnetic due to the strong hybridization between Ni and C orbitals [6, 37].

O 1s spectra for Ni surface and Ni/Graphene interface derived by CVD and RTA are shown in Figure 3.7 (g), (h) and (i), respectively. Information provided by analysis of the O 1s spectra can complement the information provided by analysis of C 1s spectra. Since the O 1s photoelectrons kinetic energies are smaller than those of the C 1s, the O 1s sampling depth is smaller, and therefore the O 1s spectra are slightly more surface specific. The O 1s spectrum for pure Ni in Figure 3.7 (g), the NiO peak is found at 529.5 eV (1). A major O 1s spectral component at the higher binding energy of 531.1 eV (2) is related to defective sites within the oxide crystal, adsorbed oxygen, or hydroxide species. The peak at 532.2 eV (3) can be related to adsorbed water or possibly adsorbed CO₂ [30]. The spectra in Figure 3.7 (h) for CVD processed Ni/Graphene film can be deconvoluted in two components at 530.8 eV (1) and 532.1 eV (2) related to O=C/H/ C=O and C-O, respectively. Deconvolution of O 1s spectrum in Figure 3.7 (i) for RTA processed Ni/Graphene surface results in two peaks located at 531.9 eV (1) and 532.3 eV (2) corresponding to C=O and C-O/C-OH bonds, respectively.

The observation of weak peaks related to the presence of oxygen in graphite has been previously observed by Hontoria-Lucas *et al.* [38] and Barinova *et al.* [39] and can be explained assuming an atmospheric oxidation of the sample in the quartz tube during graphene growth and in the XPS chamber during the measurements.

These measurements, performed on samples typically stored in ambient environment for two months, confirm that our CVD and RTA processes produce carbon films acting as an effective impermeable membrane for oxygen diffusion through the interface.

3.5.2 Raman spectroscopy of the carbon adlayer

Raman spectroscopy is a well-documented powerful and non-invasive tool to study and characterize graphitic materials. It has unique advantages in terms of differentiating the spectral fingerprints of the different forms and thickness of carbon films. A typical Raman spectrum of monolayer of graphene shows two specific structures: the G peak at ~1580 cm⁻¹ and the 2D peak at ~2700 cm⁻¹. Eventually a D peak at ~1350 cm⁻¹ appears as the uniformity of the graphene crystal degrades, e.g. graphene with broken symmetry by edges or a high defect density [40]. The G band Raman is a common feature to all sp² carbon systems and it is due to the stretching of the C-C bond. In general the G peak intensity increases linearly

with increasing the graphene thickness and its position moves to lower wavenumber when the number of graphene layers increases (from 1587 cm^{-1} for monolayer to 1581 cm^{-1} for graphite). The D band is known as the disorder or defect band. Its intensity is directly proportional to the number of defects in the sample. The band is typically very weak in graphite and high quality graphene. The 2D band is used to differentiate between single and multilayer graphene with thickness of less than 4 layers. Going from single layer to multilayer graphene the 2D band splits as a result of the symmetry lowering that takes place when increasing the number of layers. Therefore, in contrast to the G peak method for the determination of the thickness of graphene, the 2D peak method depends not only on the band position but also on its shape. In the case of monolayer graphene the 2D band can be fitted by a single Lorentzian peak with a full width at half maximum (FWHM) 30 cm^{-1} . For bulk graphite the 2D bands are broad, upshifted and with a bump on the left side that can be described with two peaks reflecting the dispersion splitting due to strong interlayer coupling. In the case of bilayer the 2D band has 4 components that are related to the four possible double resonance scattering processes resulting from the splitting of the electronic structure of graphene when a second layer is added. The number of double resonance processes increases until the point where the spectral shape converges to that of graphite, where only two peaks are observed. [41] For this reason, for more than 5 layers the Raman spectrum becomes hardly distinguishable from that of bulk graphite. Furthermore, the 2D peak is higher than G peak when the number of graphene layers is less than 4.

All these considerations related to the identification of the number of layers by Raman spectroscopy are well established only for graphene with AB Bernal stacking, in which the stacking of the graphene layers is ordered with respect to one another along the vertical axis. For example, for turbostratic graphite the random orientation of graphene layers with respect to each other, and thus the absence of an interlayer interaction between the graphene planes, makes the 2D band similar to that of monolayer graphene but with a larger linewidth [42, 9].

Raman spectra were acquired under ambient conditions using a Renishaw InVia micro-Raman spectrometer equipped with a 514 nm excitation laser ($E = 2.41\text{ eV}$). The exposure time was 10 s and the spot size was about $1.5\text{ }\mu\text{m}$. Figure 3.8 shows Raman spectra of both CVD and RTA graphene. The corresponding optical images inset highlight the quality of graphene layers.

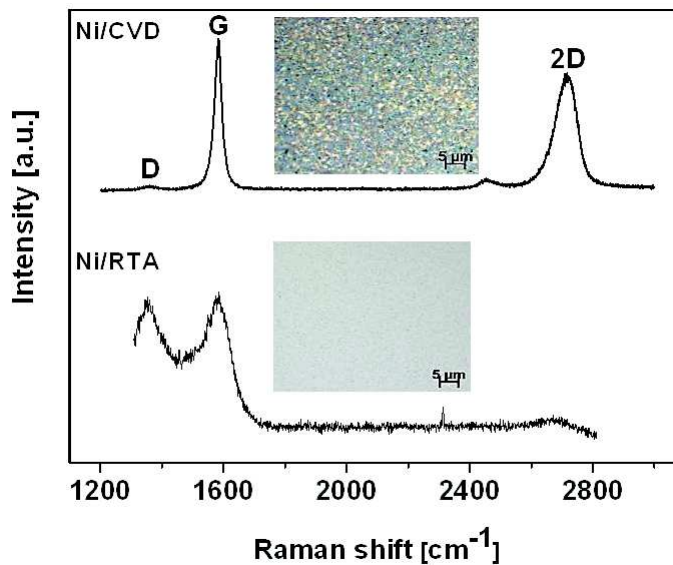


Figure 3.8 Raman spectra of CVD (top) multilayer graphene and RTA (bottom) amorphous carbon films over Ni films 100 nm thick. Insets are optical microscopy images of the samples.

Raman spectra of CVD graphene exhibits characteristics of good quality multilayer graphene: a low D band in conjunction with the distinct G and 2D peak shapes. The prominent G peak indicates the presence of a graphite hexagonal lattice structure over the surface. The very small D peak corresponds to the presence of few carbon atoms or defects. The broad and sharp 2D peak is a signature of the formation of graphene multilayers. However, despite the presence of graphene multilayers, the 2D line shape is symmetric and can be fitted by a single Lorentzian just like graphene monolayer, but with a FWHM between 45 and 80 cm^{-1} (instead of $\sim 30 \text{ cm}^{-1}$, as in monolayer graphene). This symmetry of the 2D peak is a common feature of CVD-grown multilayer graphene on Ni as it has been already reported by many groups and attributed to non-Bernal (turbostratic) graphene [42, 9, 43].

The optical microscopy image of the surface (in the inset of Figure 3.8) shows a patchwork of graphene flakes with different darkness. The color of the patches may give an indication of their thickness. To verify the homogeneity of graphene quality we probed different regions of Ni/CVD surface. The resulting Raman spectra are shown in Figure 3.9.

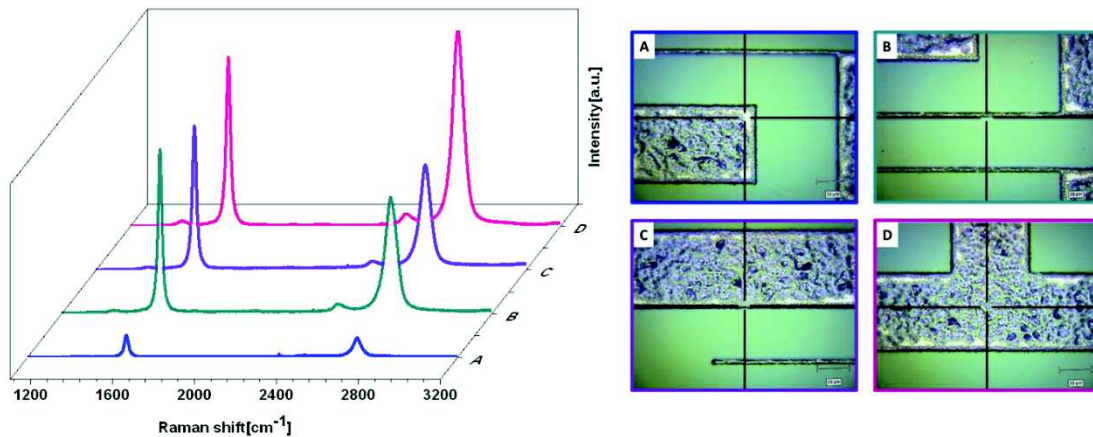


Figure 3.9 Raman spectra and related optical images of Ni/CVD electrodes.

Raman analysis of RTA graphene shows that this surface consists of disordered, discontinuous and partially graphitized layers of carbon with high and large D peak indicative of a defective material. The very small 2D peak indicates the lack of hexagonal organization of C atoms. However, the corresponding optical image shows a smooth uniform surface (Figure 3.8).

3.5.3 Surface topography

The morphology, i.e. the roughness, of Ni/CVD and Ni/RTA surfaces has been investigated by recording topographical Atomic Force Microscopy (AFM) images (Figure 3.10). AFM topographical mapping was carried out using a Bruker Dimension Edge instrument, with an antimony doped silicon tip, in intermittent contact mode. AFM analysis of the as grown Ni film is also reported as reference.

The analysis indicates that the 100 nm thick Ni film is a polycrystal formed by flat nanosized grains with an average lateral grain size $d = 22$ nm. Its surface is quite smooth, with a rough mean square (rms) roughness $R = 1.4$ nm at a scanned area of $5 \times 5 \mu\text{m}^2$. Similarly, Ni/RTA surface is made of flat grains with an average lateral size $d = 118$ nm and a rms roughness $R = 1.3$ nm. AFM image of Ni/CVD film, for which high temperatures are involved in the growth process, exhibits a texture characterized by wide protrusions and depressions as high as 40 nm and with an average lateral size $d = 1 \mu\text{m}$, which results from the recrystallization occurring upon cooling of the film during the last step of the CVD process. We also found that RTA processing at temperatures exceeding 600 °C leads to a significant

increase in the roughness of the films, with AFM imaging being reminiscent of CVD processed samples.

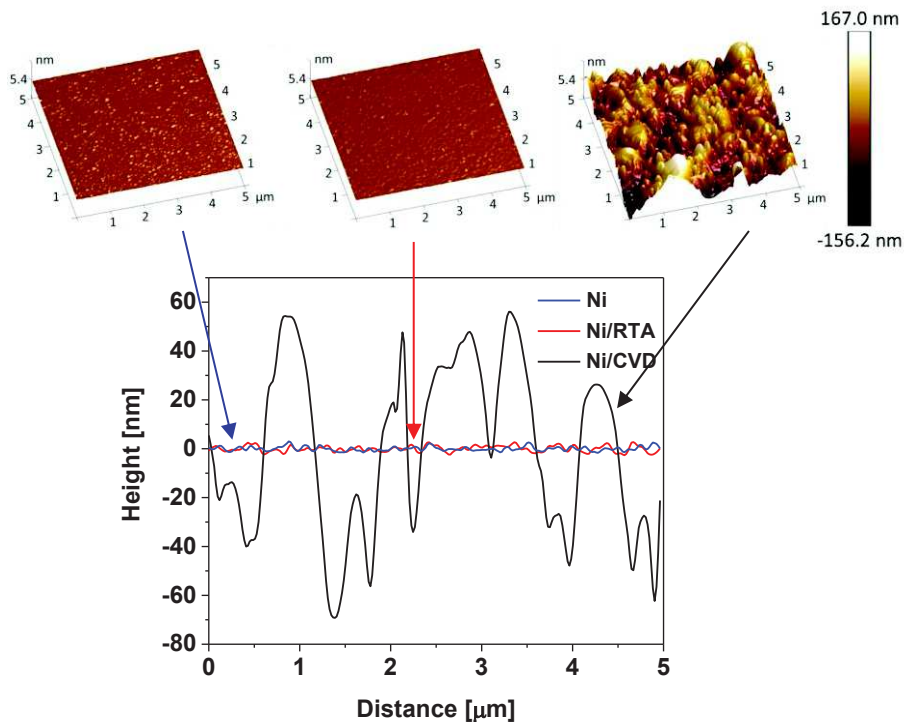


Figure 3.10 3D micrograph of the AFM topographical scans of bare Ni, Ni/RTA and Ni/CVD surfaces together with the corresponding topographical profiles providing further evidence for the very different surface roughness

In conclusion, AFM analysis reveals that temperature plays a key role in graphene synthesis defining a compromise between the quality and the crystalline structure of the grown carbon type material on one hand, and the morphology at the surface on the other hand. High temperature processes, such as CVD, have the main advantage to produce a high crystalline graphene structure but on a rough substrate which may eventually affect reliable organic devices fabrication and charge carriers injection.

3.5.4 ToF-SIMS thickness and composition analysis

Time-of-Flight Secondary Ions Mass Spectrometry (ToF-SIMS) chemically resolved depth profiling has been first used to assess the presence and form of nickel

oxide at the surface and within the bulk nickel film of the Ni/CVD/RTA and Ni reference samples complements the information obtained by XPS deeper into the sample thickness.

A ToF-SIMS 5 instrument from IONOF GmbH has been used. Profiles were acquired in high mass resolution mode with 25 keV Bi⁺ primary ions combined with interlaced 1 keV Cs⁺ sputtering ions (dual beam). Negative secondary ions in the mass range 1-500 mu were recorded from the top surface and until a sample depth of ~200 nm. To ensure representative and reproducible results, one to three randomly selected scan areas of 100x100 nm² were considered on each sample. The depth calibration has been obtained by measuring crater depth with a Dektak XT profilometer.

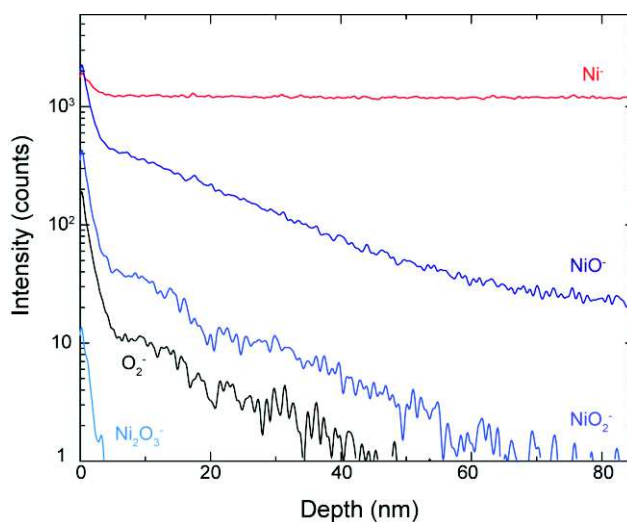


Figure 3.11 ToFSIMS depth profile of Ni exposed to air. Characteristic fragments for nickel, oxygen and nickel oxides are displayed, starting from the top surface (0 nm) until deep in the nickel layer (85 nm).

Figure 3.11 shows the in-depth evolution of characteristic fragments for nickel, oxygen, and different forms of nickel oxide in the reference sample (Ni exposed to air). The depth is determined by profilometry after exposing the sample to ion bombardment. A distinct layer of nickel oxide, mainly composed of NiO₂ and Ni₂O₃, is observed. This oxide layer spans over ~2 nm, after which a sharp drop down to 7% of the top content is observed (Ni/Ni interface). From there, all oxides exponentially decrease with increasing depth in the Ni layer. Hence, the metallic layers

prepared as described above are composed of a 2 nm-thick nickel oxide layer on top of the Ni layer, itself containing a small fraction of oxides diffusing from the top surface.

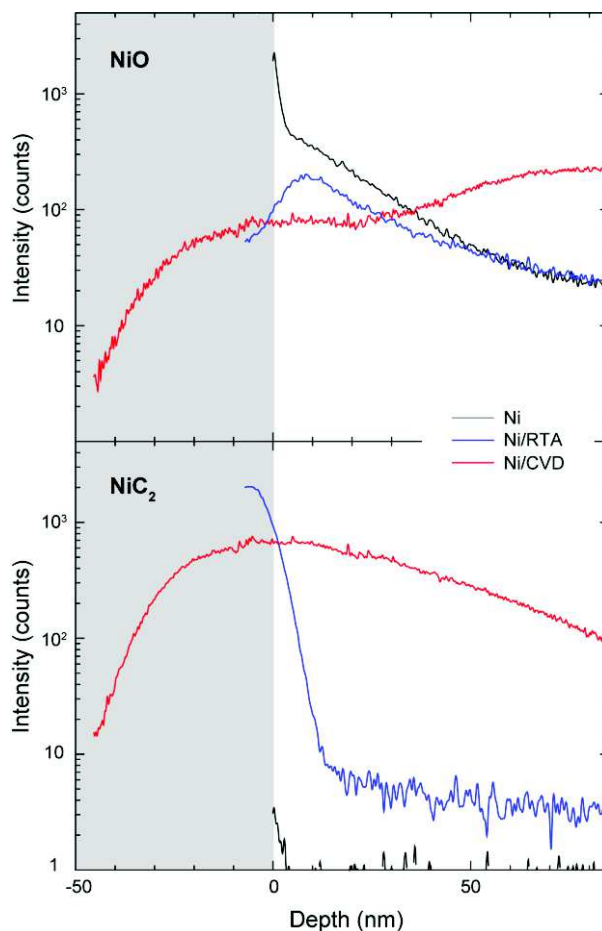


Figure 3.12 Depth profile comparison of Ni exposed to air (black), Ni/CVD (red) and Ni/RTA (blue) for the fragments NiO (top) and NiC₂ (bottom).

Figure 3.12 portrays a comparison of the depth evolution for NiO and NiC₂ in the reference Ni film (black), Ni/CVD (red) and Ni/RTA (blue). The grey shaded area indicates the deposited graphene layer, with a depth scale calibrated with the profilometer, and using the Ni/SiO₂ interface alignment point. The NiO profiles demonstrate that both deposition methods efficiently prevent the formation of a nickel oxide layer on top of nickel, in agreement with the XPS surface data. Besides the full suppression of the top oxide layer, a reduction of 97.6% is observed in Ni/RTA

at the graphene/Ni interface. Deeper in the nickel layer, the oxide trend in Ni/RTA tends to join that of the reference Ni film, with similar content of oxides at about half depth of the Ni layer. In Ni/CVD, the trend is less clear. After an initial low level of oxides at the surface, the oxide content seems to increase with depth in the Ni layer. A possible explanation would be a diffusion of oxide from the buried Ni/Si interface triggered by the higher processing temperatures. Hence, the lower temperatures RTA process appears to perform CVD processing for efficient oxide formation and diffusion prevention.

Additionally, the Ni ToF-SIMS profiles give insights into the carbon layer thickness and carbon/Ni films interface quality.

For Ni/RTA, a short plateau followed by a sharp drop is observed. This reveals a graphene layer thickness of ~5nm and further indicates no/low diffusion of carbon in the Ni layer (<1% after 10nm). In contrast, the Ni/CVD sample shows a much thicker carbon-rich layer (spanning over more than 40nm) and a large diffusion within the whole Ni layer. No clear graphene/Ni interface is visible. The profile of the reference Ni film is shown to confirm that no carbon onto or within the Ni layer is found without graphene deposition. The long tail in the negative thickness range (Figure 3.12 for CVD samples) quantifies the roughness of the sample, of the same order of magnitude as the AFM inferred data. The low temperature RTA deposition forms a superior quality of graphene layer in terms of interface sharpness and minimal carbon diffusion, as compared to the CVD process.

3.5.5 Magnetic properties: SQUID and MOKE measurements

Magnetic measurements have been performed in order to verify the CVD and RTA treatments and the related high temperatures processes could possibly impact the ferromagnetic properties of the Ni films.

Bulk measurements were performed using a superconducting quantum interference device (SQUID) magnetometer (Quantum Design MPMS3), with applied field parallel to the sample plane. The Si/Si₃N₄ substrate was measured separately and its signal subtracted to deduce the Ni film absolute magnetic moment. We estimate an uncertainty reaching 5% of the absolute data scale, resulting from errors in sample size, thickness, centering of the sample for measurements. Measurements that are more surface sensitive were performed

with a homemade Kerr setup, using a solid state red laser (wavelength of 670 nm) in longitudinal geometry.

Magnetic properties of the Ni films (unprocessed, RTA and CVD processed respectively) are shown in Figure 3.13. They exhibit properties expected for polycrystalline Ni (thick) films with no significant changes after processing. The Kerr measurements are expected to be surface sensitive and provide information more pertinent for charge injection purposes. The Ni/CVD samples displayed noisier signal, as expected from a surface with increased roughness, with a hysteresis curve appearing more squared, possibly related to a slight increase of grain size at high temperatures processing and a slightly larger coercive field (H_C).

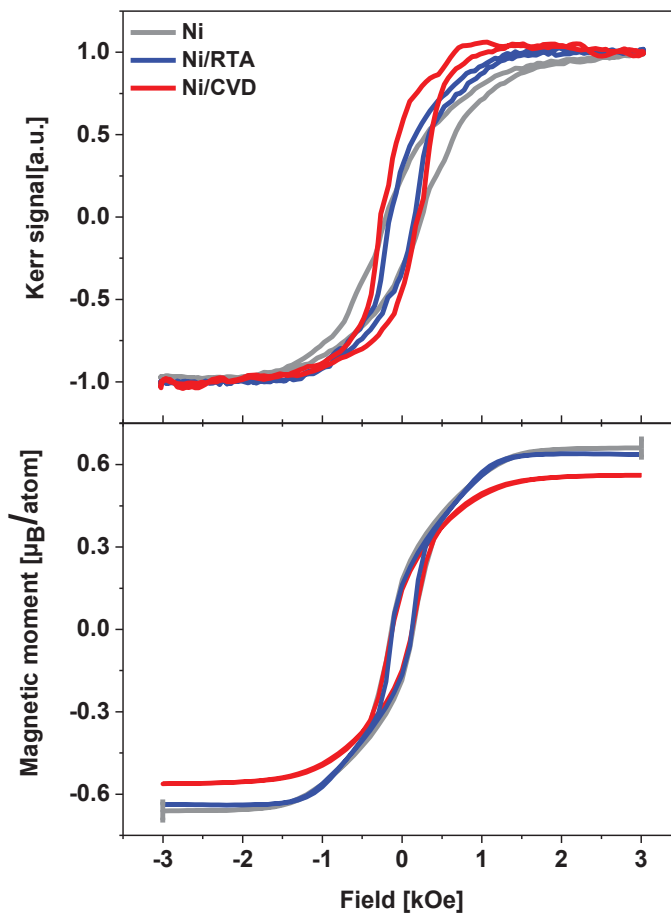


Figure 3.13 Magnetic properties of Ni films. Top: Normalized Kerr measurement performed on Ni (as produced), Ni/RTA and Ni/CVD samples. Bottom: Absolute magnetization obtained by SQUID magnetometry (with error bar of 5% of value). Both data indicate that processing samples did not significantly alter the magnetic properties of Ni.

When performing measurements on the whole volume of the samples using SQUID magnetometry, all magnetization curves are found to be similar. A small decrease of the measured absolute value of the saturation magnetization M_s of Ni/CVD sample is observed. It is however fair to note that the precise determination of the absolute magnetic moment is quite challenging, and its measured decrease is of the order of the uncertainty in measurements all providing M_s values corresponding to the one of bulk Ni ($M_s/\text{Ni atom} = 0.62$), confirming our observed limited C contamination of the bulk Ni films. Our results provide confidence that the magnetic properties of all studied samples are preserved after processing, which is essential for the spin electronics envisioned applications.

3.6 Conclusions

In this chapter, we presented a complete analysis of physical and chemical properties of Ni electrodes covered by very thin carbon films. In particular, carbon based overlayers protect the Ni from oxidation, with negligible amount of oxide only detectable by ToF-SIMS (and not observed by XPS). We found that processed Ni at temperatures below 550 °C allow keeping the structural quality of the films, with optimal composition of Ni, free from oxides and carbide species. When temperatures higher than 600°C are employed, crystalline (multilayer) graphene coverage is obtained, but we observe a deterioration of the topography of the samples

References

1. Bunch, J. *Set al.* Impermeable Atomic Membranes from Graphene Sheets. *Nano Lett.* **8**, 2458–2462 (2008).
2. Dlubak, B. *et al.* Graphene Passivated Nickel as an Oxidation Resistant Electrode for Spintronics. *ACS Nano* **6**, 10930–10934 (2012).
3. Novoselov, K. *Set al.* Two-dimensional atomic crystals. *PNAS* **301**, 10451–10453 (2005).
4. Blake, P. *et al.* Graphene Based Liquid Crystal Devices. *Nano Lett.* **8**, 1704–1708 (2008).
5. Stankovich, S. *et al.* Synthesis of graphene based nanosheets via chemical reduction of exfoliated graphite oxide. *Carbon* **45**, 1558–1565 (2007).
6. Worsley, K. *et al.* Soluble graphene derived from graphite fluoride. *Chem. Phys. Lett.* **445**, 51–56 (2007).
7. Berger, C. *et al.* Ultrathin Epitaxial Graphite: 2D Electron Gas Properties and a Route toward Graphene based Nanoelectronics. *Phys. Chem. B* **108**, 19912–19916 (2004).
8. Emtsev, K. *Vet al.* Towards wafer size graphene layers by atmospheric pressure graphitization of silicon carbide. *Nat. Mater.* **8**, 203–207 (2009).
9. Reina, A. *et al.* Large Area, Few Layer Graphene Films on Arbitrary Substrates by Chemical Vapor Deposition. *Nano Lett.* **9**, 30–35 (2009).
10. Yu, Q. *et al.* Graphene segregated on Ni surfaces and transferred to insulators. *Phys. Lett.* **93**, 113103 (2008).
11. Kim, K. *Set al.* Large scale pattern growth of graphene films for stretchable transparent electrodes. *Nature* **457**, 706–710 (2009).
12. Sun, Z. *et al.* Growth of graphene from solid carbon sources. *Nature* **468**, 549–552 (2010).
13. Peng, Z., Yan, Z., Sun, Z. & Tour, J. M. Direct Growth of Bilayer Graphene on SiO₂ Substrates by Carbon Diffusion through Nickel. *ACS Nano* **5**, 8241–8247 (2011).
14. Kwak, J. *et al.* In situ observations of gas phase dynamics during graphene growth using solid state carbon sources. *Phys. Chem. Chem. Phys.* **15**, 10446–10452 (2013).
15. Li, X. *et al.* Large Area Synthesis of High Quality and Uniform Graphene Films on Copper Foils. *Science* **324**, 1312–1314 (2009).
16. Weatherup, R. *Set al.* On the Mechanisms of Ni Catalysed Graphene Chemical Vapour Deposition. *ChemPhysChem* **13**, 2544–2549 (2012).
17. Eizenberg, M. & Blakely, J. M. Carbon monolayer phase condensation on Ir(111). *Surf. Sci.* **82**, 228–236 (1979).
18. Coraux, J., N'Diaye, A. T., Busse, C. & Michely, T. Structural Coherency of Graphene on Ir(111). *Nano Lett.* **8**, 565–570 (2008).
19. Zhang, Y., Zhang, L. & Zou, C. Review of chemical vapor deposition of graphene and related applications. *Acc. Chem. Res.* **46**, 2329–2339 (2013).
20. Di, C. *et al.* Patterned Graphene as Source/Drain Electrodes for Bottom Contact Organic Field Effect Transistors. *Adv. Mater.* **20**, 3289–3293 (2008).
21. Li, X., Cai, W., Colombo, L. & Ruoff, R. S. Evolution of graphene growth on Ni and Cu by carbon isotope labeling. *Nano Lett.* **9**, 4268–4272 (2009).

22. Muradov, N. Z. How to produce hydrogen from fossil fuels without CO₂ emission. *J. Hydrog. Energy* **18**, 211–215 (1993).
23. Sakae Takenaka, Y. S. Methane Decomposition into Hydrogen and Carbon Nanofibers over Supported Pd–Ni Catalysts: Characterization of the Catalysts during the Reaction. *J. Phys. Chem. B* **108**, (2004).
24. Fujita, D. & Homma, T. Surface precipitation of graphite layers on carbon-coated nickel and their stabilization effect against chemisorption and initial oxidation. *Interface Anal.* **19**, 430–434 (1992).
25. Shelton, J. C., Patil, H. R. & Blakely, J. M. Equilibrium segregation of carbon to a nickel (111) surface: A surface phase transition. *Surf. Sci.* **43**, 493–520 (1974).
26. Ruan, G., Sun, Z., Peng, Z. & Tour, J. M. Growth of Graphene from Food, Insects, and Waste. *ACS Nano* **5**, 7601–7607 (2011).
27. Sundararajan, P. In *Physical Properties of Polymers Handbook* (ed. Mark, J. E.)–324 (Springer New York, 2007).
28. Langmuir, I. Convection and Conduction of Heat in Gases. *Phys. Rev. Ser. I* **34**, 401–422 (1912).
29. Fonda, G. R. Evaporation of Tungsten Under Various Pressures of Argon. *Phys. Rev.* **31**, 260–266 (1928).
30. Biesinger, M. C., Payne, B. P., Lau, L. W. M., Gerson, A. & Smart, R. S. C. X-ray photoelectron spectroscopic chemical state quantification of mixed nickel metal, oxide and hydroxide systems. *Surf. Interface Anal.* **41**, 324–332 (2009).
31. Dlubak, B., Kidambi, P. R., Weatherup, R. S., Hofmann, S. & Robertson, J. Substrate assisted nucleation of ultrathin dielectric layers on graphene by atomic layer deposition. *Appl. Phys. Lett.* **100**, 173113 (2012).
32. Grosvenor, A. P., Biesinger, M. C., Smart, R. S. C. & McIntyre, N. S. New interpretations of XPS spectra of nickel metal and oxides. *Surf. Sci.* **600**, 1771–1779 (2006).
33. Zdansky, E. O. F., Nilsson, A. & Månsson, N. Induced reversible surface to bulk transformation of carbidic carbon on Ni(100). *Surf. Sci.* **310**, L583–L588 (1994).
34. VijaiBharathy, Pet al. Effect of nickel incorporation on structural, nanomechanical and biocompatible properties of amorphous hydrogenated carbon thin films prepared by low energy biased target ion beam deposition. *Thin Solid Films* **519**, 1623–1628 (2010).
35. Loviat, F., Czekaj, I., Wambach, J. & Wokaun, A. Nickel deposition on Al₂O₃ model catalysts: An experimental and theoretical investigation. *Surf. Sci.* **603**, 2210–2217 (2009).
36. Schaefer, Z. L., Weeber, K. M., Misra, R., Schiffer, P. & Schaak, R. E. Bridging hcp and Ni₃C via a Ni₃C₁ Solid Solution: Tunable Composition and Magnetism in Colloidal Nickel Carbide Nanoparticles. *Chem. Mater.* **23**, 2475–2480 (2011).
37. He, L. Hexagonal close packed nickel or Ni₃C? *Magn. Magn. Mater.* **322**, 1991–1993 (2010).
38. Hontoria-Lucas, C., López Peinado, A. J., López González, J. de D., Rojas Santos, M. L. & Marín-Aranda, R. M. Study of oxygen-containing groups in a series of graphite oxides: Physical and chemical characterization. *Carbon* **33**, 1585–1592 (1995).

39. Barinov, A., Gregoratti, L., Dudin, P., La Rosa, S. & Kiskinova, M. Imaging and Spectroscopy of Multiwalled Carbon Nanotubes during Oxidation: Defects and Oxygen Bonding. *Adv. Mater.* **21**, 1916–1920 (2009).
40. Ferrari, A. C. & Basko, D. M. Raman spectroscopy as a versatile tool for studying the properties of graphene. *Nat. Nanotechnol.* **8**, 235–246 (2013).
41. Dresselhaus, M. S., Jorio, A., Hofmann, M., Dresselhaus, G. & Saito, R. Perspectives on Carbon Nanotubes and Graphene Raman Spectroscopy. *Nat. Mater.* **10**, 751–758 (2011).
42. Malard, L. M., Pimenta, M. A., Dresselhaus, G. & Dresselhaus, M. S. Raman spectroscopy in graphene. *Phys. Rep.* **473**, 51–87 (2009).
43. Lenski, D. R. & Fuhrer, M. S. Raman and optical characterization of multilayer turbostratic graphene grown via chemical vapor deposition. *Appl. Phys. Lett.* **110**, 013720 (2011).

4

Carbon-passivated Ni electrodes for charge injection in organic semiconductors

The electrical performances of three-terminal devices integrating ultra-thin C-passivated Ni electrodes as source and drain are measured and investigated. The results provide insight into the quality of the interface between ferromagnetic contact and organic semiconductor. RTA-processed electrodes exhibit the lowest interface resistance for hole injection into organic transistor devices, on par with benchmark gold electrodes. These results indicate that our approach presents an attractive strategy for the fabrication of solution-processed organic devices of potential applicability for spintronics.

4.1 Introduction

Thanks to its combination of chemical stability, ease of fabrication, and reproducible surface state preparation gold is a material of choice for charge injection into organic semiconductors (OSC). Furthermore, its large work function value makes Au energetically well matched to p-type OSCs. Carbon is often the material of choice for electrochemical studies, owing to its attractive fabrication costs and the fact that it is chemically inert to many redox reactions. However, the mechanical fragility and the involved technical difficulties in its patterning into thin electrodes, combined with the work function highly sensitive to the impurities (type, content), and termination chemical state severely limits the use of carbon for organic electronics interconnects [1].

Carbon coating reaching several nm in thickness are considered good candidates for spin polarization currents injection or detection [2] and first results on devices using inorganic spacer grown under UHV conditions are encouraging [3, 4, 5].

In this chapter we present a study on the charge carrier injection capabilities of Ni/CVD and Ni/RTA electrodes in an electrolyte-gated transistor geometry, and compare them to pristine nickel and gold electrodes. We consider this as the most challenging test for charge injection, as it will be tested against the lowest electrode/polymer interface resistance values documented in the literature [6, 7, 8]. Our goal is therefore to validate if Ni/C electrodes, of potential interest for spintronics applications, can be used as building blocks for organic spintronics devices.

4.2 Selecting the active channel material: work function measurements

In electronic devices, such as organic transistors, the first step for the realization of ohmic contacts is the realization of specific combinations of OSC and metal electrodes chosen in order to reduce to a minimum the energy barriers for charge carriers injection into the OSC. Work function (WF) values can impact the electrode/organic charge injection probability. Low WF values usually result in a relatively high barrier for injection of holes into the highest occupied molecular orbitals (HOMO) of p-type organic semiconductors. Therefore, the knowledge of the metal electrodes WF provides a key information to choose the proper organic semiconductor. Here, we use Ultraviolet Photoelectrons Spectroscopy (UPS) technique, which is a well-documented and powerful approach for studying the electronic structure of various solids and interfaces, to estimate the WF of our electrodes.

Measurements for Ni, Ni/CVD and Ni/RTA surfaces have been performed by means of UPS using an ambient photoelectron yield counter Spectrometer, model AC-2, by RKI Instruments. Measurements were executed in a range of energy between 4.00 and 5.60 eV with step of 0.05 eV and light source intensity of 100 nW. For each sample the WF was calculated from the UPS spectrum by determining the onset of the sqrt(photoelectron yield) vs. E curve.

UPS technique yields the minimum absolute value of the work function on the probed surface, even if it is only a small fraction of the surface area and is independent of any experimental parameter except for the photon energy of the UV source [9, 10]. Measured values of WF, within an uncertainty of 0.05 eV (precision of the measurement and reproducibility for different areas of the sample), for Ni, Ni/CVD and Ni/RTA surfaces, are 4.8 eV, 5.1 eV and 5.0 eV, respectively (see Figure 4.1).

The measured WF value for Ni is below those of pure Ni surfaces, [11] possibly reduced by exposure to air oxidation and moisture. The higher WF values found for Ni/CVD and Ni/RTA may contribute to the formation of better ohmic contacts with p-type polymers, which would ultimately reduce the contact resistance.

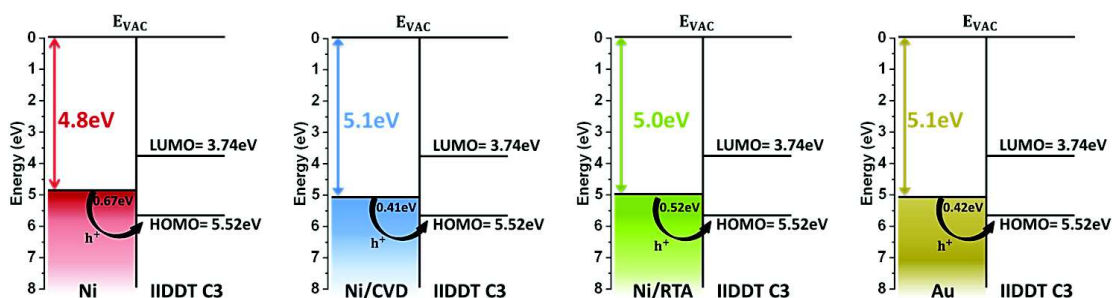


Figure 4.1 Energy diagrams of IIDDT-C3 interacting with Ni, Ni/UTC, Ni/Gr, and Au electrodes, respectively, according to our measured WF values.

Since Au is the best performing and most used material for electrodes in organic electronics, we also fabricated and studied Au OFETs in order to compare them with bare Ni and carbon-passivated Ni electrodes. The measured WF value for Au electrodes is 5.1 eV.

According to the measured WF values, the organic semiconductor (OSC) we chose to investigate in our devices is a p-type Isoindigo-based conjugated polymer poly[1,1'-bis(4-

decyltetradecyl)-6-methyl-6'-(5'-methyl-[2,2'-bithiophen]-5-yl)-[3,3' biindolinylidene]-2,2'-dione] (IIDDT-C3) with HOMO level at 5.52 eV (Figure 4.2).

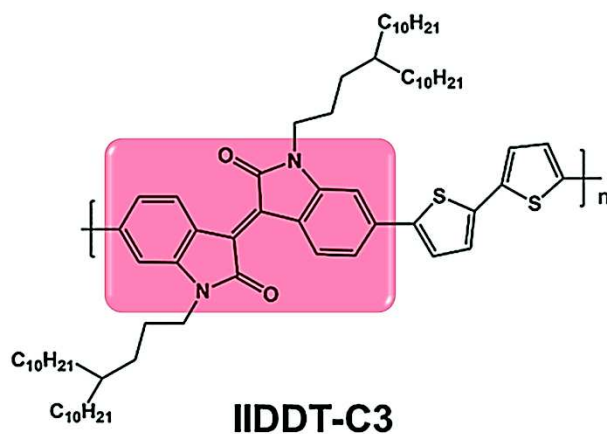


Figure 4.2 Chemical formula of the polymeric semiconductor used.

Isoindigo is a unit composed of two oxindole rings connected by a double carbon bond (red block in Figure 4.2) and it has recently been exploited in organic electronics thanks to its excellent stability and capability to form large crystalline fibrillar networks characterized by strong π - π interactions. It has been found that using branched alkyl side chains (such as decyltetradecyl) can effectively decrease interchain π - π stacking distance and improve the charge carrier mobility [12, 13]. Apart from the HOMO level value, IIDDT-C3 has other advantages such as easy processability, air-stability, and high mobility ($>3 \text{ cm}^2\text{V}^{-1}\text{s}^{-1}$) [14].

4.3 Device fabrication

Figure 4.3 (a) and (b) show a schematic design of the device geometry and the corresponding optical image, respectively. The device architecture has been designed for the purpose of performing four point probes gated conduction measurements for the measurement of the contact resistance. Top gate, bottom contact transistors with channel length L ranging from 20 to 50 μm (width $W = 1000 \mu\text{m}$) were fabricated in a rectangular geometry in the same chip.

Two thin electrodes (fingers) with L ranging from 8.5 to 14.5 μm and $W = 2.5 \mu\text{m}$ were inserted inside the channel as voltage probes. Source-drain electrodes and the voltage probes electrodes were defined by photo-lithography on a 500 nm thermally oxidized SiO_2/p^+ -doped Si substrate.

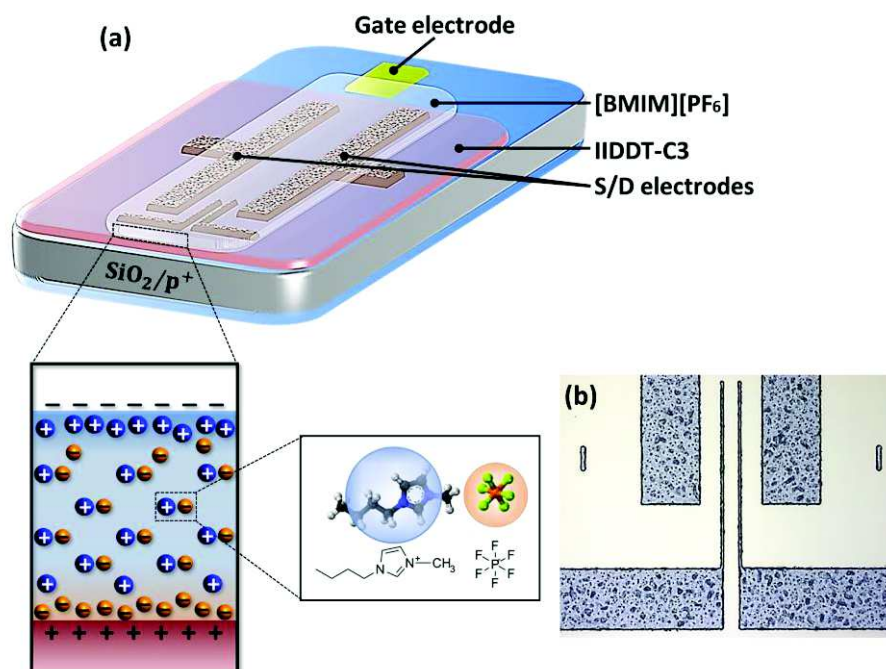


Figure 4.3 (a) Schematic of the device geometry used for the gated four probes measurements of the contact resistance, together with the cross section of the ion gel illustrating the distribution and the chemical structure of the employed ions. (b) Optical image of the CVD processed graphene on top of Ni electrodes. The texture of the graphene layers placed on the catalyst area and with the same shape is clearly distinguished.

The patterning process of Ni electrodes presented some practical fabrication limit. Ni surface often contains polymeric residues, which are difficult to remove. The photoresist material adheres to the pattern surface strongly so that lifting off metal evaporated films can be complicated especially when the thickness of the metal film exceeds 50 nm as in our case.

At the beginning the samples were fabricated using a single-step negative resist AZ 5214 process. Then Ni and Au metal films, of 100 nm thickness, were deposited by e-beam evaporation together with a 5 nm Ti adhesion layer (rate deposition of 0.5 nm/s) followed by lift-off in acetone or in heated AZ Remover. This procedure turned out in Ni electrodes edges surrounded by resist residues, as shown in Figure 4.4 (a), even after samples

immersions in heated Stripper and ultrasonic baths. These residues resulted eventually in the formation of carbon nanotubes during graphene growth process with consequent short-cutting of the device (Figure 4.4 (a), right panel).

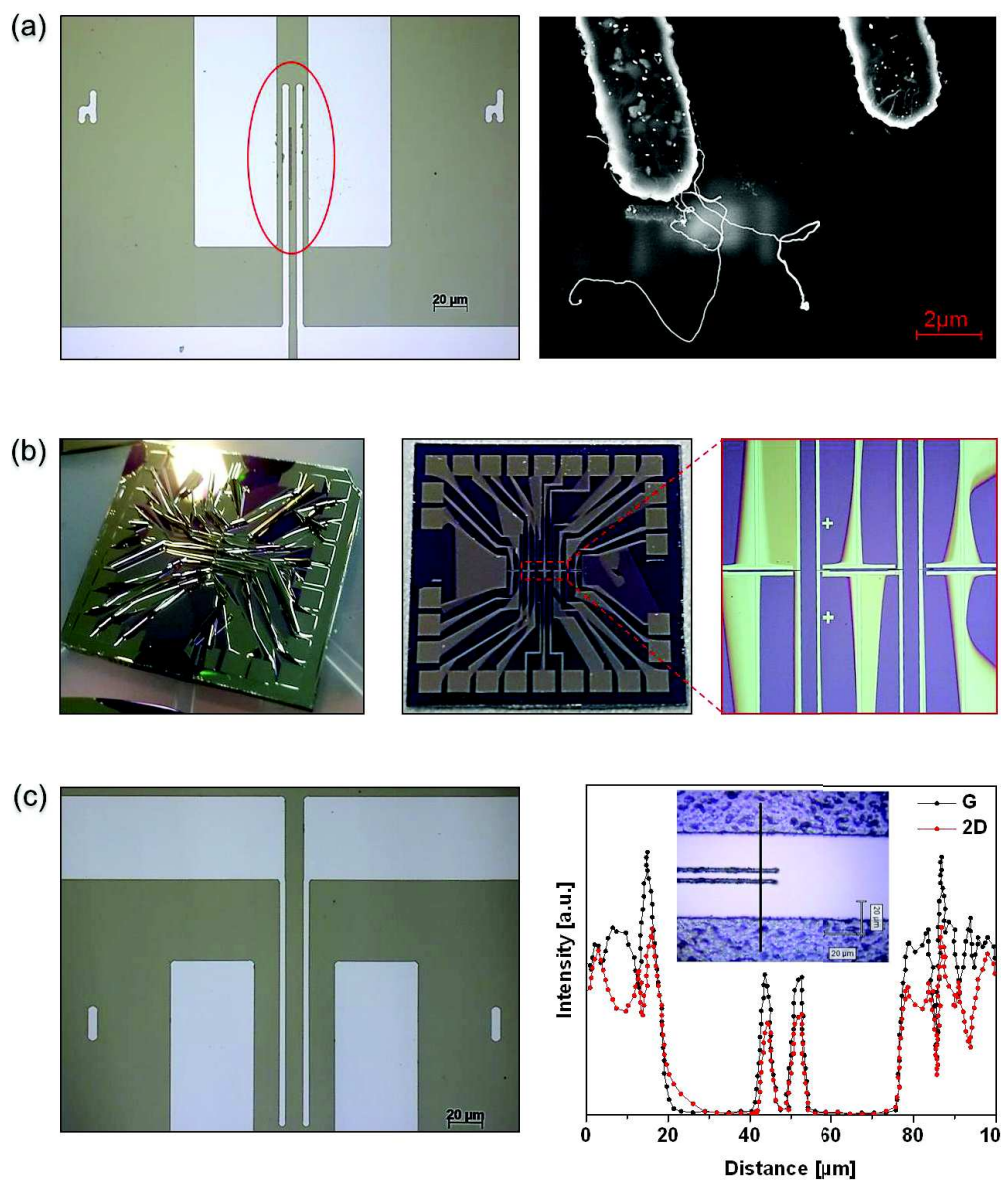


Figure 4.4 a) Optical and SEM image of the negative resist AZ 5214-processed sample. In the optical image post lift-off resist residues are easily visible. They will form carbon nanotubes during the CVD-graphene growth as it is shown in the SEM image. b) Photograph of the samples prepared by HMDS-LOR-AZ 5214 photolithography process as found right after the metal evaporation and after immersion in PG remover for the lift-off step. The zoom is an optical image clearly showing the different etched SiO₂ areas. c) Optical image of the sample fabricated using the double layer resist PMGI/AZ 5214 process (left) together with the relative G and 2D peak intensity probed by means of Raman spectroscopy (right) across the channel. The optical image shows clean and highly defined Ni patterns. From the Raman analysis no presence of amorphous carbon is evidenced.

To overcome this problem a three layers HMDS-LOR-AZ 5214 resist combination has been tried. The LOR bottom layer was used to produce a small undercut after development, which is the result of a faster dissolution of its low molecular-weight species. The presence of an undercut allows the penetration of solvent during the lift-off step, facilitating the removal of the material and resulting in structures with good edge quality. However, in this case we observed a significant quantity of the metal, together with parts of the SiO₂ of the substrate, lifted off right after the metal deposition (see Figure 4.4 (b)).

Finally a double layer resist PMGI/AZ 5214 process has been used followed by a post metal deposition lift-off process carried out in PG remover at 50 °C for several hours. This process routinely yielded clean Ni patterns, thus solving the problem of resist residues (Figure 4.4 (c)). For these samples, Raman spectroscopy has been performed in the area between the source-drain and the voltage probes electrodes to probe the possible formation of carbon nanotubes after the carbon processing at high temperatures. The spectra in Figure 4.4 (c) do not show any carbon signal in the SiO₂ region between Ni electrodes (zero intensity for both, G and 2D peaks) indicating the absence of carbon nanotubes and the consequent possible electric shorts problems between the electrodes.

Direct graphene growth (i.e., not using any mechanical transfer procedure), is then performed on these pre-patterned Ni electrodes using the CVD and RTA methods described in Chapter 3. After graphene synthesis, an Au in-plane gate electrode (50 nm thick) is integrated to the design by UHV evaporation using a stencil mask. This choice is dictated by the fact that the work function of the gate electrode can affect the performances of electrolyte-gated transistors, facilitating or preventing charge injection. In particular it has been shown that contact resistance decreases as high work function metals (such as Au) are used as gate electrode [15].

As a final step, the organic active channel is deposited. IIDDT-C3 is purchased from 1-Materials Inc. and diluted in a Chloroform solution ($\sim 0.25 \text{ g L}^{-1}$). The solution is spin-coated at 1000 rpm for 30 sec resulting in a film of thickness around 20-25 nm (measured with the profilometer). The chip is then transferred on a hotplate for 30 min at 50°C to allow solvent evaporation. Finally a Chloroform moist cotton swab is used to remove IIDDT-C3 in excess and in the exposed contact pads. All processing steps for the preparation of the organic layer were performed inside a glove box under nitrogen atmosphere.

Devices were completed in the top gate geometry using a laminating free-standing ion gel dielectric [16] and laying it over the IIDDT-C3 channel and the side gate electrode. This

side-gated configuration takes advantage of the fact that precise alignment of the gate electrode on the semiconductor channel is not required. On the other hand, due to the large effective gate-to-channel separation (~ 5 mm), a large current hysteresis between forward and reverse sweep will be observed even if a slow gate voltage is used. A gate aligned over the channel will result in a faster device. Therefore a side-gated device sacrifices speed for convenience.

Ion gel was prepared by dissolving the polymer poly(vinylidene fluoride-cohexafluoropropylene), P(VDF-HFP) and the ionic liquid 1-butyl-3-methylimidazolium, [BMIM][PF₆] in acetone. [BMIM][PF₆] and P(VDF-HFP) are purchased by Sigma-Aldrich. P(VDF-HFP) initially was in pellet form and it was ground to fine powder before further use. The weight ratio between polymer, ionic liquid, and solvent was kept to 1:4:7. The gelation happens through bridging PVDF crystals by polymer chains dissolved in the solution. Then the free-standing ion gel layer was drop casted on a glass slide and placed in a vacuum oven at 70°C for 24 hours to remove the residual solvent. Thickness of drop-casted ion gel films, measured by a profilometer, is between 400 and 500 μm . Finally, the ion gel was cut with a razor blade and transferred onto the device using tweezers in such a way to bridge the gate electrodes and to cover the active channel.

The main reason to choose an electrolyte gate is its high specific capacitance ($\sim 10 \mu\text{F}/\text{cm}^2$). This is an important parameter as the charge induced in the transistor channel is directly proportional to the capacitance ($Q = C \times (V_G - V_{Th})$), where Q is the electric charge, C is the capacitance, V_G is the applied gate voltage, and V_{Th} is the threshold voltage.

4.4 Gated-four probes measurements

Contact resistance measurements of the four different metal contact transistors have been carried out by means of gated four-probe method [17, 18, 19, 20, 21]. Transfer curves were acquired by sweeping the gate voltage (V_G) at a constant drain voltage (V_D) of -0.1 V while monitoring the source-drain current (I_{SD}) and the probe potentials (V_1, V_2) at the two fingers positions. Figure 4.5 shows a schematic of electrical connections for the measurements. Keithley 2612A SourceMeter was used to apply V_D and V_G while I_{SD} is measured. A second SourceMeter was used to monitor the two fingers potentials V_1 and V_2 . Due to the slow field-induced diffusion process of the dielectric gate ions, a V_G sweep rate of

0.001 V/s was used to allow sufficient time for their migration. All the measurements are performed inside a N₂-filled glove box at room temperature.

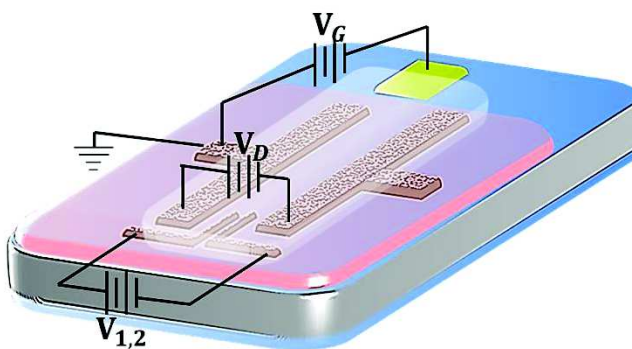


Figure 4.5 Circuit schematic for gated four-probe measurement configuration. During the measurements the source electrode is held at ground and V_D is held constant as V_G is swept. Current into the source and out of the drain electrodes is monitored.

4.4.1 Transport characteristics

Figure 4.6 shows the transfer curves for Au, Ni/RTA, Ni/CVD and Ni devices with channel length $L = 50\mu\text{m}$. The comparison of the four types of samples clearly reveals the differences in source-drain currents and electrochemical threshold voltages. The curves are well behaved and with a clear ON/OFF transition. At low bias gate the current is very low corresponding to the “OFF” state. The current sharply increases by several orders of magnitude as the bias increases. Au and Ni/RTA samples show the highest conductivity values, while the native Ni electrodes clearly exhibit much smaller currents and larger electrochemical threshold voltage. These low performances are expected to result from the lower work function measured for bare Ni and the presence of the oxide layers at the interface with the OSC. Therefore the curves suggest an improvement of the Ni electrodes behavior by passivating their surface with graphene or ultra-thin carbon layers.

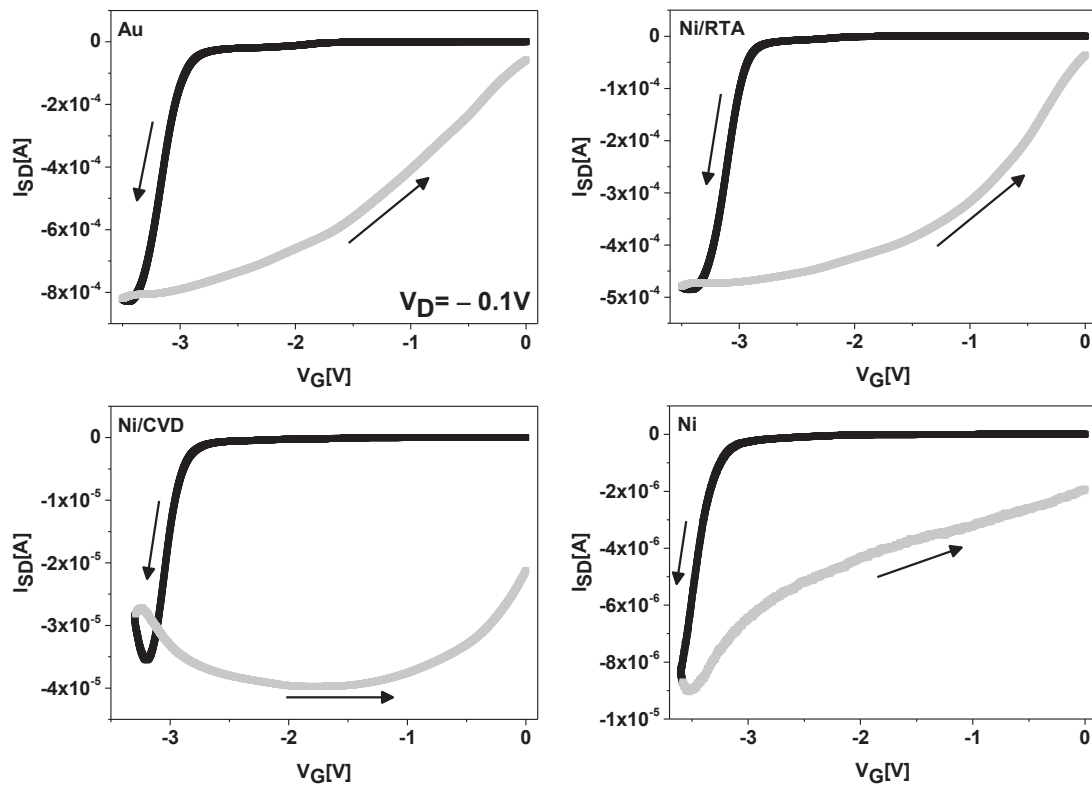


Figure 4.6 Transfer curves of IIDDT-C3 based OFETs with 100 nm thick Au, Ni/RTA, Ni/CVD and Ni electrodes. Forward and reward sweeps are indicated by the arrows.

Moreover, in the case of Au, Ni/RTA and Ni/CVD electrodes the source-drain current I_{SD} saturates above a certain V_G value (around -3.5 V, -3.4 V and -3.2 V, respectively) and a change of the I_{SD} slope, which becomes negative, is observed. This negative slope of the drain current versus gate voltage, also referred to as negative transconductance, is emerging as a common feature in both, electrolyte-gated organic crystals and polymers [22, 23], although it is still not completely understood. Different possible causes have been proposed, such as bipolaron formation [24], carrier-carrier correlation [25], and band filling [26]. Surely, the appearance of the negative transconductance indicates the maximum V_G applicable and therefore the maximum doping level.

The negative transconductance peak is not present in Ni electrodes (even sweeping up to $V_G = -3.6$ V) indicating that the sample is still not gated at its maximum.

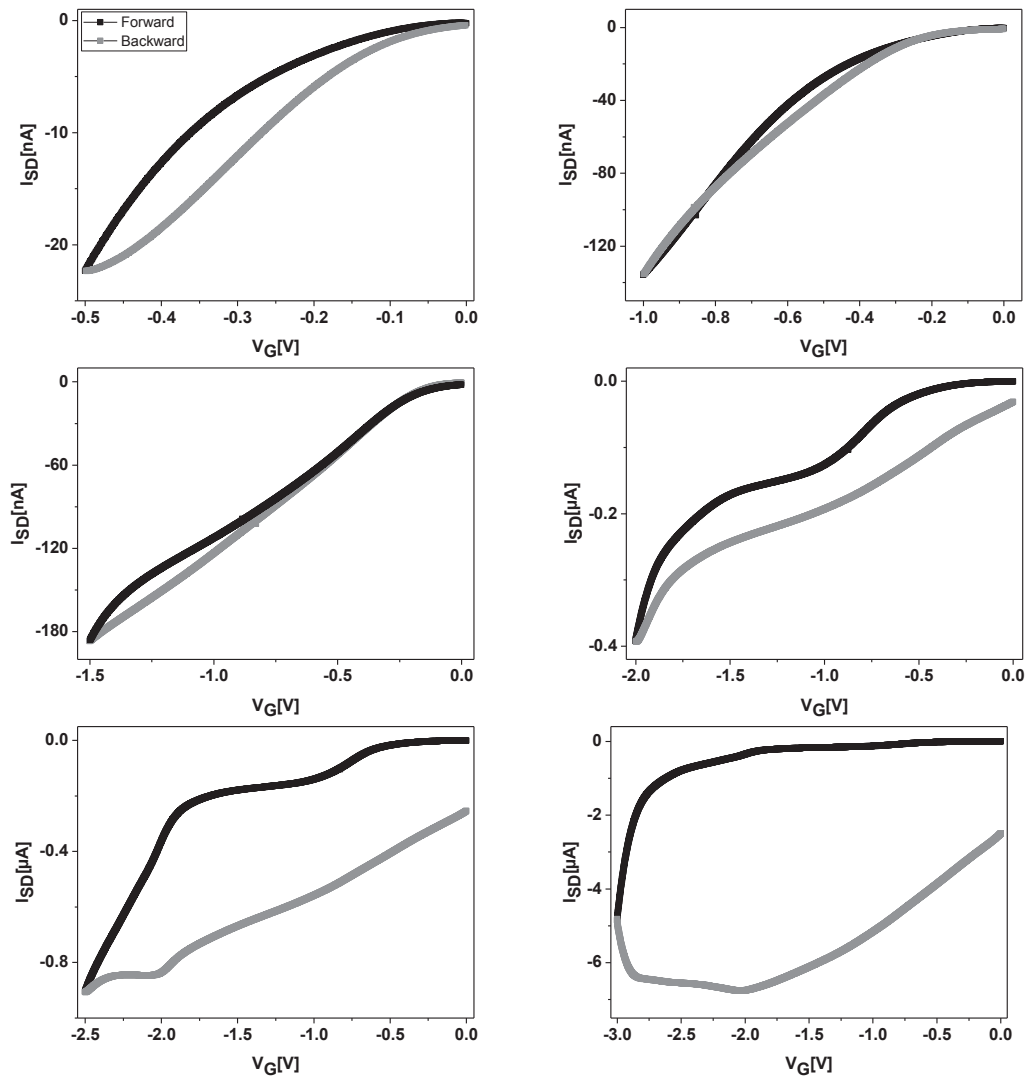


Figure 4.7 Transfer curve, for the Ni/RTA sample, showing how increasing the gate voltage opens the hysteresis in the IV curve. The gate voltage is swept at -1 mV/s. The panels show increasing values of the maximum gate voltage stress. Exceeding -2.5 V results in a significant hysteresis in the transfer curves, illustrating the emergence of electrochemical doping of the active channel.

Despite the slow V_G sweep rate, in all the cases a high degree of hysteresis between forward and reward traces is observed. This hysteresis is another sign of an important electrochemical doping of the polymer and a no-instantaneous charging of the ion gel with the application of the gate bias. It is in fact reduced under lower gate voltage stress, as shown in Figure 4.7. The electrochemical doping is a reversible process by depolarization of the electrolyte at $V_G = 0$ V maintaining source-drain bias. Therefore the operating principle of the device is based on the doping and de-doping of the polymer.

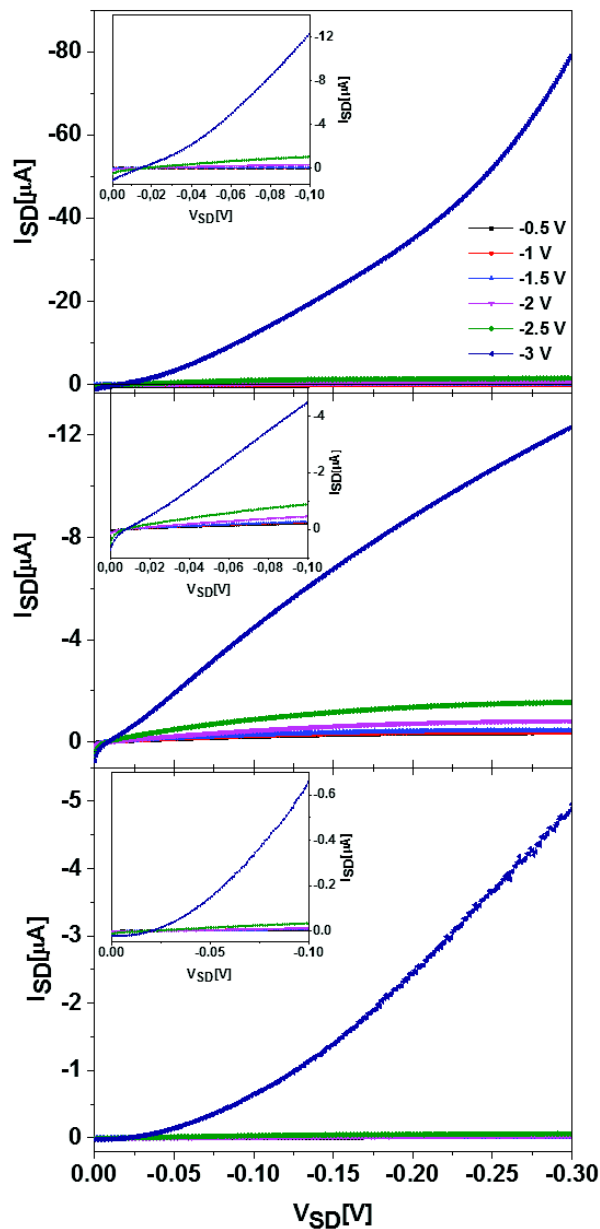


Figure 4.8 Output curves of OFET devices. Au (top), Ni/RTA (middle) and Ni (bottom) samples are tested. Insets are zoom-out plot (source-drain voltage 0V-0.1V). The 0.1V measurement choice value is a best compromise choice for ensuring uniformity in the doping and limited systematic errors due to non-linearity of the curves (in particular at bias values below 20 mV).

Output curves have been measured sweeping the source-drain bias (V_{SD}) at a rate of 0.001 V/s while keeping the gate voltage constant. For all the measurements, the value of -0.1 V chosen as source-drain bias is low enough to ensure nearly uniform doping of the active channel, and large enough to avoid non-linear behavior of the output curve, occurring

for values below 20 mV (see output curves in Figure 4.8). The nonlinearity of our output curve can lead to a typical 10% inaccuracy in our resistance data.

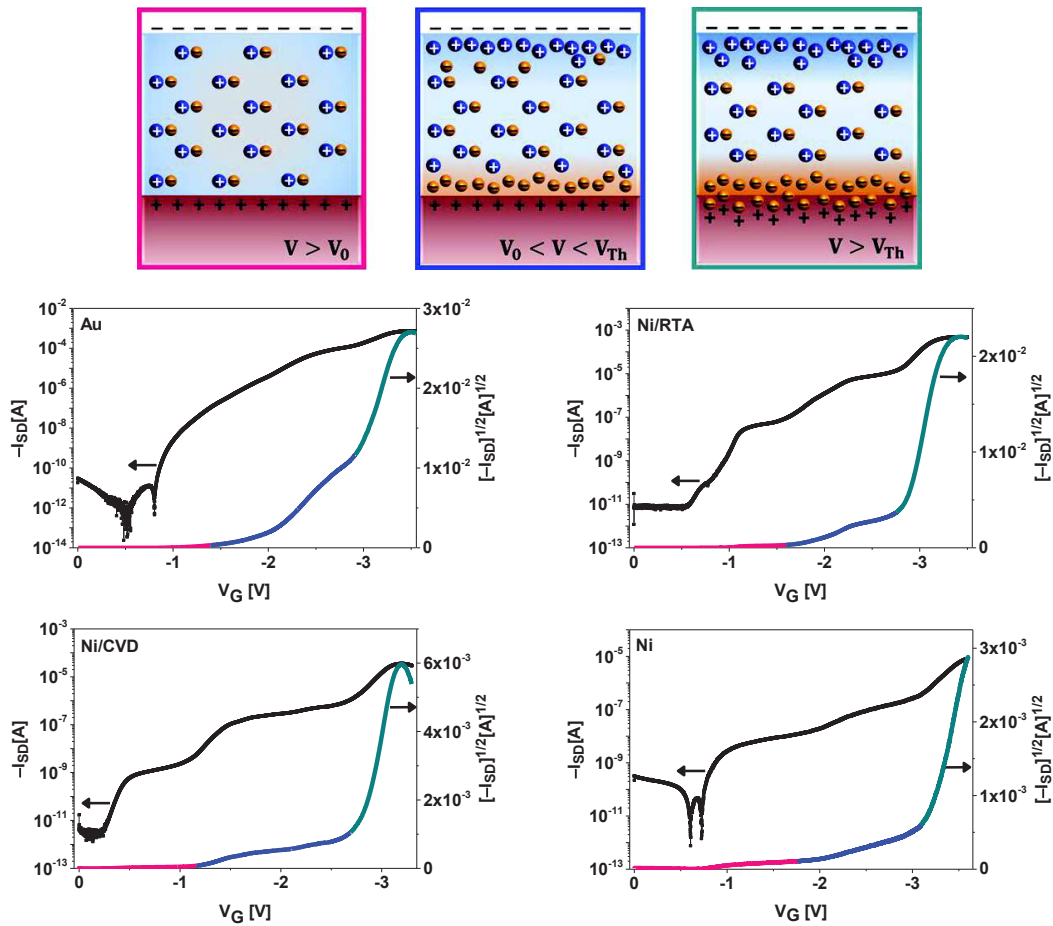


Figure 4.9 Schematic representation of the operating mechanism of the electrolyte-gated transistors at different steps of the applied V_G together with the plots of the dI_{SD} and $\sqrt{I_{SD}}$ versus V_G in log and linear coordinates, respectively. See discussion of the two linear regime of the $\sqrt{I_{SD}}$ curve. For gate voltage between -1.5 and -2.5 V, the ion gel mostly polarizes the interface. For larger negative gate voltage, volume electrochemical doping increases the effective thickness of conducting material. Only the forward trace is plotted. Threshold voltage is extracted from the linear plot of the $\sqrt{I_{SD}}$ intersecting the V_G axis in the saturation region.

The operating principle of the measured devices can be deduced from the plot of the I_{SD} square root (red curve) as a function of V_G . As shown in Figure 4.9, together with a schematic design of the electrochemical doping mechanism, the plots emphasize two distinctive voltages. The onset voltage, V_0 (first slope in Figure 4.9), is the gate voltage at

which the negative ions are first present at the ion-gel/ OSC interface (device turn-on voltage) and act as a large electric field gating of the device. Only the first nanometers at the interface between active channel and gating medium contribute to the conductivity in this regime dominated by electric field induced doping. The threshold voltage, V_{Th} (onset of the third slope in Figure 4.9), relates to an increase in $\sqrt{I_{SD}}$ slope, at the onset of electrochemical doping of the bulk of the OSC layer. This electrochemically-doped FET (EFET) regime is expected to result in significantly smaller interface resistance values, as the active channel can involve the whole thickness of the OSC [16, 27]. The region in between, that is $V_0 < V < V_{Th}$ (second slope in Figure 4.9), represents an intermediate operation mode in which the charge transport is confined to a thin layer of the semiconductor, in proximity of the ion-gel interface.

4.4.2 Contact resistance extrapolation

We take advantage of the four-probes configuration to extract the specific contact resistance ($R_C \cdot W$) and the sheet resistance (R_{Sheet}). The specific contact resistance is usually expressed as a resistance per unit length ($\Omega \cdot \text{cm}$), where W relates to the width of the active channel. Contact resistance is obtained by linear extrapolation between V_1 and V_2 as a function of the position. The difference between the extrapolated values and the applied voltage at each contact ($V_S = 0V$ and $V_D = -0.1 V$) gives the values of the voltage drops at the source (ΔV_S) and drain (ΔV_D). With the knowledge of the total current flowing through the device, the contact resistance values at source R_S , and drain R_D , can then be simply calculated from Ohm's law as $\Delta V_S / I_D$ and $\Delta V_D / I_D$ for source and drain, respectively.

Figure 4.10 shows the extracted width-normalized contact resistance and the sheet resistance for the four different metal electrodes as a function of the applied V_G . The data are truncated at V_G close to the threshold voltage where the device begins to conduct. For all the devices, a typical drop of the $R_C \cdot W$ with increasing gate voltage is observed. As it is emphasized by the star symbol in the plot of Figure 4.10, in the range of the high applied V_G (exceeding $-3 V$) the contact resistance of Ni/CVD and Ni/RTA devices are respectively one and two orders of magnitude lower than the one related to Ni device. This illustrates the role of the passivation of Ni surface in improving the metal/OSC interface.

The difference of the sheet resistance magnitude reflects the difference of the charge injection and doping processes in each device depending on the metal contact. As it is indicated by the star symbols, the same value of R_{sheet} is reached at $V_G = -3.6$ V and $V_G = -2.5$ V for Ni and Au, respectively. The high sheet resistance value for Ni contact, together with the absence of the negative transconductance, is a further indication that in the range of the applied V_G values, the sample has not yet reached the maximum doping level. The close values of both, contact and sheet resistance, for Ni/RTA and Au electrodes are a sign of reproducibility of the data and the behavior of these contacts.

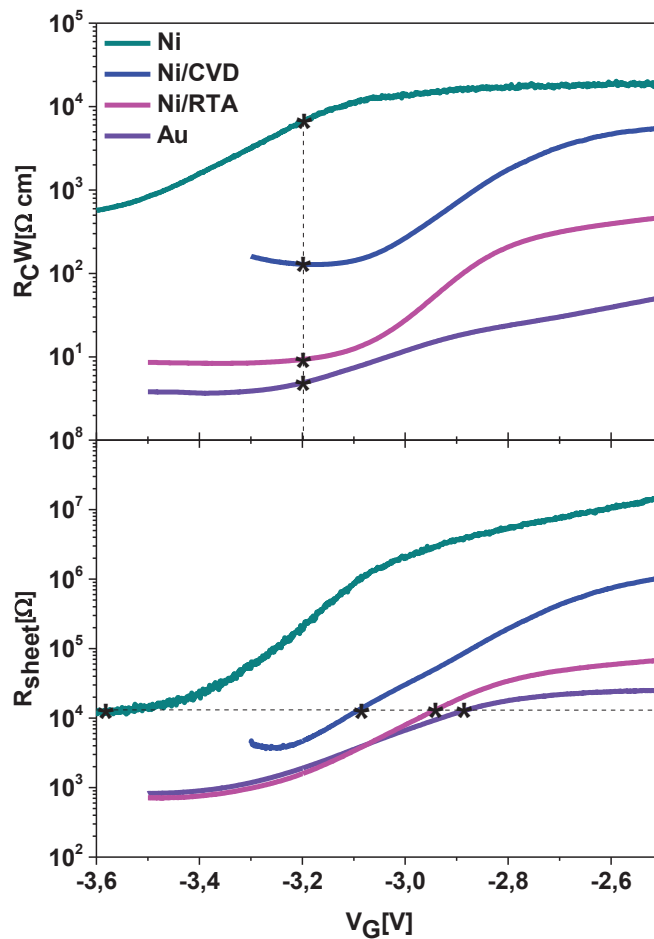


Figure 4.10 Width-normalized total contact resistance (top panel) and (bottom panel) sheet resistance as a function of gate voltage for 100 nm thick Au, Ni/ RTA, Ni/ CVD and Ni electrodes.

As already mentioned, the gated-four probes measurements make possible the probing of the potential drop inside the channel. Figure 4.11 shows a surface plot of sense

probe voltage and voltage drop for the transfer curves of the best performing Au and Ni/RTA devices, as a function of both channel position and gate voltage. The drop in potential ΔV_S and ΔV_D is given as the difference between the potential at the contacts ($V_{S,extrap}$ and $V_{D,extrap}$) from the extrapolated channel potential and the actual applied source-drain voltage. At a given V_G , the straight lines connecting the source, potential probe 1, potential probe 2, and the drain electrodes determine the channel potential profile. From the plot, it is easy to see that Au and Ni/RTA contacts induce similar potential drops.

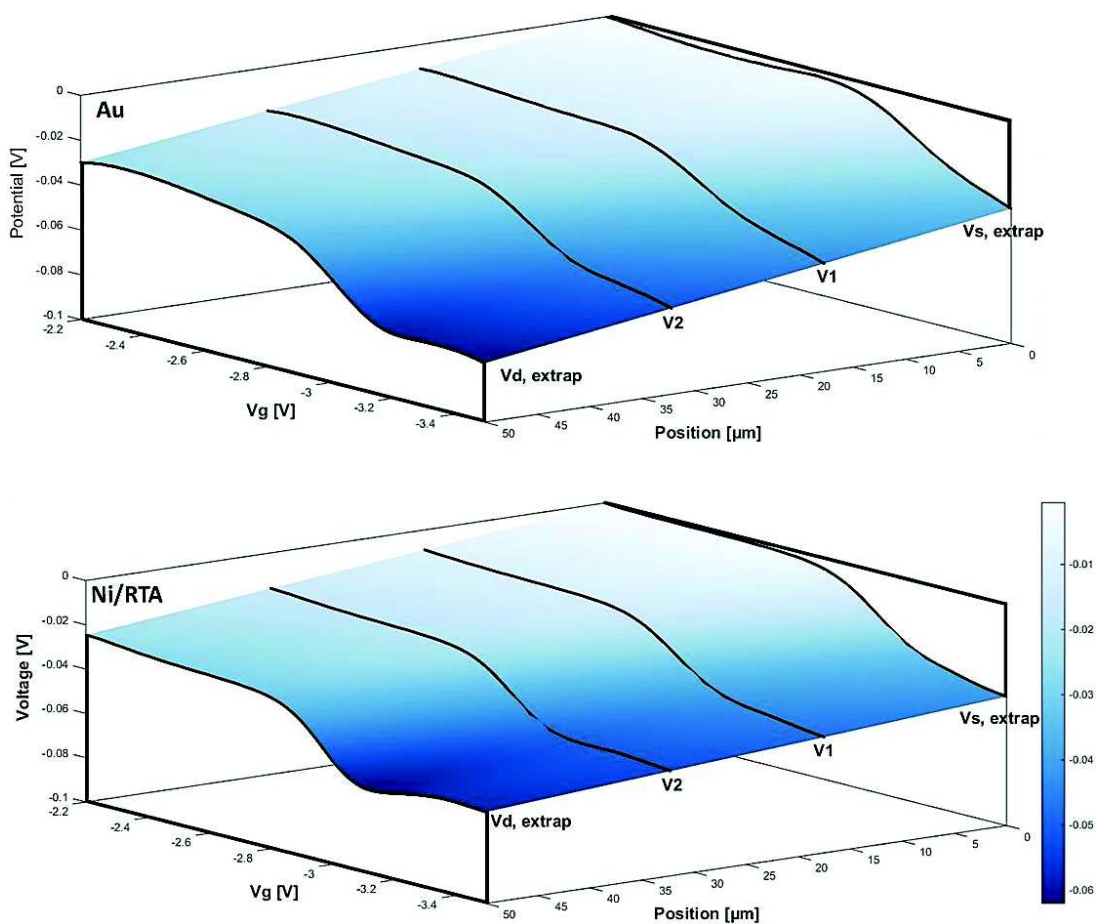


Figure 4.11 Surface plots of the channel potential as a function of gate voltage and position within the channel. V_1 and V_2 are the potentials measured at the position of the channel probes. The plots correspond to the data for Au and Ni/RTA devices in Figure 4.10 with $V_D = -0.1$ V.

Figure 4.12 shows a comparison of specific contact resistance at source and drain (R_S and R_D) as a function of V_G for devices with Au (red lines) and Ni/RTA (black lines)

electrodes, illustrating how Ni/RTA can compare favorably to the best performing Au electrodes. For both devices, R_S and R_D have the same order of magnitude and the same behavior, with Au only marginally better performing than Ni/RTA. At low V_G the contact resistance at source and drain both exhibit rather large values, with R_D significantly larger than R_S . As V_G decreases, R_S decreases weakly, while R_D decreases significantly and eventually lines out. Figure 4.12 also reveals that large gate bias makes R_S similar to R_D , suggesting that charge injection is fully optimized.

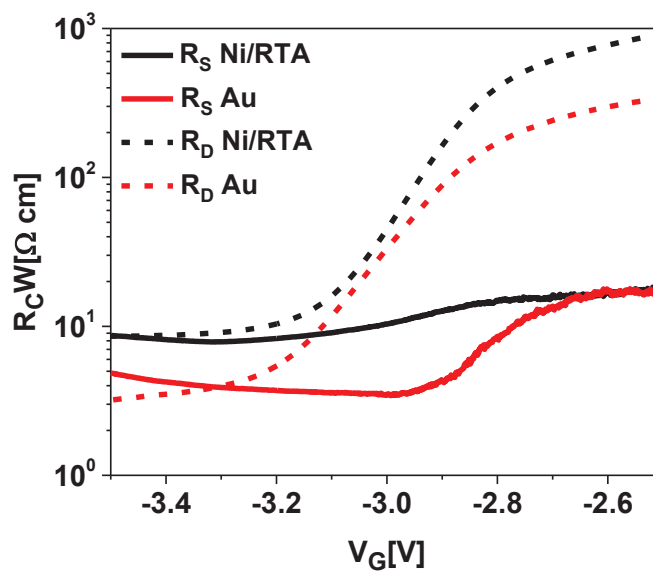


Figure 4.12 Source and drain contact resistance as a function of V_G for Au (red curves) and Ni/RTA (black curves) OFETs.

Finally, Table 4.1 summarizes the key observed conductivity/resistance values of the four studied samples. This quantitatively clearly shows how Au and Ni/RTA electrodes outperform the other two types of samples.

Metal contacts	WF [eV]	R' [$\Omega\cdot\text{cm}$] $V_G=-3.2\text{V}$	R' [$\Omega\cdot\text{cm}$] max. V_G	R _{Sheet} [K Ω] $V_G=-3.2\text{V}$	ρ [$\Omega\cdot\text{cm}$] at $V_G=-3.2\text{V}$	σ [S/cm] at $V_G=-3.2\text{V}$	V _{Th}	I _{ON/OFF}
Au	5.1	4.9	3.7	1.9	3.8×10^{-3}	263.1	-2.71	$\sim 10^9$
Ni/RTA	5.0	9.3	8.4	1.6	3.2×10^{-3}	312.5	-2.79	$\sim 10^8$
Ni/CVD	5.11	129.4	129.4	4.6	9.2×10^{-3}	108.3	-2.75	$\sim 10^7$
Ni	4.85	6.6×10^3	1.6×10^3	48.7	97.5×10^{-3}	10.2	-3.12	$\sim 10^6$

Table 4.1 Measured values of work function, contact resistance, sheet resistance, resistivity, conductance, threshold voltage and on/off current for IIDDT-C3 based OFETs with 100 nm thick Au, Ni/RTA, Ni/CVD and Ni electrodes.

4.5 Conclusions

In this chapter we presented a study on the electric performances of devices made of Ni electrodes covered with carbon based thin films processed with CVD and RTA methods. A comparison with bare Ni and Au electrodes is also shown. The outcome of our study is that the contact resistance of Ni/CVD and Ni/RTA decreases of one and two orders of magnitude, respectively, with respect to the value measured for Ni devices. In particular, our quantitative study indicates that Au and Ni/RTA electrodes outperform the other two types of samples and therefore Ni/RTA electrodes are well suited to replace gold for organic electronics devices. This might provide a clear advantage for cost issues, and is expected to be the best approach for making spin injectors and detectors for organic spintronic applications.

References

1. Silva, S. R. P. *Properties of Amorphous Carbon*. (IET, 2003).
2. Karpan, V. M. *et al.* Graphite and Graphene as Perfect Spin Filters. *Phys. Rev. Lett.* **99**, 176602 (2007).
3. Dlubak, B. *et al.* Graphene-Passivated Nickel as an Oxidation-Resistant Electrode for Spintronics. *ACS Nano* **6**, 10930–10934 (2012).
4. Godel, F. *et al.* Voltage-controlled inversion of tunnel magnetoresistance in epitaxial nickel/graphene/MgO/cobalt junctions. *Appl. Phys. Lett.* **105**, 152407 (2014).
5. Banerjee, T., van der Wiel, W. G. & Jansen, R. Spin injection and perpendicular spin transport in graphite nanostructures. *Phys. Rev. B* **81**, 214409 (2010).
6. Bürgi, L., Richards, T. J., Friend, R. H. & Sirringhaus, H. Close look at charge carrier injection in polymer field-effect transistors. *J. Appl. Phys.* **94**, 6129–6137 (2003).
7. Hamadani, B. H. & Natelson, D. Nonlinear charge injection in organic field-effect transistors. *J. Appl. Phys.* **97**, 064508 (2005).
8. Braga, D., Ha, M., Xie, W. & Frisbie, C. D. Ultralow contact resistance in electrolyte-gated organic thin film transistors. *Appl. Phys. Lett.* **97**, 193311 (2010).
9. Ertl, G. & Kupperts, J. *Low Energy Electrons and Surface Chemistry*. (Wiley-VCH Verlag GmbH, 1986).
10. Cardona, M. & Ley, L. in *Photoemission in Solids I* (eds. Cardona, M. & Ley, L.) 1–104 (Springer Berlin Heidelberg, 1978).
11. Hölzl, J. & Schulte, F. K. in *Solid Surface Physics* (eds. Hölzl, P. D. J., Schulte, D. F. K. & Wagner, D. H.) 1–150 (Springer Berlin Heidelberg, 1979).
12. Stalder, R., Mei, J., Graham, K. R., Estrada, L. A. & Reynolds, J. R. Isoindigo, a Versatile Electron-Deficient Unit For High-Performance Organic Electronics. *Chem. Mater.* **26**, 664–678 (2014).
13. Lei, T., Wang, J.-Y. & Pei, J. Design, Synthesis, and Structure–Property Relationships of Isoindigo-Based Conjugated Polymers. *Acc. Chem. Res.* **47**, 1117–1126 (2014).
14. Lei, T. *et al.* High-Performance Air-Stable Organic Field-Effect Transistors: Isoindigo-Based Conjugated Polymers. *J. Am. Chem. Soc.* **133**, 6099–6101 (2011).
15. Fabiano, S., Braun, S., Fahlman, M., Crispin, X. & Berggren, M. Effect of Gate Electrode Work-Function on Source Charge Injection in Electrolyte-Gated Organic Field-Effect Transistors. *Adv. Funct. Mater.* **24**, 695–700 (2014).
16. Lee, K. H. *et al.* ‘Cut and Stick’ Rubbery Ion Gels as High Capacitance Gate Dielectrics. *Adv. Mater.* **24**, 4457–4462 (2012).
17. *Organic Field-Effect Transistors*. **20073029**, (CRC Press, 2007).
18. Chesterfield, R. J. *et al.* Variable temperature film and contact resistance measurements on operating n-channel organic thin film transistors. *J. Appl. Phys.* **95**, 6396–6405 (2004).
19. Natali, D. & Caironi, M. Charge Injection in Solution-Processed Organic Field-Effect Transistors: Physics, Models and Characterization Methods. *Adv. Mater.* **24**, 1357–1387 (2012).

20. von Hauff, E., Spethmann, N. & Parisi, J. A Gated Four Probe Technique for Field Effect Measurements on Disordered Organic Semiconductors. *Z. Naturforschung Teil A* **63**, 591–595 (2008).
21. Pesavento, P. V., Chesterfield, R. J., Newman, C. R. & Frisbie, C. D. Gated four-probe measurements on pentacene thin-film transistors: Contact resistance as a function of gate voltage and temperature. *J. Appl. Phys.* **96**, 7312–7324 (2004).
22. Xia, Y., Xie, W., Ruden, P. P. & Frisbie, C. D. Carrier Localization on Surfaces of Organic Semiconductors Gated with Electrolytes. *Phys. Rev. Lett.* **105**, 036802 (2010).
23. Xie, W., Liu, F., Shi, S., Ruden, P. P. & Frisbie, C. D. Charge Density Dependent Two-Channel Conduction in Organic Electric Double Layer Transistors (EDLTs). *Adv. Mater.* **26**, 2527–2532 (2014).
24. Street, R. A., Salleo, A. & Chabinyk, M. L. Bipolaron mechanism for bias-stress effects in polymer transistors. *Phys. Rev. B* **68**, 085316 (2003).
25. Xia, Y., Cho, J., Paulsen, B., Frisbie, C. D. & Renn, M. J. Correlation of on-state conductance with referenced electrochemical potential in ion gel gated polymer transistors. *Appl. Phys. Lett.* **94**, 013304 (2009).
26. Paulsen, B. D. & Frisbie, C. D. Dependence of Conductivity on Charge Density and Electrochemical Potential in Polymer Semiconductors Gated with Ionic Liquids. *J. Phys. Chem. C* **116**, 3132–3141 (2012).
27. Laiho, A., Herlogsson, L., Forchheimer, R., Crispin, X. & Berggren, M. Controlling the dimensionality of charge transport in organic thin-film transistors. *Proc. Natl. Acad. Sci.* **108**, 15069–15073 (2011).

5

Study of the contact resistance in short channel EGOFETs

In this chapter nanoscale EGOFETs based on two p-type polymers, PBTTT and IIDDT-C3, are studied. High $I_{ON/OFF}$ values ($>10^6$), clear saturation of the output characteristics measured at room temperature and remarkably low values of contact resistance down to low temperatures are evident indications of the suppression of short channel effects which usually characterize short channel devices. Our findings pave the way for applications not only in organic electronics but also in organic spintronics where short channel length is a crucial requisite for the spin signal conservation.

5.1 Introduction

In the current literature, reported OFETs studies are mostly related to devices whose channel lengths typically range from millimeter down to several micrometers. They usually have interdigitated electrodes geometry, necessary to produce a large and easily measurable output current since organic semiconductors have very low carrier density. Moreover, since the cut-off frequency of OFETs is proportional to μ/L^2 (where μ is the charge carrier mobility and L the channel length), their operative frequencies are also limited to the kHz regime. To give an idea, organic electronics pixels in large screen displays, for example, require a cut-off frequency at several kHz. In this scenario, the miniaturization of OFETs down to 100 nm regime is needed to increase switching speed and the circuit density (also proportional to L^{-2}).

Moreover, due to the short spin diffusion length in OSCs (between 10 and 100 nm) [1], OFETs with nanometer channel lengths are needed for investigation of spin transport in a controllable and measurable way.

However, highly scaled channel lengths in OFETs result in a variety of detrimental short-channel effects [2] as a consequence of two main problems. First, in devices with small active areas (sub- μm^2) transport is mostly dominated by the contact resistance at the electrode/organic SC interface rather than by the bulk of the organic material. Second, shortening the active channel generally increases the longitudinal electric field strength. As a result, efficient gating through transverse electric field becomes challenging. Under these conditions, the standard formulas for studying carrier transport in OFETs, discussed in Chapter 1, do not longer apply and consequently, the parameters extracted from them are dubious.

Electrolyte gating represents an interesting approach to increase the transversal electric field thanks to the high capacitance of the very thin electric double layer (only few angstroms) formed at the electrolyte-semiconductor interface.

In this chapter we report on the fabrication of nanoscaled thieno[3,2-b]thiophene and 4,4-dialkyl 2,2-bithiophene (PBTTT)-based devices and on the study of their carrier transport properties. PBTTT has been chosen for this study for two main reasons: it is a high mobility semiconducting polymer [3] and it has been shown to exhibit a significant spin diffusion length [4]. A comparison with poly[1,1'-bis(4-decyltetradecyl)-6-methyl-6'-(5'-methyl-[2,2'-bithiophen]-5-yl)-[3,3'-biindolinylidene]-2,2'-dione] (IIDDT-C3) thin films is also discussed. We will show later that these two OSCs exhibit different structural properties at

the 100 nm scale. These properties can be particularly exploited in sub-100 nm junctions in order to have only few crystallites in the transistor channel. In this case highly mobile charge carriers will flow along the π -stacking and the π -conjugated backbone directions, avoiding or reducing the degrading effect of defects and amorphous grain boundary regions on the electronic carriers transport.

5.2 PBTTT thin films

PBTTT belongs to the family of polythiophene semiconducting polymers. Polythiophenes are made of aromatic thiophene rings, in Figure 5.1 (a), coupled together in their 2nd and 5th position to form an extended delocalized electronic π -orbital. Along the chain, the thiophene rings are ideally coplanar. Surely the most used and extensively studied polythiophene is poly(3-hexylthiophene) (P3HT in Figure 5.1 (b)).

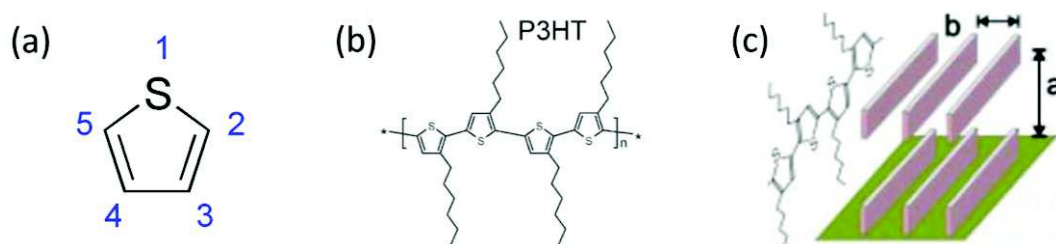


Figure 5.1 (a) Thiophene ring monomeric unit with position numbers; (b) P3HT chemical structure; (c) Edge-on arrangement of highly regioregular P3HT.

Depending on the position at which the alkyl chains are attached to the P3HT backbone, namely head-to-tail or head-to-head [5] there are several ways in which alkylthiophenes self-assemble. If the alkyl chains are attached without any particular order along the polymer chain (Figure 5.2 (a)), following for example a random sequence of head-to-tail or head-to-head building blocks, the polymer is said regiorandom. In this case the backbone contains units that are twisted with respect to each other causing poor intermolecular orbital overlap and disorder with consequent low charge carrier mobility (down to 10^{-4} $\text{cm}^2/\text{V}\cdot\text{s}$). On the other hand, if the alkyl chains are introduced in the thiophene units all pointing towards the same direction, that is, head-to-tail (Figure 5.2 (b)), the polymer is regioregular. In this case the building blocks of the backbone are

planar and self-assemble into more crystalline structures with close π -stacking and lamella packing with two-dimensional conjugated sheets perpendicular to the sample plane resulting in an edge-on configuration (Figure 5.1 (c)). In this case charge carrier mobility can reach values up to $0.1 \text{ cm}^2/\text{V}\cdot\text{s}$ [6].

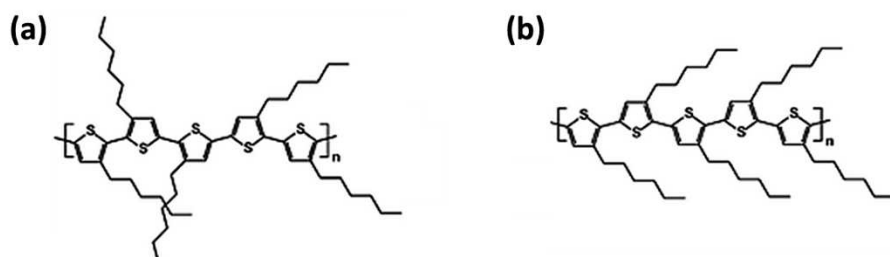


Figure 5.2 (a) Regiorandom and (b) regioregular structure of P3HT.

To avoid regio-irregularities and to improve the performance and stability of polythiophene polymers Mc Culloch *et al.* synthesized in 2006 the polymer PBTTT [3]. Two main improvements have been implemented with respect to P3HT. First, a lower density of side chains which allows the molecular stacks to interdigitate and to form closely packed lamellar structures. Second, a fused thiophene ring (thieno[3,2-b]thiophene and 4,4-dialkyl 2,2bithiophene) has been integrated in the monomer backbone which plays two main roles: it increases the ionization potential (IP=5.1eV) thus giving to the polymer better chemical stability; and it increases the rigidity of the backbone, resulting in the formation of highly-ordered crystalline domains that practically enhance the charge carriers mobility. This thienothiophene unit is appended on each side to a single thiophene unit that contains long alkyl side chains.

The typical crystalline arrangement of PBTTT is edge-on, i.e. the rings are perpendicular to the plane of the substrate and polymer backbones lie parallel to the substrate [7].

When heated above its mesophase transition temperature, PBTTT forms large crystalline domains on the length scale of lithographically accessible channel lengths (several tens of nm) thus paving the way for the realization of single-crystal polymer transistors.

PBTTT has one of the highest reported field-effect mobility to date for polymer transistors, amounting to $1\text{cm}^2\text{V}^{-1} \text{ s}^{-1}$ in optimized devices.

PBTTT used in this thesis (PBTTT-C12 in Figure 5.3) has been synthesized by Dr N. Leclerc (ICPEES, Strasbourg) according to the recipe described in literature [3], with average molecular weight (M_n) of 27 kDa and a polydispersity index (PDI) of 1.7 (PDI is a measure of the heterogeneity of the polymer chains size; it approaches 1 when all the polymer chains are identical). The chains of this PBTTT are in average formed by ~ 40 monomers, that would correspond to 50 - 60 nm chain length.

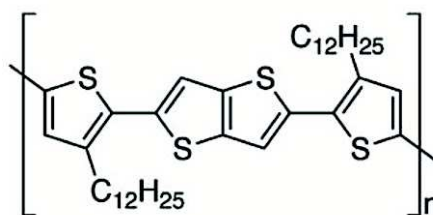


Figure 5.3 Chemical structure PBTTT monomer.

PBTTT solution in orthodichlorobenzene (ODCB) with a concentration of 4 mg/mL, is heated at 130°C - 150°C and spin-coated (~ 100 μ L per substrate) in two steps: at 1000 rpm for 120 s, and at 2000 rpm for 60 s. After deposition, the contact pads far from the central device area, the in-plane gate electrode, and the backside of the substrate are cleaned from PBTTT with a solvent-wet cotton bud. The thickness of the resulting thin films has been measured with a stylus profilometer giving values of 20 - 25 nm.

Properties of IIDDT-C3 have been already detailed in Section 4.2.

5.3 Contact resistance study on large scale EGFETs

Before studying nanosized devices we performed a comparative analysis of charge carriers transport of PBTTT and IIDDT-C3 thin films on large scales ($L = 40$ μ m) transistors. This study will be used to determine key parameters such as the intrinsic conductivity and the specific contact resistance, which are impossible to measure directly on short-channel devices.

Top gate bottom contact transistor structures, as the ones studied in Chapter 4, have been used to characterize PBTTT and IIDDT-C3 thin films as a function of gate voltage and temperature. EGFETs with 100 nm thick Au electrodes have been fabricated as described

in Section 4.3 adding a further processing step for the patterning of a SiO_2 window to minimize the contact area between the metallic contacts and the electrolyte gate and thus to reduce the leakage current. The studied EGOFET geometry together with the schematic of the used four-probe measurement circuit, is shown in Figure 5.4.

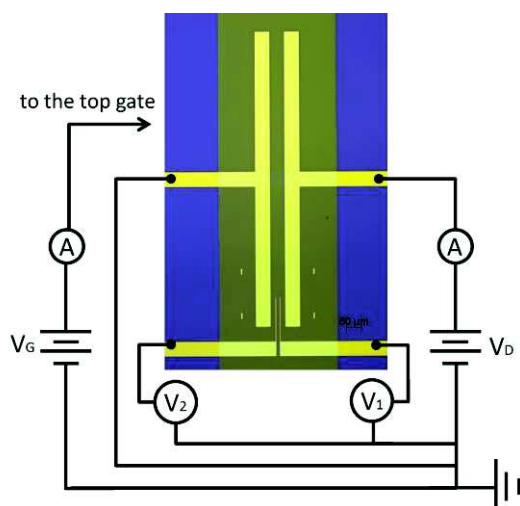


Figure 5.4 Schematic drawing of the measuring circuit for gated- four probe method on transistor geometry. SiO_2 window on top of the active area of the device is clearly visible by the contrast.

Transfer curves at room temperature were acquired inside a N_2 -filled glove box with a SourceMeter unit (Keithle2612A) applying a constant source-drain bias $V_D = -0.1$ V sweeping the gate voltage V_G from 0 to -3 V with a rate of 0.001 V/sec, made very slow in order to ensure the slow migration of the ions. For the extraction of the source/drain contact resistances and the channel resistance, gated-four probe technique has been used where the potentials of the two mid-channel sense probes (V_1 and V_2) were measured using a second SourceMeter. Transfer characteristics for both, PBTTC- and IIDDT-C3-based Au devices are plotted in Figure 5.5 (a), while Figure 5.5 (b) shows a plot of the extracted specific contact resistance ($R_c \cdot W$) at the source and drain electrodes for the two devices as a function of the gate voltage. Source and drain contact resistances behave in a very similar way for the two different polymers diminishing as V_G increases. Very low specific contact resistance values are observed, in agreement with the findings in the previous chapter.

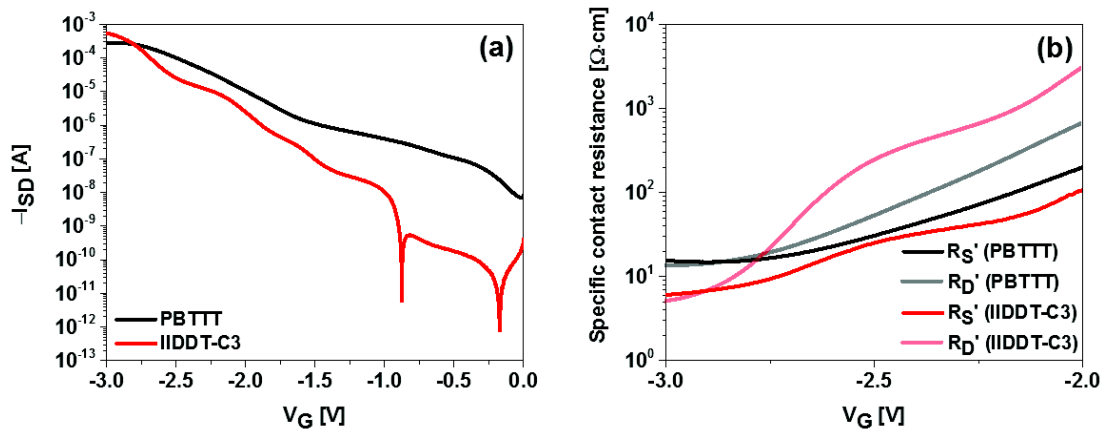


Figure 5.5 (a) Transfer curves of PBTTT- and IIDDT-C3-based large scale ($L = 40 \mu\text{m}$) EGFETs at room temperature. (b) Specific contact resistance at source and drain for the two devices as a function of V_G . Data for $V_G < -2 \text{ V}$ are not presented because the ion gel dielectric is not completely charged.

Output curves, measured sweeping the V_D (between 0 and -0.3 V) at different constant V_G (from -0.5 V to -3 V with a -0.5 V amplitude ramp 0.001 V/sec), follow the expected electrical behavior: I_{SD} increases linearly for low V_D with indication of starting to saturate at higher V_D for PBTTT (Figure 5.6). Note that we are restricted in the applied source-drain voltage if we want to ensure that the channel is rather uniformly doped. This explains why the saturation regime of the transistor is not attained.

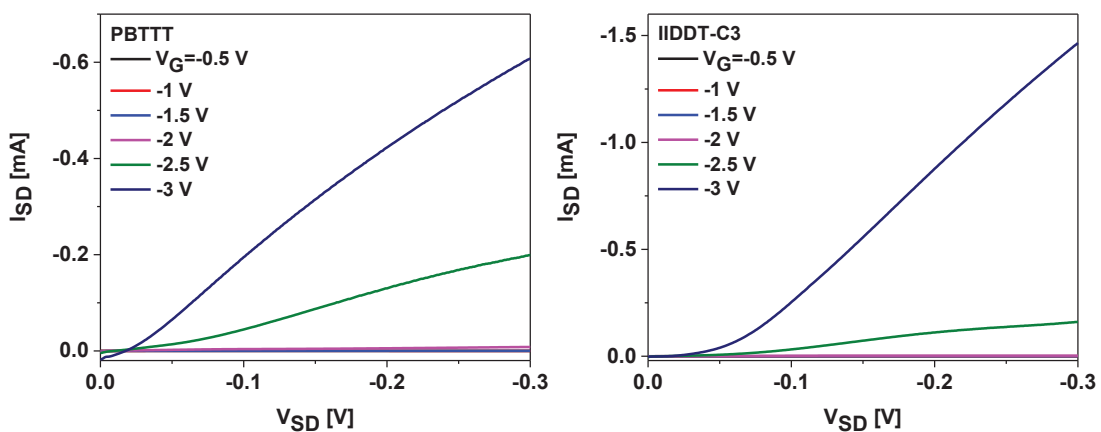


Figure 5.6 Output curves of PBTTT- and IIDDT-C3-based large scale EGFETs at room temperature.

5.3.1 Charge carriers transport at low temperature

Low temperature electrical measurements were carried out inside a low-pressure ($P < 10^6$ mbar) helium static cryostat at temperatures down to 1.5 K. Measurements of electrical properties were performed with a Keithley 2634 series SourceMeter and a Keithley 2182 nanovoltmeter using the four probes technique.

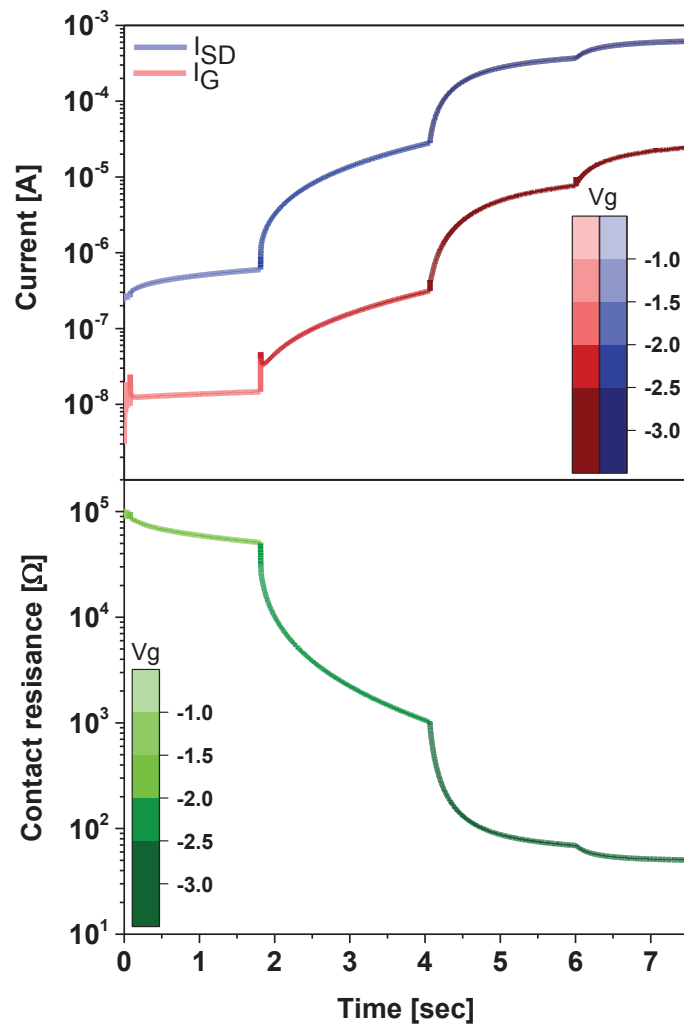


Figure 5.7 Source-drain current I_{SD} , gate current I_G and contact resistance R_C are monitored versus time during the gating process.

Before cooling, the samples were gated inside the cryostat chamber at a temperature of 300 K with a source-drain bias $V_D = -0.1$ V. Differently from the transfer curve measurements at room temperature, the gate voltage was not swept, but kept at a constant

value for at least 30 minutes. The leakage current I_G was monitored to ensure that there was no significant leak through the gate. The doping process starts with applying a gate voltage $V_G = -0.5$ V. Once the system reaches the equilibrium, indicated by a plateau of the I_{SD} and I_G versus time, the gate voltage is incremented by -0.5 V as shown in Figure 5.7. This procedure is repeated until the samples reached the maximum doping. The relative maximum gate voltage value, reproducible within 0.1 V, was calibrated as the one saturating the source-drain current before the appearance of the negative transconductance peak and without excessive gate current, both indicating unwanted electrochemical reactions with the uncovered electrodes area.

Each increment of V_G was followed by a peak of I_G as a response of the ions moving inside the electrolyte and thus starting the capacitive charging process. At the same time the resistance decreases. Once the maximum gating has been reached, the samples were cooled under constant V_G . This gating procedure is reversible upon heating the sample up to 300 K while applying a constant $V_G = 0$ V.

Figure 5.8 (a) and (b) shows the specific contact resistance $R_C \cdot W$ as a function of the temperature for PBTTT and IIDDT-C3, respectively, together with the respective IV curves taken at low temperatures (Figure 5.8 (c) and (d)). Figure 5.8 (e) and (f) shows separately the IV curves for IIDDT-C3 at 5K and 10 K, not clearly visible in Figure 5.8 (d). While the two polymers behave the same way at high temperature exhibiting similar values of contact resistance and of the current in the IV curves until 80 K, they evidently differ at low temperatures with IIDDT-C3 being less performing and showing a much stronger temperature dependence with linear IV curves persisting only down to 10 K. For comparison in PBTTT non-linearity of the IV curves appears only at 1.5 K.

Moreover, gated four-probe measurements allow us to extract the values of conductivity for the two polymers. These values at 300 K are 440 S/cm and 380 S/cm for PBTTT and IIDDT-C3, respectively.

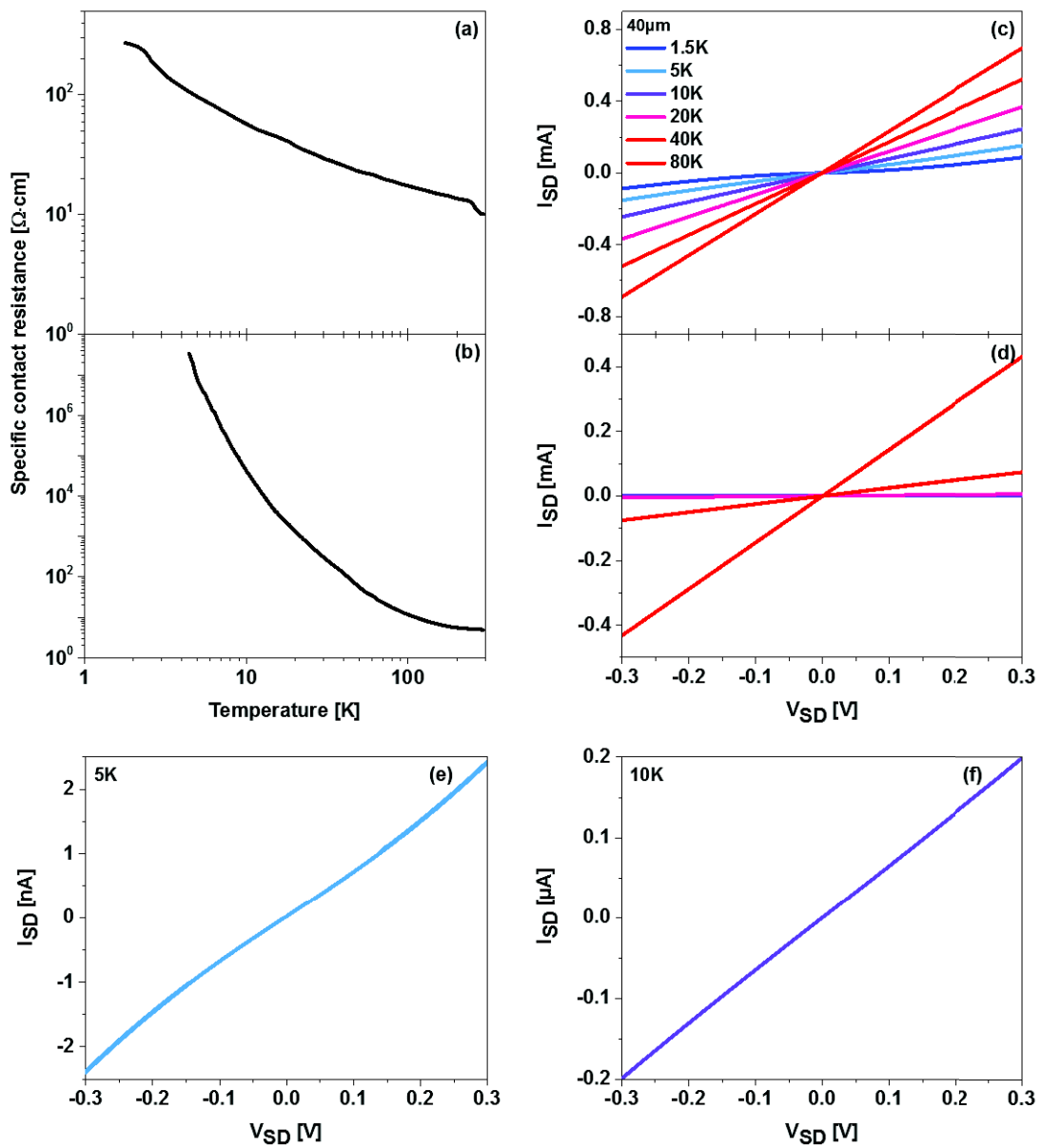


Figure 5.8 Specific contact resistance of (a) PBTTC- and (b) IIDDT-C3- based Au EGOETs with channel length $L = 40 \mu\text{m}$ together with the relative IV curves at lox temperatures ((c) and (d), respectively). The IV curves of IIDDT-C3 at 5K and 10 K not distinguishable in (d), are shown in (e) and (f).

5.3.2 AFM imaging of PBTTT and IIDDT-C3 thin films

Atomic Force Microscopy (AFM) has been performed on PBTTT and IIDDT-C3 thin films deposited on large-scale transistors to investigate the morphology of the two polymers, perhaps explaining the difference in the charge carrier transport at low temperatures observed in the previous section. AFM images have been acquired using a Nanoscope Veeco Multimode V Bruker microscope operating in tapping mode. From the transport characteristics we expect PBTTT to be more ordered. The images of the height of PBTTT and IIDDT-C3 are shown in Figure 5.9 (a) and (b), respectively. The morphology of the two polymers is quite different. IIDDT-C3 is smooth as evidenced by a root-mean square (R_{rms}) of 1.231 nm and aggregated in fibers aligned in the parallel direction with the channel. PBTTT appears more amorphous with $R_{rms} = 1.528$ nm. Therefore the morphology of the thin films cannot simply explain the different behavior of the two polymers since the better organization of IIDDT-C3 would favor charge carriers transport in this polymer.

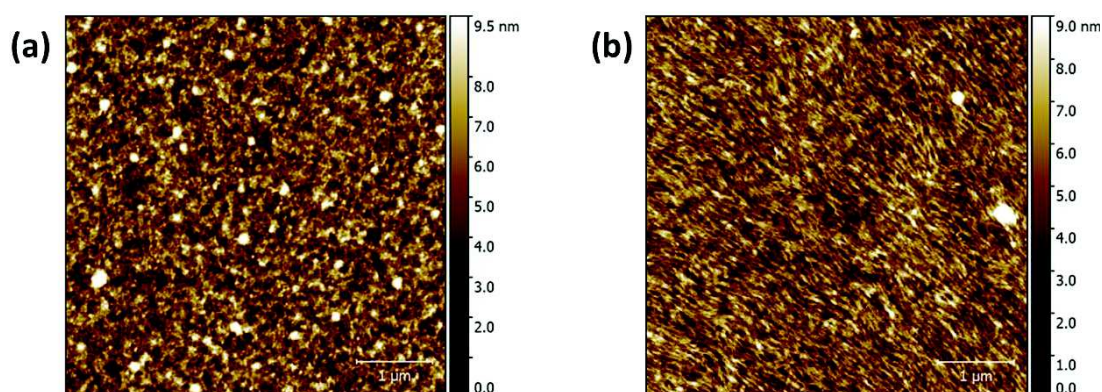


Figure 5.9 Tapping mode AFM images of height of (a) PBTTT and (b) IIDDT-C3 thin films on large scale devices. Scansion has been performed inside the channel in the parallel direction with the electrodes.

5.4 Fabrication of short channel devices

Short channel devices fabrication consists of several steps. In the following sections the entire procedure is described step by step.

5.4.1 Nanotrenches fabrication

High aspect ratio ($W/L > 100$) bottom contact nanotransistors with width W ranging from 20 to 100 μm and channel length $L = 80$ nm have been fabricated using the so-called shadow edge evaporation method. This method is based on standard optical lithography and thus avoids all the technical issues (“proximity effect”) associated to electron beam (e-beam) lithography commonly used to fabricate devices with gap size below 1 μm and aspect ratio > 10 .

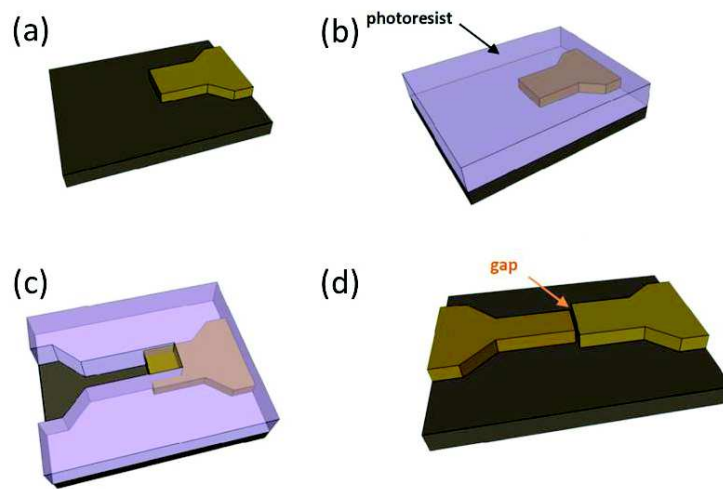


Figure 5.10 Schematic of the edge-mediated shadow mask lithography process. (a) The first electrode is patterned using standard optical lithography and deposited; (b) and (c) the second layer is defined partially superimposed on the first electrode; (d) metal deposition of the second electrode with the sample tilted at a specific angle leading the opening of the nanosized gap.

The realization of high aspect ratio nanogaps devices becomes particularly important in organic electronics where high sheet resistance materials are used. In this case it is crucial to have high aspect ratio electrodes that exhibit good interface resistance.

Because of the high aspect ratio, our samples are called “nano-trenches”. Each nanotrench is connected to four connection pads allowing us to eliminate the cryogenic wiring series resistance to the sample as well as the on-chip series resistance of the interconnects.

Nanotrenches fabrication consists of two steps optical lithography on a 500 nm thermally oxidized SiO_2/p^+ -doped Si. The first patterned electrode (first layer) is defined

using a three layers (HMDS-LOR-AZ 5214) resist process in order to facilitate the lift-off step and to have straight and well-defined edge structures (Figure 5.10 (a)). This step is very important since the resulting first layer will serve as a shadow mask for creating the gap. Therefore presence of resist residues or zigzag edges can negatively affect the quality of the gap. Then metal deposition of 54 nm of Au, with 6 nm of Ti as adhesion layer, is performed followed by lift-off in heated (50 °C) PG Remover.

The second electrodes (second layer) is patterned using a single step negative resist AZ 5214 process (Figure 5.10 (b)). In this step an open window partially covering the area of the first layer is created for the metal evaporation (see Figure 5.10 (c) and (d)). 80 nm of Au with 10 nm of Ti are deposited keeping the sample under a tilt angle θ between the substrate normal and the source direction. In this way the first layer will create a shadow effect which allows the aperture of a nanometric gap with a length L depending on the height h of the first layer as shown in Figure 5.11

$$L = h \times \tan\theta$$

Using $\theta = 65^\circ$ we obtain a gap of 80 nm as confirmed by scanning electron microscopy image in Figure 5.12 (a). Due to the tilted evaporation the thickness H of the second layer is reduced respect to the quantity of metal deposited T and it is determined as $H = T \cdot \cos\theta$ (~38 nm in our case).

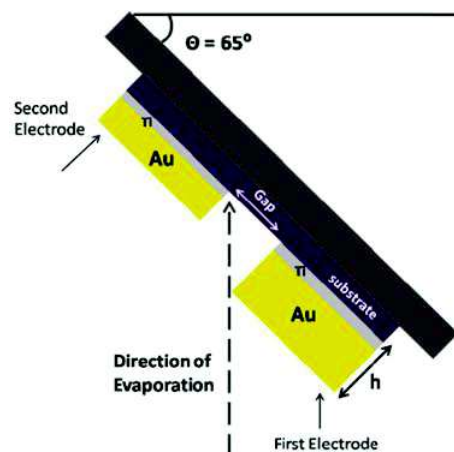


Figure 5.11 Schematic of the edge mediated shadow mask lithography process. The shadowing effect of the first electrode creates the gap whose size L is determined by the height h of the first electrode and the angle θ .

5.4.2 Device preparation

After nanotrenches fabrication, large area Au side gate electrodes, of 50 nm thickness, are implemented in the design using a stencil mask for the metal evaporation. A further fabrication step in the sample preparation is the deposition of a SiO₂ window covering most of source-drain electrodes surface and thus defining the area where the polymer makes electrical contact with the electrodes. The opening, centered on the nanotrenches, is 150 μm large and defined by optical lithography followed by RF-magnetron sputtering of 50 nm SiO₂.

After completing the sample fabrication and before the OSC deposition, the nanotrenches are systematically electrically tested to check the quality of the gaps, expected to be electrically opened and to exhibit minimal leakage current (below 10 pA) before being transferred into a N₂-filled glove-box for the deposition of PBTTT solution.

5.4.3 Top-gate electrolyte

An ion gel electrolyte, prepared as described in Chapter 4, is used as dielectric. Figure 5.12 shows an optical microscope image of the device together with a photograph of the completed sample and a schematic of the electrical connections used for the measurements. As evident from the Figure 5.12 (a), the SiO₂ opening allows us to avoid short-cut between +I and +V or -I and -V metal leads and to reduce the area of metal/electrolyte direct contact in order to minimize electrochemical reactions at the electrode surface.

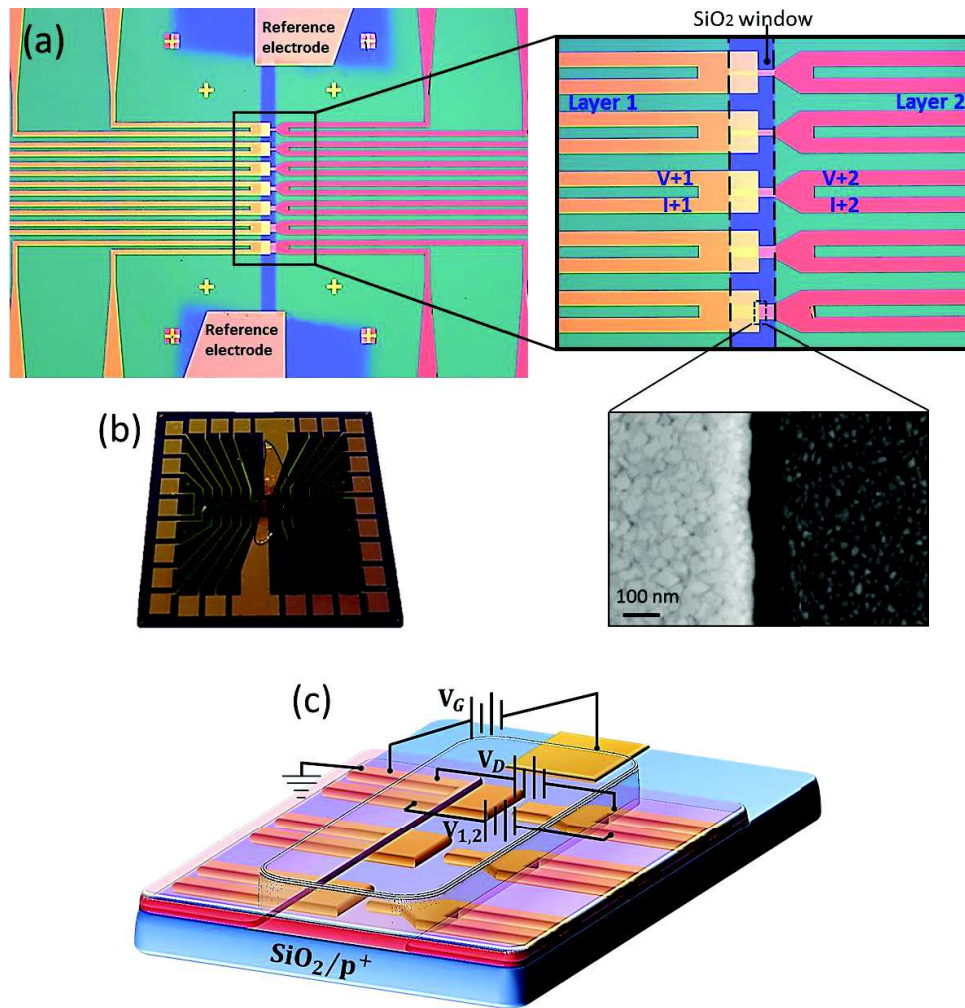


Figure 5.12 (a) Optical microscope image of the sample containing seven nanotrenches in parallel. The area marked with the black rectangle is zoomed on the right showing the SiO₂ window opened on the nanotrench. A second zoom shows a SEM image of one of the gaps. (b) Photograph of the full substrate after PBTTC spin coating and ion gel positioning. (c) Circuit schematic used for the extraction of the sample resistance. The source electrode is grounded and $V_D = -0.2$ V is kept constant while increasing V_G .

5.5 Room temperature electrical characterization of nanotransistors

Current-voltage characteristics of Au EGOFETs with $L = 80$ nm and $W = 40$ μm at room temperature have been acquired inside a N_2 -filled glove box in a two point measurement geometry using a Keithley 2621A SourceMeter unit with the source electrode grounded.

For the output characteristics in Figure 5.13 (a), the gate voltage (V_G) was held at a fixed value while source-drain bias (V_D) was swept from 0 V to -0.25 V at a rate of 0.001 V/s.

Measurements of several output curves have been done for a series of V_G , ranging from -0.25 V to -3 V, with -0.25 V increments.

We observe the typical output curves with a linear behavior at low source-drain bias, a clear saturation at large source-drain voltages and very good modulation for different gate voltages. These curves comply well with the standard equations of OFETs operating in the accumulation mode.

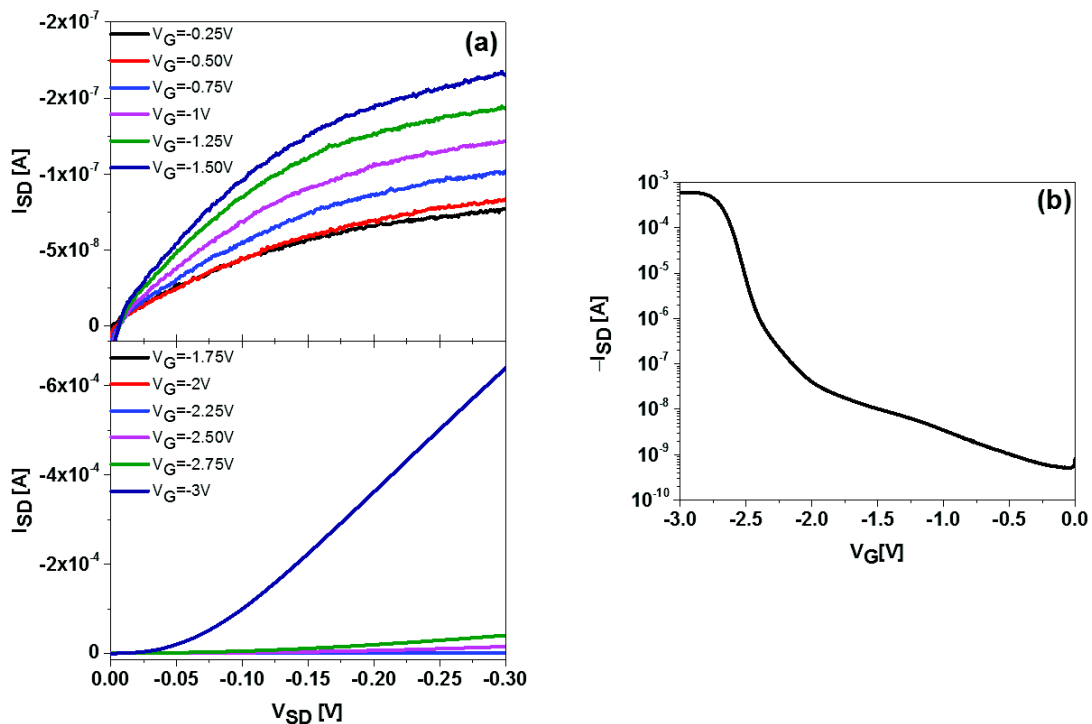


Figure 5.13 Output (a) and transfer (b) characteristics of PBTTC-based Au nanotransistor ($L = 80$ nm) at room temperature. At high drain voltages the output curves bend off as the pinch-off point is approached in agreement with long-channel OFETs behavior. I_{ON}/I_{OFF} ratio as high as 10^6 is observed in the transfer curve. Only the forward trace is plotted.

A typical transfer curve, measured by sweeping the V_G at a rate of 0.001 V/s for a given drain-source bias -0.2 V, is shown in Figure 5.13 (b). A clear modulation of the current in the semiconducting channel is observed together with a surprisingly high I_{ON}/I_{OFF} ratio of the order of 10^6 and thus comparable to transistors of standard channel lengths (> 5 μm). The hysteresis of the transfer curve (not shown here), together with the time analysis of the gate current I_G , show that polarizing the electrolyte results in significant electrochemical doping.

These results clearly indicate the absence of short channel effects in our devices, in contrast with all the results reported on similar devices up to date. These promising results motivated us to perform a complete study of these devices, investigating also the influence of the temperature and magnetic field in order to have more information about the charge transport and to deduce possible outcomes for spintronic applications.

5.6 Low temperature measurements

The gating and cooling steps are the same as the ones described in Section 5.3.1 for large scale devices with $V_D = -0.2$ V. Measurements have been performed using a pseudo-four points technique exploiting the fact that the geometry of the device has been designed with each side of the nanotrench connected to two patterned lines nearly the trench limiting the circuit series below 2Ω (see Figure 5.12).

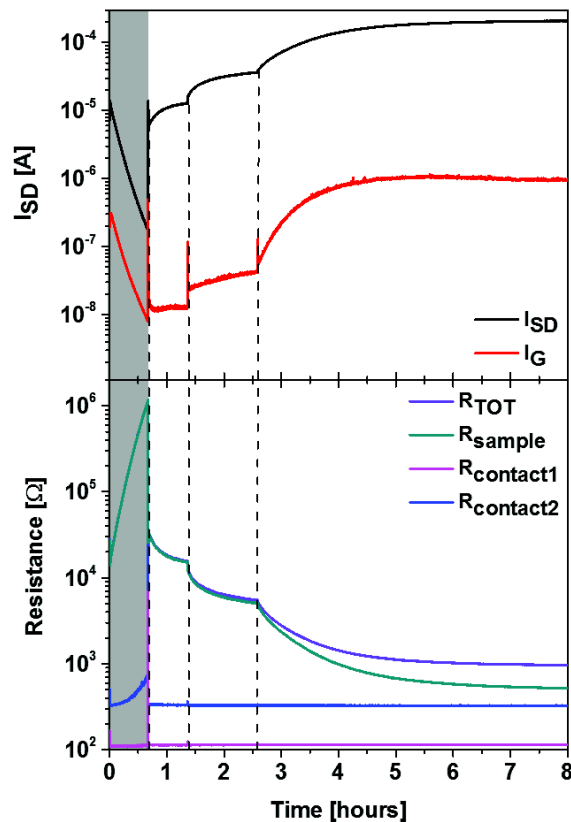


Figure 5.14 Source-drain current I_{SD} , gate current I_G and total resistance R_{TOT} together with the resistance of the sample and the two metallic tracks are monitored versus time during the gating process. The grey area indicates the de-doping process of the sample showing the reversibility of the electrochemical doping of the ion gel.

As shown in Figure 5.14 this geometry allows to discriminate between the sample resistance R_{Sample} and the metallic pads resistance of the two electrodes, $R_{contact1}$ and $R_{contact2}$ from the measured total resistance R_{Tot} . Sample resistance is then determined as $R_{Sample} = R_{Source} + R_{channel} + R_{drain} = 2R_c + R_{channel}$ (R_c is the average interface resistance at the source/drain contacts). However, we cannot independently measure the channel resistance and the contact resistance R_c . As detailed in the following sections, we determine the channel and contact resistance in the nanotrenches using the values of conductivity extracted from large scale devices under the assumption that the intrinsic properties of the polymers are maintained from sample to sample.

In Figure 5.15 we plot the sample resistance, R_{Sample} , as a function of the temperature for three nanotransistors with same channel length ($L = 80$ nm) and different width ($W = 30, 40$ and 50 μm). The dispersion in the curves is possibly related to the lack of reproducibility of the Au gate electrode potential, as well as the defective manual attachment of the slide of ion gel possibly not adhering properly over the whole active channel. As already mentioned, the maximum V_G at which the samples are doped is dictated by the appearance of the negative transconductance peak and thus it is different from sample to sample. Samples with $W = 30$ and 50 μm have been gated at $V_G = -2.4$ V while the sample with $W = 40$ μm has been gated at $V_G = -2.6$ V. The plots show remarkably low resistance values (between 26 and 56 Ω at 300 K and between 104 and 154 Ω at 1.8 K) for all the samples.

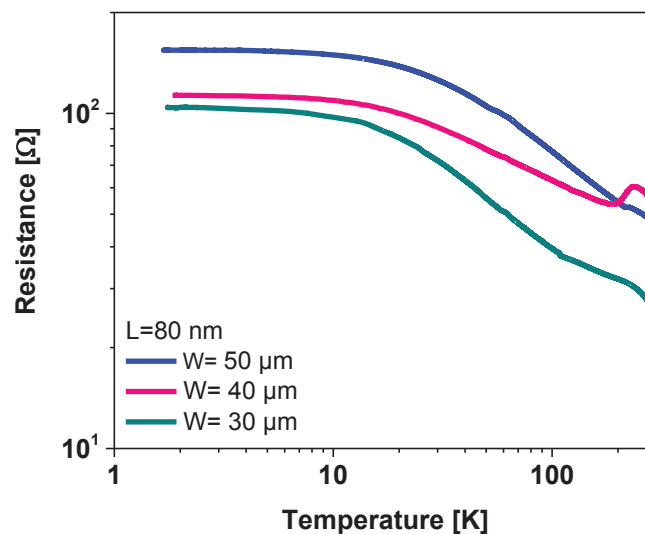


Figure 5.15 Sample resistance as a function of the temperature for three different devices (with same channel length L and different width W) gated at the maximum doping level. Remarkable low values are observed down to 1.5 K.

We also collected the same set of data for nanotrenches with different L and W . These samples have been fabricated following the same procedure as described in section 5.4.1 but without any tilted angle during the metal deposition of the second layer resulting in a short cut of the electrodes without any opening in between. Gaps of different lengths, between 30 and 500 nm, are successively created by cutting the metal, along the connection point between the two layers, with focused ion beam (FIB) milling. Temperature dependence of the resistance, together with the transfer characteristics at room temperature, for these samples are similar to the previous ones. In Figure 5.16 we show only the results for the samples with the shortest and largest channel lengths ($L = 30$ nm, $W = 20$ μm , and $L = 300$ nm, $W = 80$ μm , respectively).

In conclusion, the measured low values of the sample resistance down to 1.8 K, together with the high $I_{ON/OFF}$ ratio and the saturation of the output curves at room temperature, clearly demonstrate a suppression of the short channel effects.

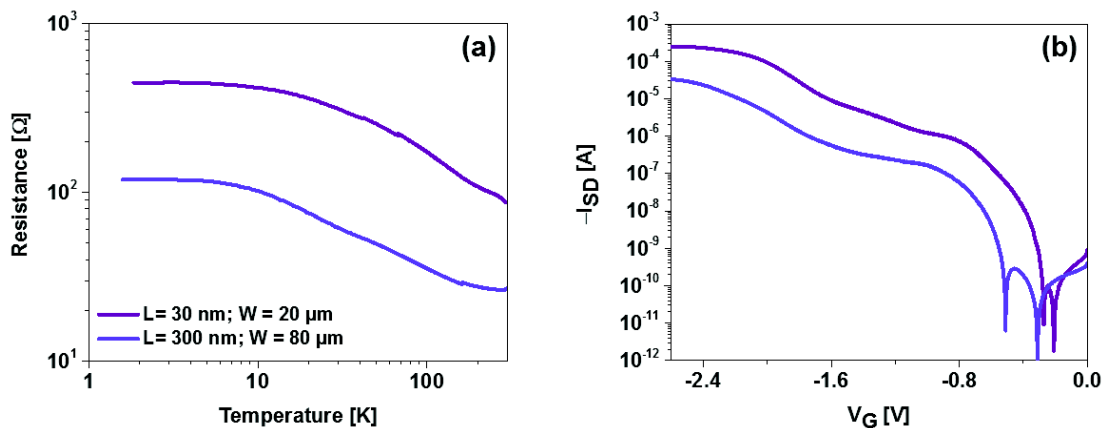


Figure 5.16 (a) Sample resistance as a function of the temperature for the smallest ($L = 30$ nm, $W = 20$ μm) and bigger ($L = 300$ nm, $W = 80$ μm) patterned nanotrenches; (b) transfer curves at room temperatures.

5.7 Measurements as a function of doping

Low temperature transport properties of Au nanotransistors with PBTTT as active channel have been also studied as a function of the applied V_G and thus the relative doping level induced. As it can be easily intuited, Figure 5.17 shows that the decreasing of the V_G (doping) significantly increases the measured sample resistance. Nevertheless, even in the case of the less doped sample ($V_G = -1.6$ V), we find at room temperature a sample

resistance, $R_{Sample} = 2R_c + R_{channel} = 6636 \Omega$, which corresponds to a specific sample resistance $R'_{Sample} = R_{Sample} \cdot W (= 30 \mu m) \sim 20 \Omega \cdot cm$. Considering that for the calculation of the specific contact resistance we have still to divide per 2 and that R_{Sample} contains $R_{channel}$, we rapidly deduce a specific (source/drain) contact resistance $R'_c < 10 \Omega \cdot cm$. This result is outstanding considering that values of $R'_c \sim 10 \Omega \cdot cm$ are of the order of the lowest values found only for highly doped large scale EGOFETs [8, 9, 10] and that usually short channel devices are severely contact limited. In our case, for the most doped sample, we find a $R'_c < 0.04 \Omega \cdot cm$!

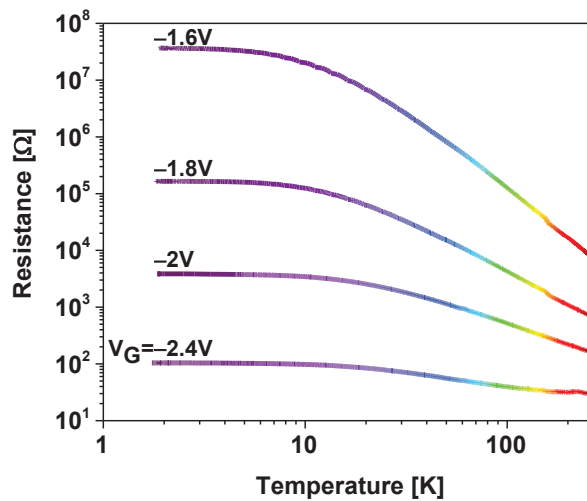


Figure 5.17 Plot of the sample resistance of the same nanotrench at different doping levels as a function of the temperature. As it is intuitive the resistance decreases as the V_G value is decreased. Nevertheless low values are still observed at 300 K even for the less doped sample.

I-V characteristics of PBTTT-based Au nanotrenches have been also measured for different doping levels, different widths, and different channel lengths, for 0.3 V range at 1.8 K and 20 K as shown in Figure 5.18 (a), (b), and (c), respectively. For most samples the output curves at 20 K are linear which is a further indication of the absence of an interface energy barrier. At 1.8 K all devices show a non-linear behavior. For some samples linearity of the IV curves down to 5 K have been observed (here not shown).

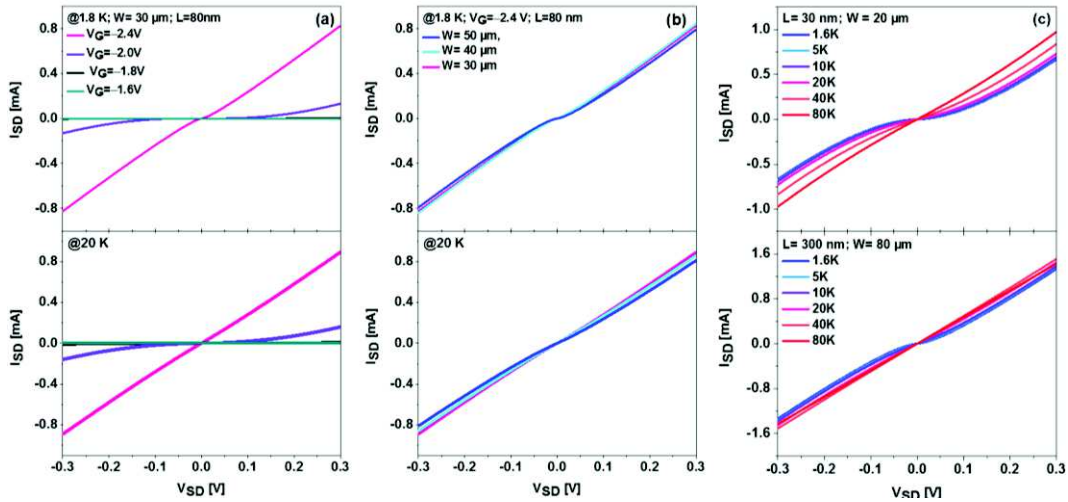


Figure 5.18 I-V characteristics at 1.8 K and 20 K of (a) the same nanotrench at different doping levels and (b) different nanotrenches gated at the maximum doping level; and (c) I-V characteristics at different temperatures for the smallest and the bigger nanodevices.

5.8 Magnetoresistance

Magneto transport properties have been studied for PBTTT Au nanotransistors with the aim to compare to previous observations in large scale devices and to study the intrinsic magnetoresistance (MR) properties of the OSC channel for spin valve studies.

Low temperature magnetoresistance curves at 1.6 K and 10 K have been collected sweeping the external magnetic field H between ± 7 Teslas in the direction parallel to the sample plane (parallel to the current direction), under constant temperature. Source-drain bias of -0.1 V and -0.2 V for large and short scale devices, respectively, have been applied during the measurements. For temperature higher than 10 K the magnetoresistance signal in both cases becomes negligible.

The measured MR, defined as $\Delta R = \frac{R(H) - R(0)}{R(0)}$ and expressed in percentage ($\Delta R \cdot 100$), is shown in Figure 5.19 (a) and (b) for large and short scale devices, respectively. Moreover, MR for nanodevices is reported for different doping levels (V_G). For large scale devices we observe an important MR signal, as large as 70% at 1.6 K while it decreases at $\sim 3\%$ at 10 K. For short channel devices we observe negligible MR in highly doped samples ($V_G = -2.4$ V). MR becomes however significant when the doping level is decreased. This behavior might be associated with the fact that, as discussed in Chapter 1, when the doping level in the OSC channel increases the type of carriers changes, namely spinless bipolarons fraction significantly increases.

The difference of MR values between large and short scale devices can be explained considering that the MR values for large scale devices are related to the channel conductivity (four points measurements), while MR curves in nanotrench devices in Figure 5.19 (b) contain contributions coming from both channel and interface. As we will show in the next chapter, contact resistances in our nanodevices approximately contribute to half of the sample resistance ($R_C \sim R_{Channel} \sim R_{Sample}$). Therefore, a reduction of the MR in our devices may stem from the fact that the MR signal of the interface is opposite to the one of the channel. This is quite interesting and important for spintronics applications because it implies that the interface with non-magnetic electrodes has a significant intrinsic MR at low temperatures. One approach to get better insight into this question would be to pattern on the same chip both large and short scale devices. In this way we are sure to have the same doping level (conductivity) on both channels to do a proper side to side comparison.

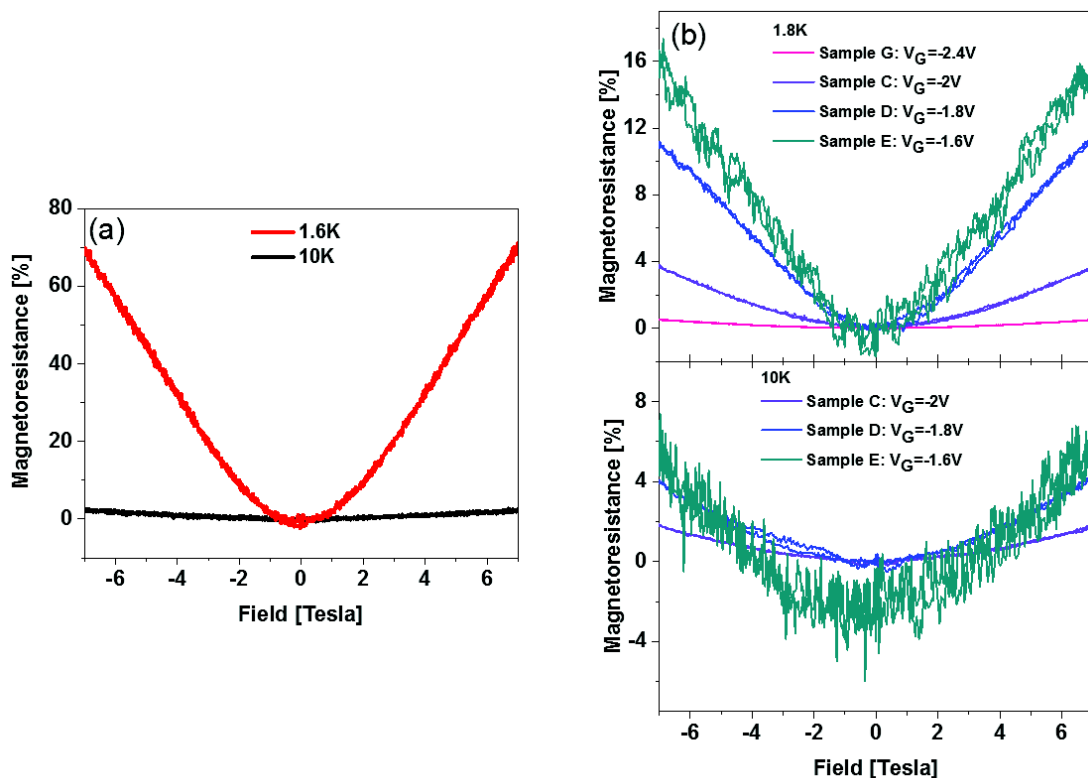


Figure 5.19 Magnetoresistance for PBTTC large scale (a) and short scale (b) devices.

Investigations of low temperature MR in large scale ($L = 400 \mu\text{m}$) PBTTT-based Au devices has been already reported for samples more conductive than ours ($\sigma > 1000 \text{ S/cm}$ at 300 K) [11]. For such high conducting samples, a reversal of the MR sign, when applying the magnetic field in the direction perpendicular to the sample plane, has been reported. This MR sign reversal is explained in terms of presence of weak localization indicating that the sample is approaching the metallic side of the metal-insulator transition. We also performed the same measurements by applying the magnetic field perpendicular to the nanotrench plane, but we never observed change in the MR sign, and our reported MR is nearly anisotropic, in agreement with the previous results on samples with comparable conductivity values [11].

5.9 Comparative study with thin film IIDDT-C3 nanodevices

The same set of measurements shown for PBTTT thin films have been also performed using another high mobility p-type polymer, previously used for interface resistance studies in Chapter 4: IIDDT-C3. Such comparative study was also motivated by the surprisingly low contact resistance we found, in order to check if the findings are specific to PBTTT. As shown in Figure 5.20 (a), for a device with $L = 80 \text{ nm}$ and $W = 50 \mu\text{m}$, even in the case of IIDDT-C3 the output curves exhibit a linear behavior at low voltages and a clear saturation at high voltages due to the pinch-off of the active OSC channel. These trends indicate that the device is not operating in the short channel regime. Modulation of the current in the channel is evident in the transfer curve (Figure 5.20 (b)) with a $I_{ON/OFF} \sim 10^{10}$ and small $I_{SD/OFF}$ current indicating that the device switches off completely, which is another unusual feature in devices with nanosized channel length.

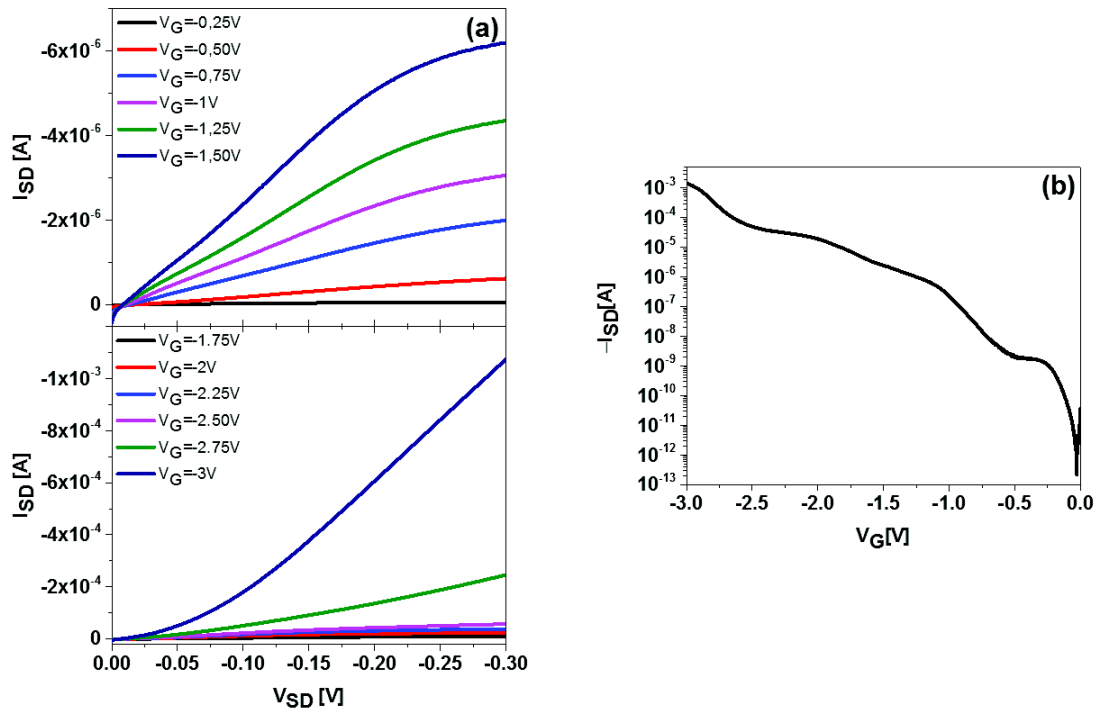


Figure 5.20 Output (a) and transfer (b) characteristics of IIDDT-C3 based Au nanotransistor measured at room temperature.

The behavior as a function of the temperature is quite different with respect to what observed in large-scale devices. The plot of the sample resistance as a function of temperature, in Figure 5.21, shows again remarkably low values which compare with the ones found for PBTTT at high temperatures but differ of one order of magnitude at ~ 1.5 K. Curves for other widths are similar and thus not shown.

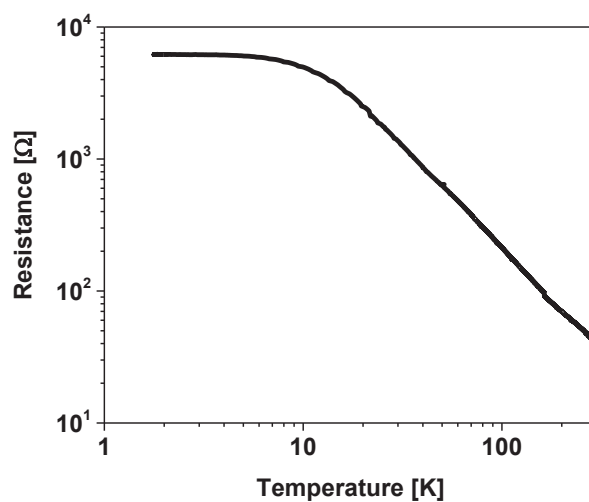


Figure 5.21 Sample resistance as a function of temperature of IIDDT-C3 based Au nanotransistor.

The higher values of sample resistance in IIDDT-C3 samples with respect to PBTTT ones at low temperature are reflected in the IV curves in Figure 5.22 where non linearity starts to appear at 40K and a more pronounced temperature dependence is shown (for comparison with PBTTT see Figure 5.18 (c)).

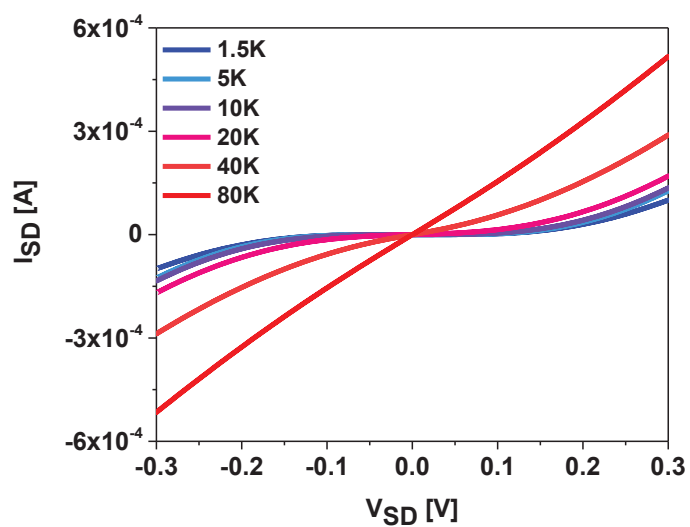


Figure 5.22 I-V characteristics as a function of temperature of IIDDT-C3 based Au nanotransistor.

The plot of the resistance as a function of the temperature in Figure 5.21 shows also relevant differences with respect to what observed for large-scale devices where the contact resistance has been observed to increase of six orders of magnitude from 80 K down to 5 K (see Figure 5.5 (b)). In the case of short channel length, only one order of magnitude of difference is observed in the plot in Figure 5.21 in the same range of temperature.

Note that our findings of low-resistance nanotrench devices do not depend explicitly on the crystalline order of the OSC. The two studied polymers have different short range (tens of nm) order, and both exhibit similar resistance values trends. For IIDDT-C3 channel lengths as small as 80 nm are able to bridge source-drain electrodes with ordered regions of the polymer improving the performance of the device compared to the case of large scale (see Figure 5.23). Nevertheless, PBTTT exhibits better low temperature properties in terms of conductivity, illustrating the key relevance of interfaces.

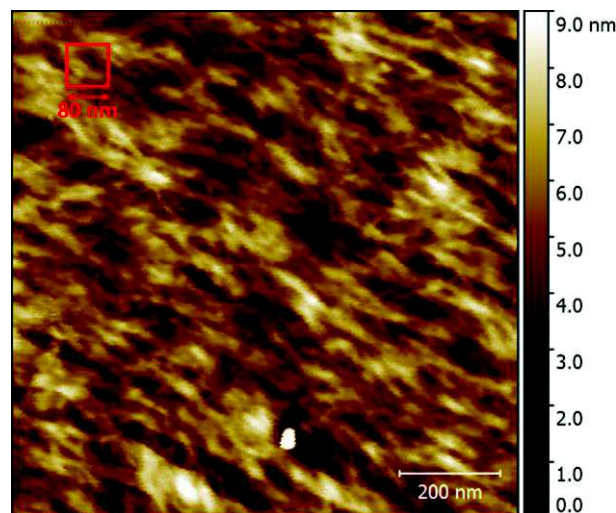


Figure 5.23 AFM image of IIDDT-C3 thin film morphology. The red square indicates an hypothetical configuration of the active channel in nanotrenches highlighting the ordered organization of the polymer in such short scales.

5.10 Estimation of the contact resistance in short channel devices

As anticipated in Section 5.3.1, in order to have a more detailed estimation of the contact resistance for all the measured samples, we used the values of conductivity σ extracted from large scale devices thanks to the gated four-probe method and calculated the sheet resistance of the thin films $R_{Sheet} = \frac{1}{\sigma \cdot t}$, with t the thickness of the OSC, and the

channel resistance $R_{Channel} = R_{Sheet} \frac{L}{W}$. Contact resistance R_C is then calculated as $R_C = (R_{Sample} - R_{Channel})/2$. Table 5.1 reports the values calculated at 300K where $\sigma = 440$ S/cm and 380 S/cm have been used for PBTTT and IIDDT-C3, respectively.

These high conductivity values may result from a long effective conjugation length along the polymer backbone. Actually for PBTTT an effective conjugation length of ~ 10 nm together with a coherent-type of intrachain-interchain hopping has been calculated by Liu and Troisi [12]. Long conjugation length translates into a long coherence length of the system, which is the distance over which the electron wavefunction of the charge carrier keeps its phase. Considering the results in [12] it seems reasonable to consider a coherence length of 25-30 nm, i.e. not much smaller than the shortest channel lengths of our nanotrenches. This could partially explain the remarkable transport properties observed in our PBTTT-based nanodevices.

Moreover, in the perspective of organic spintronics applications, an increase of the coherence length can be associated to an increase of the spin diffusion length. A spin diffusion length of 200 nm in undoped PBTTT has been recently measured by Watanabe *et al.* [4], where spin-polarized current has been injected by optical spin pumping (pure spin current), avoiding the problem of the resistance mismatch of the OSC with the metal contacts [13].

OSC	L	W	R_{Sample} [Ω]	R_{ch} [Ω]	R_C [$\Omega \cdot \text{cm}$]
PBTTT	80 nm	30 μm	26.6	2.9	0.035
PBTTT	80 nm	40 μm	56	2.2	0.1
PBTTT	80 nm	50 μm	47.8	24.64	0.11
PBTTT	30 nm	20 μm	87	43.4	0.08
PBTTT	300 nm	80 μm	26	15	0.088
IIDDT-C3	80 nm	50 μm	42	2.1	0.1

Table 5.1 Main parameters of short channel devices at 300 K.

In conclusion, the amazingly small values of the specific contact resistance R_C extracted for our nanodevices might be suitable to overcome the resistance mismatch

problem in spin-based devices. However, how we will see in the next chapter, these results are premature since more factors need to be taken into account.

5.11 Conclusions

In this chapter we reported the successful scaling of EGOFETs down to sub- μm scale with two high conductivity p-type thin films OSCs, namely C12-PBTTT and IIDDT-C3. For both polymers, in devices with closely spaced electrodes in the 30-300 nm range, a clear suppression of the short channel effects is shown. This suppression is revealed in the clear saturation of the output curves, in the high $I_{ON/OFF}$ ratio (ranging from 10^6 to 10^{10} !) and in the remarkably low contact resistance values, orders of magnitude below the record measured in the same kind of devices but with large (tens of μm) channels length [14, 10]. We are not aware of literature reporting similar performances in short channel organic electronics devices. In this context our results are thus noteworthy.

Moreover, gated four-probe measurements performed on large scale-devices allow us to extract the conductivity, and thus the sheet resistance, of the thin film polymers. This sheet resistance value is used to deduce the channel and interface contributions of the total resistance for short channel devices. Conductivity as high as 440 S/cm have been extracted for PBTTT thin films in our devices.

The calculated effective conjugation length ~ 10 nm for PBTTT, together with a measured spin diffusion length of 200 nm [4] and our measured low contact resistance values in nanodevices (in principle suitable to solve the mismatch problem), are encouraging enough to consider our short channel devices as good candidates for the fabrication of organic lateral spin valves. For this reason in the next chapter we will more concentrate on PBTTT thin films devices.

References

1. Szulczewski, G., Sanvito, S. & Coey, M. A spin of their own. *Nat. Mater.* **8**, 693–695 (2009).
2. Haddock, J. N. *et al.* A comprehensive study of short channel effects in organic field-effect transistors. *Org. Electron.* **7**, 45–54 (2006).
3. McCulloch, I. *et al.* Liquid-crystalline semiconducting polymers with high charge-carrier mobility. *Nat. Mater.* **5**, 328–333 (2006).
4. Watanabe, S. *et al.* Polaron spin current transport in organic semiconductors. *Nat. Phys.* **10**, 308–313 (2014).
5. McCullough, R. D., Lowe, R. D., Jayaraman, M. & Anderson, D. L. Design, synthesis, and control of conducting polymer architectures: structurally homogeneous poly(3-alkylthiophenes). *J. Org. Chem.* **58**, 904–912 (1993).
6. Sirringhaus, H. *et al.* Two-dimensional charge transport in self-organized, high-mobility conjugated polymers. *Nature* **401**, 685–688 (1999).
7. DeLongchamp, D. M. *et al.* High Carrier Mobility Polythiophene Thin Films: Structure Determination by Experiment and Theory. *Adv. Mater.* **19**, 833–837 (2007).
8. Braga, D., Ha, M., Xie, W. & Frisbie, C. D. Ultralow contact resistance in electrolyte-gated organic thin film transistors. *Appl. Phys. Lett.* **97**, 193311 (2010).
9. Zanettini, S. *et al.* High conductivity organic thin films for spintronics: the interface resistance bottleneck. *J. Phys. Condens. Matter Inst. Phys. J.* **27**, 462001 (2015).
10. Verduci, T. *et al.* Carbon-Passivated Ni Electrodes for Charge Injection in Organic Semiconductors. *Adv. Mater. Interfaces* **3**, n/a–n/a (2016).
11. Zanettini, S. *et al.* Magnetoconductance anisotropy of a polymer thin film at the onset of metallicity. *Appl. Phys. Lett.* **106**, 063303 (2015).
12. Liu, T. & Troisi, A. Understanding the Microscopic Origin of the Very High Charge Mobility in PBTTT: Tolerance of Thermal Disorder. *Adv. Funct. Mater.* **24**, 925–933 (2014).
13. Fert, A. & Jaffrès, H. Conditions for efficient spin injection from a ferromagnetic metal into a semiconductor. *Phys. Rev. B* **64**, 184420 (2001).
14. Braga, D., Ha, M., Xie, W. & Frisbie, C. D. Ultralow contact resistance in electrolyte-gated organic thin film transistors. *Appl. Phys. Lett.* **97**, 193311 (2010).

6

Current crowding for spintronics devices

Current crowding in staggered planar devices implies that charges are injected at distances exceeding the electrodes separation. In this chapter we discuss how this should be taken into account when designing and investigating nanoscale devices for spin electronics applications. Preliminary studies of the contact resistance on nanodevices made with ferromagnetic (FM) electrodes are also presented.

6.1 Introduction: Current crowding effect

To our knowledge, only one attempt using an electrolyte as gate dielectric on short channel devices ($L = 200$ nm) has been successfully reported by Heerlogsson *et al.*, using P3HT as active channel [1]. They observed the suppression of short channel effects as revealed by a proper saturation of the output curves and good (for short channel devices standards) $I_{ON/OFF}$ ratio (~ 25). No contact resistance study has been performed. Heerlogsson *et al.* explained their results in terms of formation of high transversal electric field generated by the thin electric double layer formed at the polyelectrolyte/semiconductor interface. As a matter of fact the increased longitudinal electric field induced in the sub-micrometer channel (with respect to the transversal one) is generally considered the main contribution to the short-channel effects. Even if the possibility of increasing the transverse electric field by using electrolyte dielectric has been one of the reasons motivating us to study electrolyte gated short channel devices, we believe that another important effect has to be taken into account when studying OFETs in staggered configuration, as the ones used in this thesis and in the report of Heerlogsson *et al.*

As already mentioned in Chapter 1, OFETs in staggered configuration are characterized by a large contact area between source/drain and gate electrodes due to their geometric overlap. In this case, as shown in Figure 6.1, carriers are injected/collected not only from the contact edge, but also from those parts of the electrode that overlap with the gate, before to travel along the accumulation channel. This effect is known as current crowding [2] and has been first discussed for inorganic Si-based transistors in a diffusive model of conduction [3, 4]. In such model with an active channel of uniform conductivity much smaller than the one of the electrodes, and under the hypothesis of ohmic interface contact resistance, a transmission-line analysis (Figure 6.1) results in a significant source-drain current at the edges of the contacts, which decreases exponentially away from the electrode edges, with a characteristic length L_T , given by:

$$L_T = \sqrt{\frac{r_b}{R_{Sheet}}} \quad (1)$$

where r_b is the specific contact resistivity, i.e. the contact resistance per unit area [$\Omega \cdot \text{cm}^2$] and R_{Sheet} is the sheet resistance of the active semiconductor layer [Ω]. L_T is the transfer length,

i.e. the length scale of the exponential increase of the current building up away from the electrodes separation. From the same analytical model the contact resistance is given as

$$R_c = L_T \cdot R_{channel} \coth\left(\frac{d}{L_T}\right) \quad (2)$$

where d is the effective contact length, that is the physical length defined by the geometric overlap between source/drain and gate electrodes.

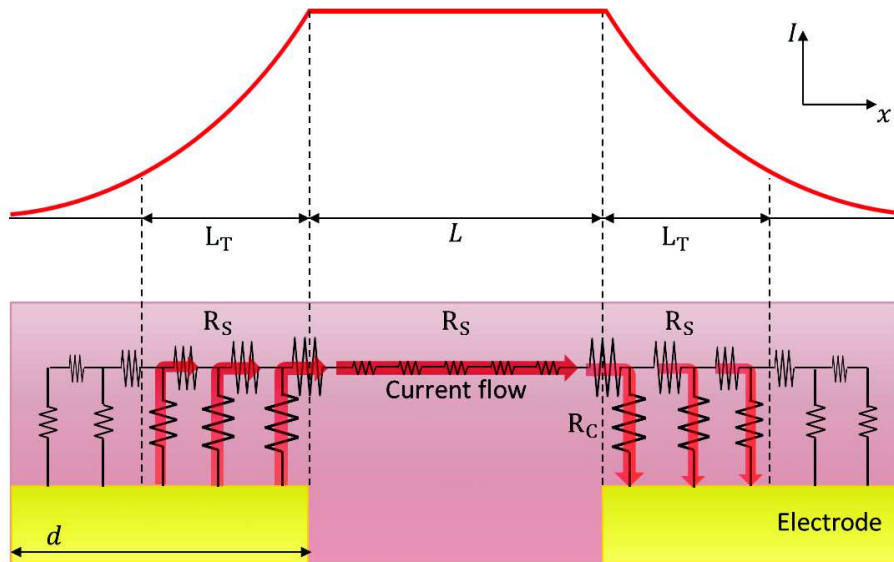


Figure 6.1 Schematic drawing of the current crowding effect showing the non uniform current flowing in a thin film more resistive than the source and drain electrodes. This makes the active channel of length $2L_T + L$, where L is the distance between electrodes, and L_T is the scaling length of the exponentially increasing current away from the gap between the electrodes. The flow of the source-drain current is indicated by arrows. Under the source (drain) contact the vertical component of the current increases (decreases) moving towards (away from) the edge. In the active channel region the current flows only horizontally. This model applied to staggered transistor structure (top gate not shown here) or to uniformly conducting layers.

Usually the specific contact resistance is expressed in unit $\Omega \cdot \text{cm}$ and correspond to the product of the contact resistance R_c [Ω] by the channel width W [cm]. Alternatively contact resistance can be expressed per unit of area [$\Omega \cdot \text{cm}^2$], also called contact resistivity. For OFETs with accumulation layer of thickness t_{acc} (~ 3 nm), the contact resistivity is: $r_b = R_c \cdot W \cdot t_{acc}$.

In the specific case of EGFETs, the doping extends for the entire volume of the semiconductor so that the whole semiconductor thickness t has to be considered in the calculation of the charge injection area and the contact resistivity is: $r_b = R_c \cdot W \cdot t$. For the sake of clarity, from now on we will refer this expression of r_b as “standard expression” since is the one commonly used in literature.

In the framework of current crowding, it is not anymore correct to use the semiconductor thickness t (or the accumulated layer t_{acc}) and the electrode width W to determine the contact area, but it is necessary to consider the effective injection area defined as $A = W \cdot (L_T + t)$, (usually $\sim A = W \cdot L_T$).

Current crowding effect leads to a decrease of the contact resistance as a function of the gate voltage. The reason is that when R_{Sheet} gets lower, either because of larger gate voltage or higher mobility, the injecting area is enlarged as a reaction to the increased current capability of the channel so that R_c is also lowered ($R_c \propto R_{Sheet}^{0.5}$). Therefore current crowding becomes increasingly important when the interface resistance dominates. This becomes a growing concern for device miniaturization and is particularly relevant for organic electronics [5], where interface should largely dominate the total resistance of a device when its dimensions approach the μm size range. Even though the transmission-line model is oversimplified for anisotropic and non-linear transport in organic materials, the crowding effects are important. Measurements of L_T indicate values decreasing with devices channel length. Recent experimental results provide rule of thumb estimates of $L_T \approx 4L$ for $L > 5 \mu\text{m}$ [6], and $L_T \approx 600 \text{ nm}$ for $100 \text{ nm} < L < 1 \mu\text{m}$ [7]. The latter results were found for several different organic semiconductor materials, with mobility values spanning the 10^{-2} - $10 \text{ cm}^2/\text{Vs}$ range. Nanoscale devices made of 2D materials also exhibit current crowding [8]. Ballistic charge injection and the significant influence of metallic contacts on 2D materials conductivity make however the transmission line model questionable. Experimental estimates on optimum metal-graphene contacts provide $L_T \sim 100$ - 400 nm [9, 10] and values of the order of 50 - 200 nm (thickness-dependent) have been reported for MoS_2 [11]. For carbon nanotubes, values as large as $210 \mu\text{m}$ [12] and as small as 200 nm [13] are reported in the literature, with values reflecting the variability in nanotubes conductivity and contact resistance properties.

In summary, staggered configurations mainly exhibit lower contact resistance owing to the possibility to inject and extract charge carriers over a broad area of the source and drain electrodes. This effect has important consequences for device scaling: the physical

contact length d must be chosen larger than the effective transfer length L_T ($d \gg L_T$) in order to minimize R_c in sub- μm devices. We believe that current crowding effect is the main reason of our low contact resistance values in short channel devices presented in the previous chapter.

6.2 Experimental extrapolation of L_T and r_b from the current crowding model

As discussed in section 5.3.1 gated four-probe measurements performed on large scale devices allow us to extract the conductivity σ and thus the sheet resistance as

$$R_{Sheet} = \frac{1}{\sigma \cdot t} \quad (3)$$

where t is the thickness of the OSC film. From the current crowding model the transfer length L_T and the contact resistivity r_b are calculated as:

$$L_T = \sqrt{\frac{r_b}{R_{Sheet}}} \quad (4)$$

$$r_b = R_c \cdot A = R_c \cdot W \cdot L_T \quad (5)$$

where $R_c = \frac{1}{2}(R_{Sample} - R_{Channel}) = \frac{1}{2}\left[R_{Sample} - R_{Sheet}\left(\frac{2L_T+L}{W}\right)\right]$ under the simplification of symmetric source and drain contact resistance. Equation (5) can be rewritten as

$$r_b = \frac{1}{2}\left[R_{Sample} - R_{Sheet}\left(\frac{2L_T+L}{W}\right)\right] \cdot W \cdot L_T \quad (6)$$

where the channel resistance is not anymore defined as in section 5.10 but now becomes $R_{Channel} = R_{Sheet}\left(\frac{2L_T+L}{W}\right)$ considering that the effective channel length is $2L_T + L$ (and not simply the channel length L).

By replacing equation (6) in equation (4) we get

$$2L_T + \frac{L}{2} = \frac{R_{Sample}}{R_{Sheet}} \cdot \frac{W}{2} \quad (7)$$

from which it is possible to determine L_T and thus r_b . Stating that, we will now provide a more careful estimation of the contact resistance for the devices studied in Chapter 5.

Table 6.1 shows the values of L_T and r_b at 300 K for the large and short channel transistors of Chapter 5, calculated from the measured values of R_{Sample} and σ (the value from large scale devices is supposed to be applicable to small ones).

OSC	L	W	σ [S/cm]	R_{Sample} [Ω]	R_{Sheet} [Ω]	L_T	R_{ch} [Ω]	R_c [Ω]	r_b [$\Omega \cdot \text{cm}^2$]
PBTTT	40 μm	0.1 cm	440	182	1100	31.36 μm	113	34.5	0.01
PBTTT	80 nm	30 μm	440	26.6	1100	160 nm	14.6	6	$2.8 \cdot 10^{-7}$
PBTTT	80 nm	40 μm	440	56	1100	480 nm	28.6	13.7	$2.6 \cdot 10^{-6}$
PBTTT	80 nm	50 μm	440	47.8	1100	520 nm	24.64	11.6	$3 \cdot 10^{-6}$
PBTTT	30 nm	20 μm	440	87	1100	380 nm	43.4	21.7	$1.6 \cdot 10^{-6}$
PBTTT	300 nm	80 μm	440	26	1100	395 nm	15	5.5	$1.7 \cdot 10^{-6}$
IIDDT-C3	40 μm	0.1 cm	380	144	$1.3 \cdot 10^3$	17.4 μm	98.36	22.8	0.0039
IIDDT-C3	80 nm	50 μm	380	42	$1.3 \cdot 10^3$	380 nm	22	10	$1.9 \cdot 10^{-6}$

Table 6.1 Main parameters extracted from current crowding model at 300 K for large and short channel devices based on PBTTT and IIDDT-C3 p-type polymers.

Under the hypothesis that the crowding length is much larger than the spacing between the electrodes ($L_T \gg L$), simple manipulations of the equation (4) show that :

$$R_c \sim \frac{1}{2} R_{channel} \sim \frac{1}{2} R_{Sample} \quad (8)$$

Equation (8) indicates that *current crowding makes the charge injection occur over a larger area, up to a contact resistance balancing the channel resistance.*

Our experimental values of L_T reported in Table 6.1 for nanodevices make the Equation (8) a reasonable assumption for our case. The outcome of these results, stating that

around 50% of the measured sample resistance is related to the interface, is remarkable since contact resistance in channel devices as short as 30-80 nm was expected to be the predominant contribution in R_{Sample} when extrapolating from the findings in large-scale devices ($R_c \sim 95-99\% R_{Sample}$).

Full temperature-dependent data example of L_T is presented in Figure 6.2 for large scale transistors and for the most conductive nanodevice ($W = 30\ \mu\text{m}$ and $L = 80\ \text{nm}$) showing how L_T significantly changes with temperature for short channel devices with a value first increasing when cooling down, then decreasing. For short channel devices we systematically observe a smaller crowding length at the lowest temperatures. While the total effective channel length ($2L_T + L$) at 300 K ranges between 500 nm and 1360 nm, values as small as 270 nm are found at low temperatures, with crowding length below 100nm, to our knowledge the smallest value reported in the literature for organic semiconductors. Moreover, the plot in Figure 6.2 reveals that the condition $L_T \gg L$ (and thus the Equation (8)) is only satisfied at high temperatures since L_T goes to small values at low temperatures.

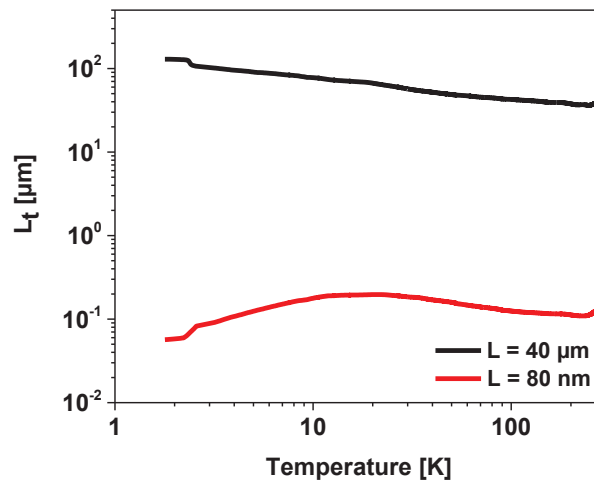


Figure 6.2 Temperature evolution of the transfer length L_T for PBTTT-based large ($L = 40\ \mu\text{m}$) and short channel ($L = 80\ \text{nm}$) devices. The plot for the short channel device is referring to the most conductive nanotrench ($W = 30\ \mu\text{m}$).

6.3 Outcomes for organic spintronics

Using organic materials for spin information transport has attracted significant interest essentially because of the expected long spin lifetime in organics [14]. However, the limited mobility of organic semiconductors severely hampers the spin current propagation

to a few tens of nm [15], eventually reaching 110 nm for C₆₀ [16] and 200 nm for PBTTC [17]. Since the reported spin memory lengths in organics compare to the smallest crowding lengths values previously mentioned, there is a strong need to raise the issue of current crowding for organic spintronics applications.

As discussed in Chapter 2, there is a well-defined condition for efficient spin injection, conservation and detection deduced by the theory of Fert and Jaffres [18] for spin transport in diffusive systems. This condition requires similar magnitudes of the contact resistivity r_b^* and the spin impedance of the non-magnetic semiconductor r_N [$\Omega \cdot \text{cm}^2$], defined as the product of the channel resistivity ρ_N [$\Omega \cdot \text{cm}$] and the spin diffusion length l_{sf}^{NM} . Equation (8) reminds this criterion, suggesting that crowding effects might provide opportunities to overcome the main issues related to spin-based devices, such as conductivity mismatch.

More specifically, following the simulations of Fert and Jaffres, the spin-dependent interface resistance r_b^* has to be carefully chosen between two threshold values in order to optimize the spin valve efficiency (Figure 6.3):

$$\rho_N t_N = r_N \frac{t_N}{l_{sf}^{NM}} = r_1 \ll r_b^* \ll r_2 = r_N \frac{l_{sf}^{NM}}{t_N} = \rho_N \frac{(l_{sf}^{NM})^2}{t_N} \quad (9)$$

where $r_b^* = r_b / (1 - \gamma^2)$ with γ the interface spin asymmetry coefficient.

If r_b^* is smaller than the lower threshold value ($r_1 = \rho_N \cdot t_N$ with t_N the length of the active channel) the spin current will accumulate at the interface flowing back into the spin polarizing injection electrode as a consequence of the resistance mismatch between metallic electrodes and organic active channel. If r_b^* is larger than the upper threshold value ($r_2 = \rho_N \cdot \frac{(l_{sf}^{NM})^2}{t_N}$), then the dwell time of the carriers will exceed the spin lifetime and the memory of the spin current will be lost before being detected. As shown in Figure 6.3, equation (9) translates into a maximum of the measured magnetoresistance in a spin valve when r_b^* and r_N are comparable: $r_b^*/r_N \approx 1$.

A first important outcome of current crowding is that, as already said, the effective channel length of a planar (staggered) device should be considered to be of the order of $2L_T + L$. Lateral devices fabrication targets electrodes separation values in the 20 nm to 100 nm range, reachable by standard nanolithography technique. Previously mentioned estimates of L_T therefore result into effective channel length larger than the electrodes

separation, exceeding the largest published estimate of the spin memory length in organic materials. Anyway, by building lateral spin valves with channel length as small as 20-30 nm, we can still hope that spin polarized current, related to charge carriers injected at the edge of the contacts, will be detected even if significantly reduced by the contribution of the charge carriers injected far from the contact edges. However, the deduced spin diffusion length values must take into account crowding length values.

Table 6.2 reports the values of r_b^*/r_N (where $\gamma = 0$ for Au electrodes) at 300 K calculated for all the measured devices considering $l_{sf}^{NM} = 2 \mu\text{m}$ in analogy to the calculations in [18]. Since for Au electrodes $\gamma = 0$, we will refer the ratio r_b^*/r_N as r_b/r_N . As we observe, even considering the transfer length L_T (two orders of magnitude larger than the accumulation layer in the case of a bottom gate through SiO_2 (~ 3 nm) and at least one order of magnitude bigger than the OSC thickness (~ 20 nm)) in the calculation of r_b , the values of the ratio r_b/r_N extracted for our nanodevices are between 0.65 and 6.8 for both PBTTT and IIDDT-C3 polymers. This result provides the hope to solve one of the main issues related to spin injection/detection (mismatch problem).

OSC	L	W	r_N [$\Omega \cdot \text{cm}^2$]	r_b [$\Omega \cdot \text{cm}^2$]	r_b/r_N
PBTTT	80 nm	30 μm	$4.4 \cdot 10^{-7}$	$2.8 \cdot 10^{-7}$	0.65
PBTTT	80 nm	40 μm	$4.4 \cdot 10^{-7}$	$2.6 \cdot 10^{-6}$	5.9
PBTTT	80 nm	50 μm	$4.4 \cdot 10^{-7}$	$3 \cdot 10^{-6}$	6.8
PBTTT	30 nm	20 μm	$4.4 \cdot 10^{-7}$	$1.6 \cdot 10^{-6}$	3.6
PBTTT	300 nm	80 μm	$4.4 \cdot 10^{-7}$	$1.7 \cdot 10^{-6}$	3.8
IIDDT-C3	80 nm	50 μm	$5.2 \cdot 10^{-7}$	$1.9 \cdot 10^{-6}$	3.6

Table 6.2 Contact resistivity r_b and spin impedance of the non-magnetic organic semiconductor r_N values at room temperature for all the measured devices according to the current crowding model. The r_b/r_N values found for nanodevices, ranging from 1 to 10, are promising for spintronic applications since obey to the conditions for efficient spin injection, conservation and detection as deduced by Fert and Jaffres.

If we add the data in Table 6.2 to the plot of the magnetoresistance MR calculated by Fert and Jaffres for a lateral spin valve as a function of r_b^*/r_N ratio, where the organic channel is supposed to have a spin diffusion length $l_{sf}^{NM} = 2 \mu\text{m}$, we easily realize that our values of contact resistance per unit area, r_b , match with the conditions for the realization of

spin-based devices (see the blue rectangle in Figure 6.3). As a matter of fact the r_b/r_N values in Table 6.2 fall in a narrow window roughly in the middle of the plot in Figure 6.3.

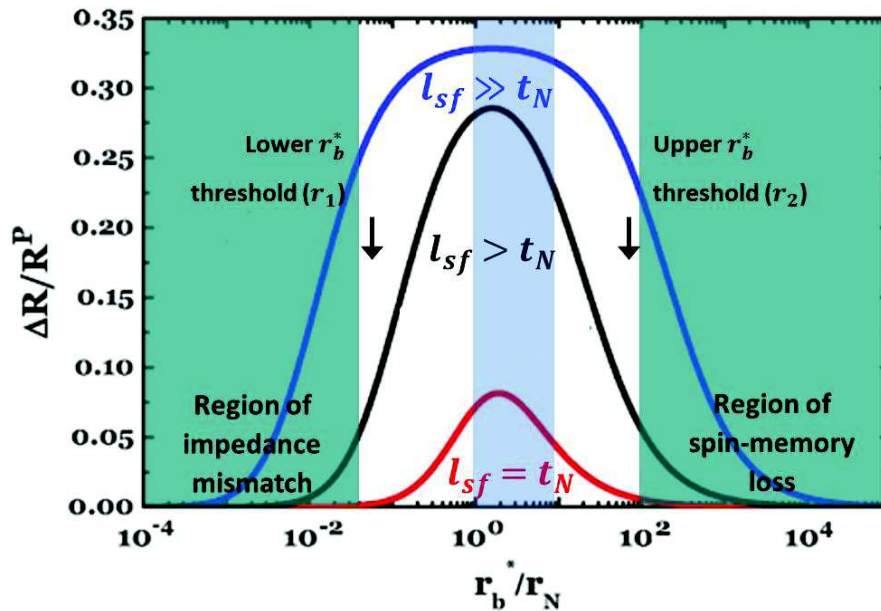


Figure 6.3 Magnetoresistance ($\Delta R/R_P$) as a function of the ratio r_b/r_N calculated for a pin valve with Co electrodes for three different channel lengths t_N (20 nm, 200 nm, and 2 μm) for a fixed spin diffusion length $L_{sf}^{NM} = 2 \mu\text{m}$. The blue rectangle represents the range of r_b/r_N values extracted from Au PBTTT-based nanodevices at room temperature. The values are centered in the optimal window for the magnetoresistance signal between the threshold values of lower resistance r_1 and upper resistance r_2 . Adopted from [18].

Knowing the temperature evolution of R_c and L_T it is possible now to obtain the contact resistivity r_b and the spin impedance of the active channel r_N as a function of the temperature. This is shown in Figure 6.4 for the most conductive sample where r_b is calculated using the current crowding model (red curve), that means $r_b = R_c \cdot W \cdot L_T$, and the standard expression (black curve) as usually reported in literature, that is $r_b = R_c \cdot W \cdot t$. A second outcome of current crowding for spintronics is illustrated by this figure: the ratio between interface and channel spin resistance varies with temperature, with the corresponding expected variations of the spin valve properties only related to the evolution of the injection area, in contrast to models involving changes in spin polarization values (reflected in asymmetry factors β and γ) with temperature.

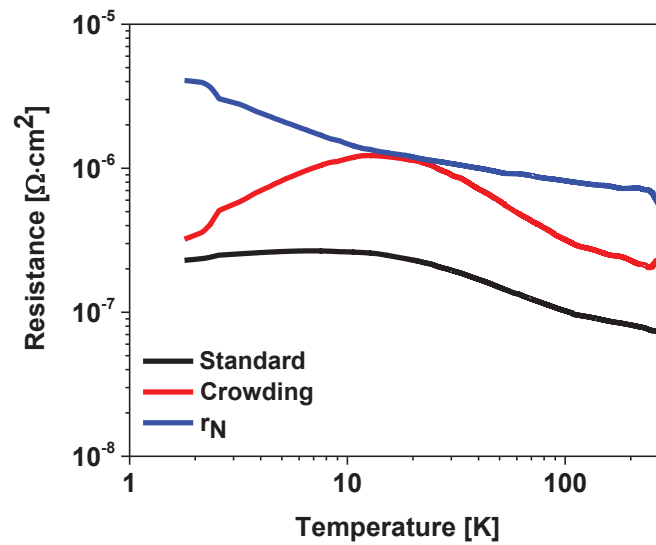


Figure 6.4 Direct comparison of the spin impedance of the organic semiconductor (r_N , blue curve) and the contact resistivity (r_b) according to the current crowding model ($r_b = R_c \cdot W \cdot L_T$, red curve) and the standard expression ($r_b = R_c \cdot W \cdot t$, black curve) as a function of the temperature.

Table 6.3 reports a collection of $R_{channel}$, R_c and r_b values at 300 K and 1.8 K for PBTTT nanodevices where L_T (current crowding) and t (standard expression of contact resistance) are used for the calculation of the contact area in r_b .

L [nm]	W [μm]	Temp [K]	R_{ch} [Ω]	R_c [Ω]	r_b [$\Omega \cdot \text{cm}^2$]	r_b/r_N
80	30	300	14.6	6	2.8×10^{-7}	0.65
80	30	1.8	65.5	19.2	3.3×10^{-7}	0.08
80	40	300	28.6	13.7	2.6×10^{-6}	5.9
80	40	1.8	66.7	23.2	8.6×10^{-6}	0.21
80	50	300	24.64	11.58	3×10^{-6}	6.8
80	50	1.8	85.3	34.5	2.95×10^{-6}	0.7
30	20	300	43.45	21.7	1.6×10^{-6}	3.6
30	20	1.8	232.17	108.5	4.6×10^{-6}	1.15
300	80	300	15	5.5	1.7×10^{-6}	3.8
300	80	1.8	78.8	20.5	2.65×10^{-6}	0.65

Table 6.3 Measured values of channel resistance ($R_{channel}$), contact resistance (R_c) and contact resistivity (r_b) at room temperature and 1.8 K calculated using the current crowding model and the standard expression for PBTTT-based Au nanotrenches. Values of the conductivity are 440 S/cm and 49.5 S/cm at 300 K and 1.8 K, respectively.

Note however that the data in Figure 6.4 is the extreme case (smallest R_{Sample} observed value). Figure 6.5 shows the trend of r_b/r_N ratio as a function of temperature for all the measured PBTTT-based devices where r_b has been calculated taking into account the current crowding model and for r_N a spin diffusion length $l_{sf}^{NM} = 2 \mu\text{m}$ has been considered again. The plot shows that the r_b/r_N ratio ranges between 0.44 -4.68 and 0.08 -1.15 at 280 K and 1.8 K, respectively. Therefore our value of r_b/r_N set in the middle of the plot in Figure 6.3 down to 1.8 K.

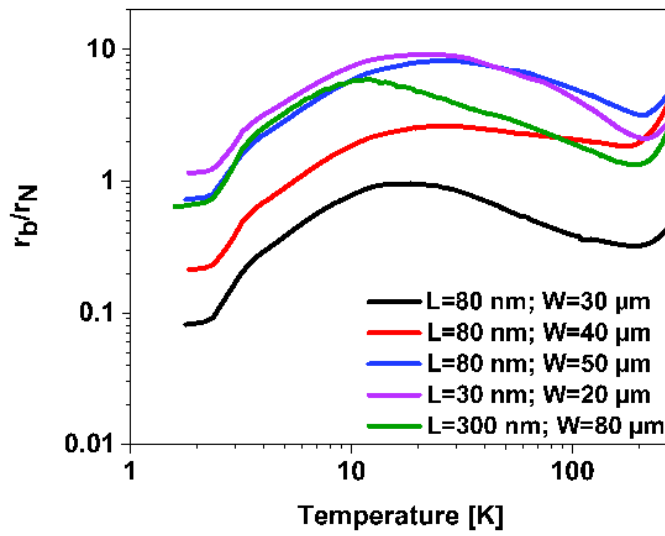


Figure 6.5 r_b/r_N ratio as a function of the temperature extracted for PBTTT nanodevices following the current crowding model.

A third outcome from current crowding model is that the equation (9) can be rewritten as

$$r_N \frac{2L_T + L}{l_{sf}^{NM}} = r_1 \ll r_b^* \ll r_2 = r_N \frac{l_{sf}^{NM}}{2L_T + L} \quad (10)$$

6.4 Nanodevices with FM electrodes

The results shown until now are related to nanodevices with contacts made of Au. These results need to be validated on FM electrodes for future investigation in the field of organic spintronics. Therefore, here we present a study of charge carrier transport in

nanodevices with Ni and carbon-passivated Ni electrodes meant to test high conductivity PBTTT thin films in lateral spin valve devices. PBTTT has been chosen for this purpose given the high predicted spin diffusion length (200 nm) [17] and the encouraging outcomes of the previous section.

6.4.1 Large scale devices measurements

Here we present a study on charge transport properties of PBTTT-based large scale devices ($L = 40 \mu\text{m}$, $W = 0.1 \text{ cm}$) with FM contacts. 100 nm thick Ni and Ni/RTA electrodes have been patterned in a top-gate, bottom-contact configuration as the one studied in the previous chapters. Low temperatures measurements have been carried out following the procedure described in Section 5.3.1. Ni/RTA electrodes have been synthesized as described in Section 3.3.

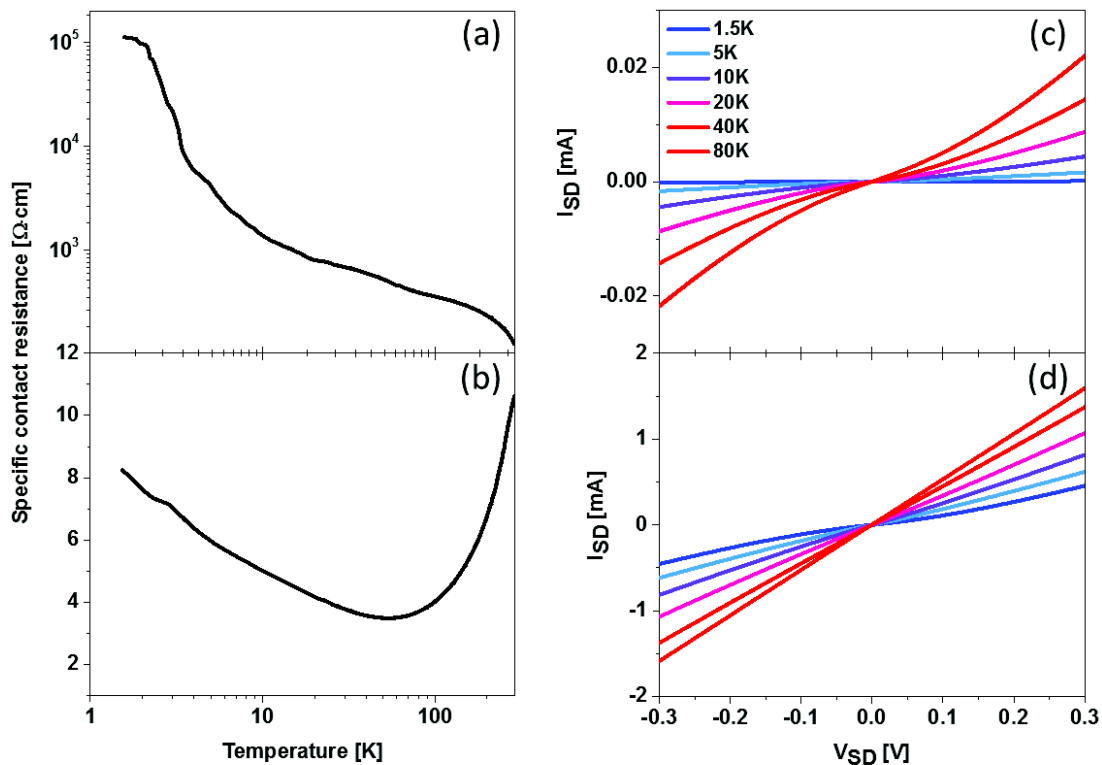


Figure 6.6 Specific contact resistance of PBTTT-based Ni (a) and (b) Ni/RTA EGOGETs together with the relative IV curves at low temperatures ((c) and (d), respectively).

Figure 6.6 (a) and (b) shows the specific contact resistance measured by means of gated four-probe method with $V_D = -0.1$ V, as a function of the temperature for Ni and Ni/RTA devices, respectively. As observed in the plots, while Ni electrodes present an increase of contact resistance of several orders of magnitudes as compared with Au electrodes, Ni/RTA sample exhibits very low R_C values, which are comparable to Au at room temperature and kept almost constant down to 1.5 K. This results confirm the findings in Chapter 3 at room temperature for devices with IIDDT-C3 thin films: passivation of bare Ni electrodes by ultra-thin layers of carbon improves the performance of the device.

IV curves at low temperature (in Figure 6.6 (c) and (d)) reflect what observed in the plot of the contact resistance. For Ni/RTA the curves are similar to the ones observed for Au electrodes, characterized by linear behavior down to 5 K and weak temperature dependence. For Ni electrodes clear non-linearity appears already at 80 K.

6.5 Nanotrenches fabrication with FM electrodes

Ni and Ni/RTA nanotrenches have been fabricated as described in Section 5.4. Carbon passivation layers are grown on the pre-patterned Ni electrodes by rapid thermal annealing (RTA) following the recipe described in Section 3.3. In this case the use of low temperature ($\sim 550^\circ\text{C}$) involved in the synthesis process is critical to avoid the melting of source/drain metal electrodes and thus the closure of the gap. In order to verify that, current-voltage data have been recorded before and after PBTTT deposition as shown in Figure 6.7 (a). IV curve of nanotrenches before PBTTT deposition (empty gap) shows no current, suggesting that the devices has not been damaged during RTA processing and that no amorphous carbon is present inside the channel. Figure 6.7 (b) shows the Raman spectra of Ni/RTA nanodevices together with the relative optical image (in the inset). Raman spectra of the two layers are similar to the one observed for large-scale devices in Chapter 3. However, using Ni electrodes with thickness less than 100 nm (54 nm for the first layer and 38 nm for the second layer) as catalyst results in a thicker carbon layer on top of the electrodes indicating that the process of graphitization, even in the case of RTA, requires a minimum thickness of the catalyst metal. The thickness of the carbon layer (around 100 nm) has been estimated considering the time required etching it by Argon plasma. At each step of 30 seconds of Argon plasma exposure, the resulting thickness was checked by AFM. While in the case of 100 nm Ni thick, 30 seconds

were enough to remove the carbon layer on top of it, some minutes were required in the case of nanotrenches with thinner Ni electrodes.

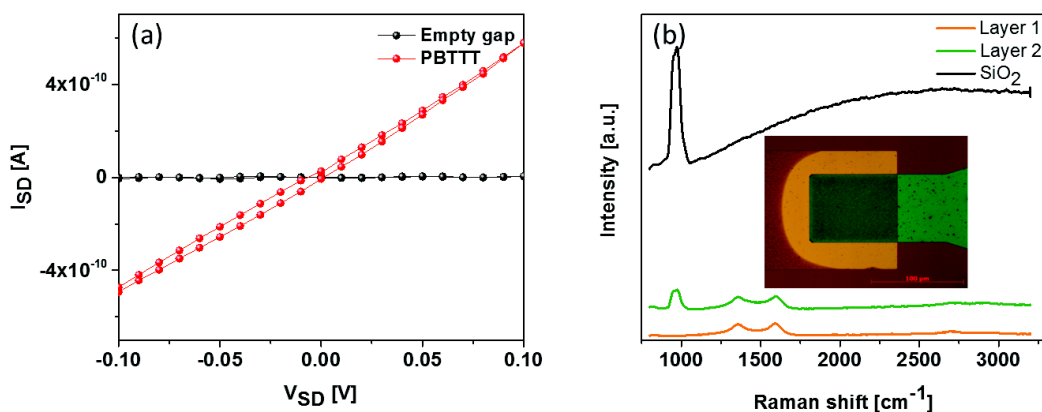


Figure 6.7 (a) Superposition of IV characteristics of a Ni/RTA nanotrench before (empty) and after PBTBT deposition. (b) Raman spectra of Ni/RTA nanotrenches on first layer (orange curve), second layer (green curve) and SiO_2 substrate (black curve).

Ni/CVD nanotrenches have been fabricated as well. However, the high temperature required in this case for graphene growth ($\sim 750^\circ C$) results in the closure of the gap. For these samples we tried to reopen a gap of ~ 100 nm by means of focused ion beam (FIB) milling. However, Raman spectroscopy performed after the cutting, reveals the presence of amorphous carbon residues filling the gap (Figure 6.8) indicating the non-reliability of the process.

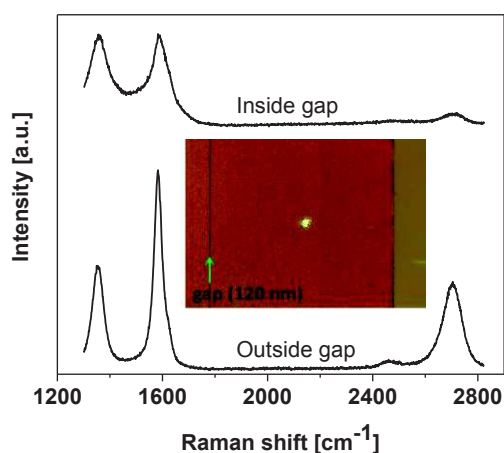


Figure 6.8 Raman spectra inside and outside the nanogap (~ 100 nm) opened by means of FIB between two melted layers of a nanotrench sample made of graphene passivated-Ni electrodes processed by CVD. Clearly the spectrum related the inside of the gap indicates the presence of amorphous carbon.

6.5.1 Study on short channel devices with FM electrodes

Study of charge carriers transport at low temperature in Ni and Ni/RTA nanodevices has been carried out as described in Section 5.6 under a source-drain bias $V_D = -0.2$ V. Figure 6.9 (a) and (b) show the plots of the sample resistance as a function of the temperature for Ni and Ni/RTA devices, respectively, after subtracting the resistance of the parallel metallic tracks. At 300 K the resistance for Ni/RTA sample is roughly two orders of magnitude smaller than Ni sample. The difference increases further as the samples are cooled.

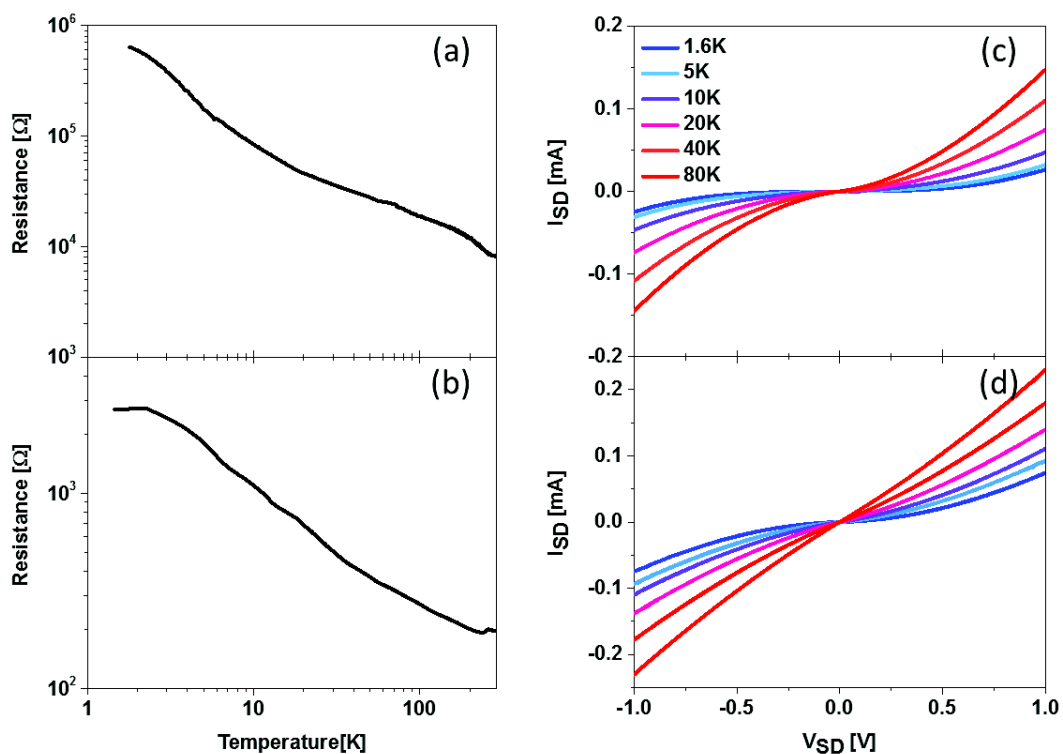


Figure 6.9 Specific contact resistance of PBTTT-based Ni (a) and (b) Ni/RTA nanodevices together with the relative IV curves at low temperatures ((c) and (d), respectively).

What is worth noticing here is the difference between large and short channel length Ni/RTA devices as compared with Au ones. While Ni/RTA large scale devices exhibit similar behavior to Au, Ni/RTA short channel devices show deteriorated performances as indicated by the increased sample resistance with respect to Au nanotrenches. This may be due to the RTA process in nanotrenches resulting in very thick amorphous carbon layers when the thickness of Ni catalyst is below 100 nm. Whatever the origin is, there is clear evidence that Ni/RTA cannot reach the impressive low interface resistance values found for Au.

Figure 6.9 (c) and (d) shows IV curves for Ni and Ni/RTA nanotrenches, respectively. IV curves for Ni devices show no-linearity ranging from 1.5 K to 80 K (Figure 6.9 (c)). Linearity is observed for Ni/RTA devices starting at 40 K (Figure 6.9 (d)).

Figure 6.10 (a) shows the plot of the transfer length L_T as a function of the temperature for both Ni and Ni/RTA nanodevices. L_T has been calculated from the equation of the current crowding model

$$2L_T + \frac{L}{2} = \frac{R_{Sample}}{R_{Sheet}} \cdot \frac{W}{2} \quad (11)$$

considering as value of the sheet resistance R_{Sheet} , the one extracted from large scale devices by means of gated four probe measurements.

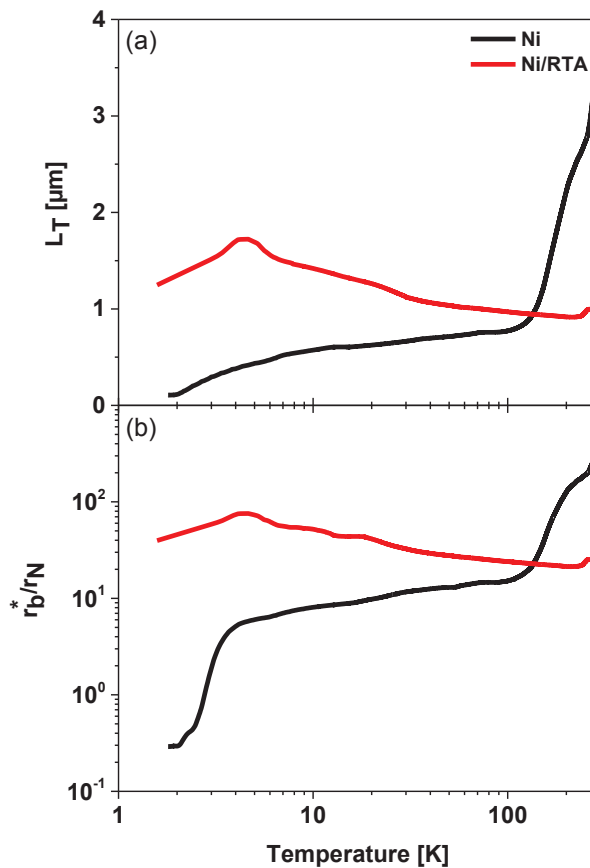


Figure 6.10 Temperature evolution of (a) the effective channel length L_T and (b) r_b^*/r_N ratio for Ni (black curve) and Ni/RTA (red curve).

In both cases we observe values of L_T larger than those found for Au nanotrenches. The reason of this difference in the case of Ni/RTA is to be attributed to the relatively high sample resistance values measured. From equation (11) it results that L_T depends on two main parameters, i.e. R_{Sample} and R_{Sheet} . At 300 K R_{Sheet} values extracted for Ni/RTA and Au large scale devices are similar (1.6 K Ω and 900 Ω , respectively) but the sample resistance R_{Sample} measured in Ni/RTA nanotrenches is around one order of magnitude higher than Au nanotrenches. Considering that $R_{Sample} = 2R_C + R_{Channel}$ and that $R_{Channel}$ is calculated from the R_{Sheet} value extracted from large scale devices (and therefore close to the one found for Au large scale devices), we believe that the increase of R_{Sample} in Ni/RTA sample comes from the contact resistance contribution R_C possibly because of a poorly defined contact interface due to the thick carbon layer on top. As a result, L_T for Ni/RTA is increased. Therefore we deduce that fabrication of 100 nm thick Ni/RTA nanotrenches is needed in order to decrease the sample resistance and thus L_T . In the case of Ni samples, both R_{Sample} and R_{Sheet} are increased, simply indicating a less performing device likely due to the oxidation of Ni electrodes surface. Interestingly, the crowding length is smaller than the Ni/RTA, reflecting a better ‘balance’ between interface and sheet resistance values. These findings should however be taken with caution, as they are observed on a limited number of samples.

Figure 6.10 (b) shows the plot of the contact resistivity, $r_b^* = r_b/(1 - \gamma^2)$ and the spin impedance of the non-magnetic organic channel r_N ratio as a function of the temperature, where a spin diffusion length $L_{sf}^{NM} = 2 \mu\text{m}$ and a spin asymmetry coefficient $\gamma = 0.14$ for Ni [19] have been considered.

For Ni/RTA sample r_b^*/r_N ratio ranges between 23 and 39.6 while for Ni it changes over three orders of magnitude. If we overlap the r_b^*/r_N values at room temperature to the plot of the magnetoresistance of Fert and Jaffres [18] as done in Section 5.3 for Au devices, we observe that r_b^*/r_N values for Ni/RTA are still inside the window defined by the threshold value of impedance mismatch and spin-memory loss (see Figure 6.3).

Table 6.4 reports the calculated values of L_T , r_b^* and r_b^*/r_N for Ni and Ni/RTA samples at 300 K and 1.5 K.

Electrode	W [μm]	Temp [K]	R_{Sample} [Ω]	σ [S/cm]	R_{Sample} [Ω]	L_T [μm]	R_{ch} [Ω]	R_c [Ω]	r_b^* [$\Omega\cdot\text{cm}^2$]	r_N [$\Omega\cdot\text{cm}^2$]	r_b^*/r_N [$\Omega\cdot\text{cm}^2$]
Ni	50	300	7.9×10^3	17.85	7.9×10^3	3.48	3.9×10^3	2×10^3	3.5×10^3	1.12×10^{-5}	350
Ni	50	1.8	6.4×10^5	0.008	6.4×10^5	0.1	3.7×10^5	1.3×10^5	7.3×10^3	0.025	0.3
Ni/RTA	40	300	196.6	254	196.6	0.98	100.27	48.2	1.8×10^5	7.8×10^{-7}	23
Ni/RTA	40	1.8	2.3×10^3	27.5	2.3×10^3	1.22	1.16×10^3	570	2.9×10^4	7.3×10^{-6}	39.6

Table 6.4 Calculated values of L_T , r_b^* and r_b^*/r_N for Ni and Ni/RTA samples at 300 K and 1.5 K.

6.6 Conclusions

In this chapter we explained our low contact resistance values, measured in short channel devices, in terms of current crowding effect usually showing up in staggered planar geometry.

We also presented a study of charge carriers transport on short channel devices made of FM electrodes in the perspective of organic spintronics applications. Preliminary results indicate that, even if Ni/RTA devices are not optimized, they still exhibit better performances with respect to bare Ni in terms of specific contact resistance and r_b^*/r_N ratio. These results show the potential of Ni/RTA nanodevices as template for building lateral spin valves, but further investigation is still needed.

Finally we discussed the consequences of our findings for organic spintronics. Current crowding effect in devices in the 100 nm size range can result in effective channel length typically one order of magnitude larger than the electrodes spacing for optimally-patterned nearby electrodes, and should be considered when deducing the spin memory length of spin currents in organic materials. Care should be also taken when interpreting temperature dependent data, as we have indications that the crowding length, and therefore the effective channel length, can vary with temperature. These considerations can be generalized to other materials like carbon nanotubes or 2D materials. Even though the expected spin memory length should be large for carbon-based nanostructures, one should note that the current crowding should be taken into account to avoid errors (reaching one order of magnitude) in spin properties parameters estimates intrinsic to these materials [20]. While these corrections should not affect experiments on graphene performed using very small contact electrodes, the expected short spin memory length in other 2D materials requires however taking into account current crowding effects [8]. Following the expression of the effective transfer length

$$L_T = \sqrt{\frac{r_b}{R_{Sheet}}}$$

it is essential to provide experimental access to materials conductivity and interface resistance values, in order to estimate properly the investigated effective channel length.

References

1. Herlogsson, L. *et al.* Downscaling of Organic Field-Effect Transistors with a Polyelectrolyte Gate Insulator. *Adv. Mater.* **20**, 4708–4713 (2008).
2. Richards, T. J. & Sirringhaus, H. Analysis of the contact resistance in staggered, top-gate organic field-effect transistors. *J. Appl. Phys.* **102**, 094510 (2007).
3. Kennedy, D. P. & Murley, P. C. A Two-dimensional Mathematical Analysis of the Diffused Semiconductor Resistor. *IBM J Res Dev* **12**, 242–250 (1968).
4. Murrmann, H. & Widmann, D. Current crowding on metal contacts to planer devices. in *Solid-State Circuits Conference. Digest of Technical Papers. 1969 IEEE International XII*, 162–163 (1969).
5. Natali, D. & Caironi, M. Charge Injection in Solution-Processed Organic Field-Effect Transistors: Physics, Models and Characterization Methods. *Adv. Mater.* **24**, 1357–1387 (2012).
6. Natali, D. *et al.* Injection Length in Staggered Organic Thin Film Transistors: Assessment and Implications for Device Downscaling. *Adv. Electron. Mater.* **2**, n/a–n/a (2016).
7. Xu, Y. *et al.* How small the contacts could be optimal for nanoscale organic transistors? *Org. Electron.* **14**, 1797–1804 (2013).
8. Allain, A., Kang, J., Banerjee, K. & Kis, A. Electrical contacts to two-dimensional semiconductors. *Nat. Mater.* **14**, 1195–1205 (2015).
9. Xia, F., Perebeinos, V., Lin, Y., Wu, Y. & Avouris, P. The origins and limits of metal-graphene junction resistance. *Nat. Nanotechnol.* **6**, 179–184 (2011).
10. Grosse, K. L., Bae, M.-H., Lian, F., Pop, E. & King, W. P. Nanoscale Joule heating, Peltier cooling and current crowding at graphene-metal contacts. *Nat. Nanotechnol.* **6**, 287–290 (2011).
11. Guo, Y. *et al.* Study on the Resistance Distribution at the Contact between Molybdenum Disulfide and Metals. *ACS Nano* **8**, 7771–7779 (2014).
12. Jackson, R. & Graham, S. Specific contact resistance at metal/carbon nanotube interfaces. *Appl. Phys. Lett.* **94**, 012109 (2009).
13. Franklin, A. D. & Chen, Z. Length scaling of carbon nanotube transistors. *Nat. Nanotechnol.* **5**, 858–862 (2010).
14. Sun, D., Ehrenfreund, E. & Vardeny, Z. V. The first decade of organic spintronics research. *Chem. Commun.* **50**, 1781–1793 (2014).
15. Szulczewski, G., Sanvito, S. & Coey, M. A spin of their own. *Nat. Mater.* **8**, 693–695 (2009).
16. Zhang, X. *et al.* Observation of a large spin-dependent transport length in organic spin valves at room temperature. *Nat. Commun.* **4**, 1392 (2013).
17. Watanabe, S. *et al.* Polaron spin current transport in organic semiconductors. *Nat. Phys.* **10**, 308–313 (2014).
18. Fert, A. & Jaffrès, H. Conditions for efficient spin injection from a ferromagnetic metal into a semiconductor. *Phys. Rev. B* **64**, 184420 (2001).

19. Moreau, C. E., Moraru, I. C., Birge, N. O. & Jr, W. P. P. Measurement of spin diffusion length in sputtered Ni films using a special exchange-biased spin valve geometry. *Appl. Phys. Lett.* **90**, 012101 (2007).
20. Hueso, L. E. *et al.* Transformation of spin information into large electrical signals using carbon nanotubes. *Nature* **445**, 410–413 (2007).

7

Conclusions and perspectives

In this thesis we investigated charge carrier transport of several OFETs with the aim to identify a type of device having properties “*a la carte*” for building organic spin valves in lateral geometry.

In the introduction and in the first part of this manuscript the main requisites towards this goal have been discussed. Suitable spin-based devices for organic spintronics in diffusive regime must be characterized by [1]:

- a long spin diffusion length, for the conservation of the spin signal during the transport throughout the channel;
- a contact resistance at the interface between organic channel and metal electrode that is very low for organic electronics standards, in order to ensure spin injection/detection.

The first condition (long spin diffusion length) requires the direct measurement of the spin diffusion lengths for the specific OSC spacer used. The only experimental fingerprint that would bring unambiguous proof of long-range spin transport in OSCs, namely the Hanle effect, has not been observed yet in organic materials. However, an interesting approach to alleviate this issue is to work with high mobility organic materials under the consideration that a highly conducting organic material presents a longer spin diffusion length (a faster charge carrier should be able to travel longer distances without losing its spin memory). The

other expectation is to alleviate the resistance mismatch conditions for proper spin currents propagation in these heterostructures.

Moreover, if we want that a charge carrier passes through the channel without losing its own spin signal, it is obvious that the spin diffusion length, predicted to be of the order of some tens of nm in OSCs [2], and hopefully reach 200 nm [3], must be larger than the channel length. This implicates the fabrication and investigation of devices with channel length in the sub-100 nm scale.

The second condition (low interface resistance) implies more specifically that, in order to have an efficient spin injection/detection, the contact resistivity r_b^* and the spin impedance of the non-magnetic semiconductor r_N (both expressed in $\Omega \cdot \text{cm}^2$) must have similar magnitudes. This is particularly difficult to achieve for organic materials, where reported values of the interface resistivity are orders of magnitudes too large. This results in short channel devices where the interface resistance largely dominates the total resistance of the device.

Finally, for spin valves in lateral geometry, it is necessary to have ferromagnetic (FM) electrodes surface with sufficient chemical inertness. Oxides formation consequent to air-exposure during processing steps is detrimental to the spin polarization properties of the FM surfaces, and therefore its interface with organics.

The problem of the FM surface oxidation has been the first issue faced during this thesis. We found out how to passivate Ni electrodes with ultra-thin (~ 5 nm) carbon layers by means of Rapid Thermal Annealing (RTA) process at low temperatures (~ 500 °C) which uses Ni as catalyst for the atop carbon layers growth. The charge injection capabilities of these Ni/RTA electrodes have been tested in p-type polymers-based devices: performances on-par with benchmark Au electrodes have been observed [4].

To solve the problem related to the first condition for efficient spin valves, we kept focusing on two high mobility p-type OSCs, PBTTT and IIDDT-C3 and adopted an electrolyte-gating technique to boost even further their conductivity. This technique offers the unique advantage of high bulk doping in the OSCs, due to charge carriers generated through electrochemical doping. Moreover, electrolyte-gated OFETs (EGOFETs) offer the possibility to reach very low values of interface resistance $\sim 10 \Omega \cdot \text{cm}$ [5]. These low values appear to be a good starting point for the fabrication of spin valves with expectation of adequate resistance match between ferromagnetic electrodes and organic channel. Therefore,

EGOFETs offer the advantage of having high conducting OSC channels and low contact resistance interfaces in a single device.

This advantage has been the main motivation to develop this work validating the benefits of electrolyte gating in several devices made of different OSC channels and metal electrodes. Encouraged by these findings we moved to the miniaturization of Au EGOFETs with typical channel length around 80 nm. These devices showed spectacular and unreported performances with clear suppression of short channel effects and highlighted the importance of current crowding effect [6] when staggered geometry (as in our case) is adopted. Current crowding effect is expected to be important when investigating nanoscale devices for spintronics applications since it causes carrier injection at distances exceeding the electrodes separation (channel length). This is expressed by a characteristic length, defined as transfer length L_T . Therefore, the effective active channel length does not correspond to the distance between the electrodes L , but reaches $2L_T + L$ in this type of devices. Taking into account L_T in the effective injection length, has two main consequences for organic spintronics devices. First, larger injection lengths require larger spin diffusion lengths to satisfy the condition for efficient spin transport. Second, L_T will substitute the OSC thickness t in the expression of the specific contact resistivity at the interface. Since our estimates of L_T are typically of values exceeding t by more than one order of magnitude the real value of the measured contact resistance increases accordingly, challenging further the interface resistance criterion for efficient spin injection/detection. This is particularly critical in sub- μm channel length devices where the contact resistance becomes the predominant term in the total resistance.

Nevertheless, our nanodevices exhibit remarkably low contact resistance values, ranging from 0.018 $\Omega\cdot\text{cm}$ to 0.17 $\Omega\cdot\text{cm}$, 2-3 orders of magnitudes lower than the values typically found for large scale EGOFETs. These contact resistance values are then low enough to satisfy the condition for efficient spin injection/detection even when the current crowding is taken into account. These results, even if less spectacular, are confirmed when FM Ni/RTA electrodes are used. However, low temperature properties reveal significantly larger interface resistivity for ferromagnetic electrodes, asking for better-controlled and improved fabrication of passivated transition metal electrodes.

The many materials properties challenges that appeared during this thesis made difficult to properly test spin valves structures in this work. Some initial magnetoresistance tests were performed on non-magnetic devices (using Au electrodes), in order to test the

intrinsic properties for the OSC channel. The significant magnetoresistance observed at low temperatures remains to be understood, and especially when reducing the size, as it can roughly be interpreted as the equal superposition of the interface and bulk properties. These initial results also indicate that caution should be taken when interpreting data using ferromagnetic electrodes, as their stray magnetic field might influence the observed properties when sweeping an external field [7].

From the discussion above it is clear how the work developed in this thesis managed to identify the best templates to make a spin valve. As a continuation of this work future studies should be addressed on the most exciting results of this thesis, i.e. short channel EGFETs, and may be focused on:

- improving the passivation of FM electrodes in nanodevices. This may be done not only by improving RTA processing but also finding alternatives methods. Working with Co electrodes can provide benefits in terms of intrinsic spin polarization of the material (Ni was initially chosen as best documented materials as carbon growth catalyst). Another, more speculative approach would be to perform chemical cleaning of the surface [8]. This approach has the advantage of room temperature processing, but the long-term chemical stability of the interface with organic materials remains very challenging.
- improving the conductivity extraction in short channel devices. As already said, our estimate of channel and contact resistance in nanodevices is obtained from the conductivity values extracted from four point measurements in large scale devices. However, to have a proper estimation of the resistance values (both channel and contact) in nanodevices, we should be sure that the conductive channel in large and short scale devices behaves the same way. More specifically we should be sure that both devices are doped at the same level. For this reason large and short scale devices should be patterned on the same chip sharing the same slide of ion gel and the same gating process. Therefore, the design of new devices should be addressed.
- reducing the transfer length. This is unclear since transfer length and the relative current crowding are intrinsic effects occurring in staggered geometry. One possibility would be to pattern SiO_2 all over the electrodes to be sure that no overlap between source/drain and gate electrodes takes place. This option, even if possible, implies several complications in the fabrication steps.

- using all the optimized OFETs properties reached in this thesis to build-up spin valves and to investigate possible injection-detection of a spin current.

References

1. Fert, A. & Jaffrès, H. Conditions for efficient spin injection from a ferromagnetic metal into a semiconductor. *Phys. Rev. B* **64**, 184420 (2001).
2. Szulczewski, G., Sanvito, S. & Coey, M. A spin of their own. *Nat. Mater.* **8**, 693–695 (2009).
3. Watanabe, S. *et al.* Polaron spin current transport in organic semiconductors. *Nat. Phys.* **10**, 308–313 (2014).
4. Verduci, T. *et al.* Carbon-Passivated Ni Electrodes for Charge Injection in Organic Semiconductors. *Adv. Mater. Interfaces* **3**, n/a–n/a (2016).
5. Braga, D., Ha, M., Xie, W. & Frisbie, C. D. Ultralow contact resistance in electrolyte-gated organic thin film transistors. *Appl. Phys. Lett.* **97**, 193311 (2010).
6. Richards, T. J. & Sirringhaus, H. Analysis of the contact resistance in staggered, top-gate organic field-effect transistors. *J. Appl. Phys.* **102**, 094510 (2007).
7. Harmon, N. J. *et al.* Including fringe fields from a nearby ferromagnet in a percolation theory of organic magnetoresistance. *Phys. Rev. B* **87**, (2013).
8. Galbiati, M. *et al.* Recovering ferromagnetic metal surfaces to fully exploit chemistry in molecular spintronics. *AIP Adv.* **5**, 057131 (2015).

Acknowledgements

First and foremost, I would really like to thank my PhD supervisors Prof. Bernard Doudin & Prof. Paolo Samorì for giving me the opportunity to perform this challenging and exiting project in IPCMS and ISIS, for the continuous support and guidance over these three years and for introducing me to the fascinating world of organic electronics.

Another big thanks goes to Emanuele Orgiu for the many stimulating scientific discussions we had and for being always ready to give help, advices and suggestions whenever I needed them. I have been pleasantly surprised since the very beginning by his way to manage with the lab as a person and as a scientist.

Several people must be acknowledge for the scientific collaborations: Jeong-O Lee and Cheol-Soo Jang from KRICT, Laetitia Bernard from EMPA and Nicolas Leclerc from iCUBE Institute. Again thanks to Jeong-O Lee for hosting me in her group where I had the possibility to learn some of the basics of graphene growth.

Also a big thanks to the STnano platform: Hicham, Sabine and Romain for keep everything running smoothly in clean-room and for making the lab a happy place to be. Thanks to Fabien Chevrier for the technical help in the lab.

I am very grateful for the friendship and fun I received from many people at IPCMS in and (specially) out of the lab: Kerstin, Nicolas, Celine, Manu, Gael, Dimitra, Ondrej, Ingrid, Dominik, Christian, Peter, Ather, Florian, Vadym and Olga– Thank You! A special thanks to Silvia, simply for everything! I got one of the best friend in life! And Michael because, no matter which party or which dinner, everytime I needed his help, he was there!

Of course, many thanks to the best women in this world: my mother and my syster Sara for all the love and support they gave me in each step of my life which made me stronger even for getting through this thesis.

Last but not least, a special thanks to my beloved fiancé (and very soon husband!) Simon. You are the biggest gift of my life from the most beautiful place in the world! I don't even dare to imagine how it would have been without you... I strive everyday to make you proud of me!

Optimizing OFETs properties for spintronics applications

Résumé

Cette thèse a pour but d'étudier le transport de porteur de charge au sein de polymères conjugués, avec comme finalité d'identifier les propriétés des appareils d'électronique organique appropriées pour des applications dans la spintronique organique. Nous avons analysé des échantillons planaires, de géométries latérales, qui offrent la possibilité d'étudier les propriétés de transport sous l'application de différents stimulus et la détection le transport de longue distance du moment angulaire (spin), au sein de semi-conducteurs organiques (OSC). Dans cette configuration, des critères bien établis doivent être satisfait pour réaliser le transport diffusif d'un courant de spin polarisé au travers d'un matériel organique. Nous avons analysé ces différent critères et trouvé des matériaux dont les propriétés physiques fournissent une solution satisfaisante. Le résultat de ce travail fut la création de transistors à effet de champ organiques dont les propriétés répondent au besoin des applications de spintronique.

Mots-clés: polymères conjugués, couche de carbone ultrafine, résistance de contact, haute-mobilité, électronique organiques, spintronique

Summary

In this thesis, charge carrier transport in conjugated polymers is studied with the aim to identify organic electronics devices properties suitable for applications in organic spintronics. We investigate planar samples, in a lateral geometry, which offer the possibility to study transport properties under the application of different stimuli and to detect long-range spin transport in OSCs. In this configuration, well-established criteria must be satisfied to realize diffusive-like transport of a spin-polarized current through an organic materials. We analyze these criteria and find possible materials properties solutions. The outcome is the realization of organic field-effect transistors with properties ad hoc for spintronics applications.

Keywords: conjugated polymers, ultra-thin carbon layers, contact resistance, high mobility, organic electronics, spintronics.